

SURFACE STRUCTURE OF HYDRATED AND Fe(II) REACTED

HEMATITE($1\bar{1}02$) AND (0001)

A

THESIS

Presented to the Faculty

of the University of Alaska Fairbanks

in Partial Fulfillment of the Requirements

for the Degree of

DOCTOR OF PHILOSOPHY

By

Kunaljeet S. Tanwar, M.S., B. Tech.

Fairbanks, Alaska

December 2008

UMI Number: 3351794

INFORMATION TO USERS

The quality of this reproduction is dependent upon the quality of the copy submitted. Broken or indistinct print, colored or poor quality illustrations and photographs, print bleed-through, substandard margins, and improper alignment can adversely affect reproduction.

In the unlikely event that the author did not send a complete manuscript and there are missing pages, these will be noted. Also, if unauthorized copyright material had to be removed, a note will indicate the deletion.

UMI[®]

UMI Microform 3351794

Copyright 2009 by ProQuest LLC.

All rights reserved. This microform edition is protected against unauthorized copying under Title 17, United States Code.

ProQuest LLC
789 E. Eisenhower Parkway
PO Box 1346
Ann Arbor, MI 48106-1346

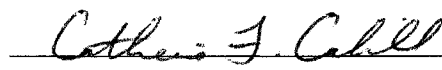
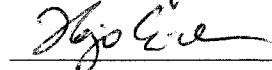
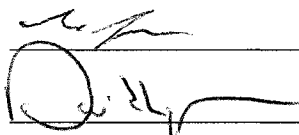
SURFACE STRUCTURE OF HYDRATED AND Fe(II) REACTED

HEMATITE($1\bar{1}02$) AND (0001)

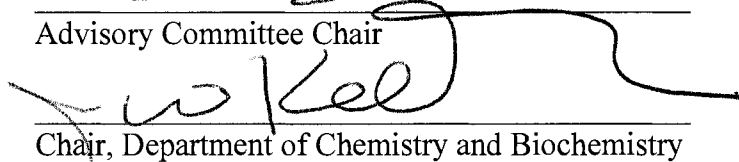
By

Kunaljeet S. Tanwar

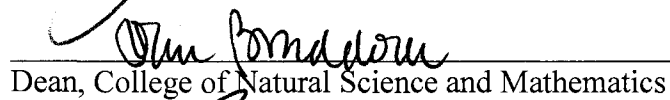
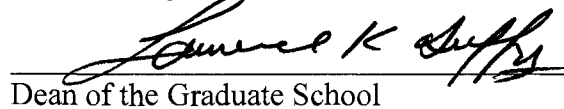
RECOMMENDED:



Advisory Committee Chair


Chair, Department of Chemistry and Biochemistry

APPROVED:


Dean, College of Natural Science and Mathematics
Dean of the Graduate School
Date

ABSTRACT

Reactions on naturally abundant hematite (α -Fe₂O₃) surfaces significantly influence the transport and bio-availability of a number of important nutrients and contaminants. The surface reactivity of α -Fe₂O₃ is dependent on the surface structure, i.e. the identity and coordination of chemical moieties exposed at the surface. The surface structure is strongly influenced by the presence of water and common aqueous species such as Fe(II). Therefore, it is important to understand how the surface structure evolves in the presence of water and aqueous species (e.g. Fe(II)) in order to model the surface reactivity of hematite in natural aquatic systems.

The current study provides a detailed experimental investigation of the surface structure of two predominant natural faces of α -Fe₂O₃, the (1 $\bar{1}$ 02) and (0001) surfaces under hydrated conditions in absence and presence of aqueous Fe(II). The surface structure of hydrated α -Fe₂O₃(1 $\bar{1}$ 02) prepared via a room-temperature wet chemical and mechanical polishing (CMP) procedure is consistent with a surface termination where the top layer of iron atoms is absent compared to the stoichiometric bulk termination. The annealing of CMP prepared α -Fe₂O₃(1 $\bar{1}$ 02) in air at 773 K results in transformation of the surface to a structure consistent with the stoichiometric termination. For CMP prepared α -Fe₂O₃(0001), the experimental results show a co-existence of two distinct structural domains on the surface. The first domain corresponds to hydroxylation of surface Fe atoms, and the second domain is formed by complete removal of the surface Fe cation leading to an exposed oxygen layer on the surface.

The exposure of CMP prepared $\alpha\text{-Fe}_2\text{O}_3(1\bar{1}02)$ and (0001) to aqueous Fe(II) results in structural modification of both surfaces due to adsorption of Fe(II) at crystallographic lattice sites followed by oxidation to Fe(III). Preliminary research conducted to identify the effect of Fe(II) induced surface modification on reactivity using Pb(II) as a reactive probe indicates that the clean and Fe(II)-modified surfaces exhibit significantly different reactivity towards Pb(II). Overall, the systematic structural characterization of hydrated and Fe(II)-modified $\alpha\text{-Fe}_2\text{O}_3$ surfaces presented in the current study will provide a basis to elucidate surface structure-reactivity relationships for hematite and will aid in developing models of mineral-water interfacial reactivity.

TABLE OF CONTENTS

	Page
SIGNATURE PAGE	i
TITLE PAGE	ii
ABSTRACT	iii
TABLE OF CONTENTS	v
LIST OF FIGURES	ix
LIST OF TABLES	xv
ACKNOWLEDGEMENTS	xvii
Chapter 1 INTRODUCTION	1
1.1 IRON (HYDR)OXIDE SURFACES IN NATURE.....	1
1.2 SURFACE MODIFICATION OF IRON (HYDR)OXIDES.....	3
1.3 RESEARCH OBJECTIVES	6
1.4 SUMMARY AND OVERVIEW OF SYSTEMS STUDIED.....	7
REFERENCES	11
Chapter 2 SURFACE DIFFRACTION STUDY OF HYDRATED HEMATITE	
(1$\bar{1}$02) SURFACE	14
ABSTRACT.....	14
2.1 INTRODUCTION	15
2.1.1 Bulk α -Fe ₂ O ₃ Structure and (1 $\bar{1}$ 02) Termination	18
2.2 METHODS	22
2.2.1 Sample Preparation and Data Collection	22

2.2.2 CTR Data Collection.....	23
2.2.3 CTR Data Analyses.....	24
2.2.4 Comparison To Density Functional Theory Calculations	27
2.3 RESULTS AND DISCUSSION	28
2.3.1 Surface Termination.....	28
2.3.2 Description Of Best-fit Structure	33
2.3.3 Comparison to DFT Models	35
2.3.4 Comparison of Best-fit CTR and DFT Models.....	39
2.4 CONCLUSIONS.....	41
ACKNOWLEDGEMENTS	44
REFERENCES	45
Chapter 3 HYDRATED α-Fe₂O₃(1$\bar{1}$02) SURFACE STRUCTURE: ROLE OF	
SURFACE PREPARATION	61
ABSTRACT.....	61
ACKNOWLEDGEMENTS.....	71
REFERENCES	72
Chapter 4 STRUCTURAL STUDY OF Fe(II) ADSORPTION ON	
HEMATITE(1$\bar{1}$02)	79
ABSTRACT.....	79
4.1 INTRODUCTION	80
4.1.1 Structural Investigation of Fe(II) Adsorption	84
4.2 METHODS	86

4.2.1 Sample Preparation	86
4.2.2 Fe(II) Adsorption on α -Fe ₂ O ₃ (1 $\bar{1}$ 02)	86
4.2.3 CTR Data Collection.....	88
4.2.4 CTR Data Analyses.....	89
4.3 RESULTS	91
4.3.1 CTR Results	91
4.3.2 GI-XRD Results.....	97
4.4 DISCUSSION	98
4.5 CONCLUSIONS.....	103
ACKNOWLEDGEMENTS	106
REFERENCES	107
Chapter 5 Fe(II) ADSORPTION ON HEMATITE(0001)	126
ABSTRACT.....	126
5.1 INTRODUCTION	127
5.1.1 α -Fe ₂ O ₃ (0001) Surface Structure.....	130
5.2 METHODS	132
5.2.1 Sample Preparation	132
5.2.2 CTR Data Collection.....	133
5.2.3 CTR Data Analysis	135
5.3 RESULTS	136
5.3.1 α -Fe ₂ O ₃ (0001) Surface Structure.....	136
5.3.1.1 Single domain analysis	137

5.3.1.2 Two domain structural analysis	140
5.3.2 Structure of Fe(II) Reacted α -Fe ₂ O ₃ (0001)	143
5.3.2.1 Single domain models of Fe(II) adsorption	144
5.3.2.2 Two domain models of Fe(II) adsorption	147
5.3.3 GI-XRD Results.....	152
5.4 DISCUSSION.....	153
5.5 CONCLUSIONS.....	157
ACKNOWLEDGEMENTS.....	162
REFERENCES	163
Chapter 6 CONCLUSIONS.....	184
6.1 HYDRATED HEMATITE SURFACE STRUCTURE.....	184
6.2 HEMATITE SURFACE MODIFICATION VIA Fe(II)	186
6.3 IMPACT OF SURFACE MODIFICATION ON SURFACE REACTIVITY: PRELIMINARY INDICATIONS	191
REFERENCES	196
APPENDIX.....	203

LIST OF FIGURES

Page

Figure 2.1 a) In-plane view of the α -Fe₂O₃ (1 $\bar{1}$ 02) surface showing zig-zag rows of oxygen and the real space basis vectors in the surface indexing, shown along with their indices in the bulk indexing; b) layer stacking sequence along the c_s axis for bulk α -Fe₂O₃ (1 $\bar{1}$ 02). The large spheres are O atoms and small spheres are Fe atoms. The ^{III}O represents the oxygen atoms which are triply coordinated to iron.....54

Figure 2.2 Experimental structure factors (F_{HKL}) as a function of perpendicular momentum transfer (L , in reciprocal lattice units) for the α -Fe₂O₃ (1 $\bar{1}$ 02) surface. The dashed lines represent calculated CTRs for the ideal stoichiometric termination (O₂-Fe₂-O₂-Fe₂-O₂-R), the dotted lines are the calculated CTRs for the bulk termination with an added oxygen layer (O₂-O₂-Fe₂-O₂-Fe₂-O₂-R), and the solid lines represent the best fit model ((**H₂O**)₂-(**H₂O**)₂-O₂-X-O₂-Fe₂-O₂-R). The atoms in boldface represent the layers added above the first layer of the stoichiometric termination.....55

Figure 2.3 a) Layer stacking sequence along the c_s axis for the model suggested by previous UHV studies [30, 31]; b) layer stacking sequence along the c_s axis along with layer spacings and percent relaxations for best fit CTR model (**H₂O**)₂-(**H₂O**)₂-O₂-X-O₂-Fe₂-O₂-R. The large spheres are O atoms and small spheres are Fe atoms. The atoms in the boldface represent the layers added above the first layer of the stoichiometric termination. The adsorbed water molecules are shown above layer 1 with arbitrary water molecule orientations. The ^{III}O, ^{II}O, and ^IO represent oxygen triply, doubly and singly coordinated to iron, respectively.....56

Figure 2.4 A comparison of calculated and experimental CTR data for models A4, A2, and A5. The dotted lines are from the direct calculation using the DFT derived coordinates and the solid lines represent the fit with varying occupancy and Debye-Waller factor for the water overlayer, where applicable.....57

Figure 2.5 A comparison of calculated and experimental CTR data for models C2, C3, and C4. The dotted lines are from the direct calculation using the DFT derived coordinates. All three models shown here have zero occupancy for layer 2 Fe.....58

Figure 2.6 A comparison of calculated and experimental CTR data for models C6, C7, and C8. The dotted lines are from the direct calculation using the DFT-derived coordinates and the solid lines represent the fit with varying occupancy and Debye-Waller factors for the water overlayer, where applicable. All three models shown here have zero occupancy for layer 2 Fe.....59

Figure 2.7 In-plane view of the hydroxylated $\alpha\text{-Fe}_2\text{O}_3$ ($1\bar{1}02$) surface showing the probable hydrogen bonding network of surface functional groups in the proposed model along with corresponding hydrogen bond distances. The dashed lines show the possible hydrogen bonds and the distance (in Å) between hydrogen bonded species. The large spheres are O atoms, medium spheres are Fe atoms, and the small spheres are H atoms.....60

Figure 3.1 Layer stacking sequence along the c_s axis for stoichiometric termination, the hydroxylated stoichiometric termination, and the termination with absent layer 2 iron. The large spheres are O atoms and small spheres are Fe atoms. Stacking sequences are shown with unrelaxed layer spacings.....77

Figure 3.2 Experimental structure factors (F_{HKL}) as a function of perpendicular momentum transfer (L , in reciprocal lattice units) for the $\alpha\text{-Fe}_2\text{O}_3$ ($1\bar{1}02$) surface. The dotted lines are the calculated CTRs from the termination model with vacant iron atoms in layer 2 [27] (model A), the dashed lines represent fit obtained for the relaxed stoichiometric termination (model B), and the solid lines represent the best fit model, which is consistent with hydroxylated stoichiometric termination (model C) (see text for details).....78

Figure 4.1 The layer stacking sequence along c_s axis for CMP prepared $\alpha\text{-Fe}_2\text{O}_3$ ($1\bar{1}02$) surface termination. The small spheres are Fe and large spheres are O atoms. The “X” denotes absence of a given layer. The $^{\text{I}}\text{O}$, $^{\text{II}}\text{O}$, and $^{\text{III}}\text{O}$ represent oxygen, which is singly, doubly, and triply coordinated to iron, respectively.....118

Figure 4.2 A comparison of experimental structure factors ($|F_{\text{HKL}}|$) as a function of perpendicular momentum transfer (L , in reciprocal lattice units) for CMP prepared $\alpha\text{-Fe}_2\text{O}_3$ ($1\bar{1}02$) (dots), and $\alpha\text{-Fe}_2\text{O}_3$ ($1\bar{1}02$) reacted with Fe(II) (squares) for a) 2 hr at pH 5.0, b) 34 d at pH 5.0, and c) 5.5 hr at pH 7.0. The data for reacted samples is scaled up by a factor of 1.5 in order to clearly show differences in CTR profiles.....119

Figure 4.3 In plane view of $\alpha\text{-Fe}_2\text{O}_3$ ($1\bar{1}02$) with various possible adsorption models. The possible coordination of adsorbed is shown in text above each model. The $^{\text{I}}\text{O}$, $^{\text{II}}\text{O}$, and $^{\text{III}}\text{O}$ represent oxygen, which is singly, doubly, and triply coordinated to Fe associated with the substrate, respectively.....120

Figure 4.4 The layer stacking sequence along c_s axis for the best-fit CTR model for $\alpha\text{-Fe}_2\text{O}_3$ ($1\bar{1}02$) reacted with Fe(II) for 2 hr at pH 5.0. The small spheres are Fe and large spheres are O atoms. The Fe atoms in circles represent adsorbed Fe(II). The water molecules are shown with random orientations. The best-fit CTR models for $\alpha\text{-Fe}_2\text{O}_3$ ($1\bar{1}02$) reacted with Fe(II) for 34 d at pH 5.0, and 5.5 hr at pH 7.0 also resulted in

similar substrate Fe/O stoichiometry of $\mathbf{O}_{2n}\text{-O}_2\text{-Fe}_{2m}\text{-O}_2\text{-Fe}_2\text{-O}_2\text{-R}$ (see text for details). The atoms in the boldface represent atoms added to unreacted termination.....121

Figure 4.5 The magnitude of experimental structure factors ($|F_{\text{HKL}}|$) normalized by $|F_{\text{CTR}}|$ (circles) as a function of perpendicular momentum transfer (L , in reciprocal lattice units) for $\alpha\text{-Fe}_2\text{O}_3(1\bar{1}02)$ reacted with Fe(II) for 2 hr at pH 5.0. The F_{CTR} can be given as $1/\{1 - \exp(-i2\pi\zeta)\}$ after excluding attenuation factor (Trainor et al., 2002b). The solid line represents the normalized structure factors calculated from the best-fit model.....122

Figure 4.6 The magnitude of experimental structure factors ($|F_{\text{HKL}}|$) normalized by $|F_{\text{CTR}}|$ (circles) as a function of perpendicular momentum transfer (L , in reciprocal lattice units) for $\alpha\text{-Fe}_2\text{O}_3(1\bar{1}02)$ reacted with Fe(II) for 34 d at pH 5.0.....123

Figure 4.7 The magnitude of experimental structure factors ($|F_{\text{HKL}}|$) normalized by $|F_{\text{CTR}}|$ (circles) as a function of perpendicular momentum transfer (L , in reciprocal lattice units) for $\alpha\text{-Fe}_2\text{O}_3(1\bar{1}02)$ reacted with Fe(II) for 5.5 hr at pH 7.0.....124

Figure 4.8 The grazing incidence in-plane X-ray diffraction data at a given incidence angle (α) for $\alpha\text{-Fe}_2\text{O}_3(1\bar{1}02)$ reacted with Fe(II) for a) 34 d at pH 5.0, and b) 5.5 hr at pH 7.0. The measured intensity is rescaled for clarity. The experiments were conducted at room temperature under hydrated He atmosphere. The data shows no evidence for surface precipitation of any ordered mineral phase.....125

Figure 5.1 Structural models and the Fe/O stoichiometry of three chemically distinct surface terminations of $\alpha\text{-Fe}_2\text{O}_3(0001)$. The notation used for representing stoichiometry identifies top three atomic layers which uniquely identify a given termination and R represents the stoichiometric stacking sequence. The layer stacking sequence is shown along the c_s axis. The large spheres are O and small spheres are Fe atoms.....176

Figure 5.2 The magnitudes of experimental structure factors ($|F_{\text{HKL}}|$) (dots) and calculated structure factor magnitudes from single domain (dashed lines) and two domain (solid lines) model as a function of perpendicular momentum transfer (L , in reciprocal lattice units) for unreacted $\alpha\text{-Fe}_2\text{O}_3(0001)$177

Figure 5.3 The layer stacking sequence along c_s axis for best fit single domain model for unreacted $\alpha\text{-Fe}_2\text{O}_3(0001)$ with Fe/O stoichiometry of $\mathbf{O}_{3y}\text{-Fe}_x\text{-O}_3\text{-Fe-R}$, where x and y represent site occupancy of given atomic layers (Table 5.1). The atoms shown in bold face represent atoms that were added to the surface unit cell. The large spheres are O and small spheres are Fe atoms.....178

Figure 5.4 The structure for the best fit two-domain model of unreacted $\alpha\text{-Fe}_2\text{O}_3(0001)$ which includes relaxed (a) O-layer termination and, (b) hydroxylated Fe-layer termination with Fe/O stoichiometry of $\mathbf{O}_3\text{-Fe-Fe-R}$ and $\mathbf{O}_3\text{-Fe-O}_3\text{-Fe-R}$, respectively.

The atoms shown in bold face were added to the surface unit cell. The layer stacking sequence is shown along c_s axis. The large spheres are O, medium spheres are Fe atoms and smallest sphere are H atoms. The water molecules are shown with random orientations. The best fit model parameters are given in Table 5.2 and 5.3.....179

Figure 5.5 A comparison of experimental structure factor magnitudes as a function of perpendicular momentum transfer (L , in reciprocal lattice units) for unreacted (dots) and Fe(II) reacted (empty squares) α -Fe₂O₃(0001). The dotted boxes are used to highlight differences in CTR profile.....180

Figure 5.6 The magnitudes of experimental structure factors ($|F_{HKL}|$) (dots) and calculated structure factor magnitudes from single domain (dashed lines) and two domain (solid lines) model as a function of perpendicular momentum transfer (L , in reciprocal lattice units) for Fe(II) reacted α -Fe₂O₃(0001).....181

Figure 5.7 The layer stacking sequence along c_s axis for best fit single domain model for Fe(II) reacted α -Fe₂O₃(0001) with Fe/O stoichiometry of **O_{3e}-Fe_d-O_{3c}-Fe_b-Fe_a-O₃-Fe-R**, where a, b, c, d, and e represent site occupancy of given atomic layers (Table 5.4). The atoms shown in bold face represent atoms that were added to the surface unit cell. The large spheres are O and small spheres are Fe atoms. The atoms shown in circles denote adsorbed Fe. The layers labeled as A, B, and C represent Fe adsorption sites.....182

Figure 5.8 The structure for the best fit two-domain model for Fe(II) reacted α -Fe₂O₃(0001) which includes relaxed (a) O-layer termination and, (b) hydroxylated Fe-layer termination with Fe/O stoichiometry of **O_{3n}-Fe_m-O₃-Fe-Fe-R** and **O_{3n}-Fe_m-O₃-Fe-Fe-O₃-Fe-R**, respectively. The m and n in above stoichiometry represent occupancy of given layers (Table 5.5 and 5.6). The atoms shown in bold face were added to the surface unit cell. The large spheres are O and small spheres are Fe atoms. The atoms shown in circles denote adsorbed Fe. The layer stacking sequence is shown along c_s axis. The layers labeled as A, B, and C represent Fe adsorption sites.....183

Figure 6.1 a) A simplified model of a hematite particle which has two predominant surface orientations (i.e. $(1\bar{1}02)$ and (0001)) of hematite, and b) structural model of the simplified hematite particle based on results from CTR studies on hydrated α -Fe₂O₃($1\bar{1}02$) and (0001) . The smaller spheres represent Fe atoms and the larger spheres represent O atoms. The ^IO, ^{II}O, and ^{III}O represent oxygen atoms singly, doubly and triply coordinated to Fe, respectively.....197

Figure 6.2 A structural model of the simplified hematite particle after reacted with Fe(II) based on results from CTR studies on Fe(II) reacted α -Fe₂O₃($1\bar{1}02$) and (0001) . The smaller spheres are Fe and the larger spheres are O atoms. The atoms shown in circles represent adsorbed Fe atoms.....198

Figure 6.3 A comparison of experimental structure factors ($|F_{HKL}|$) as a function of perpendicular momentum transfer (L , in reciprocal lattice units) for unreacted (squares) and Pb(II) reacted (diamonds) $\alpha\text{-Fe}_2\text{O}_3(1\bar{1}02)$. The data for Pb(II) reacted surface is scaled higher than unreacted surface for clarity.....199

Figure 6.4 A comparison of experimental structure factors ($|F_{HKL}|$) as a function of perpendicular momentum transfer (L , in reciprocal lattice units) for Pb(II) adsorption on $\alpha\text{-Fe}_2\text{O}_3(1\bar{1}02)$ (diamonds) and Pb(II) adsorption on Fe(II) reacted $\alpha\text{-Fe}_2\text{O}_3(1\bar{1}02)$ (circles).....200

Figure 6.5 A comparison of surface structure of unreacted and Fe(II) reacted $\alpha\text{-Fe}_2\text{O}_3(1\bar{1}02)$. The $^{\text{I}}\text{O}$, $^{\text{II}}\text{O}$, and $^{\text{III}}\text{O}$ represent oxygen atoms singly, doubly and triply coordinated to Fe, respectively. The smaller spheres are Fe and the larger spheres are O atoms. The atoms shown in circles represent adsorbed Fe atoms.....201

Figure 6.6 Structural models of two possible tri-dentate Pb(II) binding geometries on $\alpha\text{-Fe}_2\text{O}_3(1\bar{1}02)$. The small, medium and large spheres represent Fe, O and Pb atoms, respectively. The $^{\text{I}}\text{O}$, $^{\text{II}}\text{O}$ and $^{\text{III}}\text{O}$ represent oxygen atoms which singly, doubly and triply coordinated to Fe associated with the substrate, respectively. Only top four layers of the substrate are shown for clarity.....202

Figure A.1 Experimental structure factor magnitudes ($|F_{HKL}|$) as a function of perpendicular momentum transfer (L , in reciprocal lattice units) for Pb(II) reacted $\alpha\text{-Fe}_2\text{O}_3(1\bar{1}02)$216

Figure A.2 Experimental structure factor magnitudes ($|F_{HKL}|$) as a function of perpendicular momentum transfer (L , in reciprocal lattice units) for Pb(II) adsorption on Fe(II) pre-reacted $\alpha\text{-Fe}_2\text{O}_3(1\bar{1}02)$217

Figure A.3 Resonant anomalous X-ray scattering (RAXS) data, i.e. experimental structure factor magnitudes ($|F|$) as a function of incident beam energy at a fixed (HKL) value which is identified at the top of each subplot, for Pb(II) reacted $\alpha\text{-Fe}_2\text{O}_3(1\bar{1}02)$218

Figure A.4 Resonant anomalous X-ray scattering (RAXS) data, i.e. experimental structure factor magnitudes ($|F|$) as a function of incident beam energy at a fixed (HKL) value which is identified at the top of each subplot, for Pb(II) adsorbed on Fe(II) pre-reacted $\alpha\text{-Fe}_2\text{O}_3(1\bar{1}02)$219

Figure A.5 Structural models of three possible Pb binding geometries on $\alpha\text{-Fe}_2\text{O}_3(1\bar{1}02)$. The small, medium and large spheres represent Fe, O and Pb atoms, respectively. Only

top four layers of the substrate are shown and only one of the two chemically equivalent Pb atoms is shown for clarity.....220

Figure A.6 Simulations of RAXS profiles for three different models shown in Figure A.5. The solid, dashed and dotted lines represent models A, B, and C, respectively.....221

Figure A.7 Simulations of RAXS profiles for model A (Figure A.5) as a function of Pb(II) occupancy.....222

LIST OF TABLES

	Page
Table 2.1 Unrelaxed surface unit cell coordinates and best-fit model parameters from the analysis of CTR data.....	49
Table 2.2 Stoichiometry and layer sequence for various clean and hydrated surface models that were calculated using DFT and compared with experimental CTR data.....	50
Table 2.3 Percent layer relaxations (% Δ) for selected DFT models calculated by Lo et al. [20] and the best-fit experimental model.....	51
Table 2.4 Predicted proton stoichiometry and bond valence analysis for charge neutral surfaces with Fe-O stoichiometry O ₂ -X-O ₂ -Fe ₂ -O ₂ -R (C-series in Table 2.2).....	52
Table 2.5 Bond-valence sum (Σs) calculations for selected DFT models calculated by Lo et al. [20] and the best-fit experimental model.....	53
Table 3.1 Unrelaxed surface unit cell coordinates and best-fit model parameters from CTR data analysis.....	75
Table 3.2 Interlayer spacings and percent layer relaxations for the best-fit model.....	76
Table 4.1 Unrelaxed surface unit cell coordinates for clean α -Fe ₂ O ₃ (1 $\bar{1}$ 02) and best-fit model coordinates and parameters for α -Fe ₂ O ₃ (1 $\bar{1}$ 02) reacted with Fe(II) for 2 hr at pH 5.0.....	115
Table 4.2 Best-fit model coordinates and parameters for α -Fe ₂ O ₃ (1 $\bar{1}$ 02) reacted with Fe(II) for 34 d at pH 5.0.....	116
Table 4.3 Best-fit model coordinates and parameters for α -Fe ₂ O ₃ (1 $\bar{1}$ 02) reacted with Fe(II) for 5.5 hr at pH 7.0.....	117
Table 5.1 Unrelaxed surface unit cell coordinates and best fit model coordinates and parameters from CTR data analysis using a single structural domain for unreacted α -Fe ₂ O ₃ (0001).....	170
Table 5.2 Best-fit model coordinates and parameters for O-layer termination of unreacted α -Fe ₂ O ₃ (0001) obtained from two domain structural analysis.....	171
Table 5.3 Best-fit model coordinates and parameters for hydroxylated Fe-layer termination of unreacted α -Fe ₂ O ₃ (0001) obtained via two domain structural analysis..	172

Table 5.4 Best-fit model coordinates and parameters for the single domain structural model of Fe(II) reacted α -Fe ₂ O ₃ (0001).....	173
Table 5.5 Best-fit model coordinates and parameters for Fe(II) reacted O-layer termination of α -Fe ₂ O ₃ (0001) obtained via two domain structural analysis.....	174
Table 5.6 Best-fit model coordinates and parameters for Fe(II) reacted hydroxylated Fe-layer termination of α -Fe ₂ O ₃ (0001) obtained via two domain structural analysis.....	175
Table A.1 Surface unit cell coordinates for α -Fe ₂ O ₃ (1 $\bar{1}$ 02) including Pb adsorbed at the surface in a geometry similar to model A (Figure A.5).....	213
Table A.2 Surface unit cell coordinates for α -Fe ₂ O ₃ (1 $\bar{1}$ 02) including Pb adsorbed at the surface in a geometry similar to model B (Figure A.5).....	214
Table A.3 Surface unit cell coordinates for α -Fe ₂ O ₃ (1 $\bar{1}$ 02) including Pb adsorbed at the surface in a geometry similar to model C (Figure A.5).....	215

ACKNOWLEDGEMENTS

I want to thank a number of people who have helped me throughout my graduate studies. Firstly, I want to acknowledge my graduate committee's chair Dr. Tom Trainor for his help in conducting research, preparing manuscripts and guiding me through difficult decision making times. I cannot describe in words how much Dr. Trainor has contributed to my overall learning and professional development. The other people who deserve special mention for their help in conducting experiments and/or taking time to provide feedback on results are: Dr. Sarah Petitto, Dr. Sanjit Ghose, Dr. Cynthia Lo, Dr. Peter Eng, Dr. Anne Chaka and Dr. Gordon Brown Jr. I also thank all my other co-authors i.e., Dr. Don Walko, Dr. Glenn Waychunas and Dr. Jeffrey Catalano, on the manuscripts included in this thesis for their help in improving quality of the manuscripts. In addition, I am very thankful to the members of my research committee: Dr. William Simpson, Dr. Cathy Cahill, Dr. Hajo Eicken, and Dr. David Barnes for their guidance and support during my graduate program. I also want to thank all the current and former members of Dr. Trainor's research group (Kristen Williams, Vanessa Ritchie, Anastasia Ilgen, Chris Iceman, Ashley Jones and Raena Rowland) at UAF for providing helpful suggestions in preparing presentations and also for providing feedback on my research throughout my time at UAF. In the end, I am extremely grateful to my wife Sunita Rathore, my parents (Mr. Krishan Jit Singh Tanwar and Mrs. Akhilesh Tanwar) and my entire family in India for their patience and support throughout my life. Thank you all.

Chapter 1 INTRODUCTION

1.1 IRON (HYDR)OXIDE SURFACES IN NATURE

Iron-(hydr)oxides are ubiquitous in natural aquatic, soil and sediment systems and exist in various forms such as hematite ($\alpha\text{-Fe}_2\text{O}_3$), goethite ($\alpha\text{-FeOOH}$), magnetite (Fe_3O_4) and ferrihydrite ($\text{Fe}(\text{OH})_3$) [1]. Goethite and hematite are known as the two most thermodynamically stable and persistent phases of iron (hydr)oxides, where goethite is the more abundant form [1]. Hematite is the second most widespread iron (hydr)oxide phase but is generally found in association with relatively small amounts of goethite [1]. Ferrihydrite is another commonly found iron (hydr)oxide, which is often a precursor to relatively more stable phases because it generally transforms to goethite, magnetite and/or hematite with ageing [1].

All forms of natural iron (hydr)oxides generally possess a high specific surface area due to their occurrence as small particles (μm - nm size range) [1]. Under aqueous conditions, the surfaces of iron (hydr)oxides are characterized by the presence of highly reactive (hydr)oxo functional groups. Due to the presence of high reactive specific surface area, these minerals significantly influence the composition of aqueous geochemical systems [2]. For example, iron (hydr)oxides act as important substrates for heterogeneous reductive transformations of a number of environmental contaminants [3-5]. In addition, iron (hydr)oxides play a key role in controlling the transport and bioavailability of important nutrients (e.g. phosphate) and contaminants (e.g. heavy metals) via adsorption

and co-precipitation processes [6, 7]. Iron (hydr)oxides also influence the global cycling and bio-availability of Fe, primarily due to redox coupling between aqueous Fe(II) and solid phase associated Fe(III) [6, 7]. Overall, due to their widespread occurrence and high surface reactivity iron (hydr)oxides are one of the most important natural substrates for numerous environmentally relevant reactions/transformations. Therefore, it is essential to understand what controls the surface reactivity of iron (hydr)oxides and how their surface reactivity might be altered under varied environmental conditions.

The reactivity of a mineral surface is a function of the molecular scale surface structure, i.e. the type, local structure, and topographic arrangement of the chemical moieties exposed at the surface [8, 9]. The surface structure in turn is dictated by the structure and composition of the bulk material, crystallographic orientation of the terminating plane, and chemical history of the surface. The ideal stoichiometric termination of a crystalline iron oxide phase results in the presence of interfacial moieties which are under-coordinated with respect to the bulk structure. Therefore, the Fe atoms exposed at the surface tend to act as strong electron acceptor (Lewis acid) sites, and surface oxygen atoms acts as strong electron donor (Lewis base) sites.

Under aqueous conditions, the interaction of water with the atoms exposed at the surface significantly affects the surface structure and reactivity [9, 10]. The coordination shells of exposed Fe atoms are likely to be completed due to adsorption and/or dissociation of water at the under-coordinated Fe sites [11-13]. The dangling oxygen bonds at the

surface can also get saturated with H^+ in the presence of water [12, 14]. The availability of additional chemical components (H_2O , OH^- , H^+) allows for a range of possible stable (charge neutral and auto-compensated) surface structures, where a particular termination at the solid-solution interface is dictated by overall minimization of the interfacial free energy [12, 14]. Therefore, the knowledge of hydrated surface structures is critical for improved comprehension of surface reactivity of iron (hydr)oxides. However, there are only a limited number of studies that provide a detailed molecular-scale understanding of the iron (hydr)oxide surfaces in aqueous environments [11, 12]. For development of models of interfacial reactivity, a systematic investigation of iron (hydr)oxide surface structures under simulated environmental conditions is needed [10].

1.2 SURFACE MODIFICATION OF IRON (HYDR)OXIDES

In natural geochemical systems, the surface structure and corresponding reactivity of an iron (hydr)oxide surface can be modified due to microbial activity and/or abiotic chemical interactions with common aqueous species. Under anoxic conditions, the dissimilatory iron reducing bacteria (DIRB) promote reductive dissolution of iron (hydr)oxides by using Fe(III) as terminal electron acceptor during microbial respiration [15-17]. The reductive dissolution of these oxides results in release of high concentrations of ferrous ion in the system, which can adsorb on iron (hydr)oxide surfaces prevalent in the system [17, 18]. The adsorption of Fe(II) on iron (hydr)oxide surfaces not only modifies their structure and reactivity but also has important implications for the fate and transport of numerous contaminants.

The presence of aqueous and adsorbed Fe(II) is known to accelerate heterogeneous reductive transformations of numerous organic compounds including polyhalogenated hydrocarbons [19-22], and nitroaromatic compounds [23-28]. Inorganic contaminants such as U(VI), Cr(VI), and Tc(VII) are also reduced to less mobile and toxic species (i.e. U(IV), Cr(III), and Tc(IV) respectively) in presence of adsorbed Fe(II) [27, 29-33]. A few previous studies show the rate of contaminant reduction increases with an increase in amount of adsorbed Fe(II) suggesting that the Fe(II) adsorption plays a central role in catalyzing contaminant reduction [20, 27]. However, a structural knowledge of how Fe(II) adsorbs on the iron (hydr)oxide surfaces is still required to elucidate the mechanisms of processes that follow Fe(II) adsorption.

In addition to the enhancement of contaminant reduction rates, the presence and interactions of aqueous Fe(II) with iron (hydr)oxide surfaces strongly affect the structure and reactivity of these oxides. For example, co-existence of aqueous and adsorbed Fe(II) can result in inhibition of microbially promoted reductive dissolution of iron (hydr)oxides [34-37]. The adsorption of Fe(II) may lead to formation of a Fe(II)/Fe(III) mixed valence surface [38] and/or growth of the substrate in a preferred crystallographic direction [24, 39]. The interactions of Fe(II) with ferric oxides is also known to induce bulk phase transformations depending upon Fe(II)/Fe(III) molar ratio [18, 40, 41], pH [42] and structure of the iron (hydr)oxide substrate [43]. A more detailed discussion of previous work on the impact of Fe(II) adsorption on the structure of iron (hydr)oxides under

various conditions is presented in chapters 4 and 5. In brief, a common result from previous studies is that the adsorption of Fe(II) is the central step leading to structural modification/transformation of iron (hydr)oxides. However, a structural interpretation of Fe(II) adsorption on iron (hydr)oxide surfaces is not very well developed.

The Fe(II) binding on iron (hydr)oxides is mostly explained via modeling the macroscopic uptake of Fe(II) using surface complexation models [27, 31, 38, 44-46]. In most surface complexation models, the adsorbed Fe(II) is assumed to form a monodentate surface complex, i.e. $\equiv\text{Fe(III)}\text{-O-Fe(II)}^+$ and/or $\equiv\text{Fe(III)}\text{-O-Fe(II)-OH}$ [27, 31, 38, 45, 46], where $\equiv\text{Fe(III)}\text{-O}$ denotes a surface site. However, the extent of Fe(II) uptake and the reactivity of surface bound Fe(II) is likely to strongly depend upon the nature of the substrate and the local structural environment of surface bound Fe(II), which is not resolved for most iron (hydr)oxides and is not considered in the majority of existing surface complexation models. Recent research using Mossbauer spectroscopy has shown that the adsorbed Fe(II) oxidizes to Fe(III) due to interfacial electron transfer with the underlying iron (hydr)oxide substrate [45, 47, 48]. The mobility of the electron transferred from the adsorbed Fe(II) to the iron (hydr)oxide substrate is also shown to be strongly influenced by the coordination geometry of the donor Fe(II) and the surface structure of the acceptor substrate [39, 49, 50]. In summary, the results of the above discussed studies clearly emphasize the structural knowledge of Fe(II) binding geometry is essential for enhanced understanding of the structural modification of iron (hydr)oxide surfaces in Fe(II) rich environments.

1.3 RESEARCH OBJECTIVES

As discussed above, the surface reactivity of iron (hydr)oxides is strongly dependent on the surface structure. However, there are limited studies that systematically explain the surface structure-reactivity relationship for iron (hydr)oxides under aqueous conditions. The research work presented in this thesis is aimed at gaining molecular scale insights into the structure of iron (hydr)oxide surfaces in the presence of water and how their structure is modified due to interactions with aqueous Fe(II). For the current work, hematite (α -Fe₂O₃), which is a widespread and thermodynamically stable form of iron oxide under most environmental conditions, is chosen as the substrate. The natural α -Fe₂O₃ has two predominant growth faces i.e. (1 $\bar{1}$ 02) and the (0001). In the current research, natural single crystals of hematite (obtained from Bahia, Brazil) oriented along the (1 $\bar{1}$ 02) and (0001) planes are utilized as model systems for hematite surfaces. Initially, the surface structures of α -Fe₂O₃(1 $\bar{1}$ 02) and (0001) were studied in presence of water. The α -Fe₂O₃(1 $\bar{1}$ 02) and (0001) were then reacted with aqueous Fe(II) and the surface structures were identified to understand the surface binding of Fe(II) on these surfaces. Specifically, the work presented here will elucidate: (i) the molecular scale structure of hematite (1 $\bar{1}$ 02) and (0001) surfaces under hydrated conditions, (ii) how Fe(II) binding modifies the surface structure of hematite (1 $\bar{1}$ 02) and (0001), and (iii) how the surface binding of Fe(II) is affected by varying reaction time, pH, and substrate surface structure. Importantly, the structural depiction of hydrated hematite surface

structures and their modification via Fe(II) will provide the basis needed to understand the surface structure-reactivity relationship for hematite.

1.4 SUMMARY AND OVERVIEW OF SYSTEMS STUDIED

The current dissertation is divided into six chapters, where chapter 1 and 6 are general introduction and conclusions, respectively. The core of the research work is divided into four different chapters (i.e. chapters 2-5). Each of the chapters 2-5 are either published or submitted as independent manuscripts in peer reviewed journals. The citations for the published/submitted manuscripts included in this thesis are provided on the title page of each chapter.

In chapter 2, the structure of the hydroxylated α -Fe₂O₃ (1 $\bar{1}$ 02) surface prepared via a wet chemical and mechanical polishing (CMP) procedure was determined using crystal truncation rod X-ray diffraction (CTR). The results show the hydroxylated CMP-prepared surface has a vacant topmost Fe layer as compared to the ideal stoichiometric termination. The experimentally derived surface model was compared with the theoretical models developed using density functional theory (DFT) calculations [14] to identify the most likely protonation states of the surface (hydr)oxo moieties. The results illustrate that the best fit surface model has predominantly three types of (hydr)oxo functional groups exposed at the surface at circum-neutral pH: Fe-OH₂, Fe₂-OH, and Fe₃-O. These results provide a structural basis for interpreting the reactivity of model iron-(hydr)oxide surfaces under aqueous conditions.

The work presented in chapter 3 is continuation of the research highlighted in chapter 2 and is focused on understanding the role of surface preparation procedures in dictating the surface structure of hydrated $\alpha\text{-Fe}_2\text{O}_3(1\bar{1}02)$. The $\alpha\text{-Fe}_2\text{O}_3(1\bar{1}02)$ surface structure was studied under two different surface preparation conditions using crystal truncation rod (CTR) diffraction. Wet chemical and mechanical polishing (CMP) at 298 K results in a crystalline surface termination in which the top layer of iron atoms is absent compared to the stoichiometric bulk termination. Annealing the surface in air at 773 K resulted in transformation of the surface to a structure consistent with hydroxylation of the stoichiometric termination. These results show an ambient pressure surface preparation pathway leading to a stoichiometric hydroxylated surface, which is apparently a meta-stable configuration at room temperature.

The chapter 4 details the investigation of $\alpha\text{-Fe}_2\text{O}_3(1\bar{1}02)$ surface structure after reaction with Fe(II) under anoxic conditions and different conditions of reaction time and pH. The results show the crystalline termination of $\alpha\text{-Fe}_2\text{O}_3(1\bar{1}02)$ is modified due to adsorption of Fe(II) at crystallographic lattice sites, where the binding sites for adsorbed Fe are similar under all studied conditions: reaction for 2 h at pH 5.0, for 34 d at pH 5.0, and for 5.5 h at pH 7.0. The occupancy of adsorbed Fe increases with both reaction time and pH, which is consistent with typical cation adsorption behavior on iron (hydr)oxide surfaces. The Fe-O bond lengths of the (ordered) surface Fe atoms are characteristic of Fe(III), which provides indirect evidence for oxidation of adsorbed Fe(II) to Fe(III).

Overall, the structural characterization of the Fe(II) adsorption reaction results in an enhanced understanding of how reduced iron affects the structure, stability and reactivity of hematite.

The chapter 5 elucidates the surface structure of α -Fe₂O₃(0001) studied using crystal truncation rod (CTR) diffraction before and after reaction with Fe(II). The CTR results show the unreacted α -Fe₂O₃(0001) surface consists of two chemically distinct structural domains i.e., an O-layer and a hydroxylated Fe-layer termination. After exposing the α -Fe₂O₃(0001) to Fe(II), the surface structures of both co-existing structural domains were modified due to adsorption of Fe(II) at crystallographic lattice sites of the substrate resulting in six-coordinated adsorbed Fe at the surface. The average Fe-O bond lengths for adsorbed Fe were consistent with typical Fe(III)-O bond lengths (in octahedral coordination) indicating that the Fe(II) is oxidized to Fe(III) following adsorption. The molecular scale structural identification of adsorbed Fe presented here will provide an improved understanding of Fe(II) induced structural modification of hematite surfaces, which in turn will aid in assessing the effective reactivity of hematite in Fe(II) rich environments.

In chapter 6, the results presented in the chapters 2-5 are integrated to obtain a simplified molecular scale structure model of hydrated hematite and identify the surface structure modification due to interactions with aqueous Fe(II). This chapter also includes a subset of preliminary research on the impact of surface modification on the surface reactivity of

hematite, which is an important research direction that can be pursued in future. The details of the preliminary experimental work are included in the Appendix.

REFERENCES

- [1] R. M. Cornell and U. Schwertmann, (1996) 573 pp, Wiley-VCH.
- [2] W. Stumm and J. J. Morgan, (1995) 1022 pp, Wiley-Interscience.
- [3] W. Stumm, Croat. Chem. Acta 70 (1997) 71.
- [4] W. Stumm, Perspectives in Environmental Chemistry, Ed. Donald Macalady, Oxford University Press (1998) 3.
- [5] B. Wehrli, B. Sulzberger and W. Stumm, Chem. Geol. 78 (1989) 167.
- [6] W. Stumm and B. Sulzberger, Geochim. Cosmochim. Acta 56 (1992) 3233.
- [7] B. Sulzberger, D. Suter, C. Siffert, S. Banwart and W. Stumm, Mar. Chem. 28 (1989) 127.
- [8] W. Stumm, B. Sulzberger and J. Sinniger, Croat. Chem. Acta 63 (1990) 277.
- [9] W. Stumm, Colloids Surf., A 73 (1993) 1.
- [10] G. E. Brown, Jr., V. E. Henrich, W. H. Casey, D. L. Clark, C. Eggleston, A. Felmy, D. W. Goodman, M. Graetzel, G. Maciel, M. I. McCarthy, K. H. Nealson, D. A. Sverjensky, M. F. Toney and J. M. Zachara, Chem. Rev. 99 (1999) 77.
- [11] J. G. Catalano, P. Fenter and C. Park, Geochim. Cosmochim. Acta 71 (2007) 5313.
- [12] T. P. Trainor, A. M. Chaka, P. J. Eng, M. Newville, G. A. Waychunas, J. G. Catalano and G. E. Brown, Surf. Sci. 573 (2004) 204.
- [13] M. A. Henderson, S. A. Joyce and J. R. Rustad, Surf. Sci. 417 (1998) 66.
- [14] C. S. Lo, K. S. Tanwar, A. M. Chaka and T. P. Trainor, Phys. Rev. B: Condens. Matter 75 (2007) 075425/1.
- [15] D. R. Lovley, Microbiol. Rev. 55 (1991) 259.
- [16] D. R. Lovley, FEMS Microbiol. Rev. 20 (1997) 305.
- [17] C. M. Hansel, S. G. Benner, J. Neiss, A. Dohnalkova, R. K. Kukkadapu and S. Fendorf, Geochim. Cosmochim. Acta 67 (2003) 2977.
- [18] C. M. Hansel, S. G. Benner and S. Fendorf, Environ. Sci. Technol. 39 (2005) 7147.

- [19] M. Elsner, S. B. Haderlein, T. Kellerhals, S. Luzi, L. Zwank, W. Angst and R. P. Schwarzenbach, *Environ. Sci. Technol.* 38 (2004) 2058.
- [20] J. E. Amonette, D. J. Workman, D. W. Kennedy, J. S. Fruchter and Y. A. Gorby, *Environ. Sci. Technol.* 34 (2000) 4606.
- [21] M. Erbs, H. C. B. Hansen and C. E. Olsen, *Environ. Sci. Technol.* 33 (1999) 307.
- [22] K. Pecher, S. B. Haderlein and R. P. Schwarzenbach, *Environ. Sci. Technol.* 36 (2002) 1734.
- [23] D. Kim and T. J. Strathmann, *Environ. Sci. Technol.* 41 (2007) 1257.
- [24] C. L. Chun, R. L. Penn and W. A. Arnold, *Environ. Sci. Technol.* 40 (2006) 3299.
- [25] D. Colon, E. J. Weber, J. L. Anderson, P. Winget and L. A. Suarez, *Environ. Sci. Technol.* 40 (2006) 4449.
- [26] T. B. Hofstetter, C. G. Heijman, S. B. Haderlein, C. Holliger and R. P. Schwarzenbach, *Environ. Sci. Technol.* 33 (1999) 1479.
- [27] L. Charlet, E. Silvester and E. Liger, *Chem. Geol.* 151 (1998) 85.
- [28] J. Klausen, S. P. Troeber, S. B. Haderlein and R. P. Schwarzenbach, *Environ. Sci. Technol.* 29 (1995) 2396.
- [29] J. K. Fredrickson, J. M. Zachara, D. W. Kennedy, R. K. Kukkadapu, J. P. McKinley, S. M. Heald, C. Liu and A. E. Plymale, *Geochim. Cosmochim. Acta* 68 (2004) 3171.
- [30] L. Charlet, E. Liger and P. Gerasimo, *J. Environ. Eng.* 124 (1998) 25.
- [31] E. Liger, L. Charlet and P. Van Cappellen, *Geochim. Cosmochim. Acta* 63 (1999) 2939.
- [32] I. J. Buerge and S. J. Hug, *Environ. Sci. Technol.* 33 (1999) 4285.
- [33] L. E. Eary and D. Rai, *Am. J. Sci.* 289 (1989) 180.
- [34] E. E. Roden and J. M. Zachara, *Environ. Sci. Technol.* 30 (1996) 1618.
- [35] E. E. Roden and M. M. Urrutia, *Geomicrobiol. J.* 19 (2002) 209.

- [36] C. Liu, J. M. Zachara, Y. A. Gorby, J. E. Szecsody and C. F. Brown, *Environ. Sci. Technol.* 35 (2001) 1385.
- [37] R. A. Royer, B. A. Dempsey, B.-H. Jeon and W. D. Burgos, *Environ. Sci. Technol.* 38 (2004) 187.
- [38] B. R. Coughlin and A. T. Stone, *Environ. Sci. Technol.* 29 (1995) 2445.
- [39] S. V. Yanina and K. M. Rosso, *Science* 320 (2008) 218.
- [40] Y. Tamaura, K. Ito and T. Katsura, *J. Chem. Soc. Dalton Trans.* (1983) 189.
- [41] E. Tronc, P. Belleville, J. P. Jolivet and J. Livage, *Langmuir* 8 (1992) 313.
- [42] B.-H. Jeon, B. A. Dempsey and W. D. Burgos, *Environ. Sci. Technol.* 37 (2003) 3309.
- [43] H. D. Pedersen, D. Postma, R. Jakobsen and O. Larsen, *Geochim. Cosmochim. Acta* 69 (2005) 3967.
- [44] T. Hiemstra and W. H. van Riemsdijk, *Geochim. Cosmochim. Acta* 71 (2007) 5913.
- [45] E. Silvester, L. Charlet, C. Tournassat, A. Gehin, J.-M. Greneche and E. Liger, *Geochim. Cosmochim. Acta* 69 (2005) 4801.
- [46] Y. Zhang, L. Charlet and P. W. Schindler, *Colloids Surf.* 63 (1992) 259.
- [47] A. G. B. Williams and M. M. Scherer, *Environ. Sci. Technol.* 38 (2004) 4782.
- [48] P. Larese-Casanova and M. M. Scherer, *Environ. Sci. Technol.* 41 (2007) 471.
- [49] S. Kerisit and K. M. Rosso, *Geochim. Cosmochim. Acta* 70 (2006) 1888.
- [50] S. Kerisit and K. M. Rosso, *J. Chem. Phys.* 127 (2007) 124706/1.

Chapter 2 SURFACE DIFFRACTION STUDY OF HYDRATED HEMATITE ($1\bar{1}02$) SURFACE*

ABSTRACT

The structure of the hydroxylated α -Fe₂O₃ ($1\bar{1}02$) surface prepared via a wet chemical and mechanical polishing (CMP) procedure was determined using x-ray crystal truncation rod diffraction. The experimentally determined surface model was compared with theoretical structures developed from density functional theory (DFT) calculations to identify the most likely protonation states of the surface (hydr)oxo moieties. The results show that the hydroxylated CMP-prepared surface differs from an ideal stoichiometric termination due to vacancies of the near surface bulk Fe sites. This result differs from previous ultra high vacuum studies where two stable terminations were observed: a stoichiometric (1×1) termination and a partially reduced (2×1) reconstructed surface. The complementary DFT studies suggest that hydroxylated surfaces are thermodynamically more stable than dehydroxylated surfaces in the presence of water. The results illustrate that the best fit surface model has predominantly three types of (hydr)oxo functional groups exposed at the surface at circumneutral pH: Fe-OH₂, Fe₂-OH, and Fe₃-O and provide a structural basis for interpreting the reactivity of model iron-(hydr)oxide surfaces under aqueous conditions.

* Tanwar K. S., Lo C. S., Eng P. J., Catalano J. G., Walko D. A., Brown G. E., Waychunas G. A., Chaka A. M., and Trainor T. P. (2007) Surface diffraction study of the hydrated hematite ($1\bar{1}02$) surface. *Surf. Sci.* **601**, 460-474.

2.1 INTRODUCTION

Iron-(oxyhydr)oxides occur throughout natural aquatic and soil systems and play a key role in dictating the geochemistry of natural waters. Due to their high specific surface area and reactive (hydr)oxo surface functional groups, iron-(oxyhydr)oxides are often a dominant scavenger of aqueous trace metal(oids) through adsorption reactions. These minerals also act as key substrates in numerous heterogeneous chemical transformations of importance in the degradation and transformation of environmental contaminants [1-4]. Iron-(oxyhydr)oxides also play a key role in controlling the availability and geochemical cycling of iron, largely through the redox couple between aqueous Fe(II) and solid phase Fe(III) [5-7]. The macroscopic reactivity of a mineral-water interface system depends upon the coordination chemistry and topographic arrangement of the exposed surface functional groups, which in turn is a function of the structure and composition of the bulk material, crystallographic orientation of the terminating plane, and chemical/biological history of the exposed surface. However, a detailed molecular-scale understanding of the influence of these key variables on the structure and reactivity of environmental interface systems is lacking. Therefore, systematic investigation of mineral surface structures under simulated environmental conditions is needed to further development of detailed models of environmental interfacial processes [8].

An ideal stoichiometric termination of a crystalline metal-oxide phase generally results in the presence of interfacial moieties that are under-coordinated with respect to the bulk structure; therefore surface metals tend to act as strong electron acceptor (Lewis acid)

sites, and surface oxygens acts as strong electron donor (Lewis base) sites. When considering the environmental reactivity of metal-oxide surfaces, the interaction of water with the surface is of primary importance. Water interaction is likely to result in completion of the coordination shells of exposed surface cations with OH^- or H_2O , and saturation of the dangling oxygen bonds with H^+ . The availability of additional chemical components (H_2O , OH^- , H^+) also allows for a range of possible stable (charge neutral and auto-compensated) surface structures, with the particular termination at the solid-solution interface being dictated by overall minimization of the interfacial free energy and the chemical history of the surface.

Characterization of the structure and composition of clean and hydroxylated metal-oxide surfaces is critical to developing a structural interpretation of interface reactivity. Chambers et al. (2002) have shown that clean and hydroxylated metal-oxide surfaces show dramatic differences in reactivity with respect to adsorption and film growth [9]. The reactivity of hydroxylated metal-oxides has also been shown to vary depending on the predominant coordination chemistry of the surface hydroxyl functionalities. For example, the hydroxylated $\alpha\text{-Al}_2\text{O}_3$ (0001) surface is terminated by hydroxyl groups that are doubly coordinated with Al ($\text{Al}_2\text{-OH}$ or $^{\text{II}}\text{OH}$) [10]. This surface has nearly an order of magnitude lower affinity towards binding aqueous Pb(II) than the $\alpha\text{-Al}_2\text{O}_3$ ($1\bar{1}02$) surface, which has surface (hydr)oxo groups in three different coordination environments (i.e. $^{\text{I}}\text{O}$, $^{\text{II}}\text{O}$, and $^{\text{III}}\text{O}$) [11-14]. In addition, the bulk isostructural $\alpha\text{-Fe}_2\text{O}_3$ ($1\bar{1}02$) and $\alpha\text{-Al}_2\text{O}_3$ ($1\bar{1}02$) surfaces have been shown to exhibit different reactive behavior towards

U(VI) [15]. These results suggest that the coordination chemistry of the functional groups at the water-substrate interface plays a major role in dictating surface reactivity.

The systematic investigation of well-characterized metal-oxide/fluid interface systems requires experimental probes that can provide molecular-scale structural information under *in situ* (i.e. under bulk solution) or hydrated conditions [8, 16]. X-ray scattering techniques are ideally suited to study the structure of the solid-aqueous interface due to the high penetrating power of x-rays and their sensitivity to molecular-scale structure. In particular, crystal truncation rod (CTR) diffraction has emerged as a powerful technique to determine the average structure of mineral-fluid interface systems due to the surface-sensitive nature of the measured signal [17]. The scattered intensity in a CTR measurement depends directly on the structure factor of the surface unit cell, allowing for identification of the surface termination, atomic displacements, atomic occupancies, and order parameters [18, 19].

In the present study, we utilize synchrotron-based CTR diffraction to investigate the structure of the hydrated α -Fe₂O₃ ($1\bar{1}02$) surface prepared via a wet chemical and mechanical polishing procedure. The model resulting from analysis of the surface-scattering results is compared directly to models developed from *ab initio* density functional theory (DFT) calculations for a variety of surface stoichiometries [20]. These combined results are used to provide a model for both the surface termination and predominant protonation states of the surface (hydr)oxo functional groups, which is

essential for understanding differences in reactivity of the hydrated $\alpha\text{-Fe}_2\text{O}_3$ ($1\bar{1}02$) surface relative to other surfaces of hydrated $\alpha\text{-Fe}_2\text{O}_3$ as well as hydrated $\alpha\text{-Al}_2\text{O}_3$.

2.1.1 Bulk $\alpha\text{-Fe}_2\text{O}_3$ Structure and ($1\bar{1}02$) Termination

The bulk $\alpha\text{-Fe}_2\text{O}_3$ structure (space group $R\bar{3}c$) can be described as a distorted hexagonal close-packed (hcp) layer sequence of oxygen, where iron occupies two-thirds of the octahedral holes. The unit cell parameters ($a = b = 5.035 \text{ \AA}$, $c = 13.747 \text{ \AA}$) and bulk isotropic Debye-Waller factors have been previously reported [21]. The bulk unit cell has six $\text{-(Fe-O}_3\text{-Fe)-}$ stoichiometric repeat units along the c -axis with the atomic layer sequence consisting of six oxygen and twelve iron layers. The iron atoms are staggered along the c -axis from the ideal octahedral lattice site positions. As a result of this distortion, each six-coordinated iron site has three short Fe-O bonds (1.95 \AA) and three long Fe-O bonds (2.11 \AA).

The dominant growth faces exposed on natural $\alpha\text{-Fe}_2\text{O}_3$ are the ($1\bar{1}02$) and the (0001) [7]. Previous studies of the clean $\alpha\text{-Fe}_2\text{O}_3$ (0001) surface suggest that a highly relaxed stoichiometric surface ($\text{Fe-O}_3\text{-Fe-R}$, where R represents the stoichiometry and structure consistent with the bulk layer sequence) is the stable termination under ultra high vacuum (UHV) conditions [22, 23]. Under high oxygen partial pressure, ferryl (Fe=O) groups have been observed using scanning tunneling microscopy and infrared reflection absorption spectroscopy [24]. This observation of ferryl groups, which may coexist with Fe-terminated domains is consistent with previously reported DFT calculations [25]. The

(0001) surface has also been shown to readily hydroxylate at water partial pressures greater than 10^{-4} Torr [26]. A recent structural analysis of the hydroxylated $\alpha\text{-Fe}_2\text{O}_3$ (0001) surface suggests that the termination is dominated by two distinct domains: a domain consistent with dissociative water adsorption on the stoichiometric termination $((\text{HO})_3\text{-Fe-(HO)}_3\text{-Fe-R})$ and a domain consistent with hydroxylation of the oxygen-terminated surface $((\text{HO})_3\text{-Fe-Fe-R})$ [27].

The ideal $(1\bar{1}02)$ stoichiometric termination of $\alpha\text{-Fe}_2\text{O}_3$ is depicted in Figure 2.1. This surface can be described by three equivalent sets of Miller indices: $(1\bar{1}02)$, $(01\bar{1}2)$, and $(\bar{1}012)$ and is often referred to as R-plane. The atomic layer sequence along the surface normal direction is consistent with $\text{O}_2\text{-Fe}_2\text{-O}_2\text{-Fe}_2\text{-O}_2\text{-R}$, where R again represents the stoichiometric stacking sequence. The $(1\bar{1}02)$ surface unit cell can be indexed in a surface coordinate system by defining the \mathbf{a}_s basis vector with the $[1\ 1\ 0]$ bulk lattice vector and the \mathbf{b}_s basis vector with the $[-1/3\ 1/3\ 1/3]$ bulk lattice vector (Figure 2.1a). This indexing produces a rectangular surface mesh with $|a_s| = 5.04\ \text{\AA}$, and $|b_s| = 5.40\ \text{\AA}$. The \mathbf{c}_s basis vector is defined parallel to the surface normal direction, with a magnitude given by twice the $(1\bar{1}02)$ d-spacing (i.e. $2d_{(1\bar{1}02)} = |c_s| = 7.37\ \text{\AA}$). The procedure used to arrive at this cell choice is described in detail elsewhere [13, 28]. Briefly, the indexing results in a crystallographic pseudo-cell due to the lack of a rational repeat of lattice points along the surface normal direction. Because the \mathbf{c}_s axis is not defined by a bulk lattice vector, an additional lattice vector (slab repeat vector) is needed to correctly define the space filling repeat of the unit cell into the bulk. Based on this indexing, the unit cell

contains two stoichiometric layer sequences with the repeat vector defined by $\mathbf{V}_r = [-2/3 \ 2/3 \ -1/3]$. This unit cell indexing is a convenient choice for surface diffraction studies as it maintains a simple reciprocal lattice basis relative to the surface normal direction [28]. The coordinates for the un-relaxed surface unit cell are shown in Table 2.1.

Previous studies of the $\alpha\text{-Fe}_2\text{O}_3$ ($1\bar{1}02$) surface suggest that the stoichiometry of the UHV-prepared surface is consistent with the ideal bulk termination depicted in Figures 2.1a and 2.1b [29-31]. This surface cell is terminated with Fe in five-fold coordination ($^{\text{V}}\text{Fe}$), and oxygen anions in three-fold coordination ($^{\text{III}}\text{O}$). The topography of the ideal termination is characterized by raised ‘zig-zag’ rows of oxygen parallel to the \mathbf{b}_s direction, and a valley peak topography parallel to the \mathbf{a}_s direction (Figure 2.1a). When annealed in vacuum, this surface has been shown to produce a (2×1) surface reconstruction [31]. Lad and Henrich (1988) observed this reconstruction after annealing to 900 K in vacuum and suggested that it resulted from the ordering of oxygen vacancies [29]. Gautier-Soyer et al. (1996) suggested that the depth of reconstruction increases with increasing temperature and could extend up to 30 Å into the bulk [30]. They also observed that the (2×1) surface is partially reduced, with a stoichiometry similar to magnetite (Fe_3O_4), however, no evidence was found for a phase transition. Similarly, high resolution electron energy loss studies (HREELS) on the reconstructed (2×1) surface conducted by Henderson et al. (2002) supported reduction of the surface as well as the lack of magnetite formation, but suggested that the reconstruction is limited only to outer layers of the surface based on EELS analysis [32].

Thus, under UHV surface preparation the $\alpha\text{-Fe}_2\text{O}_3$ ($1\bar{1}02$) appears to have two stable states: a stoichiometric (1×1) surface and a reduced (possibly due to oxygen deficiency) (2×1) reconstructed surface stable at high temperatures. Water binds dissociatively on both the (1×1) and (2×1) surfaces resulting in the formation of terminal hydroxyls that complete the coordination shell of the exposed Fe layer, and bridging hydroxyls due to the protonation of the zig-zag oxygen rows [31, 32]. Based on vibrational frequencies, it was suggested that the bridging hydroxyl acts as a hydrogen bond donor to the terminal hydroxyl, while the hydrogen of the terminal hydroxyl is not involved in hydrogen bonding in the absence of physisorbed molecular water [31]. Previous theoretical studies also support the dissociative binding of water on the (1×1) surface resulting in hydrogen bonded bridging and terminal hydroxyls [33-35]. The molecular mechanics calculations of Rustad et al. (1999) suggest that in a system with two water molecules adsorbed per unit cell (corresponding to the number of $^{\text{V}}\text{Fe}$ surface sites), the lowest energy, charge neutral configuration was achieved when approximately 75% of the adsorbed water molecules were dissociated, resulting in a mixture of terminal, and bridging hydroxyls, and molecular water present on the surface [34]. Based on these studies it is apparent that the $\alpha\text{-Fe}_2\text{O}_3$ ($1\bar{1}02$) surface will be hydroxylated in the presence of liquid water. However, a full structural analysis of the surface prepared under aqueous conditions has not previously been reported.

2.2 METHODS

2.2.1 Sample Preparation and Data Collection

The natural single crystals of specular hematite were obtained from Bahia, Brazil. These crystals were cut to approximately 1 cm^2 and polished parallel to the $(1\bar{1}02)$ growth surface. X-ray Fluorescence (XRF) measurements (Panalytical Axios wavelength-dispersive spectrometer) showed that the bulk composition contained no detectable impurities (approximately 1 to 10 parts per million detection limit). The final stage of surface preparation utilized a chemical-mechanical polishing (CMP) procedure that consisted of polishing with a high pH (> 10) colloidal silica solution followed by washing the sample with a pH 10 NaOH solution and multiple rinses with ultra pure ($>18 \text{ M}\Omega \text{ cm}$) water. The samples were then etched in 0.01 M HNO_3 for approximately 2 hours followed again by multiple rinses with ultra pure water. This wash procedure should ensure that the surface is fully hydroxylated [26], and previous work by our group shows that this method results in a clean surface free from detectable impurities [27]. Following the CMP preparation the surfaces were characterized using atomic force microscopy (AFM). The AFM results revealed that the prepared surfaces have terrace-step morphologies, with terrace widths on the order of 200 nm and predominant step heights of approximately 3.6 \AA consistent with half the c_s unit cell dimension defined above. The r.m.s. roughness of the surface measured by AFM is consistently less than 5 \AA .

2.2.2 CTR Data Collection

All CTR measurements were performed at room temperature under a water saturated He atmosphere (relative humidity $> 90\%$, $p_{\text{H}_2\text{O}} > 20$ Torr) to ensure that the surfaces remained fully hydrated during the course of measurements. The data were collected at the Advanced Photon Source (APS) on undulator beamline 13-ID with a 10 keV incident beam energy. The beamline optics consisted of a liquid N_2 cooled, double-crystal Si (111) monochromator and Rh-coated vertical and horizontal focusing (and harmonic rejection) Si mirrors. Sample orientation and scanning was performed using a $2 + 2 + \kappa$ -geometry Newport diffractometer equipped with a sample cell with x-ray transparent windows [36]. Scattered intensity was monitored using a Bicron detector equipped with a single channel analyzer for rejecting Fe fluorescence counts. Non-specular CTR intensities were collected by performing a continuous (trajectory) rocking scan of the diffractometer ϕ -axis at a particular reciprocal lattice setting using a fixed incident angle of 2° . The specular rod was collected using ω -axis scans. Individual structure factors were determined by taking the square root of the background-subtracted intensity of the rocking curves and correcting for active area, polarization, step size and Lorentz factors [37]. The full data set used for analyses consisted of 9 crystal truncation rods and 936 unique structure factors averaged in the pl plane group. The CTR data set is presented in Figure 2.2. To check for beam-induced damage on the surface a subset of rods was repeatedly measured during data collection. Repeat rods had similar intensities within error, suggesting the surface was stable during the course of CTR measurements. A repeat data set was collected on a different but similarly prepared surface at APS

beamline 7-ID. The two data sets were identical within error suggesting that the surface preparation method discussed above produces similar ($1\bar{1}02$) surfaces on different α - Fe_2O_3 samples.

2.2.3 CTR Data Analyses

As depicted in Figure 2.1b, the clean α - Fe_2O_3 ($1\bar{1}02$) surface has 5 unique layers that may be considered potential terminating atomic planes (a layer-6 termination in Figure 2.1b would be structurally equivalent to a layer-1 termination). In the analysis, trial structures were generated starting from each of these 5 atomic layer terminations, including the addition of terminal (hydr)oxo groups, physisorbed molecular water, and the presence of vacancies within layers beneath the terminal atomic layer. The stoichiometries of some of the structurally plausible models are listed in Table 2.2. These models are grouped according to the predominant Fe-O stoichiometry of the surface: the A-series of models are consistent with the stoichiometric termination (e.g. cleavage at layer 1 or layer 6 in Figure 2.1b), the B- and C-series of models are associated with potential cleave at layer 3 or a layer 1 termination with a layer 2 vacancy, respectively. The atoms shown in boldface represent the layers added above the first layer of stoichiometric termination. Various surface protonation configurations can satisfy charge neutrality; however, because x-ray scattering is insensitive to H atoms, the models used for the CTR analysis only consider the Fe and O positions.

Our choice of surface indexing leads to two stoichiometric layers within a unit cell. The modeling procedure explicitly accounts for the presence of half unit-cell steps (as observed in the AFM analysis) by the use of two symmetry-related surface models in the structural analysis. Starting with each trial structure, a non-linear least squares analysis was performed using adjustable atomic displacements, occupancies, and Debye-Waller factors for the atoms within the surface unit cell, and a fixed set of structural parameters for the bulk unit cell [28, 38]. The magnitude of the CTR structure factor was calculated using the method outlined previously [18, 38, 39]. Briefly, the scattering intensity at a particular reciprocal lattice setting (HKL) is proportional to the square of the structure factor magnitude, $|F_T|^2$, where,

$$F_T = SR(F_{bc}F_{CTR} + F_{sc}) \quad (2.1)$$

In equation (2.1), F_{bc} is the structure factor of the bulk unit cell [40],

$F_{CTR} = 1/[1 - \exp(-i2\pi L)]$ is the CTR form factor, S is an overall scale factor, and R is a roughness factor [18]. F_{sc} is the structure factor of the surface unit cell,

$$F_{sc} = \sum_{j=1}^n \theta_j f_j \exp(i\mathbf{Q} \cdot \mathbf{r}_j) \exp[-B_j(|\mathbf{Q}|/4\pi)^2] \quad (2.2)$$

with the sum taken over all n atoms of the surface unit cell having atomic scattering factors f_j , site occupancies θ_j , fractional coordinates \mathbf{r}_j , and isotropic Debye-Waller factors B_j . \mathbf{Q} denotes the scattering vector. We note that the reciprocal lattice defined by our surface indexing results in the reciprocal vector indices H and K corresponding to the in-plane momentum transfer, and L to the perpendicular momentum transfer [28]. We also note that a slight modification to the above standard formulation is required for our

surface model due to the lack of a rational repeat vector along the surface normal direction. This modification is described in detail elsewhere [28].

The quality of the fit is characterized using a reduced χ^2 value, where

$$\chi^2 = \sum_{i=1}^N \left(|F_i| - |F_{i,c}| \right)^2 w_i / (N - p) \quad (2.3)$$

The sum of the squares of the difference between the experimental ($|F_i|$) and calculated ($|F_{i,c}|$) structure factor magnitude is over all N experimental data points, weighted by the experimental uncertainty of the data point w_i , and normalized by the number of degrees of freedom ($N-p$), with p the number of free parameters in the fit. We employed Hamilton's R -ratio test to provide a statistical comparison of the fit quality between different models [41].

An independent check on the chemical plausibility of the structural models was performed using Pauling's bond-valence principle [42]. The bond valence sum (Σs) for a central atom is defined as the sum of individual bond valence contributions from each neighboring atom, where $s=Z/CN$, Z is the formal valence, and CN is the coordination number of the central atom. According to Pauling's electrostatic valence principle, the bond valence sum for a given anion (cation) should be equal to the magnitude of the valence of the central anion (cation). In the current study, Fe-O bond valence values were calculated using the empirical bond length-bond strength relationship of Brown and Altermatt (1985) [43], while O-H bond valence contributions were calculated using the

method suggested by Bargar et al. (1997) [44]. Bond valence sums significantly greater than the formal valence of the central atom imply over-saturation or unusually short bond lengths, while bond valence sums significantly less than the formal valence imply under-saturation or unusually long bond lengths.

2.2.4 Comparison To Density Functional Theory Calculations

A number of optimized surface structure models were generated using periodic density functional theory (DFT) calculations using the generalized gradient approximation of Perdew, Burke, and Ernzerof [45] and the atom-centered double numerical basis set with polarization functions (DNP) implemented in the DMol³ code [46]. Slabs were constructed with 16-22 atomic layers separated by 10 Å of vacuum. Brillouin zone integration was performed using a 5×5×1 Monkhorst-Pack k-point grid [47, 48]. The details of the calculations are presented elsewhere [20]. Briefly, initial models were developed based on the potential stoichiometries listed in Table 2.2, and geometry optimizations and total energies were calculated without any symmetry constraints. Surface free energies were calculated in equilibrium with O₂ and H₂O [20, 49]. The models listed in Table 2.2 include a selection of the probable surface terminations with both dissociated and physisorbed water molecules. The predicted relaxations of selected theoretical models [20] are provided in Table 2.3. A detailed analysis of the structural variations with changes in surface structure and stoichiometry, and the resulting changes in surface free energy are discussed by Lo et al. (2007) [20]. The CTR profiles for each theoretical model were calculated and compared with the experimental results. For the

comparison we used a fixed scale factor (same as the experimental model), and in the cases where physisorbed water was present in the theoretical model, the occupancy and Debye-Waller factor of the water adlayers were optimized.

2.3 RESULTS AND DISCUSSION

2.3.1 Surface Termination

The (1×1) stoichiometric termination (Figure 2.1 and model A1 in Table 2.2) has been previously identified as the stable termination under low temperature (below 600 K) UHV surface preparation conditions [29-31]. Water is expected to react dissociatively on this surface leading to a structure with both terminal and bridging (hydr)oxo groups (Figure 2.3a and model A4 in Table 2.2). The calculated CTR profiles for these models (A1 and Fe-O stoichiometry consistent with A2-A4) are compared to the CTR data in Figure 2.2. Qualitatively, the CTR profile of the stoichiometric surface (model A1) is a poor match to the experimental data (Figure 2.2). The calculated profile shows sharp dips near (0 0 2.3), (0 2 2.3), (2 0 2.3), (1 1 0.4), and (2 2 3.0) that are absent in the experimental data (Figure 2.2). Fenter and Park (2004) have shown that these node features in CTR profiles provide a sensitive indicator of the surface termination, and that comparison between calculated and experimental profiles in terms of the positions (or simply the absence) of the node features can generally be used to identify the surface termination [50].

Based on the qualitative mismatch between the calculated CTR for model A1 and the experimental results it appears that under the employed surface preparation conditions the surface termination is not consistent with the clean stoichiometric surface model. The inclusion of a terminal (hydr)oxo group did not lead to substantial improvement in the fit. The CTR profile calculated for the unrelaxed stoichiometry consistent with models A2-A4 (Table 2.2) has node features similar to model A1 on the (20L) and (22L) rods, but there is a shift in position for (00L) and (11L) and a clear change in intensity in (02L) (Figure 2.2). These changes illustrate the sensitivity of the CTR profile to changes in the surface termination, and suggest that this termination is also inconsistent with the experimental data.

The comparison of the range of Fe-O surface stoichiometries presented in Table 2.2 (A, B, and C models without physisorbed water) with the experimental data leads to one “best-match” consistent with models C1-C4. In these models the occupancy of the near surface Fe (layer 2) is zero (Figure 2.2 and 2.3b). The exclusion of Fe from this site results in a significant change in the CTR profile, removing the series of strong nodes observed in the simulations for models A1 and A2-A4 and resulting in an overall intensity variation consistent with the experimental data. This is most evident on the (00L) rod, where the node observed at (0 0 2.3) in the case of the stoichiometric termination disappears, and a dip in intensity near (0 0 1.6) is observed, producing an intensity profile similar to the experimental data on either side of the bulk Bragg peak at (0 0 2). Intensity variations consistent with experimental data are also observed near other bulk Bragg peaks, for

example (0 2 1.72), (2 0 2), and (2 2 1.72), providing a qualitative interpretation that the experimental surface termination is consistent with the absence of the topmost Fe layer.

To provide a detailed analysis of the surface structure we performed least square fits of the experimental CTR data based on the subset of models with unique Fe-O stoichiometries. Fitting parameters include displacements to the atomic fractional coordinates (x , y , and z), atomic occupancies, Debye-Waller factors, and overall roughness and scale factor. The number of free parameters for all the models was reduced by constraining atoms in the same layer to maintain the same z coordinate. The fractional z -coordinate for all ten layers of the substrate (Table 2.1) were allowed to vary, but the x and y -fractional coordinates and occupancies were relaxed for only the top five layers of the substrate, including the first Fe layer (Table 2.1), as these parameters for deeper layers had insignificant displacements in preliminary analysis. Similarly, isotropic Debye-Waller factors for layers 4 and below were fixed to the bulk values reported by Finger and Hazen (1980) [21] because they retained similar values when allowed to float during the preliminary analyses. In the fits of the A- and C-series of models, the number of free parameters was reduced by constraining the oxygen atomic positions in layers 1 and 3 (or 3 and 5 for C-series) to maintain 4-fold rotational symmetry about the central coordinating Fe. This is an empirical constraint that aided in maintaining reasonable coordination geometry for the Fe layer with minimal free parameters and resulted in statistically significant improvement in the fits as compared to a model where no in-plane

constraints were imposed. The total number of parameters ranged from 26-36 and the number of free parameters varied from 16-24 for the range of models tested (Table 2.2).

Consistent with our qualitative analysis, fits to the stoichiometric model (A1) did not lead to satisfactory results. Similarly, models with adsorbed and dissociated water on the stoichiometric surface (i.e. A2 and A4, respectively) and the B-series models (Table 2.2) could also not be used to produce a reasonable fit to the experimental data. However, a model having an Fe-O stoichiometry consistent with C1-C4 (Table 2.2), (in which the layer 2 Fe site is vacant) resulted in an excellent fit ($\chi^2 = 5.6$). The structural relaxations associated with the best fit model show an expansion of the layer 1-3 spacing (11 ± 3 %) and the layer 4-5 spacing (14 ± 7 %) and a contraction of layer 3-4 spacing (-11 ± 3 %). The in-plane atomic coordinates show minimal displacements, especially for layer 3 and below.

The effect of physisorbed water on the overall fit of the structural model was investigated by the inclusion of additional oxygen positions above the terminating surface. Inclusion of one and two water layers to the model resulted in the reduction of χ^2 to 5.1 and 3.8, respectively. In each case the improvement in the fit is statistically significant at the 95% confidence interval according to Hamilton's *R*-ratio test [41]. The inclusion of more than two water adlayers did not result in a statistically significant improvement in fit. Consequently, the unit cell for the best-fit model has roughly 1.8 H₂O per unit cell. The low occupancy and high Debye-Waller factor (Table 2.1) for the water layers suggest that

these water positions have a high degree of disorder, consistent with physisorption. The addition of physisorbed water layers to the model showed the most improvement in fit of the (00L) rod, with little impact on the in-plane rods. The weak sensitivity to in-plane (i.e., x, y) positions of the water layers suggests that the x and y coordinates for these layers are poorly constrained. While the inclusion of water adlayers resulted in statistically significant improvement to the fit, their presence had an insignificant effects on the atomic relaxations of the substrate. The best-fit model has layer 1-3 and 4-5 expansion of $12 \pm 4 \%$ and $8 \pm 6 \%$, respectively, and layer 3-4 contraction of $-11 \pm 4 \%$. These values are within error of the model without water layers. The best-fit CTR model resulted in an overall roughness parameter (β) of 0.12 ± 0.01 , which results in an estimated r.m.s. roughness $< 2 \text{ \AA}$, in reasonable agreement with the AFM determined roughness of less than 5 \AA .

The structural model for the best fit is presented in Figure 2.3b, and the atomic coordinates and the layer z relaxations are listed in Table 2.1. The fitting results show that the occupancies for oxygen layers 1 and 3 are 0.61 ± 0.01 and 0.68 ± 0.03 , respectively, and the occupancy for layer 4 iron is 0.72 ± 0.01 (Table 2.1). We note that in absence of layer 1 and 3 oxygen and layer-4 iron, we recover a sequence consistent with the hydroxylated stoichiometric models (e.g., A2-A5). Therefore, the observation of partial occupancy suggests that the surface may be a mixed termination with the dominant proportion ($\sim 72\%$) having an Fe-O stoichiometry consistent with the C-series of models (layer 2 vacancy) and a lesser proportion ($\sim 28\%$) of the hydroxylated

“stoichiometric” termination (model A2-A5). Based on our results, we cannot clearly distinguish between distinct domains of these terminations and random site occupancy. However, it is evident that the observed surface termination depends strongly on surface preparation conditions. For example as discussed in Section 1.1, low temperature annealing in UHV (below ~ 600 K) results in a stoichiometric termination, whereas higher temperature UHV annealing (673 K to 1273 K) results in a partially reduced (2×1) termination [29-32]. Recent work also suggests that the CMP-prepared surface layer 2 Fe vacancy can be driven to a surface structure consistent with the stoichiometric termination (A-series) by annealing in air above 673 K (J.G. Catalano, unpublished data). Further studies to investigate the temperature dependence of surface termination are currently in progress. However, for the current study, the reproducible nature of the CTR data suggests that the CMP surface preparation procedure used here repeatedly results in a termination most consistent with the C-series of models (i.e. $\text{O}_2\text{-X-O}_2\text{-Fe}_2\text{-O}_2\text{-R}$).

2.3.2 Description Of Best-fit Structure

The best-fit model for hydroxylated $\alpha\text{-Fe}_2\text{O}_3$ ($1\bar{1}02$) has a predominant Fe-O stoichiometry consistent with $(\text{H}_2\text{O})_2\text{-(H}_2\text{O})_2\text{-O}_2\text{-X-O}_2\text{-Fe}_2\text{-O}_2\text{-R}$ (Figures 2.2 and 2.3b), where the top H_2O layers are inferred to be interfacial physisorbed water due to their positions and high disorder terms. The top Fe layer contains six-coordinated Fe^{3+} ($^{\text{VI}}\text{Fe}^{3+}$) and the surface has three types of surface (hydr)oxo groups based on their Fe coordination: Fe-O or $^{\text{I}}\text{O}$, $\text{Fe}_2\text{-O}$ or $^{\text{II}}\text{O}$, and $\text{Fe}_3\text{-O}$ or $^{\text{III}}\text{O}$ (Figure 2.3b). As discussed above, the experimental results are insensitive to the protons that might be associated

with these groups. An inference of the protonation state of the terminal hydr(oxo) group may be made considering the best-fit Fe-O bond length. The Fe-^IO bond length in the unrelaxed surface model is 2.11 Å. This bond length would be expected to decrease in the absence of protonation to compensate for reduced coordination. The best-fit model resulted in a Fe-^IO bond length of 2.18 ± 0.08 Å, which is within error of the unrelaxed surface bond length. Thus, the long Fe-^IO bond suggests that this oxygen is protonated, either singly (i.e. hydroxyl) or doubly (i.e. a water molecule). All other Fe-O bond lengths (1.92 ± 0.02 to 2.12 ± 0.04 Å) are also similar to their bulk values (1.95-2.11 Å), within the errors associated with the fit.

Bond-valence analyses can also be used to examine the chemical plausibility of the surface models and to estimate the probable protonation states of surface hydr(oxo) groups. Our results for the best-fit model show that the top Fe layer (layer 4) is near saturated, resulting in a bond-valence sum of 2.95 ± 0.04 valence units (v.u.) (Table 2.1). In addition, the bond-valence sums for all other Fe and O layers (layer 6 and below) show saturation within 0.1 v.u. (Table 2.1) suggesting that the model is reasonable from a coordination chemistry perspective. Analyses of the surface (hydr)oxo groups show that the bond-valence sum for ^IO is 0.32 ± 0.07 v.u., ^{II}O is 1.07 ± 0.03 v.u., and for ^{III}O is 1.58 ± 0.01 v.u. (Table 2.1). Thus, the three surface oxygen groups are significantly under-saturated. The missing valence is likely provided by protonation of the surface O groups, which also leads to compensation of the excess negative charge. For example, to

maintain a charge-neutral surface without oxidation of Fe(III), six protons must be added per unit cell to compensate for the two missing Fe^{3+} from layer 2.

Based on oxygen coordination, there are two reasonable ways to distribute these protons on the surface as shown in Table 2.4. In the first case, each of the under-coordinated oxygen binds one proton resulting in a stoichiometry consistent with $(\text{H}_2\text{O})_2\text{-(H}_2\text{O)}_2\text{-(HO)}_2\text{-X-(HO)}_2\text{-Fe}_2\text{-(HO)}_2\text{-R}$. Based on the work of Bargar et al. (1997), it is reasonable to assume that each proton contributes a bond-valence of approximately 0.8 v.u. [44]. After including the contribution of protons, the above stoichiometry would result in $^{\text{II}}\text{O}$ being saturated in its valence sum whereas $^{\text{I}}\text{O}$ is still under-saturated by approximately 1 v.u. and $^{\text{III}}\text{O}$ is oversaturated by 0.4 v.u. (Table 2.4a). The second protonation scheme (Table 2.4b), where $^{\text{I}}\text{O}$ binds two protons, $^{\text{II}}\text{O}$ binds one proton, and $^{\text{III}}\text{O}$ is not protonated, results in a stoichiometry consistent with $(\text{H}_2\text{O})_2\text{-(H}_2\text{O)}_2\text{-(H}_2\text{O)}_2\text{-X-(HO)}_2\text{-Fe}_2\text{-O}_2\text{-R}$. In this case, four out of six oxygens per unit cell are possibly stable and the remaining two (i.e. $^{\text{III}}\text{O}$) are undersaturated by approximately 0.4 v.u. (Table 2.4b). When comparing the two protonation schemes we expect the later to be more likely because it results in a greater number of stable surface oxygens than the former, and does not lead to oversaturation (leaving open the potential for hydrogen-bonding contributions).

2.3.3 Comparison to DFT Models

To gain further insight into the protonation of the surface oxygens and to test the CTR-derived chemical termination we compared a series of DFT-optimized structures with

various stoichiometries (listed in Table 2.2) to the experimental data set. The relaxations for selected DFT models are shown in Table 2.3 [20]. These results suggest that the pattern of relaxation is highly sensitive to the stoichiometry of the termination, and the protonation state of the surface oxygen sites. A detailed analysis of the energetics of these models is discussed elsewhere [20]; here we use the results to further test our inferences about the termination and surface protonation states.

The calculated CTRs for the DFT-optimized bulk stoichiometric termination (model A1) showed a poor match to the data (not shown), suggesting that this model does not describe the correct chemical termination under the experimental and surface preparation conditions used here. This observation is also consistent with our direct analysis as discussed above, i.e., relaxation of the stoichiometric termination could not reproduce the experimental data. The calculated CTRs for DFT model A4, which is consistent with the model of the water-reacted clean surface under UHV conditions [31] also results in poor reproduction of the data ($\chi^2 = 33.7$) (Figure 2.4), as there are significant mismatches in the locations of the intensity dips along the CTRs. Overall, calculated CTRs for the models A1-A5, and B1-B2 showed unsatisfactory matches to the data. The only models that reasonably reproduced the experimental data are those having an Fe-O stoichiometry consistent with the C-series models (Table 2.2, Figures 2.5 and 2.6). A detailed comparison of the C-series models with the experimental data provides additional information regarding the likely protonation states of the surface hydr(oxo) groups.

We may immediately rule out model C1 based on the unlikely stoichiometry under our experimental conditions (e.g., Fe would be required to be in the VI oxidation state for a charge neutral surface model). Furthermore, this model shows unusually high relaxations [20] and also resulted in a poor fit to the experimental data (not shown). The calculated CTRs for model C2 show significant improvement in fit ($\chi^2 = 8.8$) and reproduces the major structure factor variations for the (00L), (02L), and (20L) rods (Figure 2.5). However, this model is also unlikely based on the stoichiometry, which requires Fe(IV) for a charge-neutral surface model due to the addition of only four charge-balancing H^+ for the two missing Fe^{3+} per unit cell. In addition, the Fe-O bond lengths in this model are unusually short (1.83 Å) which result in unusually high bond valence sum for Fe (approximately 3.7 v.u., Table 2.5). The addition of physisorbed water to model C2 (model C5) did not improve the χ^2 value, and in both cases (C2 and C5) the models have features on the (10L) rod not present in the data. The surface free energy calculations of Lo et al. (2007) clearly show that these models (C2 and C5) are thermodynamically stable only at extremely high oxygen chemical potentials in order to stabilize Fe(IV) [20]. While models C2 and C5 provide a qualitatively reasonable match to the data, they do not appear to be chemically plausible under the experimentally studied conditions.

The calculated CTRs for models C3 and C4 (Figure 2.5) also reproduced the main features of the experimental data, with C4 ($\chi^2 = 7.1$) being a better match to the data than C3 ($\chi^2 = 17.4$) (Figure 2.5). The basic difference between these two models is the protonation states of the surface oxygens. For model C3, all of the exposed oxygens are

bound to one proton resulting in $^{\text{I}}\text{OH}$, $^{\text{II}}\text{OH}$, and $^{\text{III}}\text{OH}$ surface groups; whereas for C4 the protonation results in $^{\text{I}}\text{OH}_2$, $^{\text{II}}\text{OH}$, and $^{\text{III}}\text{O}$ groups. This comparison indicates that the protonation states of the surface oxo groups have a significant effect on the overall structure. Interestingly, the protonation states in C4 are similar to those predicted by bond-valence analyses (Table 2.4b). The addition of a physisorbed water layer to model C4 resulted in model C7 for which there was no significant improvement in fit quality. The addition of physisorbed water, however led to significant changes in relaxations, which were consistent with the best-fit model obtained via direct analysis of the experimental data (Table 2.3). The difference in surface oxo group coordination between models C4 and C7 is most evident when comparing Fe- $^{\text{I}}\text{O}$ bond distances. Model C4 has an Fe- $^{\text{I}}\text{O}$ bond distance of 2.42 Å, which is much longer than typical Fe-O bond distances in the bulk structure (1.95-2.11 Å), while the inclusion of a physisorbed water layer in model C4 results in reduction of this bond length to 2.30 Å (Model C7) [20]. Incorporating a second water layer in C7 results in minimal changes in the surface relaxations (Table 2.3) but leads to a statistically significant improvement in fit at the 95% confidence interval according to Hamilton's R-ratio test and gives the lowest overall χ^2 (= 6.3) (Figure 2.6). Inclusion of this second water layer is also consistent with the results in Table 2.3 showing that model C7 with an additional water layer (i.e. C8) exhibits the best agreement between experimentally and theoretically derived layer relaxations. The best-fit DFT model is therefore in agreement with the independent analysis of the experimental data both in terms of the Fe-O stoichiometry of the surface and the bond-valence prediction of the surface protonation.

For each model with different protonation configurations, we expect different hydrogen bonding configurations to arise on the surface. The most probable configuration should result in the lowest surface free energy. Lo et al. (2007) showed that the lowest energy surface termination with one water layer is model C7, which is also consistent with our experimental results [20]. The probable hydrogen bonding network associated with the surface hydroxyls of the proposed model is shown in Figure 2.7: the most significant feature is that the bridging ^{II}OH is donating a hydrogen bonds to the underlying ^{III}O while the terminal aquo-groups are involved in in-plane donor-acceptor hydrogen bonding. The bond valence calculations for the proposed DFT model including the contribution of protons and hydrogen bonding show that ^{III}O ($\Sigma s = 1.9$) and ^IOH₂ ($\Sigma s = 1.9$) are saturated within 0.1 v.u., whereas ^{II}OH ($\Sigma s = 1.6$) is undersaturated. However, donor hydrogen bonding from the physisorbed water layer may potentially stabilize this group.

2.3.4 Comparison of Best-fit CTR and DFT Models

The layer relaxations of models C7 (with one water layer) and C8 (with two water layers) show excellent agreement with the best-fit CTR model (Table 2.3). Further comparison between the DFT and CTR models show that Fe-^IO bond length in the best-match DFT model (C7 and C8) is 2.30 Å, which is longer than in the best fit CTR model (2.18 ± 0.08 Å). This difference could result due to the possibility of partially hydrolyzed ^IOH₂ groups in the current experimental study. The proton exchange between ^IOH₂ and the physisorbed water or overlying water reservoir [51] would result in the presence of some

^1OH groups that should have slightly contracted average Fe-O bond lengths. A second possibility is proton exchange between the terminal $^1\text{OH}_2$ and $^{\text{III}}\text{O}$ groups resulting in some combination of protonation states consistent with models C6 and C7. This latter case is similar to that considered by Rustad et al. (1999), where the lowest energy surface resulting from water reaction on the stoichiometric termination has a roughly 3:1 ratio of ^1OH to $^1\text{OH}_2$ groups [34]. Using the Fe- ^1OH and Fe- $^1\text{OH}_2$ bond lengths from DFT models C6 and C8, a roughly 50:50 mixture would result in an average bond length of 2.13 Å, consistent with the experimental distance within the error (i.e. 2.18 ± 0.08 Å).

The protons at the ^1O sites are also predicted to be highly labile based on an estimate of the pK_a value, making the deprotonation of Fe- $^1\text{OH}_2$ group likely. The pK_a values were calculated using the empirical model described by Hiemstra et al. (1996) [52] with bond valence sums given for model C7 (Table 2.5). A simplified form of the Hiemstra et al. model [52] for our case can be written as:

$$\text{pK}_a = 19.8 (2 - \Sigma s) \quad (2.4)$$

where Σs is the bond-valence sum on the oxygen including contributions from Fe, hydroxyl proton, and donor and acceptor hydrogen bonds. In model C7, there are two hydroxyl bonds, one in-plane acceptor hydrogen bond, and one Fe-O bond contributing to the bond-valence sum for the $^1\text{OH}_2$ group (Figure 2.7), whereas for the $^{\text{II}}\text{OH}$ groups the bond valence sum includes contributions from two Fe-O bonds and one hydroxyl bond (Figure 2.7). Applying equation (2.4) to the $^1\text{OH}_2$ group results in a pK_a of approximately 2.0, and for the $^{\text{II}}\text{OH}$ group the estimated pK_a is approximately 7.9. Comparing these pK_a

values with our experimental conditions ($\text{pH} \approx 7$), we may expect a highly labile proton on the $^1\text{OH}_2$ groups to exchange with the adsorbed water adlayer, whereas $^{\text{II}}\text{OH}$ should remain protonated.

2.4 CONCLUSIONS

The structure of the CMP-prepared hydroxylated $\alpha\text{-Fe}_2\text{O}_3$ ($1\bar{1}02$) has been investigated using the independent approaches of surface x-ray diffraction and density functional theory [20]. The results from both methods were compared to arrive at a best-fit model. The results show that the stoichiometry of the chemically and mechanically polished surface is consistent with $(\text{H}_2\text{O})_2\text{-(H}_2\text{O)}_2\text{-(H}_2\text{O)}_2\text{-X-(HO)}_2\text{-Fe}_2\text{-O}_2\text{-R}$. This result differs from previous UHV surface studies that reported a stoichiometric (1×1) and a partially reduced (2×1) reconstructed $\alpha\text{-Fe}_2\text{O}_3$ ($1\bar{1}02$) surface [29-31], where dissociative water reaction in both cases was found to result in terminal and bridging hydroxyls [31]. The *ab initio* DFT study of Lo et al. (2007) suggests that in the presence of gas phase water the hydroxylated surface models have a lower surface free energy than their dehydroxylated counterparts, and among the likely hydroxylated terminations the surface free energy follows the sequence $(\text{H}_2\text{O})_2\text{-X-(HO)}_2\text{-Fe}_2\text{-O}_2\text{-R} < (\text{HO})_2\text{-(HO)}_2\text{-Fe}_2\text{-O}_2\text{-Fe}_2\text{-O}_2\text{-R}$ [20]. Therefore, we hypothesize that the differences in findings between the current study and previous UHV studies are largely due to the differences in surface preparation conditions (wet chemical and mechanical polishing vs. vacuum annealing), with the CMP-preparation apparently driving the surface towards its (predicted) lowest energy hydroxylated configuration.

As mentioned above, recent evidence also suggests that air annealing of the $\alpha\text{-Fe}_2\text{O}_3$ ($1\bar{1}02$) surface may lead to a termination that is more consistent with hydroxylation of the stoichiometric surface. The previous CTR analysis of bulk isostructural $\alpha\text{-Al}_2\text{O}_3$ ($1\bar{1}02$) [13] resulted in the proposal of a surface structure similar to that found here, again differing from UHV studies that reported a stoichiometric or (2×1) reconstructed surface [53, 54]. Catalano et al. (2006) recently provided evidence for a hydroxylated $\alpha\text{-Al}_2\text{O}_3$ ($1\bar{1}02$) termination consistent with hydroxylated stoichiometric surface structure based on *in-situ* surface diffraction measurements [55]. These differences in observed termination are likely due to differences in surface preparation conditions, and perhaps predominantly influenced by sample annealing and chemical etching. Further work is currently underway to examine the dependence of observed $\alpha\text{-Fe}_2\text{O}_3$ ($1\bar{1}02$) surface termination with preparation conditions (e.g., annealing time and temperature, as well as chemical etching).

A consistent observation, however, is that water reaction has a significant impact on surface structure/stoichiometry, and in general may result in the lowering of the free energy of an oxide surface. Eng et al. (2000) [10] conducted CTR studies on hydrated $\alpha\text{-Al}_2\text{O}_3$ (0001) and proposed a hydroxyl-terminated surface which is different from previous UHV studies that suggested an Al terminated [56] or mixed Al/O terminated [57] surface. These experimental observations are consistent with the theoretical work of Wang et al. (2000) who illustrated that the hydroxyl-terminated surface is most stable

structure in presence of water [49]. Similarly, Trainor et al. (2004) reported that the best fit CTR model for hydrated $\alpha\text{-Fe}_2\text{O}_3$ (0001) was a two domain surface having exposed oxygens in the first layer, and six-fold coordinated Fe in both domains; the complementary thermodynamic calculations using DFT clearly illustrated that the hydroxylated $\alpha\text{-Fe}_2\text{O}_3$ (0001) surface was much more stable than the oxygen- or iron-terminated surfaces [27].

The results presented here for the structure of the CMP-prepared hydroxylated $\alpha\text{-Fe}_2\text{O}_3$ ($1\bar{1}02$) surface suggest the presence of several types of surface functional groups (i.e., $^{\text{I}}\text{OH}$, $^{\text{I}}\text{OH}_2$, $^{\text{II}}\text{OH}$, $^{\text{III}}\text{O}$). Characterization of surface coordination chemistry is important for understanding differences in reactivity of these model surfaces with respect to contaminants such as Pb(II) [58] and U(VI) [15] and will aid in understanding their surface charging behavior [59].

ACKNOWLEDGEMENTS

The authors would like to acknowledge Sarah Petitto and Sanjit Ghose for helpful comments on the manuscript. This research was supported by NSF grants BES-0404400 and CHE-0431425, the ACS Petroleum Research Fund, The Arctic Region Supercomputing Center (University of Alaska Fairbanks) and the Argonne National Laboratory Named Postdoctoral Fellowship Program through contract DOE W-31-109-ENG-38 (JGC). Portions of this work were performed at GeoSoilEnviroCARS (Sector 13) and MHATT-XOR (Sector 7) of the Advanced Photon Source (APS), Argonne National Laboratory. Use of the APS was supported by DOE Basic Energy Sciences, Office of Energy Research, under Contract No. W-31-109-ENG-38.

REFERENCES

- [1] T.B. Hofstetter, A. Neumann, R.P. Schwarzenbach, *Environ. Sci. Technol.* 40 (2006) 235.
- [2] T.B. Hofstetter, C.G. Heijman, S.B. Haderlein, C. Holliger, R.P. Schwarzenbach, *Environ. Sci. Technol.* 33 (1999) 1479.
- [3] M. Elsner, R.P. Schwarzenbach, S.B. Haderlein, *Environ. Sci. Technol.* 38 (2004), 799.
- [4] W. Stumm, J.J. Morgan, *Aquatic Chemistry: Chemical Equilibria and Rates in Natural Waters*, third ed., Wiley Interscience, New York, 1996.
- [5] B. Sulzberger, D. Suter, C. Siffert, S. Banwart, W. Stumm, *Mar. Chem.* 28 (1989) 127.
- [6] W. Stumm, B. Sulzberger, *Geochim. Cosmochim. Acta* 56 (1992) 3233.
- [7] R.M. Cornell, U. Schwertmann, *Iron oxides: Structure, Properties, Reactions, Occurrence, and Uses*, first ed., Wiley-VCH, 1996.
- [8] G.E. Brown, Jr. et al., *Chem. Rev.* 99 (1999) 77.
- [9] S.A. Chambers, T. Droubay, D.R. Jennison, T.R. Mattsson, *Science* 297 (2002) 827.
- [10] P.J. Eng, T.P. Trainor, G.E. Brown, Jr., G.A. Waychunas, M. Newville, S.R. Sutton, M.L. Rivers, *Science* 288 (2000) 1029.
- [11] J.R. Bargar, S.N. Towle, G.E. Brown, Jr., G.A. Parks, *Geochim. Cosmochim. Acta* 60 (1996) 3541.
- [12] A.S. Templeton, T.P. Trainor, S.J. Traina, A.M. Spormann, G.E. Brown, Jr., *Proc. Natl. Acad. Sci. USA* 98 (2001) 11897.
- [13] T.P. Trainor, P.J. Eng, G.E. Brown, Jr., I.K. Robinson, M. De Santis, *Surf. Sci.* 496 (2002) 238.
- [14] T.P. Trainor, A.S. Templeton, G.E. Brown, Jr., G.A. Parks, *Langmuir* 18 (2002) 5782.
- [15] J.G. Catalano, T.P. Trainor, P.J. Eng, G.A. Waychunas, G.E. Brown, Jr., *Geochim. Cosmochim. Acta* 69 (2005) 3555.
- [16] G. Sposito, *Chimica* 43 (1989) 169.

- [17] P. Fenter, N.C. Sturchio, *Prog. Surf. Sci.* 77 (2004) 171.
- [18] I.K. Robinson, *Phys. Rev. B* 33 (1986), 3830.
- [19] I.K. Robinson, D.J. Tweet, *Rep. Prog. Phys.* 55 (1992) 599.
- [20] C.S. Lo, K.S. Tanwar, A.M. Chaka, T.P. Trainor, *Phys Rev B* 75 (2007) 075425.
- [21] L.W. Finger, R.M. Hazen, *J. Appl. Phys.* 51 (1980) 5362.
- [22] S.A. Chambers, S.I. Yi, *Surf. Sci.* 439 (1999) L785.
- [23] S. Thevuthasan, Y.J. Kim, S.I. Yi, S.A. Chambers, J. Morais, R. Denecke, C.S. Fadley, P. Liu, T. Kendelewicz, G.E. Brown, Jr., *Surf. Sci.* 425 (1999) 276.
- [24] C. Lemire, S. Bertarione, A. Zecchina, D. Scarano, A. Chaka, S. Shaikhutdinov, H.J. Freund, *Phys. Rev. Lett.* 94 (2005) 166101.
- [25] W. Bergmeyer, H. Schweiger, E. Wimmer, *Phys. Rev. B* 69 (2004) 195409.
- [26] P. Liu, T. Kendelewicz, G.E. Brown Jr., E.J. Nelson, S.A. Chambers, *Surf. Sci.* 417 (1998) 53.
- [27] T.P. Trainor, A.M. Chaka, P.J. Eng, M. Newville, G.A. Waychunas, J.G. Catalano, G.E. Brown, Jr., *Surf. Sci.* 573 (2004) 204.
- [28] T.P. Trainor, P.J. Eng, I.K. Robinson, *J. Appl. Cryst.* 35 (2002) 696.
- [29] R.J. Lad, V.E. Henrich, *Surf. Sci.* 193 (1988) 81.
- [30] M. Gautier-Soyer, M. Pollak, M. Henriot, M.J. Guittet, *Surf. Sci.* 352-354 (1996) 112.
- [31] M.A. Henderson, S.A. Joyce, J.R. Rustad, *Surf. Sci.* 417 (1998) 66.
- [32] M.A. Henderson, *Surf. Sci.* 515 (2002) 253.
- [33] E. Wasserman, J.R. Rustad, A.R. Felmy, B.P. Hay, J.W. Halley, *Surf. Sci.* 385 (1997) 217.
- [34] J.R. Rustad, E. Wasserman, A.R. Felmy, *Surf. Sci.* 424 (1999) 28.

- [35] F. Jones, A.L. Rohl, J.B. Farrow, W.V. Bronswijk, *Phys. Chem. Chem. Phys.* 2 (2000) 3209.
- [36] T.P. Trainor, A.S. Templeton, P.J. Eng, *J. Electron. Spectrosc. Relat. Phenom.* 150 (2006) 66.
- [37] I.K. Robinson, in: G. Brown, D.E. Moncton (Eds.), *Handbook on Synchrotron Radiation*, Elsevier, Amsterdam, 1991, p. 221.
- [38] E. Vlieg, *J. Appl. Cryst.* 33 (2000) 401.
- [39] E. Vlieg, J.F. Van der Veen, S.J. Gurman, C. Norris, J.E. Macdonald, *Surf. Sci.* 210 (1989) 301.
- [40] B.E. Warren, *X-ray Diffraction*, Addison-Wesley, New York. 1969.
- [41] W.C. Hamilton, *Acta. Cryst.* 18 (1965) 502.
- [42] L. Pauling, *The Nature of the Chemical Bond*, third ed., Cornell University Press, Ithaca, New York, 1960.
- [43] I. D. Brown, D. Altermatt, *Acta Cryst.* B41 (1985) 244.
- [44] J.R. Bargar, S.N Towle, G.E. Brown, Jr., G.A. Parks, *J. Coll. Interf. Sci.* 185 (1997) 473.
- [45] J.P. Perdew, K. Burke, M. Ernzerhof, *Phys.Rev. Lett.* 77 (1996) 3865.
- [46] B. Delley, *J. Chem. Phys.* 113 (2000) 7756.
- [47] H.J. Monkhorst, J.D. Pack, *Phys. Rev.* B13 (1976) 5188.
- [48] H.J. Monkhorst, J.D. Pack, *Phys. Rev.* B16 (1977) 1748.
- [49] X.-G. Wang, A.M. Chaka, M. Scheffler, *Phys. Rev. Lett.* 84 (2000) 3650.
- [50] P. Fenter. C. Park, *J. Appl. Cryst.* 37 (2004) 977.
- [51] K.C. Haas, W.F. Schneider, A. Curioni, W. Andreoni, *Science* 282 (1998) 265.
- [52] T. Hiemstra, P. Venema, W. H. van Riemsdijk, *J. Coll. Interf. Sci.* 184 (1996) 680.
- [53] M. Gillet, J.C. Bruna, *Surf. Rev. Lett.* 5 (1998) 325.

- [54] M. Gillet, A.A. Mohammad, K. Masek, E. Gillet, *Thin Solid Films* 374 (2000) 134.
- [55] J.G. Catalano, C. Park, Z. Zhang, P. Fenter, *Langmuir* 22 (2006) 4668.
- [56] P. Guenard, G. Renaud, A. Barbier, M. Gautier-Soyer, *Surf. Rev. Lett.* 5 (1998) 321.
- [57] J. Toofan, P.R. Watson, *Surf. Sci.* 401 (1998), 162
- [58] J.R. Bargar, T.P. Trainor, J.P. Fitts, S.A. Chambers, G.E. Brown, Jr., *Langmuir* 20 (2004) 1667.
- [59] J.P. Fitts, X. Shang, G.W. Flynn, T.F. Heinz, K.B. Eisenthal, *J. Phys. Chem. B* 109 (2005) 7981.

Table 2.1 Unrelaxed surface unit cell coordinates and best-fit model parameters from the analysis of CTR data.

Layer		Unrelaxed (O ₂ -Fe ₂ -O ₂ -Fe ₂ -O ₂ -R)			Best fit model ((H ₂ O) ₂ -(H ₂ O) ₂ -O ₂ -X-O ₂ -Fe ₂ -O ₂ -R)						
		x	y	z	x	y	z	Δz (Å)	B _{iso} (Å ²)	Occ	Σs
i	O				0.22(2)	0.88(3)	2.17(1)	-	8(3)	0.37	0.00
	O				0.28(2)	0.38(3)	2.17(1)	-	8(3)	0.37	0.00
ii	O				0.90(1)	0.15(1)	2.072(6)	-	0.8(7)	0.54	0.00
	O				0.60(1)	0.65(1)	2.072(6)	-	0.8(7)	0.54	0.00
1	O	0.653	0.974	1.903	0.675(5)	0.955(9)	1.911(4)	0.06(3)	0.75	0.61(4)	0.32(7)
	O	0.847	0.474	1.903	0.825(5)	0.455(9)	1.911(4)	0.06(3)	0.75	0.61(4)	0.32(7)
2	Fe	0.000	0.831	1.855	X	X	X	X	X	X	X
	Fe	0.500	0.331	1.855	X	X	X	X	X	X	X
3	O	0.194	0.105	1.750	0.195(3)	0.105(2)	1.741(4)	-0.07(3)	0.75	0.68(3)	1.07(3)
	O	0.306	0.605	1.750	0.306(1)	0.606(1)	1.741(4)	-0.07(3)	0.75	0.68(3)	1.07(3)
4	Fe	0.000	0.380	1.645	0.000	0.380	1.647(1)	0.01(1)	0.50	0.72(1)	2.95(4)
	Fe	0.500	0.880	1.645	0.500	0.880	1.647(1)	0.01(1)	0.50	0.72(1)	2.95(4)
5	O	0.653	0.237	1.597	0.653(1)	0.237(1)	1.595(3)	-0.01(2)	0.50	0.96(3)	1.58(1)
	O	0.847	0.737	1.597	0.847(2)	0.737(1)	1.595(3)	-0.01(2)	0.50	0.96(3)	1.58(1)
6	O	0.153	0.404	1.403	0.153	0.404	1.404(3)	0.01(2)	0.40	1.00	1.94(2)
	O	0.347	0.904	1.403	0.347	0.904	1.404(3)	0.01(2)	0.40	1.00	1.94(2)
7	Fe	0.500	0.261	1.355	0.500	0.261	1.354(1)	-0.01(1)	0.32	1.00	2.97(6)
	Fe	0.000	0.761	1.355	0.000	0.761	1.354(1)	-0.01(1)	0.32	1.00	2.97(6)
8	O	0.694	0.535	1.250	0.694	0.535	1.249(3)	-0.01(2)	0.40	1.00	1.98(2)
	O	0.806	0.035	1.250	0.806	0.035	1.249(3)	-0.01(2)	0.40	1.00	1.98(2)
9	Fe	0.500	0.810	1.145	0.500	0.810	1.145	0.00	0.32	1.00	2.95(7)
	Fe	0.000	0.310	1.145	0.000	0.310	1.145	0.00	0.32	1.00	2.95(7)
10	O	0.153	0.667	1.097	0.153	0.667	1.097	0.00	0.40	1.00	1.98(2)
	O	0.347	0.166	1.097	0.347	0.166	1.097	0.00	0.40	1.00	1.98(2)

The estimated errors from least-squares fits at the 96% confidence interval are given in parentheses. Values without reported errors were held fixed in the final fits. The Δz values are change in the layer z position with respect to ideal stoichiometric termination. The B_{iso} are isotropic Debye-Waller factors and Occ are occupancy parameters. Bond valence sums (Σs) were calculated assuming unit site occupancies. The "X" denotes the absence of a given layer. The atoms in boldface represent layers added above the first layer of the stoichiometric termination.

Table 2.2 Stoichiometry and layer sequence for various clean and hydrated surface models that were calculated using DFT and compared with experimental CTR data.

Models	Layer sequence for various surface terminations						
	ii	i	1	2	3	4	5
A							
1			O ₂	Fe ₂	O ₂	Fe ₂	O ₂ R
2		(H ₂ O) ₂	O ₂	Fe ₂	O ₂	Fe ₂	O ₂ R
3		O ₂	O ₂	Fe ₂	O ₂	Fe ₂	O ₂ R
4		(HO) ₂	(HO) ₂	Fe ₂	O ₂	Fe ₂	O ₂ R
5	(H ₂ O) ₂	(HO) ₂	(HO) ₂	Fe ₂	O ₂	Fe ₂	O ₂ R
B							
1			X	X	O ₂	Fe ₂	O ₂ R
2		(H ₂ O) ₂	X	X	O ₂	Fe ₂	O ₂ R
C							
1			O ₂	X	O ₂	Fe ₂	O ₂ R
2			(HO) ₂	X	(HO) ₂	Fe ₂	O ₂ R
3			(HO) ₂	X	(HO) ₂	Fe ₂	(HO) ₂ R
4			(H ₂ O) ₂	X	(HO) ₂	Fe ₂	O ₂ R
5		(H ₂ O) ₂	(HO) ₂	X	(HO) ₂	Fe ₂	O ₂ R
6		(H ₂ O) ₂	(HO) ₂	X	(HO) ₂	Fe ₂	(HO) ₂ R
7		(H ₂ O) ₂	(H ₂ O) ₂	X	(HO) ₂	Fe ₂	O ₂ R
8	(H ₂ O) ₂	(H ₂ O) ₂	(H ₂ O) ₂	X	(HO) ₂	Fe ₂	O ₂ R

Table 2.3 Percent layer relaxations ($\% \Delta$) for selected DFT models calculated by Lo et al. [20] and the best-fit experimental model.

Models		A1	A2	A4	A5	C2	C3	C4	C6	C7	C8	Expt
Layers												
1-2	O ₂ -Fe ₂	37.0	29.0	-19.0	-19.0	0.7*	13.0*	33.0*	5.7*	20.0*	24.0*	11.8*
2-3	Fe ₂ -O ₂	-26.0	-11.0	12.0	9.3							
3-4	O ₂ -Fe ₂	7.3	3.0	5.1	5.7	-31.0	-35.0	10.0	-27.0	-3.7	-6.1	-10.9
4-5	Fe ₂ -O ₂	25.0	9.5	-7.4	-6.4	57.0	66.0	-1.3	63.0	13.0	12.0	8.4
5-6	O ₂ -O ₂	-4.3	-1.2	0.8	0.6	-12.0	-4.9	0.5	-5.6	-2.2	-1.6	-1.5
6-7	O ₂ -Fe ₂	6.6	0.1	-1.4	-0.7	7.3	43.0	-0.8	41.0	6.8	5.8	4.2
7-8	Fe ₂ -O ₂	1.7	1.3	0.6	0.7	7.6	-6.9	1.5	-6.2	1.0	0.7	0.0
8-9	O ₂ -Fe ₂	-0.8	0.2	0.6	0.6	-6.7	-1.9	-1.0	-2.0	-1.7	-2.0	-1.0
9-10	O ₂ -Fe ₂	-0.7	0.7	0.1	-0.4	-6.0	1.4	0.5	0.2	0.0	0.5	0.0

*Note: The stoichiometries of the models are listed in Table 2 and the numbers marked with * represent layer 1-3 relaxations.*

Table 2.4 Predicted proton stoichiometry and bond valence analysis for charge neutral surfaces with Fe-O stoichiometry $O_2-X-O_2-Fe_2-O_2-R$ (C-series in Table 2.2).

a) Predicted stoichiometry: $(H_2O)_2-(H_2O)_2-(HO)_2-X-(HO)_2-Fe_2-(HO)_2-R$

Type of O	Bond-valence (experimental)	Number of H added	Bond-valence with added H	Predicted stability
^I O (×2)	0.32	1	1.12	under saturated
^{II} O (×2)	1.07	1	1.87	stable
^{III} O (×2)	1.58	1	2.38	over saturated

b) Predicted stoichiometry: $(H_2O)_2-(H_2O)_2-(H_2O)_2-X-(HO)_2-Fe_2-O_2-R$

Type of O	Bond-valence (experimental)	Number of H added	Bond-valence with added H	Predicted stability
^I O (×2)	0.32	2	1.92	stable
^{II} O (×2)	1.07	1	1.87	stable
^{III} O (×2)	1.58	-	1.58	under saturated

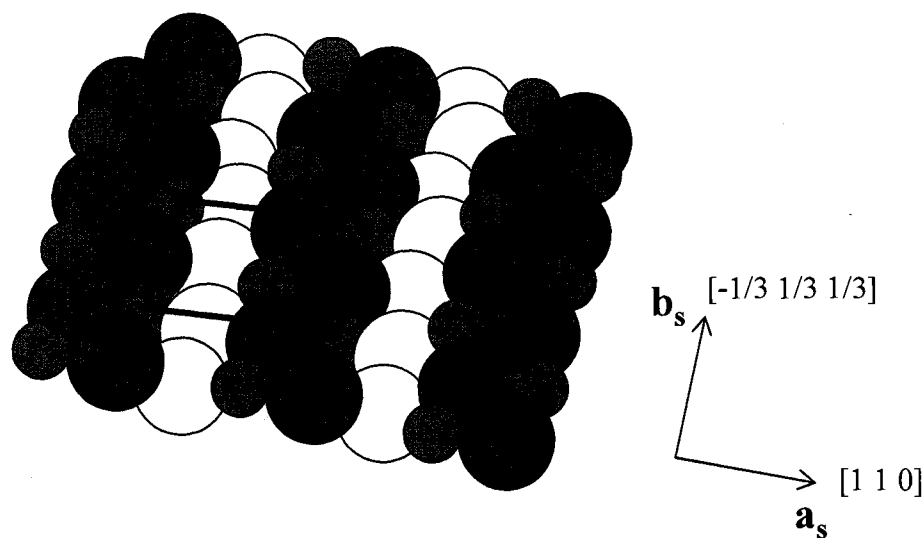
Note: The superscript in column 1 represents the coordination number of O with Fe. Each proton is assumed to contribute 0.8 v.u.[44]. The (×2) shows that there are two groups of a particular kind per unit cell and 'X' denotes the absence of a Fe layer. The atoms shown in boldface represent the layers added above the first layer of the stoichiometric termination

Table 2.5 Bond-valence sum (Σs) calculations for selected DFT models calculated by Lo et al. [20] and the best-fit experimental model.

Models		A1	A2	A4	A5	C2	C3	C4	C6	C7	C8	Expt
Layers												
1	O ₂	1.8	1.7, 1.5	1.9	1.9	1.6	1.4	1.9	1.6	1.9	1.9	1.9
2	Fe ₂	2.8	2.7, 2.8	2.8	2.8	X	X	X	X	X	X	X
3	O ₂	1.9	1.9, 1.8	1.9	1.9	1.8	1.7	1.6	2.0	1.6	1.6	1.9
4	Fe ₂	2.8	2.8	2.9	2.9	3.7	2.9	2.7	2.8	2.7	2.7	3.0
5	O ₂	2.0	2.0, 1.9	1.9	1.9	1.9	2.0	1.9	2.0	1.9	1.9	1.6
6	O ₂	1.9	1.9	1.9	1.9	1.9	1.8	1.9	1.8	1.9	1.9	1.9
7	Fe ₂	2.9	2.9	2.9	2.9	2.9	2.9	2.9	2.9	2.9	2.9	3.0
8	O ₂	2.0	2.0	1.9	1.9	2.0	2.0	2.0	2.0	2.0	2.0	2.0
9	Fe ₂	2.9	2.9	2.9	2.9	2.9	2.9	2.9, 3.0	2.9, 2.8	2.9, 3.0	2.9, 3.0	3.0
10	O ₂	1.9	1.9	1.9	2.0, 1.9	1.9	1.9	2.0, 1.9	1.8, 2.0	2.0, 1.9	2.0, 1.9	2.0

Note: The stoichiometries of the models are listed in Table 2.2. The bond-valence for the experimental model was calculated using Table 2.4b.

a)



b)

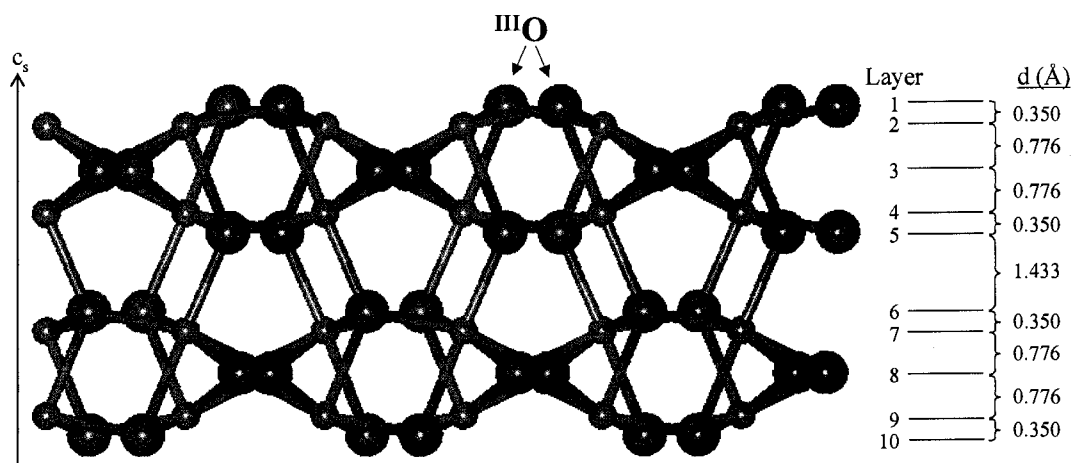


Figure 2.1 a) In-plane view of the $\alpha\text{-Fe}_2\text{O}_3$ ($1\bar{1}02$) surface showing zig-zag rows of oxygen and the real space basis vectors in the surface indexing, shown along with their indices in the bulk indexing; b) layer stacking sequence along the c_s axis for bulk a stoichiometric termination for $\alpha\text{-Fe}_2\text{O}_3$ ($1\bar{1}02$). The large spheres are O atoms and small spheres are Fe atoms. The III O represents the oxygen atoms which are triply coordinated to iron.

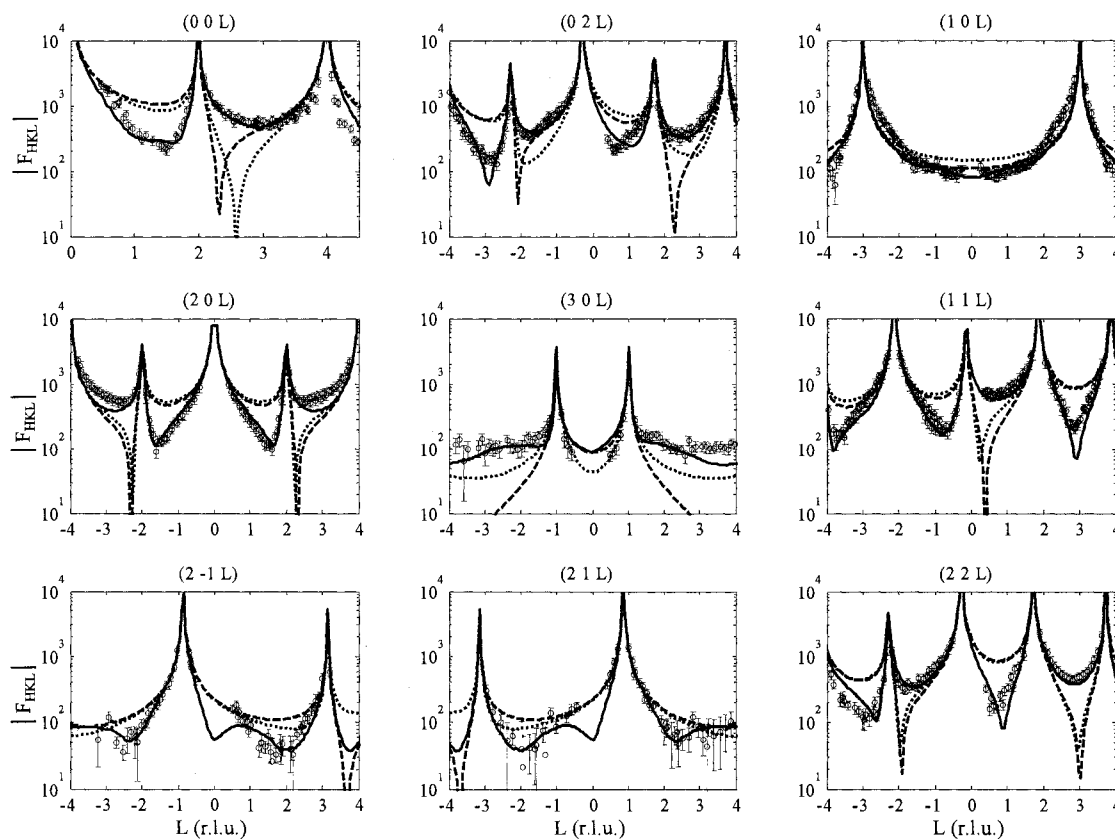


Figure 2.2 Experimental structure factors (F_{HKL}) as a function of perpendicular momentum transfer (L , in reciprocal lattice units) for the α - Fe_2O_3 ($1\bar{1}02$) surface. The dashed lines represent calculated CTRs for the ideal stoichiometric termination ($\text{O}_2\text{-Fe}_2\text{-O}_2\text{-R}$), the dotted lines are the calculated CTRs for the bulk termination with an added oxygen layer ($\text{O}_2\text{-O}_2\text{-Fe}_2\text{-O}_2\text{-Fe}_2\text{-O}_2\text{-R}$), and the solid lines represent the best fit model ($(\text{H}_2\text{O})_2\text{-(H}_2\text{O})_2\text{-O}_2\text{-X-O}_2\text{-Fe}_2\text{-O}_2\text{-R}$). The atoms in boldface represent the layers added above the first layer of the stoichiometric termination.

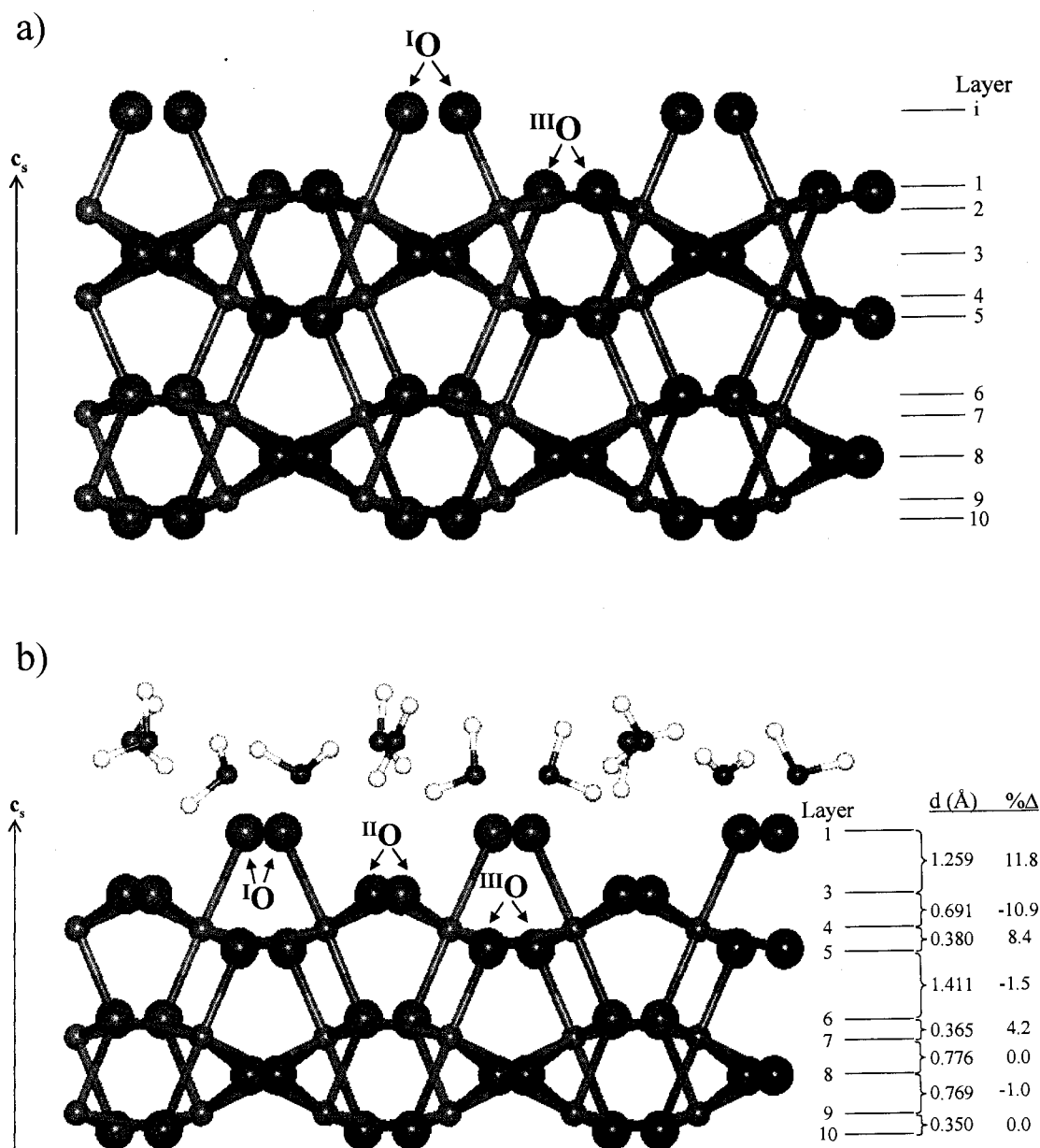


Figure 2.3 a) Layer stacking sequence along the c_s axis for the model suggested by previous UHV studies [30, 31]; b) layer stacking sequence along the c_s axis along with layer spacings and percent relaxations for best fit CTR model $(\text{H}_2\text{O})_2-(\text{H}_2\text{O})_2\text{-O}_2\text{-X-O}_2\text{-Fe}_2\text{-O}_2\text{-R}$. The large spheres are O atoms and small spheres are Fe atoms. The atoms in the boldface represent the layers added above the first layer of the stoichiometric termination. The adsorbed water molecules are shown above layer 1 with arbitrary water molecule orientations. The $\text{III}^{\text{I}}\text{O}$, $\text{II}^{\text{I}}\text{O}$, and $\text{I}^{\text{I}}\text{O}$ represent oxygen triply, doubly and singly coordinated to iron, respectively.

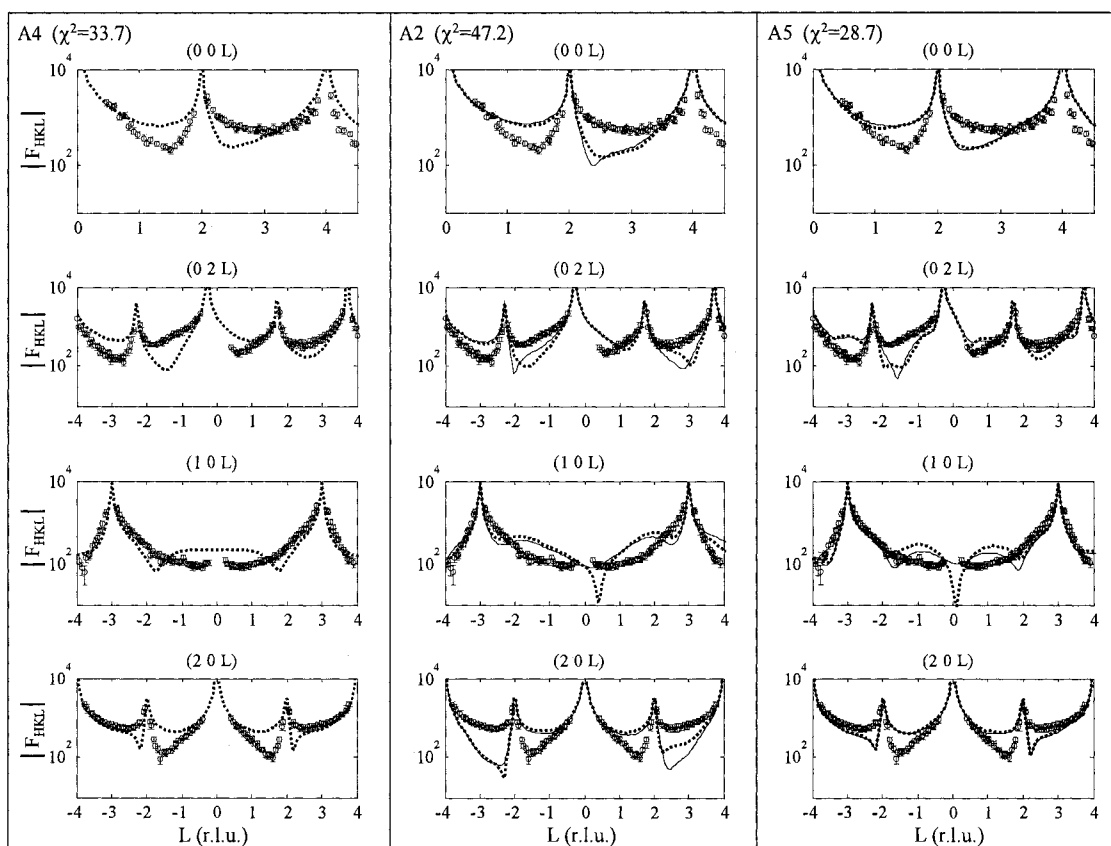


Figure 2.4 A comparison of calculated and experimental CTR data for models A4, A2, and A5. The dotted lines are from the direct calculation using the DFT derived coordinates and the solid lines represent the fit with varying occupancy and Debye-Waller factor for the water overlayer, where applicable.

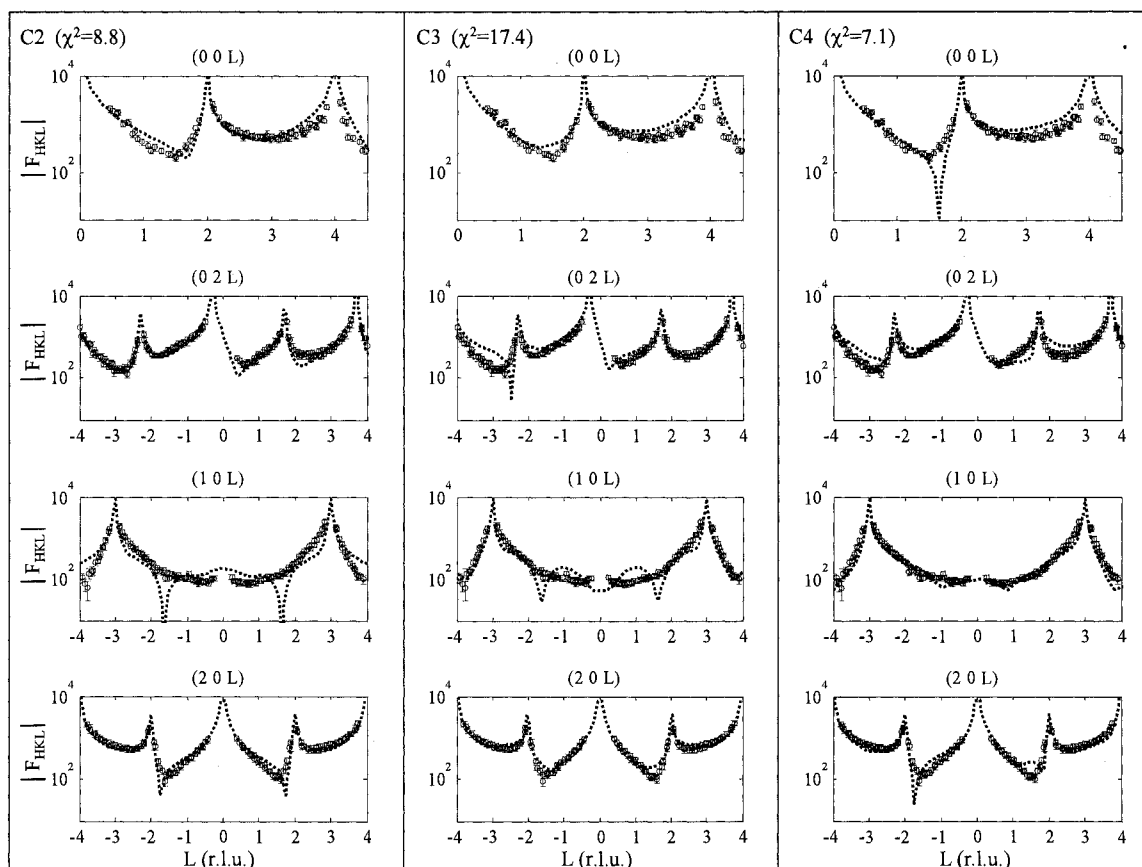


Figure 2.5 A comparison of calculated and experimental CTR data for models C2, C3, and C4. The dotted lines are from the direct calculation using the DFT derived coordinates. All three models shown here have zero occupancy for layer 2 Fe.

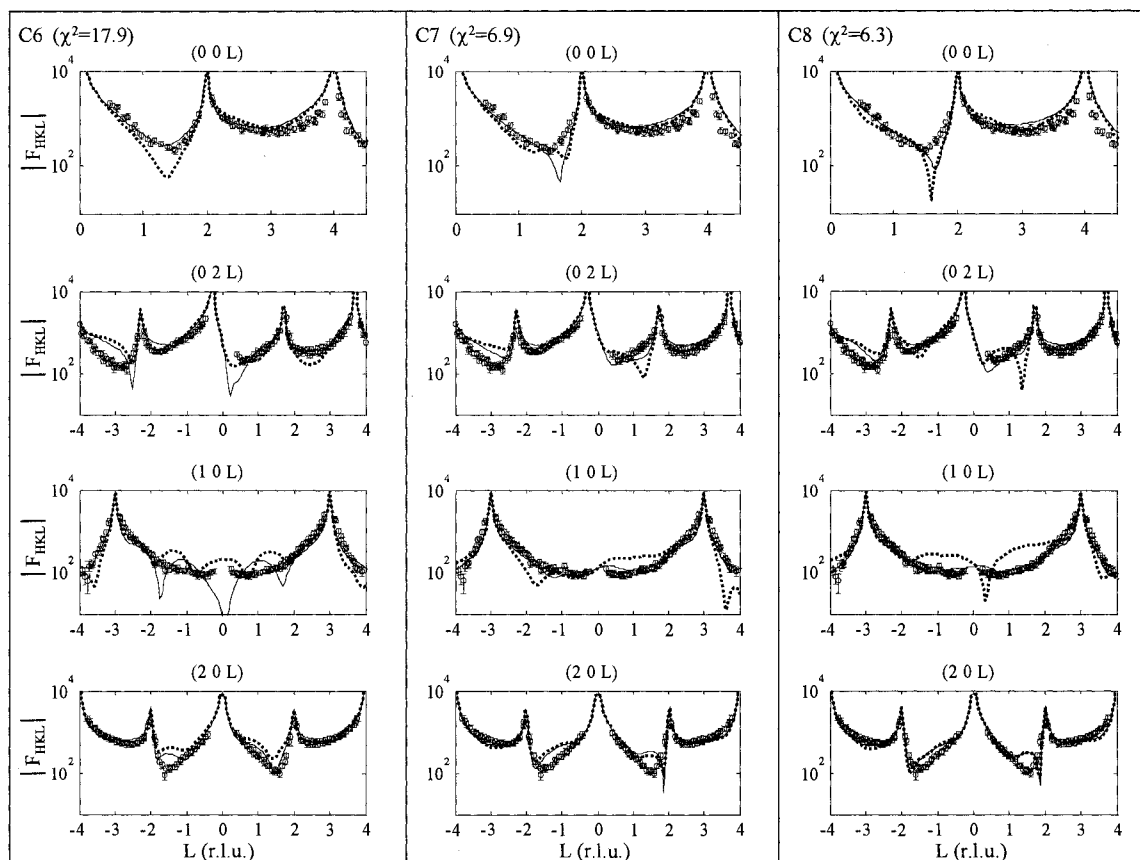


Figure 2.6 A comparison of calculated and experimental CTR data for models C6, C7, and C8. The dotted lines are from the direct calculation using the DFT-derived coordinates and the solid lines represent the fit with varying occupancy and Debye-Waller factors for the water overlayer, where applicable. All three models shown here have zero occupancy for layer 2 Fe.

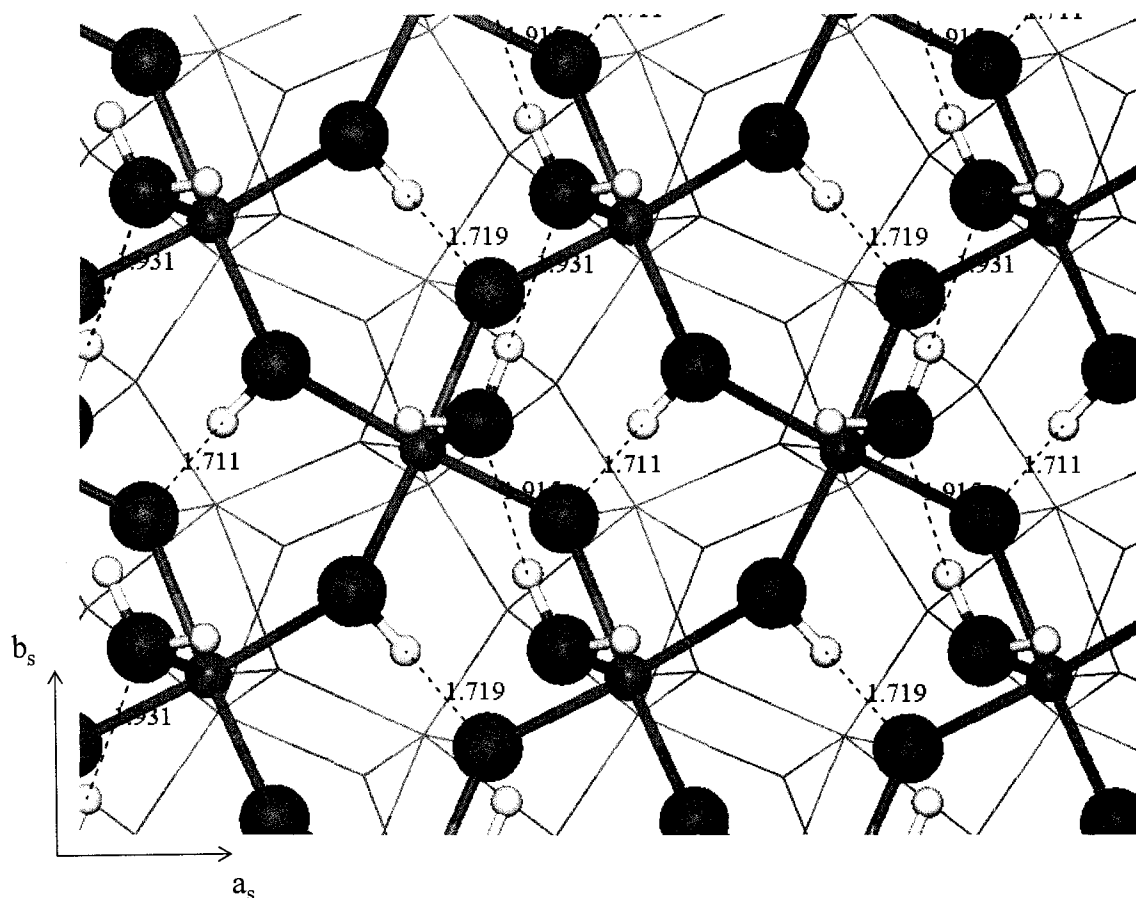


Figure 2.7 In-plane view of the hydroxylated $\alpha\text{-Fe}_2\text{O}_3$ (1102) surface showing the probable hydrogen bonding network of surface functional groups in the proposed model along with corresponding hydrogen bond distances. The dashed lines show the possible hydrogen bonds and the distance (in Å) between hydrogen bonded species. The large spheres are O atoms, medium spheres are Fe atoms, and the small spheres are H atoms.

Chapter 3 HYDRATED α -Fe₂O₃(1 $\bar{1}$ 02) SURFACE STRUCTURE: ROLE OF SURFACE PREPARATION*

ABSTRACT

The surface structure of α -Fe₂O₃(1 $\bar{1}$ 02) was studied under two different surface preparation conditions using crystal truncation rod (CTR) diffraction. Wet chemical and mechanical polishing (CMP) at 298 K results in a crystalline surface termination in which the top layer of iron atoms is absent compared to the stoichiometric bulk termination. Annealing in air at 773 K resulted in a transformation of the surface to a structure consistent with hydroxylation of the stoichiometric termination. These results agree with theoretical predictions of Lo et al. [C. S. Lo, K.S. Tanwar, A. M. Chaka, T.P. Trainor, Phys Rev B 75 (2007) 075425] and clearly show an ambient pressure surface preparation path leading to a stoichiometric hydroxylated surface, which is apparently a meta-stable configuration at room temperature.

* Tanwar K. S., Catalano J. G., Petitto S. C., Ghose S. K., Eng P. J., and Trainor T. P. (2007) Hydrated α -Fe₂O₃ (1 $\bar{1}$ 02) surface structure: Role of surface preparation. *Surf. Sci.* **601**, L59-L64.

Iron (hydr)oxides are abundant natural substrates that play an important role in the fate and transport of various contaminants, primarily through adsorption and surface precipitation processes [1, 2]. Surface reactions involving these oxides also are critical in a variety of industrial applications including catalysis [3-6], metal oxide thin film preparation [7-10], corrosion research [11-14], data storage [15], and drug delivery [16]. The chemical properties (e.g. Lewis and Bronsted acid/base character) and overall reactivity of these oxides are dictated by the type and local structure of chemical moieties exposed at the interface [17], which are dependent on the chemical and physical history of the surface.

Numerous studies have focused on determining the surface structure of iron and aluminum oxides under ultra-high vacuum (UHV) conditions [18-23] as well as under hydrated conditions [24-27]. Not surprisingly, different structural terminations for the same surface are often observed, emphasizing the important role of surface preparation [26, 27]. For example, the $\alpha\text{-Al}_2\text{O}_3(0001)$ surface has three unique proposed surface structures resulting from three different surface preparations. A hydroxyl terminated $\alpha\text{-Al}_2\text{O}_3(0001)$ surface was determined after a mild acid wash and air annealing at 623 K using crystal truncation rod (CTR) diffraction in a humidity cell [24], an Al terminated surface was identified via CTR after O_2 annealing in UHV at 1123 K [23], and a mixed Al/O terminated surface was observed with LEED after air annealing at 1773 K followed by O_2 annealing in UHV at 1173 K [20]. The $\alpha\text{-Al}_2\text{O}_3(1\bar{1}02)$ surface also is known to have discrete surface structures depending on surface preparation, where a hydroxylated

stoichiometric termination was determined after annealing in air at 623 K measured with CTR diffraction [26], while a sample annealed in air at 623 K followed by UHV O₂ annealing at 1273 K, and subsequently dosed with water (1×10^{-8} to 1.6 Torr) resulted in a termination with missing top layer of aluminum atoms measured with CTR diffraction in UHV [28].

The α -Fe₂O₃ (1 $\bar{1}$ 02) surface has been previously studied using UHV techniques exhibiting either a (1 \times 1) stoichiometric surface or a (2 \times 1) reconstructed surface after annealing in O₂ [18, 19, 29]. Water adsorption was used to probe the surface reactivity of the (1 \times 1) surface and resulted in a hydroxylated stoichiometric termination at temperatures < 350 K [18, 30]. We have previously studied the surface structure of the α -Fe₂O₃(1 $\bar{1}$ 02) prepared using a chemical mechanical polishing (CMP) procedure detailed elsewhere [27] under hydrated conditions at room temperature. The CMP prepared surface consistently results in a surface termination with a vacant top Fe layer compared to the ideal stoichiometric termination (Figure 3.1) [27].

The observation of different chemical terminations for a given crystallographic orientation demonstrates the need to understand the relationship between surface preparation and the resultant surface structure. Because surface reactivity is strongly dependent on surface structure, any changes in the surface preparation may have substantial effects on the reactivity of the substrate. Currently, there are a limited number of non-UHV studies correlating specific surface terminations with surface preparation

methods, hence there is a limited understanding about how to control surface structures through wet surface preparations. The present study provides a systematic experimental analysis of the role of ambient pressure wet preparation procedure on the structure of α - $\text{Fe}_2\text{O}_3(1\bar{1}02)$ surface.

Natural single crystals of α - $\text{Fe}_2\text{O}_3(1\bar{1}02)$ ($\sim 1 \text{ cm}^2$) obtained from Bahia, Brazil were prepared using a wet chemical mechanical polishing (CMP) procedure followed by mild acid etching (details are provided in Tanwar et al. [27]). The α - $\text{Fe}_2\text{O}_3(1\bar{1}02)$ sample was then annealed in air at $773 \pm 2 \text{ K}$ for 3 h in a pre-heated furnace. Following annealing the sample was allowed to equilibrate with room temperature (298 K) in a dessicator for 6 h. After cooling, the sample was mounted in an environmental cell used for surface diffraction measurements [31] and kept under water-saturated He atmosphere (relative humidity $> 90\%$, $p\text{H}_2\text{O} > 20 \text{ Torr}$) to ensure that the surface remained fully hydrated [32].

Crystal truncation rod (CTR) experiments were performed on undulator beamline 13-ID at Advanced Photon Source (APS) with a liquid N_2 cooled double crystal $\text{Si}(111)$ monochromator and Rh-coated vertical and horizontal mirrors for focusing and harmonic rejection. All CTR experiments were conducted at 298 K using a $2 + 2 + \text{kappa}$ -geometry diffractometer with fixed incident energy of 12 keV. The surface diffraction intensities were collected in both specular and non-specular geometries by performing rocking scans through the CTR. The intensity of each rocking curve was background subtracted and corrected for active area, polarization, scan speed, and Lorentz factors to

determine the individual structure factors [33]. The data set consisted of the four CTRs (Figure 3.2) that are most sensitive to surface termination based on theoretical simulations of CTR profiles.

The CTR data was fit using a non-linear least squares routine with fixed bulk and adjustable surface models [34]. The fit parameters include atomic relaxations along x, y, and z-directions, atomic occupancies, Debye-Waller factors, and an overall roughness factor [35]. The $\alpha\text{-Fe}_2\text{O}_3(1\bar{1}02)$ surface unit cell was indexed using the method described by Trainor et al. [28, 36] and detailed further elsewhere [27]. The modeled structure factors were calculated using two surface models to account for the two equally probable and chemically equivalent but structurally different terminations (layer-1 and layer-6 termination) (Figure 3.1) of the $\alpha\text{-Fe}_2\text{O}_3(1\bar{1}02)$ surface [27,34, 35, 37]. The final magnitude of structure factor was determined by in-phase summation of structure factor magnitudes of the two chemically equivalent surfaces [27, 28]. Hydrogen atoms were not included in the CTR analysis because of their weak X-ray scattering cross section.

For the $\alpha\text{-Fe}_2\text{O}_3(1\bar{1}02)$ CTR data analysis, we considered various possible surface terminations [27, 38]. The three most probable chemically distinct terminations based on previous UHV and ambient pressure experiments are: a surface where the first layer of iron atoms are absent [27] (model A), bulk stoichiometric [18] (model B), and hydroxylated stoichiometric termination [18] (model C) (Figure 3.1). For the purpose of discussion, we refer to these terminations as models A, B, and C, respectively.

The CTR data for air annealed $\alpha\text{-Fe}_2\text{O}_3(1\bar{1}02)$ surface was initially analyzed using model A, which is obtained via CMP preparation [27], to observe what affects, if any, annealing has on the surface structure. The calculated CTRs for model A did not reproduce the surface sensitive features in the experimental data including the intensity variations observed on either side of the bulk Bragg peaks at $(0\ 0\ 2)$, $(2\ 0\ 2)$, and $(0\ 2\ -2.28)$, and the features at $(1\ 0\ 1.1)$ and $(1\ 0\ -1.1)$ (Figure 3.2). Allowing atomic relaxations during the analysis did not improve fit quality ($\chi^2 > 9$) (not shown). The unsatisfactory fit obtained using model A for the air annealed CTR data suggests significant structural change occurred during annealing.

The calculated CTRs using unrelaxed model B (stoichiometric bulk termination) also resulted in poor agreement with the air annealed $\alpha\text{-Fe}_2\text{O}_3(1\bar{1}02)$ experimental data (not shown). Allowing atomic position and occupancy parameters of model B to vary resulted in a significantly improved fit ($\chi^2 = 1.7$) (Figure 3.2). However, this model still fails to reproduce the features at $(1\ 0\ 1.1)$ and $(1\ 0\ -1.1)$ along with significant disagreements at $(0\ 2\ 2)$, $(0\ 2\ -1.46)$ and $(0\ 0\ 2.65)$ (Figure 3.2).

The third potential surface model (C) accounts for the likely adsorption of water at the five-fold coordinated Fe sites of stoichiometric surface model. Therefore, in terms of Fe/O stoichiometry, model C only differs from the stoichiometric termination (model A) by the addition of the layer i oxygen (Figure 3.1). The relaxed model C shows an

excellent fit to the experimental data ($\chi^2 = 1.2$) (Figure 3.2) where all the structure factor variations and especially the (10L) features are reproduced. The best-fit model atomic coordinates, z-layer displacements, and atomic occupancies are listed in Table 3.1, and the percent inter-layer relaxations are listed in Table 3.2. The best-fit model results in partial occupancies for the oxygen/hydroxyl overlayer (layer i) 70 ± 20 % and the first iron layer (layer 2) 71 ± 5 % with errors reported at 96% confidence interval (Table 3.1). The partial occupancy of layer 2 suggests that 29 ± 5 % of the surface may be consistent with the termination having layer 2 iron atom vacancies (i.e. model A); the surface previously observed from CMP preparation and no annealing [27]. We note that these results cannot clearly distinguish between random site occupancy and presence of distinct domains; however, these results clearly show the hydroxylated stoichiometric termination is predominant on the surface prepared via air-annealing.

Comparison of the above results with the recent *ab initio* thermodynamic predictions of Lo et al. [38] suggest that the observed surface transformation, induced by ambient pressure annealing, is driven by the difference in temperature dependence of the surface free energies of the various surface stoichiometries. Lo et al.'s DFT study predicts that the lowest energy surface termination at room temperature has a Fe/O stoichiometry consistent with the experimentally determined CMP prepared surface (model A) [27, 38]. This study also observed that differences in the protonation states of the surface oxygen anions (for a given Fe/O stoichiometry) lead to significant changes in relaxations and free energy of the surfaces, thereby uniquely identifying the lowest energy surface in terms of

Fe, O and H stoichiometry. In the lowest energy room temperature stoichiometry the layer 1 oxygen are doubly protonated (aquo groups) and the layer 3 oxygen are singly protonated (hydroxo groups) (Fig 1 A) [27,38]. This model results in a charge balanced surface (replacement of one Fe(III) cation by three H^+) and is hypothesized by Lo et al. [38] to lead to a lower surface free energy due to reduction of cation-cation repulsion in the near surface layer. The *ab initio* thermodynamics calculations further predict that with increasing temperatures (at fixed water partial pressures) the hydroxylated stoichiometric surface becomes the lowest energy configuration; the Fe/O stoichiometry is consistent with model C and the layer i and layer 1 oxygen anions are both singly protonated (hydroxo groups), again resulting in an overall charge neutral surface stoichiometry. Further increase in temperature is predicted to result in stabilization of the stoichiometric $\alpha\text{-Fe}_2\text{O}_3(1\bar{1}02)$ surface (model B) [38]. This sequence is consistent with progressive dehydroxylation of the surface; however, Lo et al. also predicted that the room temperature lowest energy surface may be stabilized at higher temperatures (e.g. up to 600K) by maintaining the water partial pressures at the saturation vapor pressure [38].

Tanwar et al. previously used these results, as well as crystal chemical analysis, to show that the CMP prepared surface structure was consistent with the predicted lowest energy stoichiometry at 298 K, including the surface protonation states [27,38]. The experimental model presented here for the ambient pressure annealed CMP surface is structurally consistent with the hydroxylated stoichiometric surface predicted by Lo et al. to be stable in the temperature range of 435 K to 565 K (fixed $p_{H_2O} = 3.2\text{kPa}$). These

results suggest that annealing the $\alpha\text{-Fe}_2\text{O}_3(1\bar{1}02)$ surface at 773 K provides sufficient thermal energy for Fe mobility to repopulate the missing top layer Fe sites, likely resulting in the predicted minimum energy stoichiometric surface at 773 K (i.e., model B). Rapid cooling of the sample after annealing presumably quenches the surface in this configuration (model B) which is then kinetically inhibited from reaching the room temperature minimum energy structure (model A). In addition, the reaction of water with the stoichiometric termination (model B) results in the hydroxylation of the surface (model C).

In summary, the CMP prepared $\alpha\text{-Fe}_2\text{O}_3(1\bar{1}02)$ results in a termination with nearly 100 % first layer vacancy of Fe atoms [27], whereas air annealing followed by rapid cooling and exposure to high humidity trapped the surface in a meta-stable hydroxylated stoichiometric configuration. These two structurally different terminations may exhibit significantly different reactivity trends. For example, sorption of Fe(II) on the CMP prepared $\alpha\text{-Fe}_2\text{O}_3(1\bar{1}02)$ results in the partial filling of the missing Fe lattice sites described in model A (K. Tanwar, unpublished data). Similar sorption geometry may be expected from other transition metals ions (e.g. Mn(II), Mn(IV), Cr(III)), which are comparable in size to Fe(III) [39]. In absence of such Fe vacancies (i.e. model C) the metal ion sorption geometry, and therefore, the reactivity are expected to be significantly different. Alternatively, for cases where the surface oxygen groups that are singly coordinated with iron are the primary binding sites [40, 41], the reactivity is expected to be similar since these groups are structurally equivalent for both terminations (layer 1 in

model A and layer i in model C) (Figure 3.1) as recently shown by Catalano et al. [41] for the case of arsenate adsorption on the $\alpha\text{-Fe}_2\text{O}_3(1\bar{1}02)$ surface.

Overall, the current study shows that the $\alpha\text{-Fe}_2\text{O}_3(1\bar{1}02)$ surface structure is highly dependent on surface preparation conditions (Figure 3.1). These results also emphasize that having a detailed understanding of the surface preparation pathways and the resultant surface structure is critical for interpreting surface reactivity under variable in-situ reaction conditions.

ACKNOWLEDGEMENTS

The authors would like to acknowledge Anne Chaka, Gordon Brown Jr. and Cynthia Lo for helpful comments on the results and manuscript. This research was supported by NSF grants CBET-0404400 and CHE-0431425, University of Alaska Fairbanks Graduate Fellowship (KST), the Arctic Region Supercomputing Center (University of Alaska Fairbanks) and the Argonne National Laboratory Named Postdoctoral Fellowship Program through contract DOE DE-AC02-06CH11357 (JGC). This work was performed at GeoSoilEnviroCARS (Sector13) of the Advanced Photon Source (APS), Argonne National Laboratory. Use of the APS was supported by DOE Basic Energy Sciences, Office of Energy Research, under Contract No. DE-AC02-06CH11357.

REFERENCES

- [1] W. Stumm, J.J. Morgan, *Aquatic Chemistry: Chemical Equilibria and Rates in Natural Waters*, third ed., Wiley Interscience, New York, 1996.
- [2] R.M. Cornell, U. Schwertmann, *Iron oxides: Structure, Properties, Reactions, Occurrence, and Uses*, first ed., Wiley-VCH, 1996.
- [3] W. Weiss, W. Ranke, *Prog. Surf. Sci.* 70 (2002) 1.
- [4] N. Apostolescu, B. Geiger, K. Hizbullah, M.T. Jan, S. Kureti, D. Reichert, F. Schott, W. Weisweiler, *Appl. Catal., B: Environmental* 62 (2006) 104.
- [5] E. Lee, K. Jung, O. Joo, Y. Shul, *Appl. Catal., A: General* 284 (2005), 1.
- [6] Y. Zheng, Y. Cheng, Y. Wang, F. Bao, L. Zhou, X. Wei, Y. Zhang, Q. Zheng, *J. Phys. Chem. B* 110 (2006) 3093.
- [7] E. Celik, A.Y. Yildiz, N.F. Ak Azem, M. Tanoglu, M. Toparli, O.F. Emrullahoglu, I. Ozdemir, *Mater. Sci. Eng., B: Solid-State Materials for Advanced Technology* 129 (2006) 193.
- [8] S. Kumari, C. Tripathi, A.P. Singh, D. Chauhan, R. Shrivastav, S. Dass, V.R. Satsangi, *Curr. Sci.* 91 (2006) 1062.
- [9] K. Shi, L. Peng, Q. Chen, R. Wang, W. Zhou, *Microporous Mesoporous Mater.* 83 (2005) 219.
- [10] K. Chung, K. Kim, S. Han, H. Lee, *J. Electrochem. Soc.* 152 (2005) C560.
- [11] A. Kuch, *Corros. Sci.* 28 (1988) 221.
- [12] N. Kouloumbi, G.M. Tsangaris, C. Vourvahi, F. Molnar, *J. Coat. Technol.* 69 (1997) 53.
- [13] D. Neff, S. Reguer, L. Bellot-Gurlet, P. Dillmann, R. Bertholon, *J. Raman Spectrosc.* 35 (2004) 739.
- [14] S.A.M. Refaey, F. Taha, H.S. Shehata, *J. Appl. Electrochem.* 34 (2004) 891.
- [15] G. Reiss, A. Huetten, *Nat. Mater.* 4 (2005) 725.
- [16] D.K. Kim, Y. Zhang, W. Voit, K.V. Rao, J. Kehr, B. Bjelke, M. Muhammed, *Scr. Mater.* 44 (2001) 1713.

- [17] W. Stumm, *Colloids Surf., A: Physicochemical and Engineering Aspects* 73 (1993) 1.
- [18] M.A. Henderson, S.A. Joyce, J.R. Rustad, *Surf. Sci.* 417 (1998) 66.
- [19] M. Gautier-Soyer, M. Pollak, M. Henriot, M.J. Guittet, *Surf. Sci.* 352-354 (1996) 112.
- [20] J. Toofan, P.R. Watson, *Surf. Sci.* 401 (1998), 162.
- [21] M. Gillet, J.C. Bruna, *Surf. Rev. Lett.* 5 (1998) 325.
- [22] S. Thevuthasan, Y.J. Kim, S.I. Yi, S.A. Chambers, J. Morais, R. Denecke, C.S. Fadley, P. Liu, T. Kendelewicz, G.E. Brown, Jr., *Surf. Sci.* 425 (1999) 276.
- [23] P. Guenard, G. Renaud, A. Barbier, M. Gautier-Soyer, *Surf. Rev. Lett.* 5 (1998) 321.
- [24] P.J. Eng, T.P. Trainor, G.E. Brown Jr., G.A. Waychunas, M. Newville, S.R. Sutton, M.L. Rivers, *Science* 288 (2000) 1029.
- [25] T.P. Trainor, A.M. Chaka, P.J. Eng, M. Newville, G.A. Waychunas, J.G. Catalano, G.E. Brown Jr., *Surf. Sci.* 573 (2004) 204.
- [26] J.G. Catalano, C. Park, Z. Zhang, P. Fenter, *Langmuir* 22 (2006) 4668.
- [27] K.S. Tanwar, C.S. Lo, P.J. Eng, J.G. Catalano, D.K. Walko, G.E. Brown Jr., G.A. Waychunas, A.C. Chaka, T.P. Trainor, *Surf. Sci.* 601 (2007) 460.
- [28] T.P. Trainor, P.J. Eng, G.E. Brown Jr., I.K. Robinson, M. De Santis, *Surf. Sci.* 496 (2002) 238.
- [29] R.J. Lad, V.E. Henrich, *Surf. Sci.* 193 (1988) 81.
- [30] M.A. Henderson, *Surf. Sci.* 515 (2002) 253.
- [31] T.P. Trainor, A.S. Templeton, P.J. Eng, *J. Electron. Spectrosc. Relat. Phenom.* 150 (2006) 66.
- [32] P. Liu, T. Kendelewicz, G.E. Brown Jr., E.J. Nelson, S.A. Chambers, *Surf. Sci.* 417 (1998) 53.
- [33] I.K. Robinson, in: G. Brown, D.E. Moncton (Eds.), *Handbook on Synchrotron Radiation*, Elsevier, Amsterdam, 1991, p. 221.

- [34] E. Vlieg, *J. Appl. Cryst.* 33 (2000) 401.
- [35] I.K. Robinson, *Phys. Rev. B* 33 (1986), 3830.
- [36] T.P. Trainor, P.J. Eng, I.K. Robinson, *J. Appl. Cryst.* 35 (2002) 696.
- [37] E. Vlieg, J.F. Van der Veen, S.J. Gurman, C. Norris, J.E. Macdonald, *Surf. Sci.* 210 (1989) 301.
- [38] C. S. Lo, K.S. Tanwar, A. M. Chaka, T.P. Trainor, *Phys Rev B* 75 (2007) 075425.
- [39] D.R. Shannon, C.T. Prewitt, *Acta Cryst.* B25 (1969) 925.
- [40] J.G. Catalano, T.P. Trainor, P.J. Eng, G.A. Waychunas, G.E. Brown, Jr., *Geochim. Cosmochim. Acta* 69 (2005) 3555.
- [41] J.G. Catalano, Z. Zhang, C. Park, P. Fenter, M.J. Bedzyk, *Geochim. Cosmochim. Acta* 71 (2007) 1883.

Table 3.1 Unrelaxed surface unit cell coordinates and best-fit model parameters from CTR data analysis.

Layer	Unrelaxed (O ₂ -Fe ₂ -O ₂ -Fe ₂ -O ₂ -R)				Best fit model (O ₂ -O ₂ -Fe ₂ -O ₂ -Fe ₂ -O ₂ -R)				$\chi^2 = 1.2$ $\beta = 0.15(5)$	
	x	y	z		x	y	z	Δz (Å)	B _{iso} (Å ²)	Occ.
i	O				0.13(7)	0.86(3)	2.119(7)	-	1.0	0.7(2)
	O				0.37(7)	0.36(3)	2.119(7)	-	1.0	0.7(2)
1	O	0.653	0.974	1.903	0.66(1)	0.98(1)	1.899(9)	-0.03(7)	0.50	0.91(9)
	O	0.847	0.474	1.903	0.84(1)	0.48(1)	1.899(9)	-0.03(7)	0.50	0.91(9)
2	Fe	0.000	0.831	1.855	0.00(4)	0.82(4)	1.857(7)	0.02(5)	0.32	0.71(5)
	Fe	0.500	0.331	1.855	0.50(4)	0.33(4)	1.857(7)	0.02(5)	0.32	0.71(5)
3	O	0.194	0.105	1.750	0.20(6)	0.10(5)	1.749(7)	-0.01(5)	0.50	0.8(2)
	O	0.306	0.605	1.750	0.30(6)	0.60(5)	1.749(7)	-0.01(5)	0.50	0.8(2)
4	Fe	0.000	0.380	1.645	0.00(1)	0.38(1)	1.642(4)	-0.02(3)	0.32	0.90(9)
	Fe	0.500	0.880	1.645	0.50(1)	0.88(1)	1.642(4)	-0.02(3)	0.32	0.90(9)
5	O	0.653	0.237	1.597	0.66(3)	0.23(2)	1.591(9)	-0.04(6)	0.40	1.00
	O	0.847	0.737	1.597	0.84(3)	0.73(2)	1.591(9)	-0.04(6)	0.40	1.00
6	O	0.153	0.404	1.403	0.153	0.404	1.403	0.00	0.40	1.00
	O	0.347	0.904	1.403	0.347	0.904	1.403	0.00	0.40	1.00
7	Fe	0.500	0.261	1.355	0.500	0.261	1.355	0.00	0.32	1.00
	Fe	0.000	0.761	1.355	0.000	0.761	1.355	0.00	0.32	1.00
8	O	0.694	0.535	1.250	0.694	0.535	1.250	0.00	0.40	1.00
	O	0.806	0.035	1.250	0.806	0.035	1.250	0.00	0.40	1.00
9	Fe	0.500	0.810	1.145	0.500	0.810	1.145	0.00	0.32	1.00
	Fe	0.000	0.310	1.145	0.000	0.310	1.145	0.00	0.32	1.00
10	O	0.153	0.667	1.097	0.153	0.667	1.097	0.00	0.40	1.00
	O	0.347	0.166	1.097	0.347	0.166	1.097	0.00	0.40	1.00

The estimated errors from least-squares fits at the 96 % confidence interval are given in parentheses. Values without reported errors were held fixed in the final fits. The Δz values are change in the layer z-position with respect to ideal stoichiometric termination, β is the roughness factor, B_{iso} are isotropic Debye-Waller factors and Occ is the fractional occupancy of the atom.

Table 3.2 Interlayer spacings and percent layer relaxations for the best-fit model.

Interlayer		Layer spacing (Å)
1-2	O ₂ -Fe ₂	0.305 (-12)
2-3	Fe ₂ -O ₂	0.797 (3)
3-4	O ₂ -Fe ₂	0.795 (2)
4-5	Fe ₂ -O ₂	0.370 (6)
5-6	O ₂ -O ₂	1.389 (-3)
6-7	O ₂ -Fe ₂	0.000
7-8	Fe ₂ -O ₂	0.000
8-9	O ₂ -Fe ₂	0.000
9-10	Fe ₂ -O ₂	0.000

The percent relaxations are shown in parentheses.

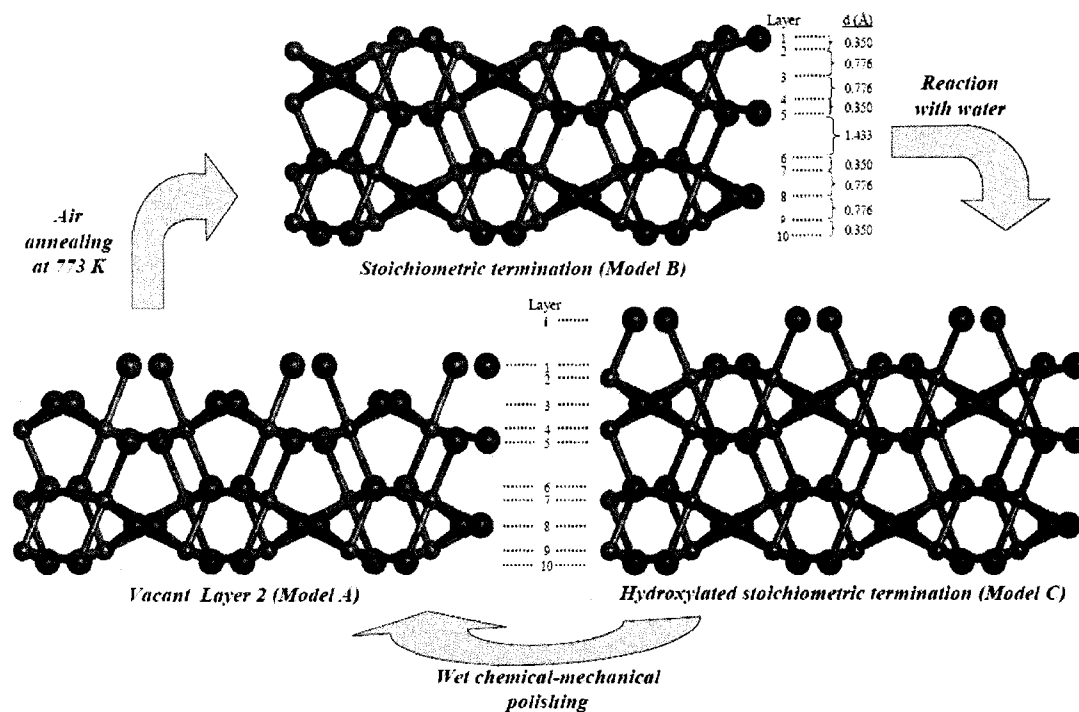


Figure 3.1 Layer stacking sequence along the c_s axis for stoichiometric termination, the hydroxylated stoichiometric termination, and the termination with absent layer 2 iron. The large spheres are O atoms and small spheres are Fe atoms. Stacking sequences are shown with unrelaxed layer spacings.

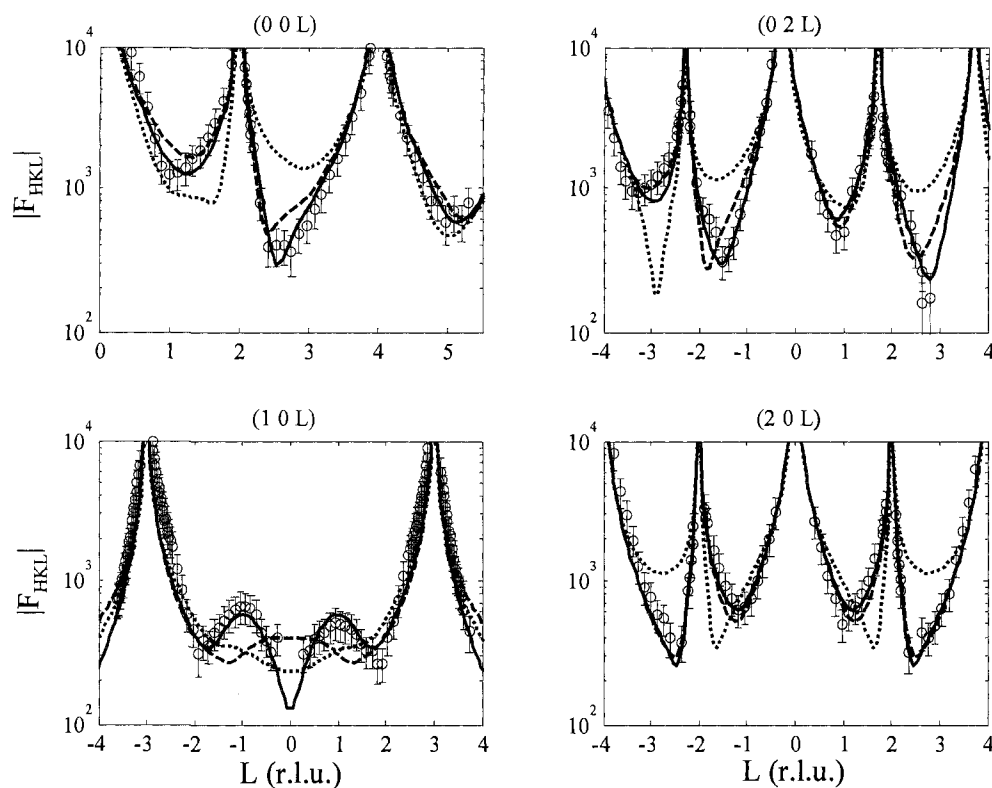


Figure 3.2 Experimental structure factors (F_{HKL}) as a function of perpendicular momentum transfer (L , in reciprocal lattice units) for the $\alpha\text{-Fe}_2\text{O}_3$ (1102) surface. The dotted lines are the calculated CTRs from the termination model with vacant iron atoms in layer 2 [27] (model A), the dashed lines represent fit obtained for the relaxed stoichiometric termination (model B), and the solid lines represent the best fit model, which is consistent with hydroxylated stoichiometric termination (model C) (see text for details).

Chapter 4 STRUCTURAL STUDY OF Fe(II) ADSORPTION ON HEMATITE($1\bar{1}02$)*

ABSTRACT

The structure of $\alpha\text{-Fe}_2\text{O}_3(1\bar{1}02)$ reacted with Fe(II) under anoxic conditions was studied using crystal truncation rod (CTR) diffraction. The CTR results show the crystalline termination of $\alpha\text{-Fe}_2\text{O}_3(1\bar{1}02)$ is modified due to adsorption of Fe(II) at crystallographic lattice sites. In addition, the binding sites for adsorbed Fe are similar for all studied conditions: reaction for 2 hr pH 5.0, for 34 d at pH 5.0, and for 5.5 hr at pH 7.0. The occupancy of adsorbed Fe increases with both reaction time and pH, which is consistent with typical cation adsorption behavior on iron (hydr)oxide surfaces. The metal-oxygen bond lengths of the (ordered) surface Fe atoms are characteristic of Fe(III), which provides indirect evidence for oxidation of adsorbed Fe(II) and is consistent with recent studies indicating that Fe(III)-hydroxides are effective oxidants for dissolved ferrous iron. Grazing-incidence X-ray diffraction measurements indicate that no crystalline surface reaction products formed during the course of Fe(II) reaction. Overall, the structural characterization of the Fe(II) adsorption reaction results in an enhanced understanding of how reduced iron affects the structure, stability and reactivity of hematite.

* Tanwar K. S., Petitto S. C., Ghose S. K., Eng P., and Trainor T. (2008) Structural study of Fe(II) adsorption on hematite ($1\bar{1}02$). *Geochim. Cosmochim. Acta*, **72**, 3311-3325.

4.1 INTRODUCTION

Iron (hydr)oxides are abundant in the environment and play a key role in the biogeochemical cycling and bioavailability of Fe. The chemistry of Fe in aquatic and soil/sediment systems also strongly influences the sequestration, transformation and bioavailability of various nutrients (e.g. C, N, and P) and contaminants (e.g. heavy metals) (Stumm and Sulzberger, 1992; Sulzberger et al., 1989; Cornell and Schwertmann, 1996). To a large extent these later processes are driven by reactions at the mineral-fluid interface, and hence are strongly influenced by the stability and surface reactivity of iron (hydr)oxides under varied aqueous geochemical conditions. In anaerobic systems, dissimilatory iron reducing bacteria (DIRB) facilitate reduction of iron (hydr)oxides by using Fe(III) as terminal electron acceptor during microbial respiration, resulting in release of high concentration ($> 10^{-3}$ M) of ferrous ion (Dong et al., 2003; Fredrickson et al., 2003; Hansel et al., 2003; Kostka and Nealson, 1995; Liu et al., 2001b; Lovley, 1991; Lovley, 1993; Lovley, 1997; Roden and Zachara, 1996; Roden et al., 2000; Zachara et al., 2001; Zachara et al., 2002). The released aqueous Fe(II) can further interact with iron oxides which may possibly inhibit microbial reduction (Roden and Urrutia, 2002; Royer et al., 2002; Royer et al., 2004), result in structural modification/transformation of various iron oxide phases (Hansel et al., 2005; Hansel et al., 2003; Kukkadapu et al., 2005; Pedersen et al., 2005; Tamaura et al., 1983; Tronc et al., 1992), or result in surface precipitation of mineral phases that can passivate the system towards further reduction/reaction (Coughlin and Stone, 1995; Stumm and Sulzberger, 1992; Urrutia et al., 1999).

The prevalence of soluble Fe(II) in a system also leads to the highly reactive Fe(II)-ferric (hydr)oxide redox couple, which has important implications for the fate and transport of various contaminants. Sorbed Fe(II) is known to accelerate reductive transformations of organic compounds including polyhalogenated hydrocarbons (Amonette et al., 2000; Elsner et al., 2004; Erbs et al., 1999; Pecher et al., 2002), and nitroaromatic compounds (Charlet et al., 1998b; Chun et al., 2006; Colon et al., 2006; Hofstetter et al., 1999; Kim and Strathmann, 2007; Klausen et al., 1995). In addition, inorganic contaminants such as U(VI), Cr(VI), and Tc(VII) are reduced to less mobile and hazardous species (i.e. U(IV), Cr(III), and Tc(IV) respectively), in presence of sorbed Fe(II) (Buerge and Hug, 1999; Charlet et al., 1998a; Charlet et al., 1998b; Eary and Rai, 1989; Fredrickson et al., 2004; Liger et al., 1999). A general observation from these studies is that the adsorption of Fe(II) is the central step leading to enhanced reductive transformations of contaminants and/or structural modification/transformation of iron (hydr)oxides. Thus, a structural understanding of how Fe(II) interacts with iron (hydr)oxides is required to elucidate the mechanisms of processes that follow Fe(II) adsorption.

The uptake affinity and pH dependence of Fe(II) sorption by various iron (hydr)oxides such as hematite (α -Fe₂O₃), goethite (α -FeOOH), magnetite (Fe₃O₄), lepidocrocite (γ -FeOOH), and ferrihydrite (Fe(OH)₃), as well as, studies of contaminant reduction in mixed Fe(II)-Fe(III) (hydr)oxide systems have traditionally been modeled using a constant capacitance (Charlet et al., 1998b; Liger et al., 1999; Silvester et al., 2005;

Zhang et al., 1992) or a triple layer surface complexation model for Fe(II) sorption (Coughlin and Stone, 1995). In these models, adsorbed Fe(II) is assumed to form a mono-dentate surface complex, i.e. $\equiv\text{Fe(III)-O-Fe(II)}^+$ and/or $\equiv\text{Fe(III)-O-Fe(II)-OH}$ (Charlet et al., 1998b; Coughlin and Stone, 1995; Liger et al., 1999; Silvester et al., 2005; Zhang et al., 1992), where $\equiv\text{Fe(III)-O}$ denotes a surface site. However, the extent of Fe(II) uptake and reactivity of surface bound Fe(II) can be expected to strongly depend on the nature of the substrate and the local structural environment of adsorbed Fe(II), which is not resolved for most iron (hydr)oxides, and not considered in the existing surface complexation models.

Previous Fe(II) adsorption studies that have included mass balance analysis report an incomplete recovery of initially added Fe(II) after mild chemical extractions (e.g. using 0.5 N HCl) (Coughlin and Stone, 1995; Jeon et al., 2003; Jeon et al., 2001). The incomplete recovery of Fe(II) is attributed to iron oxidation, which may subsequently result in the structural transformation of the substrate and/or surface precipitation of oxide phases such as goethite and magnetite (Coughlin and Stone, 1995; Hansel et al., 2005; Hansel et al., 2003; Jeon et al., 2003; Jeon et al., 2001). Recent Mossbauer spectroscopy studies have confirmed the oxidation of adsorbed Fe(II) due to interfacial electron transfer to the underlying bulk oxide ($\alpha\text{-Fe}_2\text{O}_3$, $\alpha\text{-FeOOH}$, and Fe(OH)_3) (Larese-Casanova and Scherer, 2007; Silvester et al., 2005; Williams and Scherer, 2004). These studies also proposed that Fe(II) is adsorbed at crystallographic lattice sites of the substrate, leading to growth of the underlying substrate upon Fe(II) adsorption/oxidation

(Larese-Casanova and Scherer, 2007; Silvester et al., 2005; Williams and Scherer, 2004).

The above-mentioned Fe(II) adsorption/oxidation pathway is also supported by a recent transmission electron microscopy (TEM) study showing growth of goethite along a crystallographic direction following Fe(II) adsorption (Chun et al., 2006).

The details of mineral growth/precipitation following oxidation of adsorbed Fe(II) is highly dependent on the structure of the substrate, pH, Fe(III)/Fe(II) molar ratio, and presence of aqueous species such as carbonate and phosphate. For example, Fe(II) adsorption on ferrihydrite and lepidocrocite has been shown to result in the formation of goethite and/or magnetite (Hansel et al., 2003; Pedersen et al., 2005; Tamaura et al., 1983). Pedersen et al. (2005) suggested that Fe(II) sorption on hematite does not result in formation of distinct mineral phases, however, it is also proposed that magnetite precipitation is likely at $\text{pH} > 5.9$ (Jeon et al., 2001; 2003). At a Fe(III)/Fe(II) molar ratio of 2 and pH 7.3 lepidocrocite was observed to transform to magnetite but in case of goethite there was no magnetite formation (Tamura et al., 1983). In addition, Hansel et al. (2005) observed the transformation of ferrihydrite to goethite and lepidocrocite at low Fe(II) concentration (i.e. 0.67 mmol Fe(II)/g ferrihydrite) and to magnetite, goethite and lepidocrocite at high Fe(II) concentration (6.7 mmol Fe(II)/g ferrihydrite) at circumneutral pH. The formation of mineral phases can also be influenced by the presence and nature of background electrolyte ions. For instance, precipitation of vivianite ($\text{Fe}_3(\text{PO}_4)_2$) (Zachara et al., 2001) and siderite (FeCO_3) (Liu et al., 2001a;

Zachara et al., 2001) was observed on the surface of goethite in presence of phosphate and carbonate buffers, respectively.

The studies cited above have greatly enhanced existing knowledge of Fe(II) reaction with various iron (hydr)oxides, however, there is still a limited molecular scale understanding of how Fe(II) binds to mineral surfaces, and how the binding varies with differences in substrate surface structure. Likewise, there is a limited understanding of how the Fe(II) reaction (particularly the incipient reaction) modifies the structure and hence, the reactivity of iron (hydr)oxide surfaces. In this study, we have investigated the structure of Fe(II) adsorbed on the $\alpha\text{-Fe}_2\text{O}_3(1\bar{1}02)$ surface as a function of reaction time (2 hr - 34 d) and pH (5.0 - 7.0) using synchrotron based crystal truncation rod (CTR) diffraction to develop a detailed structural depiction of adsorption of Fe(II) on a well characterized Fe(III)-oxide surface, as a model for incipient reaction of Fe(II) with Fe(III) hydroxides. Our approach is discussed in next section.

4.1.1 Structural Investigation of Fe(II) Adsorption

The high penetration power of X-rays and their sensitivity to molecular scale structure make techniques such as X-ray absorption spectroscopy (XAS) and surface X-ray scattering, including crystal truncation rod (CTR) diffraction, powerful tools for determining the average structure of the mineral-fluid interface (Brown et al., 1999; Fenter and Sturchio, 2004). Crystal truncation rods are particularly sensitive to crystalline surface structure because the measured intensity depends on the structure

factor of the surface unit cell, which allows for the identification of surface terminations, atomic occupancies, atomic displacements, and order parameters (Robinson, 1986; Robinson and Tweet, 1992; Eng et al., 2000; Fenter, 2002).

The $(1\bar{1}02)$ plane of $\alpha\text{-Fe}_2\text{O}_3$, also known as the R-plane, can be described equivalently by $(01\bar{1}2)$ and $(\bar{1}012)$ indices in the right handed hexagonal notation, which are equivalent to $(1\bar{1}2)$, (012) and $(\bar{1}02)$ in condensed notation. We have previously studied the surface structure of hydrated $\alpha\text{-Fe}_2\text{O}_3(1\bar{1}02)$ using CTR (Tanwar et al., 2007a; Tanwar et al., 2007b) and ab initio density functional theory (DFT) calculations (Lo et al., 2007). Our results show the $\alpha\text{-Fe}_2\text{O}_3(1\bar{1}02)$ surface prepared via chemical-mechanical polishing (CMP) at room temperature results in a termination that has a vacant top layer of Fe atoms as compared to the bulk stoichiometric termination (Lo et al., 2007; Tanwar et al., 2007a; Tanwar et al., 2007b) (Figure 4.1). In addition, surface preparation via annealing in air for 3 hr under ambient pressure at 773 K followed by cooling to room temperature and then exposure to humid environment (relative humidity $> 90\%$, $p_{\text{H}_2\text{O}} > 20$ Torr) results in a hydroxylated stoichiometric termination (Tanwar et al., 2007a), which is apparently a meta-stable configuration according to the theoretical stability predictions based on DFT calculations (Lo et al., 2007). The recent study by Catalano et al. (2007) also proposed a hydroxylated stoichiometric termination for $\alpha\text{-Fe}_2\text{O}_3(1\bar{1}02)$ surface prepared via annealing at 723 K for 24 hr. In the current study, we determined the surface structure of initially CMP prepared $\alpha\text{-Fe}_2\text{O}_3(1\bar{1}02)$ following

reaction with Fe(II) under anoxic conditions using CTR diffraction. The structure of Fe(II) reacted $\alpha\text{-Fe}_2\text{O}_3(1\bar{1}02)$ is directly compared to the structure of un-reacted hydrated surface to deduce how Fe(II) binds to the surface. These structural results are complemented with grazing incidence powder X-ray diffraction (GI-XRD) measurements to identify mineral phase surface precipitates.

4.2 METHODS

4.2.1 Sample Preparation

All the experiments were conducted on natural single crystals of specular hematite obtained from Bahia, Brazil. The samples were cut ($\approx 1\text{ cm}^2$) and polished parallel to $(1\bar{1}02)$ growth surface. The hematite samples were then CMP prepared followed by etching in 0.01 N HNO_3 for 2 hr and subsequently thoroughly rinsed with ultra-pure ($> 18\text{ M}\Omega$) water (Tanwar et al., 2007b). Our previous work has shown that the employed surface preparation and wash procedure results in high quality $\alpha\text{-Fe}_2\text{O}_3$ surfaces for CTR measurements (Tanwar et al., 2007b; Trainor et al., 2004). Additional details on $\alpha\text{-Fe}_2\text{O}_3(1\bar{1}02)$ sample preparation and detailed description of the resulting surface structure are provided in Tanwar et al. (2007a).

4.2.2 Fe(II) Adsorption on $\alpha\text{-Fe}_2\text{O}_3(1\bar{1}02)$

All the Fe(II) adsorption experiments were performed at room temperature in a glove box (under N_2 atmosphere) to maintain strict anoxic conditions. The Fe(II) aqueous solutions (4 mM) were prepared using ultrapure ($> 18\text{ M}\Omega$) deoxygenated water and ferrous

chloride tetrahydrate ($\text{FeCl}_2 \cdot 4\text{H}_2\text{O}$) purchased from VWR ($> 99\%$ purity). The prepared Fe(II) solutions were titrated under continuous N_2 purge to $\text{pH } 5.0 \pm 0.2$ and 7.0 ± 0.2 using 0.001 M NaOH and were kept inside the glove box under N_2 atmosphere for approximately 26 h. The Fe(II) concentration in the solutions (aged for 26 h) was determined spectrophotometrically at 562 nm using the ferrozine assay (Stookey, 1970). The analysis showed no loss of aqueous Fe(II) suggesting the anoxic conditions were maintained in the glove box.

During our initial experiments, $\alpha\text{-Fe}_2\text{O}_3(1\bar{1}02)$ single crystals were reacted with freshly prepared 4 mM Fe(II) at $\text{pH } 5.0 \pm 0.2$ for 24 h. After the employed reaction time, the recovered Fe(II) solutions were analyzed for Fe(II) concentration via ferrozine method (Stookey, 1970). The concentration of these solutions were similar (within error) to initially added Fe(II) indicating that the macroscopic uptake of Fe(II) on $\alpha\text{-Fe}_2\text{O}_3(1\bar{1}02)$ single crystals could not be quantified using the ferrozine method. This is not surprising considering the available surface area for reaction ($\approx 1 \text{ cm}^2$); even a monolayer uptake would result in a net decrease ($< 0.1\%$) of solution concentration well below the ferrozine assay precision (2%).

The CMP prepared $\alpha\text{-Fe}_2\text{O}_3(1\bar{1}02)$ single crystal samples used for CTR measurements were reacted with 4 mM Fe(II) for two different reaction times (2 hr and 34 d) at $\text{pH } 5.0 \pm 0.2$ and for 5.5 hr at $\text{pH } 7.0 \pm 0.2$, under anoxic conditions (N_2 atmosphere). For samples reacted for more than 24 hr the Fe(II) solutions were exchanged with fresh Fe(II)

solutions every 24 hr to ensure that there was no oxidation of aqueous Fe(II) in contact with $\alpha\text{-Fe}_2\text{O}_3(1\bar{1}02)$ single crystals. After the desired reaction time, the samples were taken out of Fe(II) solution and were washed with ultrapure ($> 18\text{ M}\Omega$) de-oxygenated water followed immediately by CTR measurements (discussed in next section).

4.2.3 CTR Data Collection

Crystal truncation rod (CTR) diffraction data was collected at Advanced Photon Source (APS) on undulator beamline 13-IDC. Energy selection of the incident beam was performed using a liquid N_2 cooled double crystal Si(111) monochromator. A $2 + 2 + \text{kappa}$ -geometry Newport diffractometer equipped with a sample cell with X-ray transparent windows was used for sample orientation and scanning (Trainor et al., 2006). The X-ray beam was focused onto the center of the diffractometer to a beam size of $0.2 \times 1.5\text{ mm}$ (horizontal \times vertical) using two Rhodium (Rh) coated Si mirrors capable of suppressing third harmonic by a factor of greater than 10^4 . To ensure the sample remains fully hydrated, a near water-saturated He atmosphere (relative humidity $> 90\%$, $\text{pH}_2\text{O} > 20\text{ Torr}$) was maintained in contact with the sample during the course of CTR measurements (Liu et al., 1998). The CTR data for the substrate reacted with Fe(II) for 2 hr at pH 5.0 and for 5.5 hr at pH 7.0 were collected using 12 keV incident X-ray energy. For the substrate reacted with Fe(II) for 34 d, the data was collected at 10 keV incident X-rays. X-ray scattering intensity was measured using a scintillation detector equipped with a single channel analyzer set for rejecting both lower energy Fe fluorescence counts and higher harmonics. All the non-specular rods were collected at a fixed incident angle

of 2° and rocking scans through the truncation rods were performed using a continuous (trajectory) scan of the diffractometer ϕ -axis at a particular reciprocal lattice setting. Specular rods were collected by scanning the ω -axis. The magnitudes of individual structure factors ($|F_{\text{HKL}}|$) at each (HKL) value were determined by taking square root of background subtracted intensity of the rocking curves correcting for active area, polarization, step size and Lorentz factors (Robinson, 1991). In our notation, the reciprocal vector indices H and K correspond to in-plane momentum transfer and L corresponds to perpendicular momentum transfer. The full data set consisted of nine crystal truncation rods for each of the three Fe(II) reacted $\alpha\text{-Fe}_2\text{O}_3(1\bar{1}02)$ samples. All the data sets were averaged in p1 plane group. A subset of rods measured repeatedly to check for beam induced surface damage had similar intensities (within errors) indicating the surfaces were stable during the course of data collection. Following CTR data collection, grazing incidence powder X-ray diffraction (GI-XRD) measurements were also conducted on $\alpha\text{-Fe}_2\text{O}_3(1\bar{1}02)$ reacted with Fe(II) for 34 d at pH 5.0 and for 5.5 hr at pH 7.0. The GI-XRD experiments were also performed at room temperature and under hydrated He atmosphere. These measurements were conducted at incidence angles below the critical angles for total reflectivity ($0.05^\circ - 0.20^\circ$) to enhance surface sensitivity to ordered mineral phase precipitates.

4.2.4 CTR Data Analyses

For the bulk crystal structure and isotropic Debye-Waller factors for $\alpha\text{-Fe}_2\text{O}_3$ we used the values reported previously by Finger and Hazen (1980). The $\alpha\text{-Fe}_2\text{O}_3(1\bar{1}02)$ surface

unit cell was indexed using a method described previously (Trainor et al. 2002a; 2002b; Tanwar et al., 2007b). Briefly, the surface unit cell is described by the in-plane basis vectors \mathbf{a}_s defined by the $[1\ 1\ 0]$ bulk lattice vector and \mathbf{b}_s defined by the $[-1/3\ 1/3\ 1/3]$ bulk lattice vector, which results in a rectangular surface mesh with $|\mathbf{a}_s| = 5.04\ \text{\AA}$, and $|\mathbf{b}_s| = 5.40\ \text{\AA}$ (Tanwar et al., 2007b). The \mathbf{c}_s basis vector was defined in surface normal direction with magnitude given by twice the $(1\ \bar{1}\ 02)$ d-spacing i.e. $|\mathbf{c}_s| = 7.37\ \text{\AA}$. The full details of $\alpha\text{-Fe}_2\text{O}_3(1\ \bar{1}\ 02)$ surface indexing are provided elsewhere (Tanwar et al., 2007b).

The CTR data was modeled using a non-linear least squares fitting routine with fixed bulk and adjustable surface models (Robinson, 1986; Vlieg et al., 1989; Vlieg, 2000; Trainor et al., 2002b;). Due to relatively small X-ray scattering cross-section of H atoms compared to those of Fe and O it was not possible to determine H positions. The above-discussed surface indexing leads to a unit cell that consists of two layers that are chemically equivalent but crystallographically distinct (Tanwar et al., 2007a; Tanwar et al., 2007b). Therefore, for every tested structure, two symmetry related surface models were included, and the final structure factor magnitudes were calculated by performing summation of the structure factor magnitudes for the two surface models (Tanwar et al., 2007a; Tanwar et al., 2007b; Trainor et al., 2002a). The fit parameters include atomic displacements in x, y, and z directions, atomic occupancies, isotropic Debye-Waller factors, and an overall roughness factor (β) (based on roughness model derived by Robinson (1986)). The number of free parameters in the fit was reduced by constraining the atoms in each layer (along z direction) to maintain similar z-coordinate, occupancy

and Debye-Waller factor. The Z-displacements were allowed for all ten layers but the in-plane displacements were allowed for top 5 layers of the substrate only as other in-plane displacements had insignificant effect on the fit. The fit quality between different models was compared using Hamilton's R-ratio test (Hamilton, 1965).

The chemical plausibility of the models was examined using Pauling's bond-valence principle in which the bond-valence sum for a given cation/anion is expected to be similar to the magnitude of formal valence for that cation/anion (Pauling, 1960). In this study, the bond-valence for each atom was calculated as a function of bond lengths based on the bond length - bond strength relationships for metal oxides given by Brown and Altermatt (1985). A bond-valence sum significantly lower than the formal valence of the central atom represents unusually long bond lengths or under-coordination. Conversely, a bond-valence sum significantly higher than the formal valence represents unusually short bond lengths or over-coordination.

4.3 RESULTS

4.3.1 CTR Results

A qualitative comparison of the measured CTR profiles for clean and the three Fe(II) reacted surfaces shows distinct differences for the (10L), (2-1L), and (21L) rods (Figure 4.2). These differences clearly show the surface structure of $\alpha\text{-Fe}_2\text{O}_3(1\bar{1}02)$ is modified after reaction with Fe(II). Furthermore, the data for three Fe(II) reaction conditions show variations in CTR profile (Figures 4.2a, 4.2b and 4.2c). For instance, a hump in CTR

data can be observed at (HKL) between (2 -1 -2) to (2 -1 -3) for $\alpha\text{-Fe}_2\text{O}_3(1\bar{1}02)$ reacted for 34 d at pH 5.0 (Figure 4.2b) and for 5.5 hr at pH 7.0 (Figure 4.2c), which is absent in the case of reaction for 2 hr at pH 5.0 (Figure 4.2a). Additionally, the hump in CTR profile seen at (HKL) equal to (1 0 -1.1) and (1 0 1.1) for all three Fe(II) reaction conditions is less prominent in case of Fe(II) reaction for 2 hr at pH 5.0 (Figure 4.2a) as compared to the other two reaction conditions (Figure 4.2b, c). These differences indicate that the extent and/or nature of surface modification due to reaction of $\alpha\text{-Fe}_2\text{O}_3(1\bar{1}02)$ with Fe(II) under the three studied reaction conditions may not be similar.

To identify structural modification of $\alpha\text{-Fe}_2\text{O}_3(1\bar{1}02)$ surface, the three CTR datasets were analyzed independently using various possible structural models. As discussed before, the surface structure of CMP prepared $\alpha\text{-Fe}_2\text{O}_3(1\bar{1}02)$ is consistent with a model that has a vacant top layer of Fe atoms compared to the bulk stoichiometric termination leading to half of a stoichiometric layer as the terminating plane, with an additional oxygen coordinating the terminal Fe (Figure 4.1) (Lo et al., 2007; Tanwar et al., 2007b). The DFT study of Lo et al. (2007) predicted this termination to be the lowest energy surface under hydroxylated conditions at room temperature, with the stoichiometric or hydroxylated stoichiometric surfaces predicted to be thermodynamically stable only under elevated temperatures (Lo et al., 2007; Tanwar et al., 2007a; Catalano et al., 2007). The Fe/O stoichiometry of such a termination along the surface normal direction can be described as $\text{O}_2\text{-X-O}_2\text{-Fe}_2\text{-O}_2\text{-R}$, where R represents stoichiometric stacking sequence and X denotes the vacant Fe lattice sites (Figure 4.1). The unrelaxed coordinates for this

surface termination are given in Table 4.1. The $O_2\text{-X-O}_2\text{-Fe}_2\text{-O}_2\text{-R}$ termination results in a surface that has three types of under-coordinated oxygen groups (i.e. singly (^IO), doubly (^{II}O), and triply coordinated (^{III}O) to Fe) (Figure 4.1), which are potential binding sites for adsorbates (Catalano et al., 2005; Lo et al., 2007; Tanwar et al., 2007b). To account for Fe(II) adsorption and surface hydroxylation, various surface models were generated by adding Fe and O atoms to the above-mentioned surface model at various plausible reaction sites. The models tested include mono-dentate and bi-dentate adsorption complexes, where the Fe was assumed to bind with one and two ^IO surface groups, respectively (i.e. $\text{Fe-}^I\text{O}$ and $\text{Fe-}^I\text{O}_2$) (Figure 4.3). An additional bi-dentate adsorption geometry was tested where the Fe was assumed to bind with two ^{II}O groups (i.e. $\text{Fe-}^{II}\text{O}_2$) was also analyzed (Figure 4.3). In addition, tri- and tetra-dentate adsorption geometries were also considered along with a model where Fe was assumed to bind at hematite lattice sites (i.e. at site X in $O_2\text{-X-O}_2\text{-Fe}_2\text{-O}_2\text{-R}$) resulting in a five coordinated Fe at the surface (Figure 4.3). It is also possible that Fe(II) adsorption on $\alpha\text{-Fe}_2\text{O}_3(1\bar{1}02)$ may result in multiple types of adsorption complexes e.g. simultaneous mono-dentate and bi-dentate adsorption. Therefore, structural models that incorporate multiple adsorption geometries were also examined. For each model, a non-linear least squares analysis was performed using adjustable atomic x, y, and z positions, occupancies, Debye-Waller factors, and an overall roughness factor. During initial analysis, only limited atomic displacements were allowed in order to maintain a particular sorption geometry. For example, for a bi-dentate model ($\text{Fe-}^I\text{O}_2$) the adsorbed Fe atom and the ^IO surface group

displacements were allowed to vary within limits that maintain a bi-dentate adsorption complex.

In the case of Fe(II) adsorption for 2 hr at pH 5.0, the only model that provided an acceptable fit was the one in which the adsorbed Fe was assumed to occupy hematite Fe lattice sites. Interestingly, removing the limits on adsorbed Fe displacements in all above discussed models resulted in similar final Fe positions, which were consistent with crystallographic lattice sites of the substrate. Based on these results, the structural refinement was conducted with the model where the adsorbed Fe was initially at crystallographic lattice sites (i.e. in layer 2 of Figure 4.1). The unit cell of α -Fe₂O₃(1 $\bar{1}$ 02) has two such chemically equivalent lattice sites. Therefore, a Fe atom was added at both of these sites and symmetry constraints were applied to the atomic displacements so that the two Fe atoms maintain a chemically equivalent environment. The model with adsorbed Fe at crystallographic lattice sites resulted in a good fit to experimental data ($\chi^2 = 2.4$) suggesting that adsorbed Fe is likely occupying lattice sites.

The final Fe position in the model discussed above resulted in an adsorption complex where the surface bound Fe is under-coordinated (i.e. five coordinated: two Fe-I-O, two Fe-II-O, and one Fe-III-O bonds). However, under aqueous conditions the interaction of water is likely to complete the coordination shell of surface bound Fe. Therefore, a terminal (hydr)oxo group (which completes the coordination shell of Fe) was included for each added Fe (Figure 4.4). The resultant model showed an excellent fit with the

experimental data ($\chi^2 = 1.3$) and the observed improvement in fit was statistically significant based on Hamilton's R-ratio test (Hamilton, 1965).

We also examined the effect of physisorbed water on the overall fit by including additional oxygen positions above the surface. Inclusion of one water layer improved the fit ($\chi^2 = 1.1$) (Figure 4.4 and 4.5) and the observed improvement was statistically significant at 95% confidence interval (Hamilton, 1965). Including second water layer resulted in similar fit parameters (within errors) showing no statistically significant improvement in the fit. Thus, the final model (Figure 4.4 and 4.5 and Table 4.1) consists of octahedrally coordinated Fe at the surface, which is forming five bonds with the substrate and a terminal Fe-O bond, and one physisorbed water layer (Figure 4.4 and Table 4.1). The final Fe/O stoichiometry for this model along the surface normal is consistent with $\text{O}_{2n}\text{-O}_2\text{-}\mathbf{Fe}_{2m}\text{-O}_2\text{-Fe}_2\text{-O}_2\text{-R}$, where m and n represent site occupancy of each of the two chemically equivalent sites per unit cell (refer to Table 4.1), and R represents stoichiometric stacking sequence. The Fe and O atoms shown in boldface represent atoms that were added to un-reacted surface termination.

A similar approach was followed for modeling the other two datasets collected after Fe(II) adsorption on $\alpha\text{-Fe}_2\text{O}_3(1\bar{1}02)$ for 34 d at pH 5.0 and for 5.5 hr at pH 7.0 (Figure 4.6 and 4.7). The analysis for both datasets resulted in models where the final Fe/O stoichiometry and the coordination environment of surface bound Fe is qualitatively similar to the one discussed above (i.e $\text{O}_{2n}\text{-O}_2\text{-}\mathbf{Fe}_{2m}\text{-O}_2\text{-Fe}_2\text{-O}_2\text{-R}$) but with different

adsorbed Fe occupancy (Table 4.2 and 4.3). Additionally, the best-fit models for both these datasets consist of two physisorbed water layers (i.e. inclusion of two water layers resulted in statistically significant improvement in fit at 95% confidence interval). For all three models examined, Fe(II) adsorption appears to result in a surface that is structurally similar to the hydroxylated stoichiometric termination, however with incomplete site occupancies of the near surface Fe sites (i.e. sorption sites). The site occupancy of adsorbed Fe is 0.30 ± 0.04 and 0.47 ± 0.05 for reaction time of 2 hr and 34 d respectively at pH 5.0. At pH 7.0, adsorption for 5.5 hr results in adsorbed Fe occupancy of 0.39 ± 0.03 .

The $\alpha\text{-Fe}_2\text{O}_3(1\bar{1}02)$ structure obtained after Fe adsorption at crystal lattice sites can be viewed as a peak valley topography, with $^{\text{I}}\text{O}$ groups as peaks and the valleys are located over $^{\text{III}}\text{O}$ groups (Figure 4.4). The lower water layer is located over the valleys (Figure 4.4) for all models and the second water layer over the peaks (not shown). The distances between surface oxo groups and O of water layers are in the range 2.4 Å to 3.3 Å. The best-fit model parameters, layer relaxations, and bond-valence calculations for Fe(II) adsorption on $\alpha\text{-Fe}_2\text{O}_3(1\bar{1}02)$ for 2 hr at pH 5.0, 34 d at pH 5.0, and 5.5 hr at pH 7.0 are listed in Table 4.1, 4.2, and 4.3, respectively. For each model, the bond lengths, occupancies, and coordination environment for all the substrate layers (layers 1 and 3-10) were consistent (within errors) with the bulk oxide (Table 4.1, 4.2, and 4.3). The overall roughness factor (β) increased from 0.15 ± 0.03 to 0.28 ± 0.02 with increase in reaction time from 2 hr to 34 d at pH 5.0, respectively. The β for reaction time of 5.5 hr at pH 7.0

is 0.18 ± 0.04 suggesting the roughness did not show a significant increase with increase in pH for short reaction times. The rms roughness corresponding to β (Robinson, 1986) for each model is less than 5 Å i.e. 1.7 ± 0.4 Å, 2.7 ± 0.2 Å, and 1.9 ± 0.5 Å for reaction time of 2 hr at pH 5.0, 34 d at pH 5.0, and 5.5 hr at pH 7.0, respectively. The significance of the observed increased roughness with increase in reaction time is discussed further below.

4.3.2 GI-XRD Results

Previous studies have indicated that Fe(II) adsorption on iron (hydr)oxides can induce bulk phase transformations (Hansel et al., 2005; Pedersen et al., 2005; Tamaura et al., 1983; Tronc et al., 1992). In the current room temperature study conducted on α -Fe₂O₃(1 $\bar{1}$ 02) single crystals, the rates for dissolution/re-precipitation reaction are expected to be extremely low. Thus, it is unlikely that any bulk phase transformation would be observed to occur in a α -Fe₂O₃(1 $\bar{1}$ 02) single crystal within the reaction time used in the current study. However, the possibility of surface precipitation of iron oxide phases associated with the interfacial reaction of Fe(II) cannot necessarily be excluded. To identify any surface precipitation, GI-XRD experiments were conducted for surfaces reacted with Fe(II) for 34 d at pH 5.0 and for 5.5 hr at pH 7.0. No evidence for crystalline phases was observed above the detection limit in GI-XRD results (Figure 4.8). In a previous study, Jeon et al. (2003) hypothesized that interfacial electron transfer following Fe(II) adsorption results in an amorphous oxide layer on the surface of hematite, which ultimately transforms to magnetite (at pH > 6.8). We note that the GI-

XRD data is sensitive only to crystalline phases. Therefore, we cannot entirely exclude possible surface precipitation of an amorphous oxide layer, though no evidence for magnetite surface precipitation even at pH 7.0 was observed. We suspect that lattice mismatch between $\alpha\text{-Fe}_2\text{O}_3(1\bar{1}02)$ and magnetite inhibits possible surface precipitation of magnetite. Under the employed reaction conditions, the possibility of hematite precipitation cannot be ignored. The GI-XRD results showed no evidence of surface precipitation of a hematite powder, or textured growth which is incommensurate with the substrate symmetry. However, GI-XRD data will not identify epitaxial growth of hematite over-layer on a hematite substrate.

4.4 DISCUSSION

A major goal of the current study was to identify the binding geometry of Fe adsorbed on $\alpha\text{-Fe}_2\text{O}_3(1\bar{1}02)$ under different reaction conditions. A comparison of Fe/O stoichiometry for clean $\alpha\text{-Fe}_2\text{O}_3(1\bar{1}02)$ ($\text{O}_2\text{-X-O}_2\text{-Fe}_2\text{-O}_2\text{-R}$) with Fe(II) reacted $\alpha\text{-Fe}_2\text{O}_3(1\bar{1}02)$ ($\text{O}_{2n}\text{-O}_2\text{-Fe}_{2m}\text{-O}_2\text{-Fe}_2\text{-O}_2\text{-R}$) shows the adsorbed Fe binds at crystal lattice sites resulting in partial filling of vacant Fe layer (denoted by X in clean surface). The binding geometry of adsorbed Fe is similar under all three studied reaction conditions but a comparison of best-fit model parameters highlights one key difference within the models, which can also explain the observed differences in CTR profiles (discussed in section 3.1). For the case of Fe(II) adsorption on $\alpha\text{-Fe}_2\text{O}_3(1\bar{1}02)$ for 2 hr at pH 5.0, the best-fit model resulted in adsorbed Fe occupancy (denoted by m in above mentioned stoichiometry) of 0.30 ± 0.04 (Table 4.1). In other words, $30 \pm 4\%$ of the given lattice

sites were occupied by adsorbed Fe. We note that total Fe uptake may also involve random binding to edge and/or defect sites that are not visible in CTR measurements. At pH 5.0, long term adsorption of Fe(II) (for 34 d) results in occupancy of 0.47 ± 0.05 for the adsorbed Fe (Table 4.2). In comparison, adsorption for 5.5 hr at pH 7.0 results in adsorbed Fe occupancy of 0.39 ± 0.03 . These Fe site occupancy results show that extent of Fe(II) adsorption on the ordered sites of $\alpha\text{-Fe}_2\text{O}_3(1\bar{1}02)$ increases by a factor of approximately 1.6 at pH 5.0 with increase in reaction time from 2 hr to 34 d. The Fe(II) uptake also increases about 1.3 times with increasing pH from 5.0 to 7.0 and reaction time from 2 hr to 5.5 hr.

The observed increase in Fe(II) adsorption with reaction time in the current study is in agreement with previous long term Fe(II) adsorption studies conducted by Jeon et al. (2001), where an approximately 1.5 to 2.0 fold increase in Fe(II) uptake by powdered $\alpha\text{-Fe}_2\text{O}_3$ was reported after increasing reaction time from 5 to 30 d for the pH range 4.5 - 5.5. The increase in Fe(II) adsorption with increase in pH is also observed in the current study, however, the extent of increase is lower than that observed in previous studies using powdered $\alpha\text{-Fe}_2\text{O}_3$, where more than 5 fold increase has been reported with a change in pH from 5.0 to 7.0 (Charlet et al., 1998b; Jeon et al., 2001; Liger et al., 1999). Similar results are also reported in the case of Fe(II) adsorption on iron (hydr)oxides other than $\alpha\text{-Fe}_2\text{O}_3$ (Coughlin and Stone, 1995; Klausen et al., 1995; Liger et al., 1999; Silvester et al., 2005; Zhang et al., 1992).

Another major result from the current study is that adsorbed Fe is occupying crystallographic lattice sites of $\alpha\text{-Fe}_2\text{O}_3(1\bar{1}02)$ under all three studied reaction conditions (Figure 4.4). These results are in agreement with previous experimental studies, which speculated that adsorption of Fe(II) occurs at sites resulting in growth of the substrate (Chun et al., 2006; Silvester et al., 2005; Williams and Scherer, 2004). In addition, the bond lengths obtained for adsorbed Fe fall in the range 1.93 Å to 2.18 Å for all the three models, which are in good agreement (within errors) with ideal Fe-O bond lengths in hematite bulk lattice (i.e. 1.95 Å and 2.11 Å). The average Fe-O bond lengths for the adsorbed Fe (i.e. topmost Fe site in the model) are 2.04 ± 0.02 Å, 2.06 ± 0.01 Å, and 2.04 ± 0.02 Å for reaction time of 2 hr at pH 5.0, 34 d at pH 5.0, and 5.5 hr at pH 7.0, respectively. These average bond lengths are shorter than typical Fe(II)-O bond lengths where Fe(II) has an octahedral coordination environment (2.14 Å - 2.18 Å) (Apted et al., 1985; Farges et al., 2004; Jackson et al., 2005; Waychunas et al., 1988; 1989; Wilke et al., 2006). Moreover, the average bond lengths for adsorbed Fe in the current study are in a good agreement with typical Fe(III)-O bond lengths in octahedral coordination (Apted et al., 1985; Tossell, 1980; Whittaker and Muntus, 1970). Based on these results, it is likely that Fe(II) adsorbed on $\alpha\text{-Fe}_2\text{O}_3(1\bar{1}02)$ is oxidized resulting in a Fe(III)-layer on the surface, which is also supported by bond-valence calculations where the bond-valence sum for adsorbed Fe is close to three (Tables 4.1, 4.2, and 4.3).

The results of the current study are in agreement with previous Mossbauer spectroscopy studies, which demonstrated Fe(II) adsorbed on hematite oxidizes due to interfacial

electron transfer between adsorbed Fe(II) and structural Fe(III) of the substrate (Larese-Casanova and Scherer, 2007; Williams and Scherer, 2004). The electron transfer between adsorbed Fe(II) and underlying substrate is also shown for iron (hydr)oxide other than hematite (i.e. goethite, and ferrihydrite) (Silvester et al., 2005; Williams and Scherer, 2004). Furthermore, previous theoretical studies suggest that there is a thermodynamic driving force for oxidation of the surface bound Fe(II) under aqueous conditions (Kerisit and Rosso, 2006; Rosso et al., 2003; Wang and Rustad, 2006). Thus, it is likely that the surface Fe(III) layer observed in the current study is a result of interfacial electron transfer between adsorbed Fe(II) and structural Fe(III).

The experimental CTR data presented in the current study does not provide any information about electron transfer mechanism or fate of the injected electron. However, a comparison of experimental observations of the current study with recent theoretical work may provide some interesting insights regarding electron mobility. Recent studies suggest there are at least three possible fates of the injected electron; (i) the electron is trapped in the near surface region, (ii) the electron migrates to bulk lattice, or (iii) the electron transport results in reduction of Fe(III) to Fe(II) at edge or defect sites, which is followed by release of Fe(II) from substrate to the solution. The first possibility is consistent with the energy optimizations conducted by Wang and Rustad (2006), where an electron is transferred between surface Fe(II) and structural Fe(III) resulting in a structure in which the reduced Fe(II) remains localized in the near surface region.

The bond lengths and bond-valence sums of the near surface Fe sites determined in the current study show no evidence for a significant fraction of Fe(II) in the surface unit cell (Table 4.1, 4.2, and 4.3), thus are inconsistent with the surface trapping model. The model proposed by Rosso et al. (2003) indicates that electron transport in hematite basal planes can occur via an electron hopping mechanism between nearest neighbor Fe atoms. Kerisit and Rosso (2006) extended this model by including molecular dynamics simulations and studied electron mobility in both $(1\bar{1}02)$ and (0001) surface of $\alpha\text{-Fe}_2\text{O}_3$. They find that Fe(III) on the $\alpha\text{-Fe}_2\text{O}_3(1\bar{1}02)$ surface is stabilized in presence of water resulting in electron transfer away from the initial acceptor site (Kerisit and Rosso, 2006). Based on this electron hopping model, we would not expect Fe(II) defects to localize in surface region consistent with observations of the current study. A recent study has also suggested that the injected electron is likely to be trapped at defect sites and may result in dissolution to occur at these defect sites (Kerisit and Rosso, 2007).

We note the CTR data is insensitive to the detailed structure of non-ordered features, such as step edges or surface defect sites. Rather, such features will in most cases contribute to the overall surface roughness factor refined during the analysis. Hence, if dissolution at defect sites results in significant changes in the step height distribution it will be observed as a variation in surface roughness in CTR measurements. As shown above, we do observe an increase in surface roughness with increase in reaction time. The CTR derived r.m.s. roughness for reaction time of 2 hr and 34 d at pH 5.0 is 1.7 ± 0.4 Å and 2.7 ± 0.2 Å, respectively. However, this small increase in r.m.s. roughness (~ 1 Å)

could possibly be due to the extrinsic effect of initial surface preparation. Additional work is on going to further investigate the influence of Fe(II) reaction on surface roughness.

4.5 CONCLUSIONS

The results of the current study show the adsorption of Fe(II) on $\alpha\text{-Fe}_2\text{O}_3(1\bar{1}02)$ occurs at the lattice sites of the substrate under all three studied reaction conditions: adsorption for 2 hr and 34 d at pH 5.0, and for 5.5 hr at pH 7.0 (Figure 4.4). Furthermore, the bond lengths for the adsorption complex are consistent with typical Fe(III)-O bond-lengths providing indirect evidence for oxidation of Fe(II) after adsorption. These results are in good agreement with previous studies that proposed Fe(II) adsorption is followed by interfacial electron transfer resulting in a Fe(III) overlayer, which is structurally similar to bulk oxide (Larese-Casanova and Scherer, 2007; Silvester et al., 2005; Williams and Scherer, 2004). The incorporation of adsorbed Fe into lattice sites coupled with electron transfer and possible hydroxylation (under aqueous conditions) suggests the surface bound Fe is likely to be highly coordinated to surface oxo/hydroxo groups, which is observed in current study where adsorbed Fe forms five Fe-O bonds with the substrate. These results indicate that the existing surface complexation models can be improved to account for multi-dentate Fe(II) adsorption complex, and possible oxidation Fe(II) after adsorption on hematite and possibly other iron(III) oxides. A recent Fe(II) surface complexation modeling study accounts for the oxidation of adsorbed Fe(II) by utilizing a charge distribution (CD) model (Hiemstra and van Riemsdijk, 2007). However, improvement to existing models of Fe(II) adsorption and their underlying assumptions

will require additional direct structural investigations involving a wider array of iron (hydr)oxide surfaces.

Our results raise an interesting question regarding filling of surface binding sites. The maximum occupancy of adsorbed Fe in the current study is 0.47 ± 0.05 (for reaction time of 34 d at pH 5.0) resulting in the addition of approximately one Fe per surface unit cell. The adsorbed Fe occupancy of 0.47 ± 0.05 would mean roughly half of the total available binding sites are occupied (even for reaction time of 34 d) suggesting a plateau in the adsorption reaction after filling half of the sites. As discussed above, there are two chemically equivalent binding sites per unit cell of $\alpha\text{-Fe}_2\text{O}_3(1\bar{1}02)$. A site occupancy of more than 50% results in both of these sites being filled within a single surface unit cell. However, filling one of these lattice sites would alter the local coordination environment of second available site, which could possibly result in an energetic barrier that limits adsorption on the other site. Furthermore, occupation of only one of the two available Fe lattice sites per unit cell could explain why no substrate growth is observed under the conditions examined in this study. To address this question, we are currently performing ab initio density functional theory (DFT) calculations to predict thermodynamic stability of $\alpha\text{-Fe}_2\text{O}_3(1\bar{1}02)$ as a function of topmost iron layer occupancy.

It is also important to ask how different substrate structures affect Fe(II) adsorption? Recent theoretical studies suggest that efficacy and direction of electron transport is different depending on coordination environment of Fe (Yanina and Rosso, 2008; Kerisit

and Rosso, 2006; Rosso et al., 2003). Thus, it seems likely that the underlying substrate structure may have a large impact on Fe(II) adsorption behavior. To address this question additional research is needed to identify Fe(II) adsorption complexes on other iron oxide phases such as goethite. Finally, our investigation of the structural underpinning of Fe(II) adsorption on $\alpha\text{-Fe}_2\text{O}_3(1\bar{1}02)$ surface significantly improves our understanding of surface structure and reactivity of hematite under iron reducing conditions.

ACKNOWLEDGEMENTS

The authors acknowledge Anne Chaka, Gordon Brown Jr., Cynthia Lo, and Christopher Iceman for helpful comments on the results and the manuscript. This research was supported by NSF grants CBET-0404400 and CHE-0431425, University of Alaska Fairbanks Graduate Fellowship (K.S.T.), and the Arctic Region Supercomputing Center (University of Alaska Fairbanks). This work was performed at GeoSoilEnviroCARS (Sector 13), Advanced Photon Source (APS), Argonne National Laboratory. GeoSoilEnviroCARS is supported by National Science Foundation - Earth Sciences (EAR-0622171) and Department of Energy - Geosciences (DE-FG02-94ER14466). Use of APS was supported by U.S. Department of Energy, Office of Science, Office of Basic Energy Sciences, under Contract No. DE-AC02-06CH11357.

REFERENCES

- Amonette J. E., Workman D. J., Kennedy D. W., Fruchter J. S., and Gorby Y. A. (2000) Dechlorination of carbon tetrachloride by Fe(II) associated with goethite. *Environ. Sci. Technol.* **34**, 4606-4613.
- Apted M. J., Waychunas G. A., and Brown G. E. (1985) Structure and specification of iron complexes in aqueous solutions determined by x-ray absorption spectroscopy. *Geochim. Cosmochim. Acta* **49**, 2081-2089.
- Brown G. E., Jr., Henrich V. E., Casey W. H., Clark D. L., Eggleston C., Felmy A., Goodman D. W., Graetzel M., Maciel G., McCarthy M. I., Nealson K. H., Sverjensky D. A., Toney M. F., and Zachara J. M. (1999) Metal oxide surfaces and their interactions with aqueous solutions and microbial organisms. *Chem. Rev.* **99**, 77-174.
- Brown I. D. and Altermatt D. (1985) Bond-valence parameters obtained from a systematic analysis of the inorganic crystal structure database. *Acta Cryst.*, **B41**, 244-247.
- Buerge I. J. and Hug S. J. (1999) Influence of mineral surfaces on chromium(VI) reduction by iron(II). *Environ. Sci. Technol.* **33**, 4285-4291.
- Catalano J. G., Trainor T. P., Eng P. J., Waychunas G. A., and Brown G. E., Jr. (2005) CTR diffraction and grazing-incidence EXAFS study of U(VI) adsorption onto α -Al₂O₃ and α -Fe₂O₃ (1 $\bar{1}$ 02) surfaces. *Geochim. Cosmochim. Acta* **69**, 3555-3572.
- Catalano J. G., Fenter, P., Park, C. (2007) Interfacial water structure on (012) surface of hematite: Ordering and Reactivity in comparison with corundum. *Geochim. Cosmochim. Acta* **71**, 5313-5324.
- Charlet L., Liger E., and Gerasimo P. (1998a) Decontamination of TCE- and U-rich waters by granular iron: role of sorbed Fe(II). *J. Environ. Eng.* **124**, 25-30.
- Charlet L., Silvester E., and Liger E. (1998b) N-compound reduction and actinide immobilization in surficial fluids by Fe(II): the surface $\equiv\text{Fe}^{\text{III}}\text{OFe}^{\text{II}}\text{OH}^0$ species, as major reductant. *Chem. Geol.* **151**, 85-93.
- Chun C. L., Penn R. L., and Arnold W. A. (2006) Kinetic and microscopic studies of reductive transformations of organic contaminants on goethite. *Environ. Sci. Technol.* **40**, 3299-3304.

- Colon D., Weber E. J., Anderson J. L., Winget P., and Suarez L. A. (2006) Reduction of nitrosobenzenes and N-hydroxylanilines by Fe(II) species: Elucidation of the reaction mechanism. *Environ. Sci. Technol.* **40**, 4449-4454.
- Cornell R. M. and Schwertmann U. (1996) *The Iron Oxides: Structure, Properties, Reactions, Occurrence and Uses*, Wiley- VCH.
- Coughlin B. R. and Stone A. T. (1995) Nonreversible adsorption of divalent metal ions (Mn^{II} , Co^{II} , Ni^{II} , Cu^{II} , and Pb^{II}) onto goethite: Effects of acidification, Fe^{II} addition, and picolinic acid addition. *Environ. Sci. Technol.* **29**, 2445-2455.
- Dong H., Kukkadapu R. K., Fredrickson J. K., Zachara J. M., Kennedy D. W., and Kostandarithes H. M. (2003) Microbial reduction of structural Fe(III) in illite and goethite. *Environ. Sci. Technol.* **37**, 1268-1276.
- Eary L. E. and Rai D. (1989) Kinetics of chromate reduction by ferrous ions derived from hematite and biotite at 25° C. *Am. J. Sci.* **289**, 180-213.
- Elsner M., Haderlein S. B., Kellerhals T., Luzi S., Zwank L., Angst W., and Schwarzenbach R. P. (2004) Mechanisms and products of surface-mediated reductive dehalogenation of carbon tetrachloride by Fe(II) on goethite. *Environ. Sci. Technol.* **38**, 2058-2066.
- Eng P. J., Trainor T. P., Brown G. E. Jr., Waychunas G. A., Newville M., Sutton S. R., and Rivers M. L. (2000) Structure of the hydrated $\alpha-Al_2O_3$ (0001) surface. *Science* **288**, 1029-1033.
- Erbs M., Hansen H. C. B., and Olsen C. E. (1999) Reductive Dechlorination of carbon tetrachloride using iron(II) iron(III) hydroxide sulfate (green rust). *Environ. Sci. Technol.* **33**, 307-311.
- Farges F., Lefrere Y., Rossano S., Berthereau A., Calas G., and Brown G. E. (2004) The effect of redox state on the local structural environment of iron in silicate glasses: a combined XAFS spectroscopy, molecular dynamics, and bond valence study. *J. Non-Cryst. Solids* **344**, 176-188.
- Fenter P. (2002) X-ray reflectivity as probe of mineral-fluid interfaces: A user guide. In *Applications of synchrotron radiation in low temperature geochemistry and environmental science* (ed. P. Fenter, M. Rivers, N. Sturchio, and S. Sutton) *Rev. Mineral. Geochem.* **49**, 149-220.
- Fenter P. and Sturchio N. C. (2004) Mineral-water interfacial structures revealed by synchrotron x-ray scattering. *Prog. Surf. Sci.* **77**, 171-258.

- Finger L. W. and Hazen R. M. (1980) Crystal structure and isothermal compression of Fe_2O_3 , Cr_2O_3 , and V_2O_3 to 50 kbars. *J. Appl. Phys.* **51**, 5362–5367.
- Fredrickson J. K., Kota S., Kukkadapu R. K., Liu C., and Zachara J. M. (2003) Influence of electron donor/acceptor concentrations on hydrous ferric oxide (HFO) bioreduction. *Biodegradation* **14**, 91-103.
- Fredrickson J. K., Zachara J. M., Kennedy D. W., Kukkadapu R. K., McKinley J. P., Heald S. M., Liu C., and Plymale A. E. (2004) Reduction of TcO_4^- by sediment-associated biogenic Fe(II). *Geochim. Cosmochim. Acta* **68**, 3171-3187.
- Hamilton W. C. (1965) Significance tests on the crystallographic R factor. *Acta Cryst.* **18**, 502-510.
- Hansel C. M., Benner S. G., and Fendorf S. (2005) Competing Fe(II)-induced mineralization pathways of ferrihydrite. *Environ. Sci. Technol.* **39**, 7147-7153.
- Hansel C. M., Benner S. G., Neiss J., Dohnalkova A., Kukkadapu R. K., and Fendorf S. (2003) Secondary mineralization pathways induced by dissimilatory iron reduction of ferrihydrite under advective flow. *Geochim. Cosmochim. Acta* **67**, 2977-2992.
- Hiemstra T. and van Riemsdijk W. H. (2007) Adsorption and surface oxidation of Fe(II) on metal (hydr)oxides. *Geochim. Cosmochim. Acta* **71**, 5913-5933
- Hofstetter T. B., Heijman C. G., Haderlein S. B., Holliger C., and Schwarzenbach R. P. (1999) Complete reduction of TNT and other (poly)nitroaromatic compounds under iron-reducing subsurface conditions. *Environ. Sci. Technol.* **33**, 1479-1487.
- Jackson W. E., Farges F., Yeager M., Mabrouk P. A., Rossano S., Waychunas G. A., Solomon E. I.; Brown G. E. (2005) Multi-spectroscopic study of Fe(II) in silicate glasses: Implications for the coordination environment of Fe(II) in silicate melts. *Geochim. Cosmochim. Acta* **69**, 4315-4332.
- Jeon B.-H., Dempsey B. A., and Burgos W. D. (2003) Kinetics and mechanisms for reactions of Fe(II) with iron(III) oxides. *Environ. Sci. Technol.* **37**, 3309-3315.
- Jeon B. H., Dempsey B. A., Burgos W. D., and Royer R. A. (2001) Reactions of ferrous iron with hematite. *Colloids Surf., A* **191**, 41-55.
- Kerisit S. and Rosso K. M. (2006) Computer simulation of electron transfer at hematite surfaces. *Geochim. Cosmochim. Acta* **70**, 1888-1903.

- Kerisit S. and Rosso K. M. (2007) Kinetic Monte Carlo model of charge transport in hematite (α -Fe₂O₃). *J. Chem. Phys.* **127**, 124706/1 - 124706/10.
- Kim D. and Strathmann T. J. (2007) Role of organically complexed iron(II) species in the reductive transformation of RDX in anoxic environments. *Environ. Sci. Technol.* **41**, 1257-1264.
- Klausen J., Troeber S. P., Haderlein S. B., and Schwarzenbach R. P. (1995) Reduction of substituted nitrobenzenes by Fe(II) in aqueous Mineral suspensions. *Environ. Sci. Technol.* **29**, 2396-2404.
- Kostka J. E. and Nealson K. H. (1995) Dissolution and reduction of magnetite by bacteria. *Environ. Sci. Technol.* **29**, 2535-2540.
- Kukkadapu R. K., Zachara J. M., Fredrickson J. K., Kennedy D. W., Dohnalkova A. C., and McCready D. E. (2005) Ferrous hydroxy carbonate is a stable transformation product of biogenic magnetite. *Am. Mineral.* **90**, 510-515.
- Larese-Casanova P. and Scherer M. M. (2007) Fe(II) sorption on hematite: new insights based on spectroscopic measurements. *Environ. Sci. Technol.* **41**, 471-477.
- Liger E., Charlet L., and Van Cappellen P. (1999) Surface catalysis of uranium (VI) reduction by iron(II). *Geochim. Cosmochim. Acta* **63**, 2939-2955.
- Liu C., Kota S., Zachara J. M., Fredrickson J. K., and Brinkman C. K. (2001a) Kinetic analysis of the bacterial reduction of goethite. *Environ. Sci. Technol.* **35**, 2482-2490.
- Liu C., Zachara J. M., Gorby Y. A., Szecsody J. E., and Brown C. F. (2001b) Microbial reduction of Fe(III) and sorption/precipitation of Fe(II) on shewanella putrefaciens strain CN32. *Environ. Sci. Technol.* **35**, 1385-1393.
- Liu P., Kendelewicz T., Brown G. E., Jr., Nelson E. J., and Chambers S. A. (1998) Reaction of water vapor with α -Al₂O₃(0001) and α -Fe₂O₃(0001) surfaces: synchrotron X-ray photoemission studies and thermodynamic calculations. *Surf. Sci.* **417**, 53-65.
- Lo C. S., Tanwar K. S., Chaka A. M., and Trainor T. P. (2007) Density functional theory study of the clean and hydrated hematite (1 $\bar{1}$ 02) surfaces. *Phys. Rev. B: Condens. Matter* **75**, 075425/1-075425/15.
- Lovley D. R. (1991) Dissimilatory iron(III) and manganese(IV) reduction. *Microbiol. Rev.* **55**, 259-287.

- Lovley D. R. (1993) Dissimilatory metal reduction. *Annu. Rev. of Microbiol.* **47**, 263-290.
- Lovley D. R. (1997) Microbial Fe(III) reduction in subsurface environments. *FEMS Microbiol. Rev.* **20**, 305-313.
- Pauling L. C. (1960) *The nature of the chemical bond and the structure of molecules and crystals. An introduction to modern structural chemistry. 3rd ed.*
- Pecher K., Haderlein S. B., and Schwarzenbach R. P. (2002) Reduction of polyhalogenated methanes by surface-bound Fe(II) in aqueous suspensions of iron oxides. *Environ. Sci. Technol.* **36**, 1734-1741.
- Pedersen H. D., Postma D., Jakobsen R., and Larsen O. (2005) Fast transformation of iron oxyhydroxides by the catalytic action of aqueous Fe(II). *Geochim. Cosmochim. Acta* **69**, 3967-3977.
- Robinson I. K. (1986) Crystal truncation rods and surface roughness. *Phys. Rev. B: Condens. Matter* **33**, 3830-3836.
- Robinson I. K. (1991) Surface Crystallography. In *Handbook on Synchrotron Radiation*, Vol. 3 (ed. G. S. Brown and M. D. E.), pp. 221-226. North-Holland.
- Robinson I. K. and Tweet D. J. (1992) Surface x-ray diffraction. *Rep. Prog. Phys.* **55**, 599-651.
- Roden E. E. and Urrutia M. M. (2002) Influence of biogenic Fe(II) on bacterial crystalline Fe(III) oxide reduction. *Geomicrobiol. J.* **19**, 209-251.
- Roden E. E., Urrutia M. M., and Mann C. J. (2000) Bacterial reductive dissolution of crystalline Fe(III) oxide in continuous-flow column reactors. *Appl. Environ. Microb.* **66**, 1062-1065.
- Roden E. E., Zachara J. M. (1996) Microbial reduction of crystalline Fe(III) oxides: influence of oxide surface area and potential for cell growth. *Environ. Sci. Technol.* **30**, 1618-1628.
- Rosso K. M., Smith D. M. A., and Dupuis M. (2003) An ab initio model of electron transport in hematite (α -Fe₂O₃) basal planes. *J. Chem. Phys.* **118**, 6455-6466.
- Royer R. A., Burgos W. D., Fisher A. S., Jeon B.-H., Unz R. F., and Dempsey B. A. (2002) Enhancement of hematite bioreduction by natural organic matter. *Environ. Sci. Technol.* **36**, 2897-2904.

- Royer R. A., Dempsey B. A., Jeon B.-H., and Burgos W. D. (2004) Inhibition of biological reductive dissolution of hematite by ferrous iron. *Environ. Sci. Technol.* **38**, 187-193.
- Silvester E., Charlet L., Tournassat C., Gehin A., Grenèche J.-M., and Liger E. (2005) Redox potential measurements and moessbauer spectrometry of Fe^{II} adsorbed onto Fe^{III} (oxyhydr)oxides. *Geochim. Cosmochim. Acta* **69**, 4801-4815.
- Stookey L. L. (1970) Ferrozine-a new spectrophotometric reagent for iron. *Anal. Chem.* **42**, 779-781.
- Stumm W. and Sulzberger B. (1992) The cycling of iron in natural environments: Considerations based on laboratory studies of heterogeneous redox processes. *Geochim. Cosmochim. Acta* **56**, 3233-3257.
- Sulzberger B., Suter D., Siffert C., Banwart S., and Stumm W. (1989) Dissolution of iron(III) (hydr)oxides in natural waters, laboratory assessment on the kinetics controlled by surface coordination. *Mar. Chem.* **28**, 127-144.
- Tamaura Y., Ito K., and Katsura T. (1983) Transformation of $\gamma\text{-FeO(OH)}$ to magnetite by adsorption of iron(II) ion on $\gamma\text{-FeO(OH)}$. *J. Chem. Soc., Dalton Trans.* 1983, 189-194.
- Tanwar K. S., Catalano J. G., Petitto S. C., Ghose S. K., Eng P. J., and Trainor T. P. (2007a) Hydrated $\alpha\text{-Fe}_2\text{O}_3$ (1 $\bar{1}$ 02) surface structure: Role of surface preparation. *Surf. Sci.* **601**, L59-L64.
- Tanwar K. S., Lo C. S., Eng P. J., Catalano J. G., Walko D. A., Brown G. E., Waychunas G. A., Chaka A. M., and Trainor T. P. (2007b) Surface diffraction study of the hydrated hematite (1 $\bar{1}$ 02) surface. *Surf. Sci.* **601**, 460-474.
- Tossell J. A. (1980) Calculation of bond distances and heats of formation for BeO, MgO, SiO_2 , TiO_2 , FeO and ZnO using ionic model. *Am. Mineral* **65**, 163-173.
- Trainor T. P., Chaka A. M., Eng P. J., Newville M., Waychunas G. A., Catalano J. G., and Brown G. E. (2004) Structure and reactivity of the hydrated hematite (0001) surface. *Surf. Sci.* **573**, 204-224.
- Trainor T. P., Eng P. J., Brown G. E., Robinson I. K., and De Santis M. (2002a) Crystal truncation rod diffraction study of the $\alpha\text{-Al}_2\text{O}_3$ (1 $\bar{1}$ 02) surface. *Surf. Sci.* **496**, 238-250.

- Trainor T. P., Eng P. J., and Robinson I. K. (2002b) Calculation of crystal truncation rod structure factors for arbitrary rational surface terminations. *J. of Appl. Crystallogr.* **35**, 696-701.
- Trainor T. P., Templeton A. S., and Eng P. J. (2006) Structure and reactivity of environmental interfaces: Application of grazing angle X-ray spectroscopy and long-period x-ray standing waves. *J. Electron Spectrosc. Relat. Phenom.* **150**, 66-85.
- Tronc E., Belleville P., Jolivet J. P., and Livage J. (1992) Transformation of ferric hydroxide into spinel by iron(II) adsorption. *Langmuir* **8**, 313-319.
- Urrutia M. M., Roden E. E., and Zachara J. M. (1999) Influence of aqueous and solid-phase Fe(II) complexants on microbial reduction of crystalline iron(III) oxides. *Environ. Sci. Technol.* **33**, 4022-4028.
- Vlieg E. (2000) ROD: a program for surface X-ray crystallography. *J. of Appl. Crystallogr.* **33**, 401-405.
- Vlieg E., Van der Veen J. F., Gurman S. J., Norris C., and Macdonald J. E. (1989) X-ray diffraction from rough, relaxed and reconstructed surfaces. *Surf. Sci.* **210**, 301-321.
- Wang J. and Rustad J. R. (2006) A simple model for the effect of hydration on the distribution of ferrous iron at reduced hematite (012) surfaces. *Geochim. Cosmochim. Acta* **70**, 5285-5292.
- Waychunas G. A., Brown G. E. Jr., Ponader C. W., and Jackson W. E. (1988) Evidence from X-ray absorption for network-forming Fe²⁺ in molten alkali silicates. *Nature* **332**, 251-253.
- Waychunas G. A., Brown G. E. Jr., Jackson W. E., and Ponader C. W. (1989) *In-situ* high temperature x-ray absorption study of iron in alkali silicate melts and glasses. *Physica B* **21**, 144-146.
- Whittaker E. J. W., and Muntus R. (1970) Ionic radii for use in geochemistry. *Geochim. Cosmochim. Acta* **34**, 945-956.
- Wilke M., Schmidt C., Farges F., Malavergne V., Gautron L., Simionovici A., Hahn M., and Petit P.E. (2006) Structural environment of Fe in water-bearing silicate glass and melt-evidence from X-ray absorption spectroscopy. *Chem. Geol.* **229**, 144-161.

- Williams A. G. B. and Scherer M. M. (2004) Spectroscopic evidence for Fe(II)-Fe(III) electron transfer at the iron oxide-water interface. *Environ. Sci. Technol.* **38**, 4782-4790.
- Yanina S. V. and Rosso K. M. (2008) Linked reactivity at mineral-water interfaces through bulk crystal conduction. *Science* **320**, 218-222.
- Zachara J. M., Fredrickson J. K., Smith S. C., and Gassman P. L. (2001) Solubilization of Fe(III) oxide-bound trace metals by a dissimilatory Fe(III) reducing bacterium. *Geochim. Cosmochim. Acta* **65**, 75-93.
- Zachara J. M., Kukkadapu R. K., Fredrickson J. K., Gorby Y. A., and Smith S. C. (2002) Biomineralization of poorly crystalline Fe(III) oxides by dissimilatory metal-reducing bacteria (DMRB). *Geomicrobiol. J.* **19**, 179-207.
- Zhang Y., Charlet L., and Schindler P. W. (1992) Adsorption of protons, iron(II) and aluminum on lepidocrocite (γ -FeOOH). *Colloids Surf.* **63**, 259-268.

Table 4.1 Unrelaxed surface unit cell coordinates for clean $\alpha\text{-Fe}_2\text{O}_3(1\bar{1}02)$ and best-fit model coordinates and parameters for $\alpha\text{-Fe}_2\text{O}_3(1\bar{1}02)$ reacted with Fe(II) for 2 hr at pH 5.0.

Layer	Clean Unrelaxed (O ₂ -X-O ₂ -Fe ₂ -O ₂ -R)			Best fit model (O _{2n} -O ₂ -Fe _{2m} -O ₂ -Fe ₂ -O ₂ -R)						$\chi^2 = 1.1$ $\beta = 0.15(3)$	
	x	y	z	x	y	z	Δz (Å)	B _{iso} (Å ²)	Occ.	Σ_s	
ii	O(H ₂ O)			0.66(2)	0.83(5)	2.21(2)	-	3.00	0.34(7)	0.00	
		O(H ₂ O)		0.84(2)	0.33(5)	2.21(2)	-	3.00	0.34(7)	0.00	
i	O			0.14(2)	0.80(4)	2.10(3)	-	0.50	0.25(7)	0.6(2)	
		O		0.36(2)	0.30(4)	2.10(3)	-	0.50	0.25(7)	0.6(2)	
1	O	0.653	0.974	1.903	0.658(6)	0.98(1)	1.906(5)	0.02(4)	0.50	0.92(9)	1.32(1)
		O	0.847	0.474	1.903	0.842(6)	0.48(1)	1.906(5)	0.02(4)	0.50	0.92(9)
2	Fe	X	X	X	0.005(4)	0.833(3)	1.852(5)	-	0.32	0.30(4)	2.9(2)
		Fe	X	X	X	0.495(4)	0.333(3)	1.852(5)	-	0.32	0.30(4)
3	O	0.194	0.105	1.750	0.197(5)	0.10(1)	1.740(6)	-0.08(4)	0.40	1.00(7)	1.98(7)
		O	0.306	0.605	1.750	0.303(5)	0.60(1)	1.740(6)	-0.08(4)	0.40	1.00(7)
4	Fe	0.000	0.380	1.645	0.997(1)	0.392(7)	1.646(4)	0.01(3)	0.32	0.95(6)	3.00(6)
		Fe	0.500	0.880	1.645	0.504(1)	0.891(7)	1.646(4)	0.01(3)	0.32	0.95(6)
5	O	0.653	0.237	1.597	0.657(6)	0.237	1.597	0.00	0.40	1.00	2.00(1)
		O	0.847	0.737	1.597	0.843(6)	0.737	1.597	0.00	0.40	1.00
6	O	0.153	0.404	1.403	0.153	0.404	1.402(3)	-0.01(2)	0.40	1.00	1.95(3)
		O	0.347	0.904	1.403	0.347	0.904	1.402(3)	-0.01(2)	0.40	1.00
7	Fe	0.500	0.261	1.355	0.500	0.261	1.353(2)	-0.01(2)	0.32	1.00	2.94(4)
		Fe	0.000	0.761	1.355	0.000	0.761	1.353(2)	-0.01(2)	0.32	1.00
8	O	0.694	0.535	1.250	0.694	0.535	1.249(4)	-0.01(3)	0.40	1.00	1.98(1)
		O	0.806	0.035	1.250	0.806	0.035	1.249(4)	-0.01(3)	0.40	1.00
9	Fe	0.500	0.810	1.145	0.500	0.810	1.145	0.00	0.32	1.00	2.97(5)
		Fe	0.000	0.310	1.145	0.000	0.310	1.145	0.00	0.32	1.00
10	O	0.153	0.667	1.097	0.153	0.667	1.097	0.00	0.40	1.00	1.98(1)
		O	0.347	0.166	1.097	0.347	0.166	1.097	0.00	0.40	1.00

The estimated errors from least squares fit at the 96% confidence interval are given in parentheses. Values without errors were held fixed in the final fits. The Δz values are change in layer position with respect to unrelaxed termination. The B_{iso} are isotropic Debye-Waller factors and Occ are occupancy parameters. The bond-valence sums were calculated assuming unit site occupancies. The X denotes absence of a given layer. The atoms in the boldface represent atoms added to unreacted surface termination. The physisorbed water layers are not included in presented model stoichiometry.

Table 4.2 Best-fit model coordinates and parameters for $\alpha\text{-Fe}_2\text{O}_3(1\bar{1}02)$ reacted with Fe(II) for 34 d at pH 5.0.

Layer	Best fit model (O _{2n} -O ₂ -Fe _{2m} -O ₂ -Fe ₂ -O ₂ -R)					$\chi^2 = 1.1$ $\beta = 0.28(2)$		
	x	y	z	Δz (Å)	B _{iso} (Å ²)	Occ.	Σ_s	
iii	O(H ₂ O)	0.26(2)	0.96(3)	2.41(1)	-	1.00	0.46(6)	0.00
	O(H ₂ O)	0.24(2)	0.46(3)	2.41(1)	-	1.00	0.46(6)	0.00
ii	O(H ₂ O)	0.65(3)	0.82(5)	2.24(2)	-	1.00	0.39(8)	0.00
	O(H ₂ O)	0.85(3)	0.33(5)	2.24(2)	-	1.00	0.39(8)	0.00
i	O	0.12(2)	0.86(2)	2.114(9)	-	0.50	0.7(1)	0.61(1)
	O	0.38(2)	0.36(2)	2.114(9)	-	0.50	0.7(1)	0.61(1)
1	O	0.64(1)	0.96(1)	1.898(7)	0.04(5)	0.50	0.90(9)	1.4(3)
	O	0.86(1)	0.46(1)	1.898(7)	0.04(5)	0.50	0.90(9)	1.4(3)
2	Fe	0.004(3)	0.831(5)	1.862(6)	-	0.32	0.47(5)	2.81(4)
	Fe	0.496(3)	0.331(5)	1.862(6)	-	0.32	0.47(5)	2.81(4)
3	O	0.223(5)	0.078(6)	1.745(7)	-0.03(5)	0.40	0.97(5)	1.99(5)
	O	0.277(5)	0.578(6)	1.745(7)	-0.03(5)	0.40	0.97(5)	1.99(5)
4	Fe	0.998(1)	0.379(7)	1.643(5)	-0.01(3)	0.32	1.00	3.08(2)
	Fe	0.502(1)	0.879(7)	1.643(5)	-0.01(3)	0.32	1.00	3.08(3)
5	O	0.653	0.237	1.596(6)	-0.01(5)	0.40	1.00	1.91(1)
	O	0.843	0.737	1.596(6)	-0.01(5)	0.40	1.00	1.91(1)
6	O	0.153	0.404	1.404(5)	0.01(4)	0.40	1.00	1.98(3)
	O	0.347	0.904	1.404(5)	0.01(4)	0.40	1.00	1.98(3)
7	Fe	0.500	0.261	1.352(3)	-0.02(2)	0.32	1.00	2.96(8)
	Fe	0.000	0.761	1.352(3)	-0.02(2)	0.32	1.00	2.96(8)
8	O	0.694	0.535	1.250	0.00	0.40	1.00	1.99(2)
	O	0.806	0.035	1.250	0.00	0.40	1.00	1.99(2)
9	Fe	0.500	0.810	1.145	0.00	0.32	1.00	2.95(4)
	Fe	0.000	0.310	1.145	0.00	0.32	1.00	2.95(4)
10	O	0.153	0.667	1.097	0.00	0.40	1.00	1.99(2)
	O	0.347	0.166	1.097	0.00	0.40	1.00	1.99(2)

The estimated errors from least squares fit at the 96% confidence interval are given in parentheses. Values without errors were held fixed in the final fits. The Δz values are change in layer position with respect to unrelaxed termination. The B_{iso} are isotropic Debye-Waller factors and Occ are occupancy parameters. The bond-valence sums were calculated assuming unit site occupancies. The X denotes absence of a given layer. The atoms in the boldface represent atoms added to unreacted surface termination. The physisorbed water layers are not included in presented model stoichiometry. The H₂O in parentheses represent simulated water layers.

Table 4.3 Best-fit model coordinates and parameters for $\alpha\text{-Fe}_2\text{O}_3(1\bar{1}02)$ reacted with Fe(II) for 5.5 hr at pH 7.0.

Layer	Best fit model ($\text{O}_{2n}\text{-O}_2\text{-Fe}_{2m}\text{-O}_2\text{-Fe}_2\text{-O}_2\text{-R}$)							$\chi^2 = 1.2$ $\beta = 0.18(4)$
	x	y	z	Δz (Å)	B_{iso} (Å ²)	Occ.	Σ_s	
iii	O(H₂O)	0.194	0.2(1)	2.43(5)	-	5.00	0.15(8)	0.00
	O(H₂O)	0.306	0.7(1)	2.43(5)	-	5.00	0.15(8)	0.00
ii	O(H₂O)	0.62(4)	0.97(6)	2.23(3)	-	2.00	0.28(6)	0.00
	O(H₂O)	0.88(4)	0.47(5)	2.23(3)	-	2.00	0.28(6)	0.00
i	O	0.13(2)	0.82(2)	2.107(8)	-	0.70	0.6(1)	0.59(6)
	O	0.37(2)	0.32(2)	2.107(8)	-	0.70	0.6(1)	0.59(6)
1	O	0.660(7)	0.97(1)	1.906(7)	0.02(5)	0.50	0.92(8)	1.35(5)
	O	0.840(7)	0.47(1)	1.906(7)	0.02(5)	0.50	0.92(8)	1.35(5)
2	Fe	0.008(3)	0.82(1)	1.855	-	0.32	0.39(3)	2.89(1)
	Fe	0.492(3)	0.32(1)	1.855	-	0.32	0.39(3)	2.89(1)
3	O	0.201(8)	0.099(8)	1.746(8)	-0.03(6)	0.50	0.90(9)	1.97(1)
	O	0.299(8)	0.599(8)	1.746(8)	-0.03(6)	0.50	0.90(9)	1.97(1)
4	Fe	0.993(1)	0.385(6)	1.649(4)	0.03(3)	0.32	0.95(5)	2.94(8)
	Fe	0.507(1)	0.885(6)	1.649(4)	0.03(3)	0.32	0.95(5)	2.94(8)
5	O	0.652(8)	0.233(8)	1.593(5)	-0.03(4)	0.40	1.00	1.99(2)
	O	0.848(8)	0.733(8)	1.593(5)	-0.03(4)	0.40	1.00	1.99(2)
6	O	0.153	0.404	1.404(4)	0.01(3)	0.40	1.00	1.90(3)
	O	0.347	0.904	1.404(4)	0.01(3)	0.40	1.00	1.90(3)
7	Fe	0.500	0.261	1.352(3)	-0.02(2)	0.32	1.00	3.00(4)
	Fe	0.000	0.761	1.352(3)	-0.02(2)	0.32	1.00	3.00(4)
8	O	0.694	0.535	1.250	0.00	0.40	1.00	1.99(2)
	O	0.806	0.035	1.250	0.00	0.40	1.00	1.99(2)
9	Fe	0.500	0.810	1.145	0.00	0.32	1.00	2.95(3)
	Fe	0.000	0.310	1.145	0.00	0.32	1.00	2.95(3)
10	O	0.153	0.667	1.097	0.00	0.40	1.00	1.99(2)
	O	0.347	0.166	1.097	0.00	0.40	1.00	1.99(2)

The estimated errors from least squares fit at the 96% confidence interval are given in parentheses. Values without errors were held fixed in the final fits. The Δz values are change in layer position with respect to unrelaxed termination. The B_{iso} are isotropic Debye-Waller factors and Occ are occupancy parameters. The bond-valence sums were calculated assuming unit site occupancies. The X denotes absence of a given layer. The atoms in the boldface represent atoms added to unreacted surface termination. The physisorbed water layers are not included in presented model stoichiometry. The H₂O in parentheses represent simulated water layers.

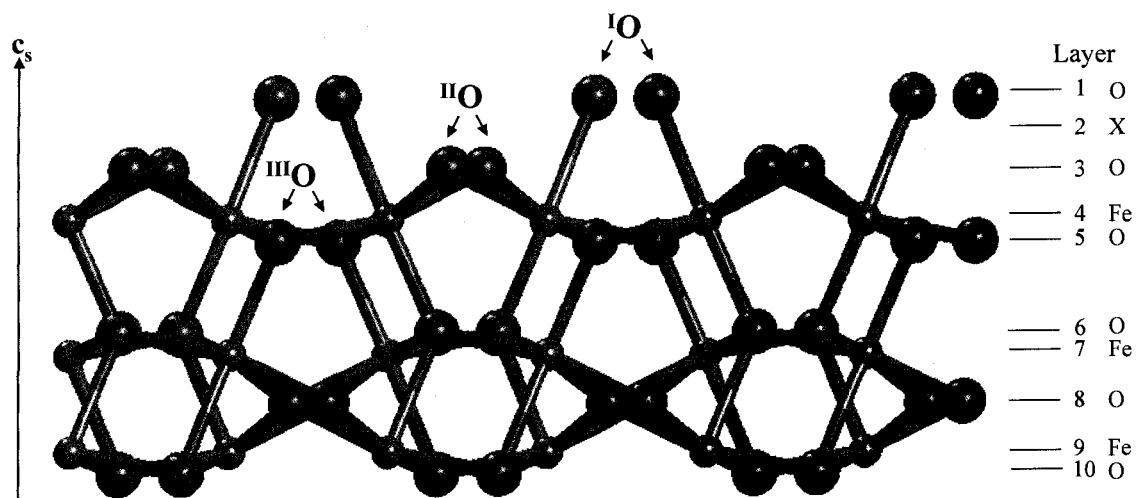


Figure 4.1 The layer stacking sequence along c_s axis for CMP prepared $\alpha\text{-Fe}_2\text{O}_3(1\bar{1}02)$ surface termination. The small spheres are Fe and large spheres are O atoms. The "X" denotes absence of a given layer. The I^{O} , II^{O} , and III^{O} represent oxygen, which is singly, doubly, and triply coordinated to iron, respectively.

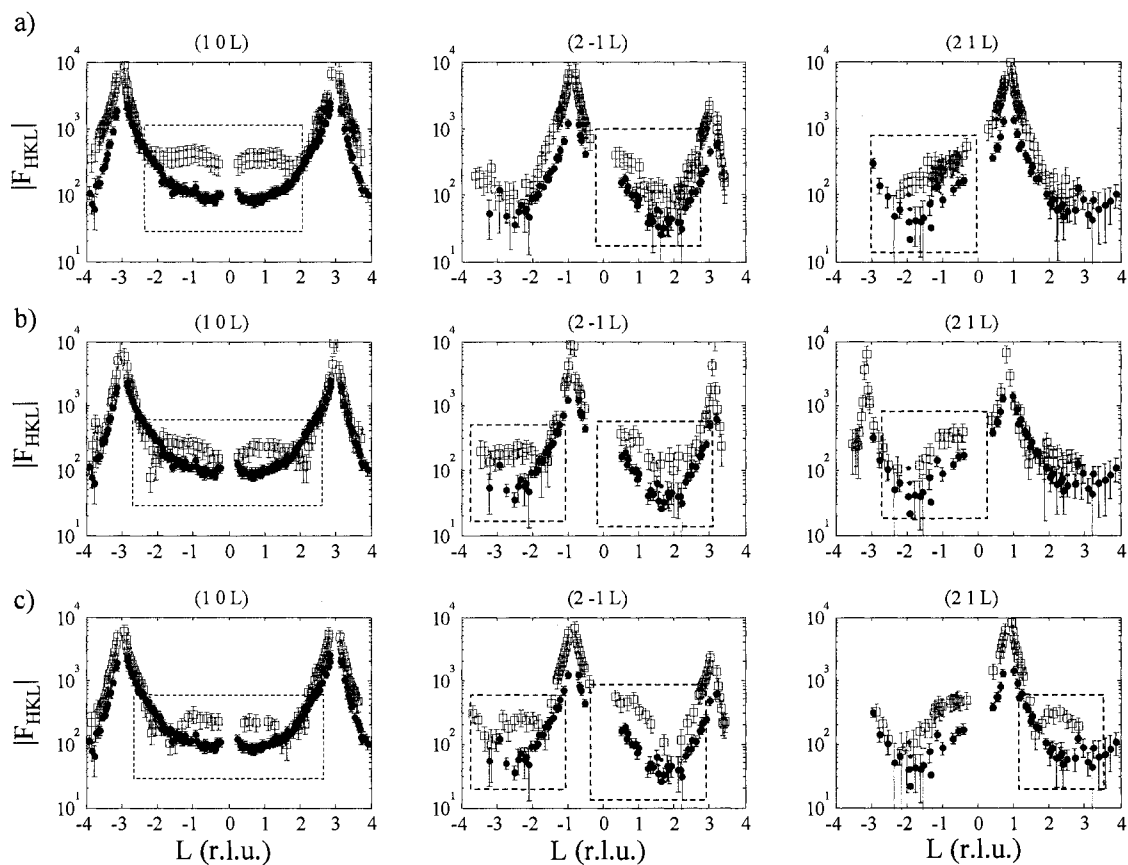


Figure 4.2 A comparison of experimental structure factors ($|F_{HKL}|$) as a function of perpendicular momentum transfer (L , in reciprocal lattice units) for CMP prepared α - $\text{Fe}_2\text{O}_3(1\bar{1}02)$ (dots), and α - $\text{Fe}_2\text{O}_3(1\bar{1}02)$ reacted with Fe(II) (squares) for a) 2 hr at pH 5.0, b) 34 d at pH 5.0, and c) 5.5 hr at pH 7.0. The data for reacted samples is scaled up by a factor of 1.5 in order to clearly show differences in CTR profiles.

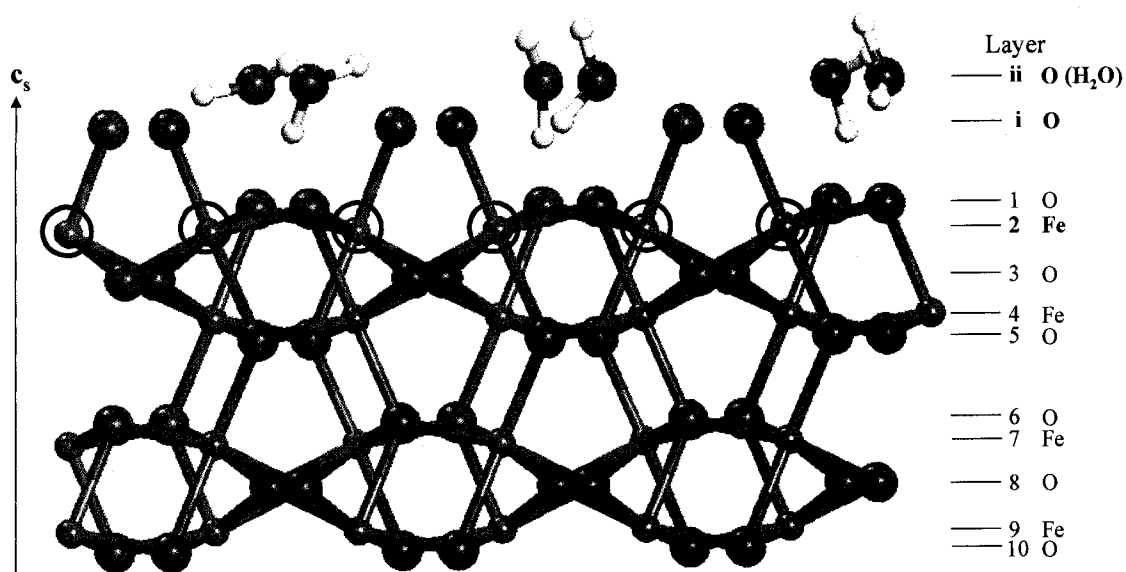


Figure 4.4 The layer stacking sequence along c_s axis for the best-fit CTR model for α - $\text{Fe}_2\text{O}_3(1\bar{1}02)$ reacted with Fe(II) for 2 hr at pH 5.0. The small spheres are Fe and large spheres are O atoms. The Fe atoms in circles represent adsorbed Fe(II). The water molecules are shown with random orientations. The best-fit CTR models for α - $\text{Fe}_2\text{O}_3(1\bar{1}02)$ reacted with Fe(II) for 34 d at pH 5.0, and 5.5 hr at pH 7.0 also resulted in similar substrate Fe/O stoichiometry of $\text{O}_{2n}\text{-O}_2\text{-Fe}_{2m}\text{-O}_2\text{-Fe}_2\text{-O}_2\text{-R}$ (see text for details). The atoms in the boldface represent atoms added to unreacted termination.

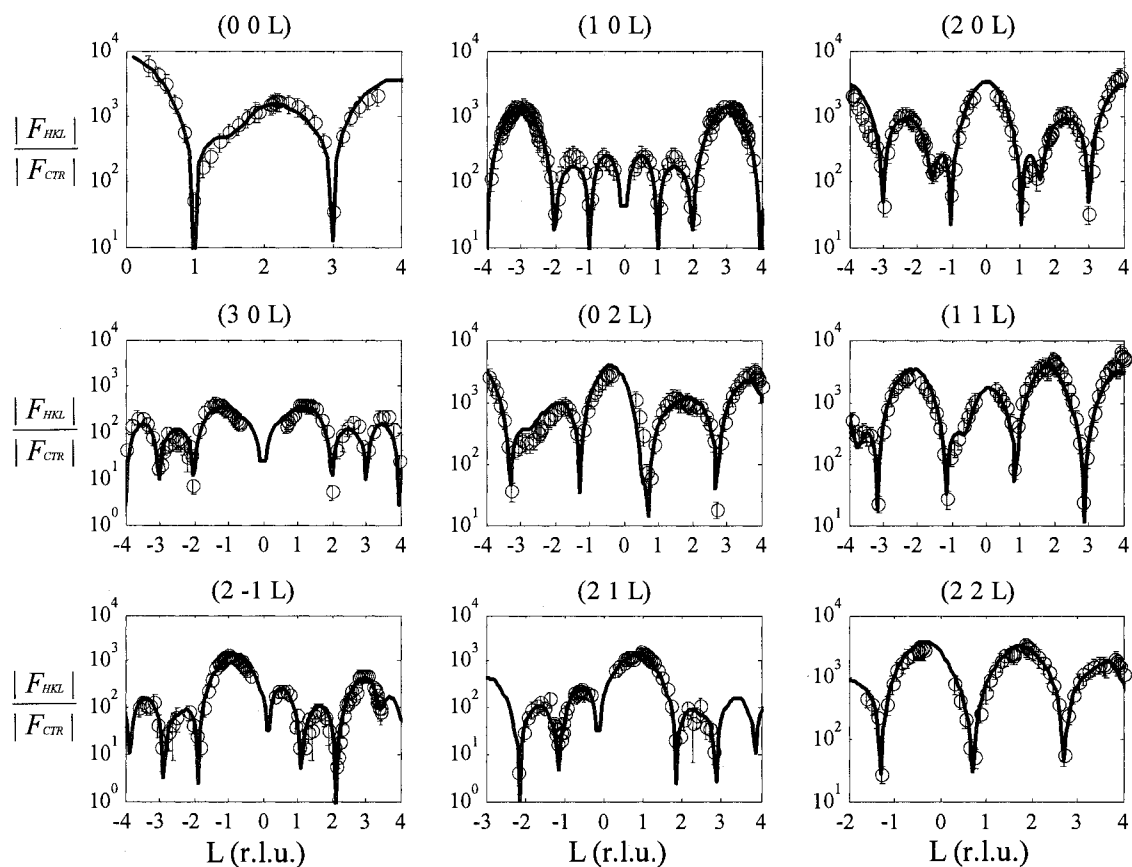


Figure 4.5 The magnitude of experimental structure factors ($|F_{HKL}|$) normalized by $|F_{CTR}|$ (circles) as a function of perpendicular momentum transfer (L , in reciprocal lattice units) for $\alpha\text{-Fe}_2\text{O}_3(1\bar{1}02)$ reacted with Fe(II) for 2 hr at pH 5.0. The F_{CTR} can be given as $1/\{1-\exp(-i2\pi\zeta)\}$ after excluding attenuation factor (Trainor et al., 2002b). The solid line represents the normalized structure factors calculated from the best-fit model.

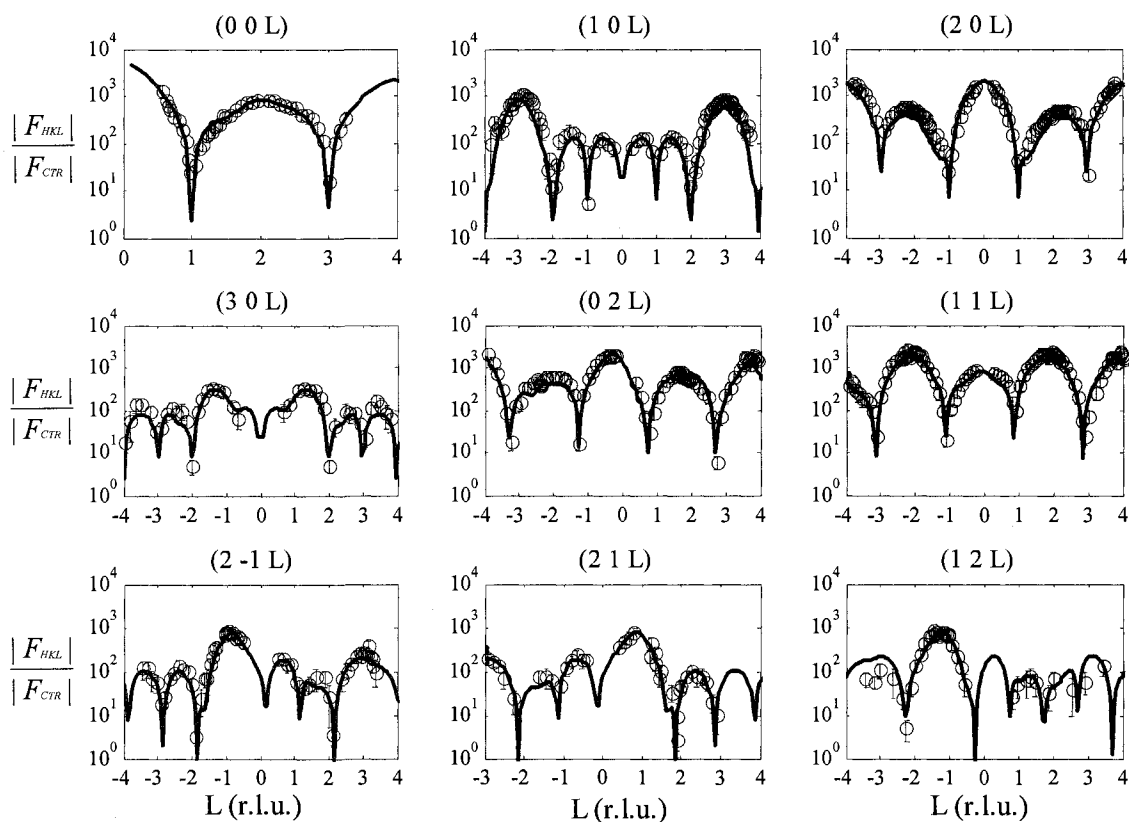


Figure 4.6 The magnitude of experimental structure factors ($|F_{HKL}|$) normalized by $|F_{CTR}|$ (circles) as a function of perpendicular momentum transfer (L , in reciprocal lattice units) for $\alpha\text{-Fe}_2\text{O}_3(1\ \bar{1}\ 02)$ reacted with Fe(II) for 34 d at pH 5.0.

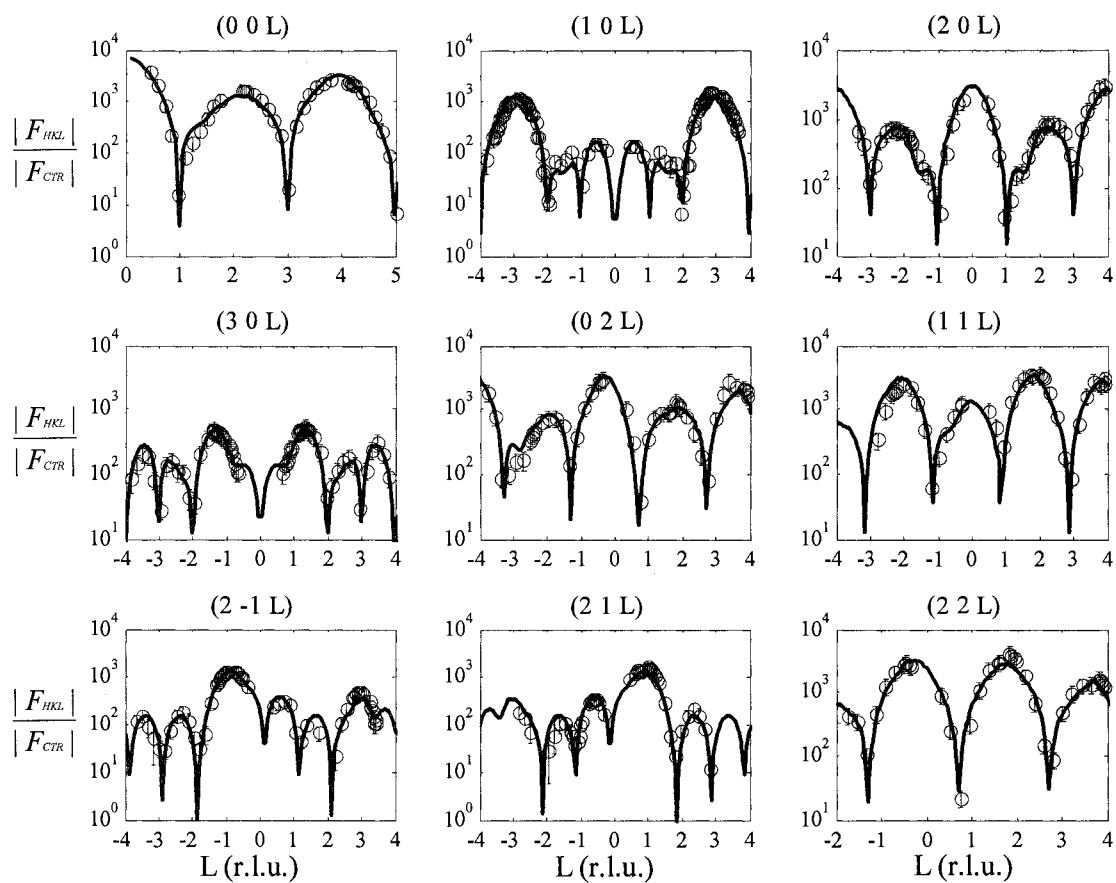


Figure 4.7 The magnitude of experimental structure factors ($|F_{HKL}|$) normalized by $|F_{CTR}|$ (circles) as a function of perpendicular momentum transfer (L , in reciprocal lattice units) for $\alpha\text{-Fe}_2\text{O}_3(1\ \bar{1}\ 02)$ reacted with Fe(II) for 5.5 hr at pH 7.0.

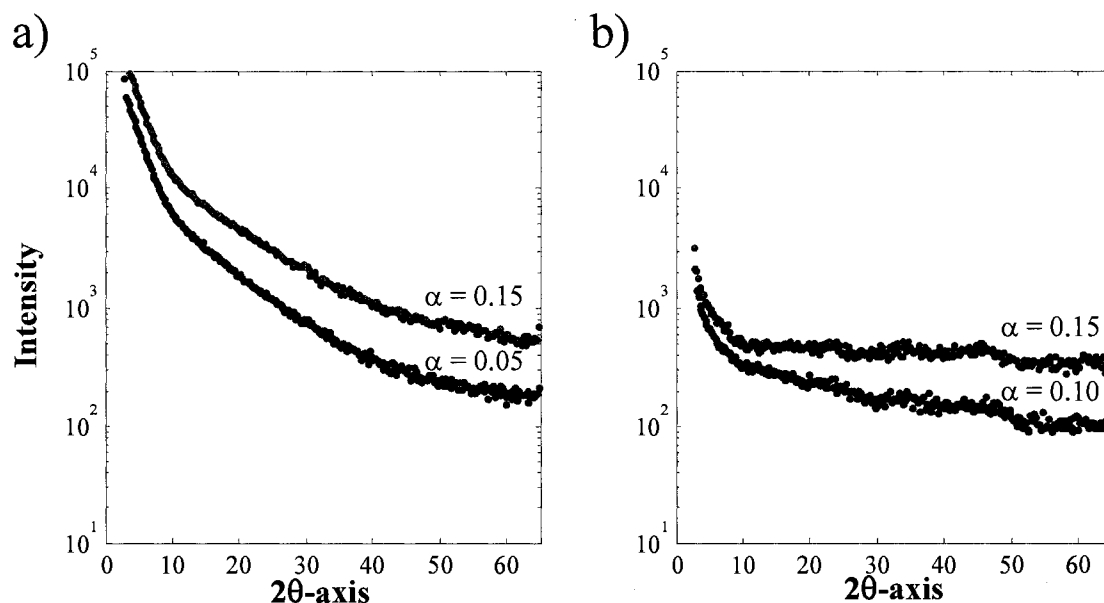


Figure 4.8 The grazing incidence in-plane X-ray diffraction data at a given incidence angle (α) for α -Fe₂O₃(1 $\bar{1}$ 02) reacted with Fe(II) for a) 34 d at pH 5.0, and b) 5.5 hr at pH 7.0. The measured intensity is rescaled for clarity. The experiments were conducted at room temperature under hydrated He atmosphere. The data shows no evidence for surface precipitation of any ordered mineral phase.

Chapter 5 Fe(II) ADSORPTION ON HEMATITE(0001)*

ABSTRACT

The surface structure of α -Fe₂O₃(0001) was studied using crystal truncation rod (CTR) X-ray diffraction before and after reaction with aqueous Fe(II) at pH 5. The CTR results show that the unreacted α -Fe₂O₃(0001) surface consists of two chemically distinct structural domains: an O-layer terminated domain and a hydroxylated Fe-layer terminated domain. After exposing the α -Fe₂O₃(0001) surface to aqueous Fe(II), the surface structure of both co-existing structural domains was modified due to adsorption of Fe at crystallographic lattice sites of the substrate, resulting in six-coordinated adsorbed Fe at the surface. The average Fe-O bond lengths for the adsorbed Fe are consistent with typical Fe(III)-O bond lengths (in octahedral coordination), providing evidence for the oxidation of Fe(II) to Fe(III) upon adsorption. These results highlight the important role of substrate surface structure in controlling Fe(II) adsorption. Furthermore, the molecular scale structural characterization of adsorbed Fe provides insight into the process of Fe(II) induced structural modification of hematite surfaces, which in turn aids in assessing the effective reactivity of hematite surfaces in Fe(II) rich environments.

* Tanwar K. S., Petitto S. C., Ghose S. K., Eng P., and Trainor T. (2008) Fe(II) adsorption on hematite(0001), *Prepared for submission to Geochim. Cosmochim. Acta.*

5.1 INTRODUCTION

Iron (hydr)oxides are abundant in many geochemical systems and play an important role in controlling transport and bio-availability of nutrients and environmental contaminants, primarily due to adsorption and co-precipitation processes (Cornell and Schwertmann, 1996; Stumm and Sulzberger, 1992). The biogeochemical cycling of Fe is also strongly influenced by iron (hydr)oxides via the redox couple connecting solid-phase ferric (hydr)oxides and soluble Fe(II) (Cornell and Schwertmann, 1996; Stumm and Sulzberger, 1992; Sulzberger et al., 1989). Under anoxic conditions, aqueous Fe(II) is generally released by reductive dissolution of ferric oxides promoted by dissimilatory iron reducing bacteria (DIRB) (Hansel et al., 2003; Lovley, 1991; Lovley, 1993; Roden, 2006; Roden and Zachara, 1996; Zachara et al., 1998). The interaction of aqueous Fe(II) with iron (hydr)oxide surfaces has a significant impact on both their stability and reactivity. For example, the co-existence of aqueous and adsorbed Fe(II) can result in inhibition of microbially promoted reduction of iron (hydr)oxides (Liu et al., 2001; Roden and Urrutia, 2002; Roden and Zachara, 1996; Royer et al., 2004). The adsorption of Fe(II) can also lead to formation of an Fe(II)/Fe(III) mixed valence surface (Coughlin and Stone, 1995) and/or the growth of the substrate in a preferred crystallographic direction (Chun et al., 2006; Yanina and Rosso, 2008). Interactions of Fe(II) with ferric oxides is also known to induce bulk phase transformations depending upon Fe(II)/Fe(III) molar ratio (Hansel et al., 2005; Tamaura et al., 1983; Tronc et al., 1992), pH (Jeon et al., 2003) and structure of the iron (hydr)oxide substrate (Pedersen et al., 2005).

The presence of aqueous Fe(II) can also result in significant enhancement of reduction rates for a number of organic (Amonette et al., 2000; Charlet et al., 1998b; Elsner et al., 2004a; Elsner et al., 2004b; Pecher et al., 2002; Tobler et al., 2007a; Tobler et al., 2007b) and inorganic (Buerge and Hug, 1999; Charlet et al., 1998a; Eary and Rai, 1989; Fredrickson et al., 2004; Liger et al., 1999) contaminants in systems containing ferric (hydr)oxide substrates. Furthermore, rates of contaminant reduction have been found to increase with increases in the amount of adsorbed Fe(II), suggesting that Fe(II) adsorption plays a central role in catalyzing contaminant reduction (Amonette et al., 2000; Charlet et al., 1998b). However, the understanding of how Fe(II) associates with the iron (hydr)oxide surfaces is not very well developed. The conceptual picture of Fe(II) sorption has been mostly developed via modeling macroscopic uptake data using surface complexation models (Charlet et al., 1998b; Coughlin and Stone, 1995; Hiemstra and van Riemsdijk, 2007; Liger et al., 1999; Silvester et al., 2005; Zhang et al., 1992). While this approach provides insight into the sorption energetics, it has limited ability to discern the structure and binding mode of the adsorbed Fe(II), and therefore cannot provide a detailed assessment of the relationship between substrate surface structure and reactivity with respect to Fe(II) sorption.

Recent work also suggests that Fe(II) reaction with ferric (hydr)oxides is more complex than a simple surface complexation process. Mossbauer spectroscopy studies have shown that adsorbed Fe(II) is oxidized to Fe(III) via interfacial electron transfer with the underlying iron (hydr)oxide substrate (Larese-Casanova and Scherer, 2007; Silvester et

al., 2005; Williams and Scherer, 2004). The mobility of the electron transferred from adsorbed Fe(II) to the iron (hydr)oxide substrate has been suggested to be strongly influenced by the coordination geometry of the donor Fe(II) and the surface structure of the acceptor substrate (Kerisit and Rosso, 2006; Kerisit and Rosso, 2007; Yanina and Rosso, 2008). The results of these studies clearly emphasize that knowledge of Fe(II) binding geometry is essential for understanding the complete picture of the structural modification of iron (hydr)oxides (and/or their surfaces) in anoxic/Fe(II) rich environments.

The current study utilizes single crystal hematite (α -Fe₂O₃) (0001) as a model system for detailed experimental analysis of Fe(II) adsorption on iron (hydr)oxide surfaces. This study complements and builds upon our recent analysis of the structure of adsorbed Fe on α -Fe₂O₃(1 $\bar{1}$ 02) using synchrotron based crystal truncation rod (CTR) X-ray diffraction (Tanwar et al., 2008). The results of this previous study indicate that the adsorbed Fe binds at crystallographic lattice sites on the α -Fe₂O₃(1 $\bar{1}$ 02) surface. The adsorbed Fe was found to be octahedrally coordinated with five bonds to the surface (hydr)oxo groups and one terminal Fe-O bond, presumably to hydroxo or aquo group (Tanwar et al., 2008). In this manuscript, we present the structural analysis of Fe(II) adsorbed on α -Fe₂O₃(0001). Previous work on the surface structure of α -Fe₂O₃(0001) and our approach for determining structure of adsorbed Fe is discussed in the next section.

5.1.1 α -Fe₂O₃(0001) Surface Structure

The bulk crystal structure of α -Fe₂O₃ has been previously described by Finger and Hazen (1980). The unit cell parameters for α -Fe₂O₃ (space group $R\bar{3}c$) are, $a = 5.035 \text{ \AA}$ and $c = 13.747 \text{ \AA}$. The bulk terminated α -Fe₂O₃(0001) surface can have three chemically distinct terminations, including an Fe-layer (Fe-O₃-Fe-R) termination, an O-layer (O₃-Fe-Fe-R) termination and a double Fe-layer termination (Fe-Fe-O₃-R) as displayed in Figure 5.1. The above notation uses the top three atomic layers to uniquely identify the given surface termination and R represents the continuation of the bulk atomic layer stacking sequence.

The structure of the α -Fe₂O₃(0001) surface has been shown to depend strongly on the surface preparation and experimental conditions. Exposure to oxygen at high ambient pressure (1 mbar at $T \sim 1100 \text{ K}$) during the formation of α -Fe₂O₃(0001) films on Pt(111) substrate resulted in a surface consistent with the O-layer termination (O₃-Fe-Fe-R) (Ketteler et al., 2001; Shaikhutdinov and Weiss, 1999), while oxygen pressures of 10^{-4} - 10^{-1} mbar (at $T \sim 1100 \text{ K}$) lead to formation of two surface domains in roughly equal proportions; an O-layer termination domain and an Fe-layer termination domain (Shaikhutdinov and Weiss, 1999). At same temperature and at low oxygen pressure (i.e. 10^{-5} mbar) the surface was predominantly an Fe-layer termination (Shaikhutdinov and Weiss, 1999). These experimental results are consistent with density functional theory (DFT) based thermodynamic calculations, which suggest that the Fe-layer termination and O-layer termination are the most stable surfaces at low and high oxygen chemical potentials, respectively, and that the co-existence of an Fe-layer termination and an O-

layer termination is likely at intermediate oxygen chemical potentials (Wang et al., 1998). However, $\alpha\text{-Fe}_2\text{O}_3(0001)$ grown on $\alpha\text{-Al}_2\text{O}_3(0001)$ substrate using molecular beam epitaxy (MBE) was found to have a surface structure consistent with an Fe-layer termination at low oxygen pressure (1.33×10^{-6} mbar) (Chambers and Yi, 1999; Thevuthasan et al., 1999), which remained stable even after cooling to room temperature under highly oxidizing oxygen plasma (Chambers and Yi, 1999).

More recently, the DFT based thermodynamic calculations of Bergermeyer et al. (2004) suggested a possible ferryl termination for $\alpha\text{-Fe}_2\text{O}_3(0001)$ surface ($\text{O}=\text{Fe}-\text{O}_3\text{-Fe-R}$), which was not considered in prior studies. Lemire et al. (2005) also suggest that the ferryl termination, possibly co-existing with Fe terminated domains, is the most stable surface under highly oxidizing conditions on $\alpha\text{-Fe}_2\text{O}_3(0001)$ films grown on Pt(111) substrate (Lemire et al., 2005). A possible reversible conversion of an Fe-layer termination to a ferryl termination due adsorption and desorption of oxygen has been proposed by Jarvis and Chaka (2007). In comparison, recent experimental work on natural single crystals of $\alpha\text{-Fe}_2\text{O}_3(0001)$ suggest that the surface stoichiometry is consistent with the O-layer termination at 573 K and an oxygen pressure of 10^{-7} - 10^3 mbar (Barbier et al., 2007), while at a temperature of 773 K, the ferryl termination was observed at oxygen pressures in range of 10^{-6} - 10^3 mbar (Barbier et al., 2007).

In systems that contain water as a component an additional range of potential surface structures/stoichiometries must be considered. The $\alpha\text{-Fe}_2\text{O}_3(0001)$ is known to

hydroxylate at water vapor pressures greater than 10^{-4} Torr (Liu et al., 1998). Recent DFT studies have proposed that the heterolytic dissociation of water is the preferred mechanism of surface hydroxylation for an Fe-layer termination of $\alpha\text{-Fe}_2\text{O}_3(0001)$ (Trainor et al., 2004; Yin et al., 2007). Under aqueous conditions, the scanning tunneling microscopy (STM) study of natural $\alpha\text{-Fe}_2\text{O}_3(0001)$ by Eggleston et al. (2003) showed that two chemically distinct structural domains were present on the $\alpha\text{-Fe}_2\text{O}_3(0001)$ surface. A previous CTR and DFT study of the hydroxylated $\alpha\text{-Fe}_2\text{O}_3(0001)$ surface also resulted in a model with two chemically distinct structural domains; these were identified as the hydroxylated Fe-layer termination ($((\text{OH})_3\text{-Fe-O}_3\text{-Fe-R})$) and hydroxylated O-layer termination ($((\text{OH})_3\text{-Fe-Fe-R})$) (Trainor et al., 2004). In the current study, we have employed CTR diffraction to determine the structure of the $\alpha\text{-Fe}_2\text{O}_3(0001)$ surface prepared via wet chemical and mechanical polishing (CMP). The CMP prepared $\alpha\text{-Fe}_2\text{O}_3(0001)$ surface was then reacted with Fe(II) followed by CTR data collection and structural analysis. The structures of unreacted and Fe(II) reacted surfaces were directly compared to identify the adsorbed Fe on the $\alpha\text{-Fe}_2\text{O}_3(0001)$ surface.

5.2 METHODS

5.2.1 Sample Preparation

All experiments were conducted on a natural single crystal of specular hematite which was obtained from Bahia, Brazil. The sample, of dimensions approximately $1\text{ cm} \times 1\text{ cm}$, was polished along (0001) growth face. For CTR measurements on the unreacted $\alpha\text{-Fe}_2\text{O}_3(0001)$, the sample was prepared using a chemical and mechanical polishing (CMP)

procedure as described in Tanwar et al. (2007b). Following the CMP procedure, the sample was etched in 0.01 N HNO_3 for 2 h and then thoroughly rinsed with ultra-pure ($> 18 \text{ M}\Omega$) water. This sample preparation and cleaning procedure results in high quality surfaces (low roughness) suitable for CTR data collection (Tanwar et al., 2007b; Trainor et al., 2004). CTR measurements on the unreacted sample were carried out in a sample cell that maintained a He gas environment with water vapor at near saturation ($> 90\%$ relative humidity at $\sim 25^\circ\text{C}$) as described below.

Following data collection, the unreacted sample was removed from the cell and again thoroughly washed using ultra-pure ($> 18 \text{ M}\Omega$) water. The sample was then reacted with 4 mM Fe(II) at $\text{pH } 5.0 \pm 0.2$ for 2 h at room temperature under strict anoxic conditions. The Fe(II) solutions were prepared using de-oxygenated ultra-pure water ($>18 \text{ M}\Omega$) and ferrous chloride tetra-hydrate ($\text{FeCl}_2 \cdot 4\text{H}_2\text{O}$) purchased from VWR ($> 99\%$ purity). The anoxic conditions were maintained using a N_2 glove box. Our previous work shows that 4 mM Fe(II) will remain stable for more than 24 h under the employed conditions (Tanwar et al., 2008). After the reaction period, the sample was washed with ultra-pure water and immediately placed back in the sample cell under hydrated He environment for CTR data collection.

5.2.2 CTR Data Collection

All CTR measurements were conducted at the Advanced Photon Source (APS) on undulator beamline 13-IDC using a $2 + 2 + \text{kappa}$ -geometry Newport diffractometer for

sample orientation and scanning. The diffractometer is equipped with a sample cell that allows for controlling the environmental conditions (liquid or gas) in contact with the exposed surface during data collection (Trainor et al., 2006). For our experiments, a near water-saturated He atmosphere (relative humidity > 90%, p_{H_2O} > 20 Torr) at room temperature was maintained in the sample cell in order to ensure the sample remains fully hydrated during the course of CTR measurements (Liu et al., 1998). The incident beam energy was tuned to 12 keV using a liquid N₂ cooled double crystal Si(111) monochromator. The X-ray beam was focused on the center of the diffractometer to a beam size of 0.26×1.50 mm (horizontal \times vertical) using two Rhodium (Rh) coated Si mirrors. X-ray scattering intensity was measured using a 100k Pilatus pixel array detector with an energy threshold set for individual pixels to reject Fe fluorescence counts (Schlepütz et al., 2005). To collect non-specular rods the incident angle was fixed at 2° and rocking scans through the truncation rods were performed using a continuous (trajectory) scan of the diffractometer ϕ -axis at a particular reciprocal lattice setting. Specular rods were collected by scanning the diffractometer ω -axis with the direction of sample miscut ($< 0.4^\circ$) oriented in the scattering plane to ensure collection of all CTR intensity.

The magnitudes of individual structure factors ($|F_{HKL}|$) at each (HKL) value were determined by taking square root of background subtracted intensity of the rocking curves and correcting for active area, polarization, step size and Lorentz factors (Robinson, 1991). In the notation used above, the reciprocal vector indices H and K

correspond to in-plane momentum transfer and L corresponds to perpendicular momentum transfer. The data was averaged in the p_3 plane group. The full data set consisted of six crystal truncation rods for both the unreacted and the Fe(II) reacted α -Fe₂O₃(0001) surface with a total of 1013 and 945 unique structure factors for each respective data set. A subset of the data set was repeated periodically to check for beam induced surface damage; these repeats showed no intensity changes during the course of measurements indicating the surfaces were stable during data collection. Following CTR data collection, we also conducted grazing incidence powder X-ray diffraction (GI-XRD) measurements on the Fe(II) reacted sample to determine if any ordered surface precipitates and/or textured overlayer had formed as a result of Fe(II) adsorption. Similar to CTR measurements, GI-XRD experiments were also conducted under a hydrated He environment.

5.2.3 CTR Data Analysis

The CTR data was analyzed using a non-linear least squares fitting routine with fixed bulk and adjustable surface models (Robinson, 1986; Trainor et al., 2002; Vlieg, 2000; Vlieg et al., 1989). The fit parameters include atomic displacements in x , y and z directions, atomic occupancies, Debye-Waller factors, and an overall roughness factor as derived by Robinson (1986). The possible atomic positions of H atoms cannot be determined from the CTR measurements due to their small X-ray scattering cross-section and therefore, were not included in the analysis. In order to reduce the number of fitting parameters, the atoms in each atomic layer of the surface cell (along z -direction) were

constrained to maintain the same z-displacements, occupancies and Debye-Waller factors. The p3 surface symmetry was maintained by fixing the in-plane coordinates of the Fe atoms (at their bulk positions) and constraining the displacement of the oxygen atoms within a given layer in order to maintain the in-plane trigonal symmetry. The in-plane displacements were allowed for top 3 oxygen layers of the surface and z-displacements were not allowed below layer 12 of the surface unit cell. The Hamilton's R-ratio test was used to compare the fit quality between different models (Hamilton, 1965). An independent check of the chemical plausibility of structural models was performed by conducting a bond valence analysis, where a bond valence sum considerably higher than the magnitude of formal valence for any ion indicates over-saturation and vice versa (Pauling, 1960). The bond valence sums were calculated using the bond length - bond strength relationships provided by Brown and Altermatt (1985). The possible bond valence contribution of H atoms and hydrogen bonding were not included in the bond valence analysis.

5.3 RESULTS

5.3.1 α -Fe₂O₃(0001) Surface Structure

Previous studies of the hydrated α -Fe₂O₃(0001) have indicated the co-existence of chemically distinct surface structural domains (Eggleston et al., 2003; Trainor et al., 2004). The relative proportions of distinct domains and/or the presence of a single dominant chemical domain likely depends strongly on the surface preparation conditions (Tanwar et al., 2007a), and chemical environment of the surface system (Wang et al.,

1998; Chambers and Yi, 1999; Shaikhutdinov and Weiss, 1999; Eggleston et al., 2003; Bergermeyer et al., 2004; Trainor et al., 2004; Lemire et al., 2005; Barbier et al., 2007). Therefore, prior to analysis of the Fe(II) reacted surface it was essential that the surface structure of sample under consideration, following the preparation procedure described above, be identified. In the analysis of freshly prepared “unreacted” surface we did not preclude the possibility of the α -Fe₂O₃(0001) surface being dominated by a single structural domain and therefore conducted initial structural refinements using single domain surface models.

5.3.1.1 Single domain analysis

As discussed above, the α -Fe₂O₃(0001) surface can have three chemically distinct terminations; an Fe-layer (Fe-O₃-Fe-R), an O-layer (O₃-Fe-Fe-R), and a double Fe-layer termination (Fe-Fe-O₃-R) (Figure 5.1). According to the symmetry of the surface unit cell, there are six equally probable but crystallographically distinct choices for terminating the unit cell for each chemical termination. This was accounted for in the structural analysis by calculating the final structure factor as a weighted sum of the structure factor magnitudes of each symmetry equivalent surface.

The CTR data was initially analyzed using single domain models where all of the three chemically distinct terminations were examined individually as the starting point of the analysis. We note the surface Fe atoms on the Fe-layer termination (i.e. Fe-O₃-Fe-R) and the double Fe-layer termination (Fe-Fe-O₃-R) are under coordinated (three Fe-O bonds)

relative to the bulk hematite structure (six Fe-O bonds for each Fe) (Figure 5.1). As shown in previous studies, the coordination shell of surface Fe atoms is likely to be completed by hydroxyls and/or adsorbed water under hydrated conditions (Catalano et al., 2007; Tanwar et al., 2007a; Tanwar et al., 2007b; Trainor et al., 2004). Therefore, to each of the chemically distinct terminations we added oxygen atoms at initial positions consistent with six-fold coordination of the surface Fe sites, presumably modeling surface oxo-, hydroxo- or aquo groups present at the mineral surface. The positions, occupancy factors and Debye-Waller parameters of the added oxygens were then refined in the analysis.

The only model that produced a reasonable fit to the experimental data ($\chi^2 = 1.97$) was consistent with a hydroxylated Fe-layer termination where the surface Fe layer was partially occupied. The Fe/O stoichiometry of this model can be expressed as **O**_{3y}-Fe_x-O₃-Fe-R, where x and y represent occupancy of given atomic layers (Figure 5.2 and 5.3). In the notation used above, the O atoms shown in the bold face represent those that were added to the surface unit cell to account for the surface hydroxylation. Inclusion of an additional adsorbed water layer to the above model had insignificant effect on surface relaxations and did not result in a statistically significant improvement in the fit (at 95% confidence interval) based on Hamilton's R-ratio test. Therefore adsorbed water layers were not included in the final structural model. The atomic coordinates and the best fit model parameters are provided in Table 5.1. The Fe-O bond lengths in the best fit model

were in the range of 1.94 Å - 2.12 Å, which are comparable (within errors) to Fe-O bond lengths in the bulk hematite structure (i.e. 1.95 Å and 2.11 Å).

The best fit single domain model yields an occupation factor of $x = 0.44 \pm 0.02$ for the top Fe layer (i.e., layer 1 in Figure 5.3) as indicated by occupancies listed in Table 5.1. The occupancy of the first Fe layers is consistent within errors to the occupancy $y = 0.52 \pm 0.08$ of the layer i oxygen (Figure 5.3), consistent with the surface exposed Fe layer in six-coordination (layer 1 in Figure 5.3). The observation of partial occupancy in the top Fe layer is qualitatively consistent with the single domain analysis of a previous CTR study where the corresponding Fe layer was reported to be $40 \pm 2\%$ occupied (Trainor et al., 2004). In this previous study, a second model was also considered in which the surface was assumed to consist of two distinct chemical domains. In the two domain analysis, the first domain was taken to be consistent with a hydroxylated Fe-layer termination where the top Fe layer is fully occupied, and a second domain that can be described as an O-layer termination where the corresponding Fe layer is absent as shown in Figure 5.4 (Trainor et al., 2004). This two domain model was shown to provide an equally good fit to the data as the single domain model and was consistent with the STM work of Eggleston et al. (2003) that shows the hydroxylated $\alpha\text{-Fe}_2\text{O}_3(0001)$ surface consists of two chemically distinct structural domains. Based on the results from previous studies, it appears likely that the partial occupancy of the topmost Fe layer (layer 1 in Figure 5.3) in the current study may also be a result of the co-existence of two chemically distinct domains (i.e., hydroxylated Fe-layer and O-layer termination).

Therefore, we further analyzed the CTR data using structural models that explicitly account for this co-existence assumption.

5.3.1.2 Two domain structural analysis

Based on the results discussed above, the two structural domains (and their symmetry related chemically equivalent surface models) included in the analysis were the O-layer ($\text{O}_3\text{-Fe-Fe-R}$) and hydroxylated Fe-layer ($\text{O}_3\text{-Fe-O}_3\text{-Fe-R}$) terminations. The CTR data analysis using the two domain structural models was conducted following the approach described previously by Trainor et al. (2004). In this method, an additional fit parameter was included to analyze the fraction of the surface covered by each structural domain where the sum of surface fractions of the two domains is constrained to unity. The structural refinement was carried out using two approaches: (1) coherent (or in-phase) summation of calculated structure factors from each domain, which implies that domain sizes are significantly smaller than the coherence length of X-rays, and (2) by performing incoherent summation (i.e., sum of magnitudes) of calculated structure factors from each domain, which assumes that domain sizes are larger than the coherence length of X-rays.

During CTR data analysis, the models using an incoherent summation did not provide reasonable fits to the experimental data while the models using a coherent summation did show good fits. These results indicate the domain sizes are significantly smaller than coherence length of X-rays (on the order of hundreds of nanometers), which is in agreement with previous STM observations of domain sizes on the $\alpha\text{-Fe}_2\text{O}_3(0001)$

surface that are on the order of tens of nanometers (Eggleston et al., 2003). Therefore, the models discussed below were refined using the coherent summation approach.

Initially, the CTR data analysis was conducted using independent displacement parameters for atoms in both of the above discussed structural domains. However, the displacements for atoms in layers 2 to 12 of the O-layer termination (Figure 5.4a) were similar (within errors) to the displacements of atoms in layers 2 to 12 of the hydroxylated Fe-layer termination (Figure 5.4b). Therefore, to reduce the number of parameters the atomic relaxations for layers 2 to 12 in the hydroxylated Fe-layer termination were constrained to maintain the same relaxations as the atoms in layers 2 to 12 of O-layer termination. The two domain structural analysis using this approach resulted in a good fit to the data ($\chi^2 = 1.98$) with domain ratios of 0.54 ± 0.02 and 0.46 ± 0.02 for the O-layer and hydroxylated Fe-layer terminations, respectively.

Further analysis led us to observe that the fit improved, particularly on the (00L) rod, when one additional water layer was included for each domain (with independent fit parameters). The Debye-Waller factors for the included water layers were relatively high (i.e. 1.5 - 2.0) and their in-plane positions are poorly constrained suggesting they are only weakly contributing to the overall CTR data. In addition, their inclusion did not significantly affect the surface relaxations but did result in a statistically significant reduction in the reduced chi-squared value ($\chi^2 = 1.66$) at the 95% confidence interval. The addition of more water layers to the model had insignificant effect on the fit quality.

Consequently, the best-fit two domain model ($\chi^2 = 1.66$) consists of one water layer for each of the two structural domains (Figure 5.2 and 5.4). The best-fit model parameters are provided in Tables 5.2 and 5.3. This model yields a surface fraction of 0.54 ± 0.02 for the O-layer termination and 0.46 ± 0.02 for the hydroxylated Fe-layer termination domain. All the Fe-O bond lengths in the best fit model were in the range 1.94 - 2.13 Å for both structural domains except for the terminal Fe-O bond length on the hydroxylated Fe-layer termination, which was 2.18 ± 0.01 Å. The oxygen atoms of the water layer (layer i in Figure 5.4a, and layer ii in Figure 5.4b) were at a distance of 2.29 ± 0.02 Å and 3.0 ± 0.3 Å from the surface oxygen atoms of the O-layer and the hydroxylated Fe-layer termination, respectively. The O-O distance of the water layers is in the range 2.5 - 3.1 Å, where the shortest O-O distance is 2.8 ± 0.1 Å (for layer i in Figure 5.4a) and 2.5 ± 0.6 Å (for layer ii in Figure 5.4b) for O-layer and hydroxylated Fe-layer termination, respectively. These in-plane O-O distances are consistent with hydrogen bonded water molecules, however, the precise location, particularly the in-plane positions of the water layers are poorly constrained by the analysis due to their weak influence on the fit, particularly the in-plane rods.

In comparison to the single domain model ($\chi^2 = 1.97$), the two domain model resulted in a better fit especially on the (00L) rod (Figure 5.2), and the improvement in fit was statistically significant (at 95% confidence interval) based on Hamilton's R-ratio test (Hamilton, 1965). The improvement in the fit on the (00L) rod can be attributed to

inclusion of the contribution of the two water layers (one for each domain) which could not be properly accounted for in a single domain analysis using a single adsorbed water layer. Based on the results of the two domain analysis, the partial occupancy of the Fe layer in single domain analysis can be reasonably attributed to the presence of two chemically distinct structural domains on the surface. The present results are also consistent with previous research (Eggleston et al., 2003; Trainor et al., 2004) which suggests that two distinct chemical domains likely co-exist on the hydrated α -Fe₂O₃(0001) surface. On the CMP prepared α -Fe₂O₃(0001) surface analyzed here, the first domain is consistent with O-layer termination ($54 \pm 2\%$) with an Fe/O stoichiometry of O₃-Fe-Fe-R and the second domain can be described as a hydroxylated Fe-layer termination ($46 \pm 2\%$) with an Fe/O stoichiometry of O₃-Fe-O₃-Fe-R (Figure 5.4).

5.3.2 Structure of Fe(II) Reacted α -Fe₂O₃(0001)

A comparison of the CTR data for the Fe(II) reacted vs. the unreacted α -Fe₂O₃(0001) surface shows distinct changes in CTR profile after exposing the surface to aqueous Fe(II) (Figure 5.5). For example, there is a shift in the position of an anti-node feature between (HKL) of (0 0 2) and (0 0 4) (Figure 5.5). Such anti-node features in CTR data are highly sensitive to surface termination and a shift in their position is usually indicative of surface structure modification (Fenter and Park, 2004). Therefore, the observed changes in the CTR data profile indicate that the α -Fe₂O₃(0001) surface structure is modified due to Fe(II) adsorption. To identify the structural modification, the CTR data was analyzed

using the approach discussed above for the unreacted surface, where both single and two domain structural models were considered.

5.3.2.1 Single domain models of Fe(II) adsorption

Our previous work on Fe(II) adsorption on $\alpha\text{-Fe}_2\text{O}_3(1\bar{1}02)$ surface shows that adsorbed Fe binds at crystallographic lattice sites, and we consider a similar case here for Fe(II) adsorption on the $\alpha\text{-Fe}_2\text{O}_3(0001)$ surface. As discussed in section 3.1.1, the single domain model for the unreacted surface has a partially occupied top Fe layer. After exposure to Fe(II), the occupancy of the partially filled Fe layer (layer 1 in Figure 5.3) would likely increase due to Fe adsorption at previously vacant lattice sites. However, the models that accounted for the increased occupancy of Fe layer as the only possible adsorption sites (sites A in Figure 5.7) did not produce reasonable fits to the experimental data. Therefore, we included in the analysis additional Fe atoms allowing their x, y and z coordinates to vary. Interestingly, the in-plane coordinates of the added Fe atoms were refining to positions that were similar to bulk Fe sites indicating the Fe(II) adsorption is predominantly occurring at crystallographic lattice sites. Therefore, for further structural refinement we fixed the in-plane coordinates of added Fe layer(s) to be same as in-plane positions of bulk Fe sites.

The only model that resulted in a good fit ($\chi^2 = 1.02$) (Figure 5.6) consisted of two additional adsorbed Fe layers (labeled as sites B and C in Figure 5.7), both of which correspond to bulk Fe site positions (based on in-plane coordinates). In this refinement,

the occupancy of the layer 1 Fe (sites A in Figure 5.7) is $75 \pm 2\%$, which is higher in comparison to the unreacted surface ($44 \pm 2\%$). The additional Fe adsorption sites B and C were $47 \pm 2\%$ and $29 \pm 2\%$ occupied, respectively (Table 5.4). We note that an additional oxygen layer (i.e. layer iv in Figure 5.7) was also required to obtain a reasonable fit. The occupancy of this additional oxygen layer ($25 \pm 6\%$) is consistent, within errors, with the occupancy of surface bound Fe at site C (Table 5.4). Furthermore, inclusion of this additional oxygen layer resulted in a surface model where all the Fe atoms are six-coordinated (Figure 5.7 and Table 4). The inclusion of adsorbed water layers did not result in a significant improvement in fit quality and hence, were not included in the analysis.

The single domain analysis suggests that Fe adsorption results in (partial) occupancy of three distinct atomic layers A, B and C on the $\alpha\text{-Fe}_2\text{O}_3(0001)$ surface (Figure 5.7). We note the above discussed model is crystallographically indistinguishable from a model where B and C adsorption sites (i.e. layers i and iii) are removed and the Fe in layers 1, 3 and 4 are partially occupied (the symmetry of $\alpha\text{-Fe}_2\text{O}_3(0001)$ results chemically equivalent terminations when the crystal termination is shifted by an integer factor of $c_s/6$). Since the layers 1, 3, and 4 were completely occupied in the unreacted surface, a decrease in their occupancy after Fe(II) exposure would indicate dissolution of Fe from the surface unit cell. However, the dissolution of hematite under employed reaction conditions (reaction time of 2 h at pH 5) is unlikely based on previous Fe(II) adsorption studies on hematite single crystals (Tanwar et al., 2008) and colloidal hematite (Jeon et

al., 2001), where uptake of Fe(II) has been observed for up to 34 days and 30 days, respectively. In addition, a recent study also shows uptake of Fe(II) on an α -Fe₂O₃(0001) surface at pH 2-3 (reaction time of 12 h at temperature of 348 K) (Yanina and Rosso, 2008). Therefore, we believe the observation of partial occupancies for adsorbed Fe at sites A, B and C (Figure 5.7) is consistent with adsorption of Fe(II) from solution onto these sites. Furthermore, Yanina and Rosso (2008) observed growth of hematite on the α -Fe₂O₃(0001) surface after exposure to Fe(II) for 12 h at pH 2-3 in presence of oxalate (at 348 K). The conditions employed in their study resulted in a relatively rapid growth of the (0001) surface (Yanina and Rosso, 2008). In comparison, the experimental conditions used in the current study are more consistent with sub-monolayer levels of Fe(II) uptake (Tanwar et al., 2008; Jeon et al., 2001).

Based on the results from single domain analysis, the Fe/O stoichiometry of the surface after Fe(II) exposure can be expressed as **O_{3e}-Fe_d-O_{3c}-Fe_b-Fe_a-O₃-Fe-R**, where atoms shown in bold face represent those added to surface unit cell, and the subscripts denote occupancy of a given layer (Table 5.4). The single domain structural model shows a good fit to the data and suggests the adsorption of Fe is occurring at crystallographic lattice sites. However, this model suggests that there are multiple adsorbed Fe layers partially occupied. For example, Fe occupies the B sites before completely filling vacant A sites (Figure 5.7). Similarly, Fe adsorption on C sites is observed with B type sites partially occupied (Figure 5.7).

The partially occupied adsorbed Fe layers resulting from the single domain analysis can be interpreted as a highly defective $\alpha\text{-Fe}_2\text{O}_3(0001)$ surface (due to vacancies in top three Fe layers). On the other hand, these results can also be arising from the formation of clusters of adsorbed Fe covering only a certain fraction of the surface and thus resulting in partial occupancy. We note that the single domain analysis cannot distinguish between random site occupancy of adsorbed Fe layers and sorption leading to clustering (or formation of islands). If there is formation of clusters/islands associated with Fe(II) adsorption, the resulting surface can also be described using a two domain surface model. Additionally, as discussed in section 3.1.2, the unreacted surface is also likely consisting of two chemically distinct structural domains. Therefore, it is important to explore the possibility of a two domain surface model for Fe(II) reacted $\alpha\text{-Fe}_2\text{O}_3(0001)$ surface.

5.3.2.2 Two domain models of Fe(II) adsorption

The two domain analysis of the CTR data for the Fe(II) reacted $\alpha\text{-Fe}_2\text{O}_3(0001)$ was initiated using the model obtained for the unreacted surface that consisted of the O-layer and hydroxylated Fe-layer terminations (Table 5.2 and 5.3 respectively, Figure 5.4). The structural analysis was again performed using coherent summation of structure factors from the two domains because incoherent summation did not provide good fits to the data. To account for Fe(II) adsorption, the Fe atoms were initially added to the two domain surface models at crystallographic lattice sites based on the findings from the single domain analysis discussed above.

The first model considered is that of Fe adsorption on the O-layer termination at sites chemically (and crystallographically) equivalent to the top Fe layer of the Fe-layer termination (i.e. sites A in Figure 5.8a which are equivalent to layer 1 Fe in Figure 5.4b). Sorption at these sites (i.e. A in Figure 5.8a) is considered likely since it would result in highly coordinated surface bound species, where the adsorbed cation lies above the structural cation vacancy in the layer below, and hence would be assumed to be a favorable site due to minimal cation-cation repulsion. This model would simply result in a conversion of a fraction of the O-layer termination to the hydroxylated Fe-layer termination domain. This would imply that sorption results in complete site occupancy within localized regions, and hence non-uniform sorption (i.e. clustering). Alternatively, if sorption occurred at these sites randomly, the Fe adsorption can be modeled as partial occupancy of Fe bound at sites A of Figure 5.8a with the surface fractions held fixed at the values from the unreacted two domain analysis. In either case, complete site filling on the original O-layer termination would result in a single domain hydroxylated Fe-termination surface model. Refinements based solely on varying the surface fraction of the two domains (as well as allowing atomic layer relaxations) with the individual site occupancies fixed did not result in a satisfactory fit to the experimental data. Similarly, allowing the occupancies of sites A (Figure 5.8a) to vary with fixed surface fractions did not result in a reasonable fit. The unsatisfactory fits using this approach suggest that consideration of Fe adsorption only at sites A (Figure 5.8a) on the O-layer termination is insufficient to describe the changes in surface structure after Fe(II) adsorption. This led

us then to consider Fe adsorption on both the O-layer and the hydroxylated Fe layer terminations.

Considering independent Fe sorption onto both domains leads to a number of possible sorbate geometries (and model parameter sets) that must be considered. In our approach, the surface fraction of each domain was fixed to values which were obtained from CTR data analysis of the unreacted surface (i.e., 0.54 for O-layer and 0.46 for hydroxylated Fe-layer termination). The fixing of fractions leads to the assumption that Fe adsorption is occurring randomly (but independently) at available sites on each domain. To reduce the number of free parameters, the relaxations of layers 2 to 12 in hydroxylated Fe-layer termination were linked to layers 2 to 12 of O-layer termination as discussed in section 3.1.2. Based on the single domain analysis, adsorption sites similar to A, B, and C were considered on both the O-layer and hydroxylated Fe-layer domains. In addition, we included additional oxygen atom positions in the analysis which resulted in six-coordinated Fe species on the surface in agreement with the results of single domain surface model.

The model that resulted in an excellent fit to data ($\chi^2 = 1.01$) was consistent with adsorption of Fe at crystallographic lattice sites. The best fit model suggested that adsorbed Fe is bound at sites A on the O-layer termination (Figure 5.8a) and on the hydroxylated Fe-layer termination both B and C sites were occupied by adsorbed Fe (Figure 5.8b). Adsorbed water layers were not included the model as they did not affect

surface relaxations and resulted in an insignificant improvement in fit. The refinement of this best fit model resulted in Fe adsorption sites (i.e. sites A) on O-layer termination being $48 \pm 4\%$ occupied (Figure 5.8a). The Fe/O stoichiometry of O-layer termination after including adsorbed Fe layer can be expressed as $\mathbf{O}_{3n}\text{-}\mathbf{Fe}_m\text{-O}_3\text{-Fe-Fe-R}$, where atoms shown in bold face denote the atoms that were added to the unit cell to account for adsorbed Fe, and m and n denote their site occupancies. On the hydroxylated Fe-layer termination, the first adsorption layer (i.e. sites B) is fully occupied (Figure 5.8b) and the second adsorbed layer (i.e. sites C) is $53 \pm 4\%$ occupied (Figure 5.8b). The Fe/O stoichiometry for Fe(II) reacted hydroxylated Fe-layer termination can be expressed as $\mathbf{O}_{3b}\text{-}\mathbf{Fe}_a\text{-O}_3\text{-Fe-Fe-O}_3\text{-Fe-R}$, where a, and b denote occupancies of the corresponding atomic layers.

A comparison of the Fe/O stoichiometry of the O-layer and hydroxylated Fe-layer termination after exposure to Fe(II) shows that the chemical environment at the exposed surface of both domains is approximately similar (Figure 5.8). For instance, a partially occupied hydroxylated Fe layer is exposed at the surface of each domain with all subsequent atomic layers are fully occupied (Figure 5.8). Furthermore, the occupancy of exposed Fe layer on both domains differs only by 5%, and are essentially equivalent within error (i.e., sites A $48 \pm 4\%$ on the O-layer and sites C $53 \pm 4\%$ on the hydroxylated Fe-layer termination).

Because of the similarity of occupancies of near surface Fe for both domains, and hence overall surface structures, we performed an additional refinement in which the occupancies and displacements for atoms in chemically similar environment were linked. Therefore, in this analysis the occupancies and displacements of layer **i** on the O-layer termination (Figure 5.8a) is constrained to be similar to layer **iii** on the hydroxylated Fe-layer termination (Figure 5.8b) (i.e. $m = a$, $n = b$ in above stoichiometry). Thus, the Fe/O stoichiometry of the Fe(II) reacted O-layer and hydroxylated Fe-layer terminations are given as $\text{O}_{3n}\text{-Fe}_m\text{-O}_3\text{-Fe-Fe-R}$ and $\text{O}_{3n}\text{-Fe}_m\text{-O}_3\text{-Fe-Fe-O}_3\text{-Fe-R}$, respectively.

The application of the above constraints implies that the reaction of Fe(II) with the two chemically distinct domains results in a convergence to the same stoichiometry, although in the analysis they remain crystallographically distinct. The model with reduced number of fit parameters also resulted in an excellent fit to data ($\chi^2 = 1.07$) (Figure 5.6, and Table 5.5 and 5.6) although the previous fit (with independent parameters for adsorbed Fe layers) was statistically superior (at 95% confidence interval) based on Hamilton's R-ratio test. In terms of discussing the overall reaction however, we prefer the model with the above discussed constraints because it simplifies description of the chemical environment at the exposed surface to a partially filled ($51 \pm 3\%$) hydroxylated Fe layer on both structural domains of $\alpha\text{-Fe}_2\text{O}_3(0001)$ (Figure 5.8, and Table 5.5 and 5.6).

The resulting occupancies (per surface unit cell) of sites A, B and C in the two domain analysis correlate well with the occupancies obtained for these sites via the single domain

analysis (Table 5.4, 5.5, and 5.6). However distributing the adsorbed Fe layers over two domains resolves the concerns highlighted in the single domain model. In particular, the two domain model implies that there are two adsorbed Fe layers on hydroxylated Fe-layer termination (Figure 5.8b). Importantly, the first adsorption layer (sites B) is fully occupied (Figure 5.8b) in the two domain model. This is in contrast to the single domain model where a second adsorption layer was observed even though the first adsorption layer was partially occupied. Overall, the two domain structural analysis results in a chemically more reasonable structure as compared to the single domain model.

5.3.3 GI-XRD Results

The GI-XRD results (not shown) suggest that no crystalline surface precipitates or (incommensurate) ordered surface overlayer formed during the employed reaction time of 2 h at pH 5 (at room temperature). In comparison, a recent study has shown growth of α -Fe₂O₃ over the α -Fe₂O₃(0001) surface as result of Fe(II) reaction for 12 h at pH 2-3 in the presence of oxalate (at a temperature of 348 K) (Yanina and Rosso, 2008). We suspect that no ordered overlayer was formed in the current study due to a difference in employed reaction conditions as compared to the study of Yanina and Rosso (2008). However, we note the GI-XRD measurements conducted in the current study are insensitive to the epitaxial growth of α -Fe₂O₃ overlayer. Therefore, we cannot rule out the possible epitaxial growth of α -Fe₂O₃ on the α -Fe₂O₃(0001) surface, however, as discussed above, the conditions used in the current study were chosen to be consistent with sub-monolayer Fe uptake.

5.4 DISCUSSION

An important result of the current study is the identification of the binding sites and coordination geometry of Fe(II) adsorbed on the α -Fe₂O₃(0001) surface. The CTR results presented above indicate that the unreacted surface consists of two chemically distinct structural domains: an O-layer termination ($54 \pm 2\%$) with an Fe/O stoichiometry of O₃-Fe-Fe-R and a hydroxylated Fe-layer termination ($46 \pm 2\%$) with an Fe/O stoichiometry of **O₃-Fe-O₃-Fe-R** (Figure 5.4). After exposure to aqueous Fe(II), the Fe/O stoichiometry of the O-layer termination is modified due to adsorption of Fe at crystallographic lattice sites (sites A in Figure 5.8a) and can be expressed as **O_{3n}-Fe_m-O₃-Fe-Fe-R**, where $m (= 0.51 \pm 0.03)$ denotes occupancy of the adsorbed Fe (Figure 5.8). The stoichiometry of the hydroxylated Fe-layer termination is also modified to **O_{3n}-Fe_m-O₃-Fe-Fe-O₃-Fe-R** due to inclusion of two adsorbed Fe layers (shown in bold face), again at crystallographic lattice sites (i.e. sites B and C in Figure 5.8b). The first adsorption layer (B site) is fully occupied and the occupancy of the second adsorbed Fe layer (C site) is denoted by $m (= 0.51 \pm 0.03)$.

The structural analysis indicates that the adsorbed Fe is octahedrally coordinated on both the O-layer and the hydroxylated Fe-layer termination (Figure 5.8). The average Fe-O bond length for the adsorbed Fe on O-layer termination (sites A in Figure 5.8a) is 2.05 ± 0.01 Å. On hydroxylated Fe-layer termination, the average Fe-O bond length for the first (sites B in Figure 5.8b) and second (sites C in Figure 5.8b) adsorbed Fe's are 2.02 ± 0.01 Å and 2.05 ± 0.01 Å, respectively. We note these average Fe-O bond lengths are

significantly shorter than typical Fe(II)-O bond lengths (2.14 to 2.18 Å) (Apted et al., 1985; Farges et al., 2004; Jackson et al., 2005; Waychunas et al., 1988; Wilke et al., 2006). However, these average bond lengths are consistent with Fe(III)-O bond lengths in octahedral coordination environments (Apted et al., 1985; Tossell, 1980; Whittaker and Muntus, 1970), and therefore indicate the Fe(II) is likely oxidized to Fe(III) after adsorption on α -Fe₂O₃(0001) surface. The computed bond valence sums for adsorbed Fe are also all within approximately 0.15 v.u. of three (Table 5.5 and 5.6), which provides strong evidence for the oxidation of surface bound Fe(II) to Fe(III).

Previous Mossbauer spectroscopy studies have shown that Fe(II) adsorbed on various ferric (hydr)oxides, including hematite, oxidizes due to interfacial electron transfer between surface bound Fe(II) and the underlying substrate (Larese-Casanova and Scherer, 2007; Silvester et al., 2005; Williams and Scherer, 2004). Therefore, we suggest that the same reaction pathway likely explains our observations; that adsorbed Fe(II) is oxidized via interfacial electron transfer to the substrate. Furthermore, the structural results of the current study (e.g. the bond valence sums in Table 5.5 and 5.6) suggest there is no Fe(II) in the surface unit cell. This result is in agreement with previous theoretical work that has shown the electron transferred due to oxidation of surface Fe(II) is likely to migrate away from the initial donor/acceptor site, potentially getting trapped at under-coordinated Fe sites, such as surface defects, distant to the adsorption site (Kerisit and Rosso, 2006; Kerisit and Rosso, 2007; Yanina and Rosso, 2008). It is also possible that the electron might be trapped at defect sites on the surface or in the bulk, but the insensitivity of the

CTR technique to the molecular scale structure of non-ordered sites (e.g. defects) means that the fate of electron cannot be resolved based on the data presented in the current study.

The recent study of Yanina and Rosso (2008) also suggests that the electron transferred from adsorbed Fe(II) to the substrate is likely to result in enhanced dissolution of the substrate along certain crystallographic directions. These previous results show growth of hematite on the (0001) surface accompanied with dissolution of non (0001) surfaces (Yanina and Rosso, 2008). In the current study, we did not observe the growth of hematite, likely due to relatively milder reaction conditions, but we suggest that our results are representative of incipient reaction of Fe(II) with the α -Fe₂O₃(0001) surface (i.e. Fe(II) adsorption and oxidation resulting in Fe(III) occupying bulk lattice sites).

A comparison of the results of current study with previous results on the structure of adsorbed Fe on α -Fe₂O₃(1 $\bar{1}$ 02) (Tanwar et al., 2008) highlights two similarities. First, the common observation that on both α -Fe₂O₃(0001) and (1 $\bar{1}$ 02) substrates Fe(II) reaction leads to the adsorption of Fe at crystallographic lattice sites. One possible explanation to why lattice sites are preferred on both surfaces is because the adsorption at these sites maximizes the coordination of adsorbed Fe with surface (hydr)oxo groups of the substrate. For instance, the adsorbed Fe is forming five Fe-O bonds with the surface oxygens on α -Fe₂O₃(1 $\bar{1}$ 02) (Tanwar et al., 2008) which is the maximum possible number of bonds with the surface while maintaining a chemically reasonable structure.

Similarly, binding at lattice sites on both structural domains of $\alpha\text{-Fe}_2\text{O}_3(0001)$ also results in maximum possible number of bonds between adsorbed Fe and surface oxo groups (Figure 5.8). Qualitatively, the higher coordination of the adsorbed Fe with the surface oxo groups as compared to other possible binding geometries may maximize the binding energy.

The second qualitative similarity between the Fe(II) reacted $\alpha\text{-Fe}_2\text{O}_3(0001)$ and $(1\bar{1}02)$ surfaces is the occupancy of top Fe layer in the resulting surface structure. The adsorption of Fe(II) on $(1\bar{1}02)$ was observed to reach a plateau after filling approximately half of the available sites resulting in a surface where the top Fe layer is ~50% occupied (Tanwar et al., 2008). Similarly, the reaction of Fe(II) with $\alpha\text{-Fe}_2\text{O}_3(0001)$ is resulting in a surface where the top Fe layer is ~50% filled (Figure 5.8). The observance of half filled surface Fe layer on both surfaces raises an interesting question as to whether there is a thermodynamic (or kinetic) barrier which hinders more than 50% filling of the top Fe layer on hematite surfaces? To answer above question and to explore thermodynamics of Fe(II) adsorption on hematite, we are currently conducting theoretical thermodynamic calculations as a function of topmost Fe layer occupancy on both $\alpha\text{-Fe}_2\text{O}_3(0001)$ and $(1\bar{1}02)$ using ab initio density functional theory (DFT).

Further comparison between the current study and the previous study of Fe(II) adsorption on $\alpha\text{-Fe}_2\text{O}_3(1\bar{1}02)$ surface (Tanwar et al., 2008) suggest that the surface structure of the substrate influences Fe(II) adsorption. For example, only one adsorbed Fe layer was

observed on $\alpha\text{-Fe}_2\text{O}_3(1\bar{1}02)$ surface (Tanwar et al., 2008) whereas multiple adsorbed Fe layers were observed on $\alpha\text{-Fe}_2\text{O}_3(0001)$ (i.e. two adsorbed Fe layers on hydroxylated Fe-termination and one on O-layer termination) (Figure 5.8). The substrate surface structure is also shown to influence the transport of electron injected into the substrate due to oxidation of Fe(II) at the surface (Kerisit and Rosso, 2007). In addition, a previous study reported growth of hematite along $\alpha\text{-Fe}_2\text{O}_3(0001)$ surface coupled with dissolution of surfaces other than (0001) in presence of aqueous Fe(II) and oxalate (Yanina and Rosso, 2008). These results indicate that the structure of adsorbed Fe is strongly influenced by the surface orientation and therefore, surface structure of the hematite substrate.

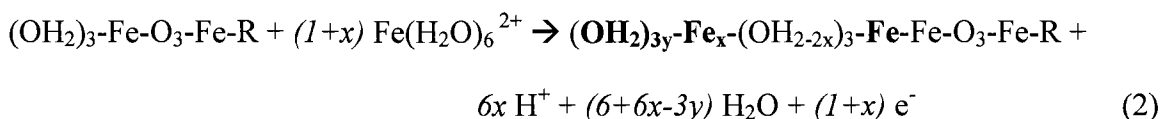
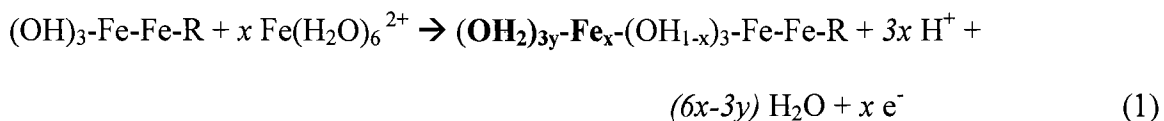
5.5 CONCLUSIONS

In the present study we have used the hydrated $\alpha\text{-Fe}_2\text{O}_3(0001)$ surface as a model system for the structural analysis of Fe(II) sorption to a ferric-oxide substrate. The results show that the CMP prepared (unreacted) hydrated $\alpha\text{-Fe}_2\text{O}_3(0001)$ surface consists of two chemically distinct structural domains; an O-layer termination and a hydroxylated Fe-layer termination (Figure 5.4), consistent with previous studies (Trainor et al., 2004; Eggleston et al., 2003). Reaction with aqueous Fe(II) results in chemical modification of the surface structure due to adsorption of Fe at crystallographic lattice sites (Figure 5.8). There is one adsorbed Fe layer (sites A) on the O-layer termination domain of $\alpha\text{-Fe}_2\text{O}_3(0001)$ which is 51 ± 3 % occupied (Figure 5.8). On the hydroxylated Fe-layer termination there are two adsorbed Fe layers where the first layer (sites B) is fully occupied and the second layer (sites C) is 51 ± 3 % occupied (Figure 5.8). The Fe-O

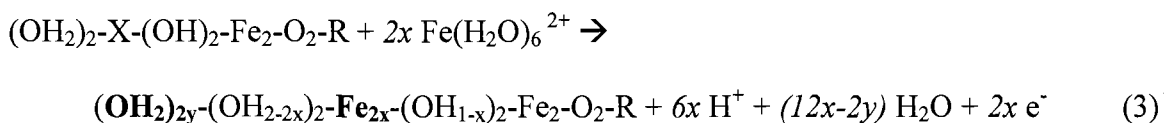
bond lengths determined from our structural analysis indicate that the adsorbed Fe(II) has been oxidized to Fe(III), consistent with the results of previous experimental and theoretical studies of Fe(II)/ferric-(hydr)oxide systems (Yanina and Rosso, 2008; Larese-Casanova and Scherer, 2007; Kerisit and Rosso, 2006; Williams and Scherer, 2004). These findings on the α -Fe₂O₃(0001) surface parallel those of our previous study on the (1 $\bar{1}$ 02) surface (Tanwar et al., 2008), and in both cases Fe(II) reaction leads to surface structure modification. The structural results of Fe(II) adsorption on α -Fe₂O₃(0001) and (1 $\bar{1}$ 02) suggest a different conceptual picture for Fe(II) adsorption than that used in the past modeling studies.

A number of previous surface complexation modeling studies have used a stoichiometry consistent with Fe(II) binding to surface hydroxyl groups in a mono-dentate fashion to analyze Fe(II) sorption behavior on ferric hydroxides (Charlet et al., 1998b; Coughlin and Stone, 1995; Liger et al., 1999; Silvester et al., 2005; Zhang et al., 1992). A recent study by Hiemstra and van Riemsdijk (2007) has considerably advanced the surface comeplexation modeling of Fe(II) adsorption by including multi-dentate adsorption complexes, accounting for Fe(II) oxidation at the surface, and considering reaction sites based on the substrate (i.e. goethite, lepidocrocite and hydrous ferric oxide) structure. However, the results of our current and previous (Tanwar et al., 2008) study show that Fe(II) adsorption (and oxidation) on the α -Fe₂O₃(0001) and (1 $\bar{1}$ 02) surface can be viewed as a modification of the stoichiometry; incorporation of adsorbed Fe at lattice sites results in a surface that remains structurally and compositionally consistent with a

termination of the hematite structure. We can express the reaction stoichiometry for the O-layer and hydroxylated Fe-layer terminations of α -Fe₂O₃(0001) surface as:



On the α -Fe₂O₃(1 $\bar{1}$ 02) surface the reaction stoichiometry can be expressed as:



In the above equations, protons are added to the surface oxo groups based on the assumptions that the valences of oxygen atoms which are singly (^IO) and doubly (^{II}O) coordinated to Fe are completed by adding two and one protons, respectively. Additionally, the triply (^{III}O) coordinated surface oxo groups are not assumed to hydroxylate because addition of a proton to these groups results in over-saturation. We note that these assumptions are consistent with the previous structural studies of hydrated α -Fe₂O₃(1 $\bar{1}$ 02) (Tanwar et al., 2007; Lo et al., 2007). The x and y represent the occupancies of given atomic layers.

The above reactions show that the Fe(II) is oxidized indicating that the reaction must be coupled with a reduction reaction to proceed as written, which is consistent with the

previous experimental and theoretical studies which show that the electrons in the substrate are mobile, and can possibly reduce Fe(III) at defects or relatively unstable surface sites resulting in release of Fe(II) in solution (Yanina and Rosso, 2008; Kerisit and Rosso, 2006). Furthermore, the reactions also show that the resulting surface, while of modified stoichiometry, will presumably provide additional reactive sites for continued reaction consistent with the recent observation of continued growth of the (0001) surface (Yanina and Rosso, 2008). The modified (or product) surface (stoichiometry) may have a substantially different reactivity than the initial surface (stoichiometry). If the conceptual model shown in equations (1-3) is correct, it suggests that the distinction between Fe(II) sorptive behavior and substrate growth is limited by overcoming the (presumably thermodynamic) barrier of uptake on the product surfaces of reactions (1-3). These results may also have significant implications for understanding the binding (and heterogeneous transformations) of other species at the hematite-water interface. As shown reactions (1-3), the substrate in contact with Fe(II) effectively may act as electrode to promote reduction distal to Fe(II) binding site, which may have important implications for understanding mechanism of heterogeneous reductive transformations of contaminants (Williams and Scherer, 2004; Kerisit and Rosso, 2006; Rosso et al., 2003a; 2003b). Further, the chemical modification of the surfaces due to the adsorption of Fe(II) results in a change in the predominant coordination environments of the surface functional groups. For example, the unreacted O-layer termination of α -Fe₂O₃(0001) consists of ^{II}O surface groups, whereas the Fe(II)-reacted O-layer termination is characterized by ^IO and ^{III}O surface oxo groups. The changes in

predominant coordination chemistry is, in turn, likely to impact the overall reactivity of the surface, where for example the ability of a surface hydroxyl to act as an effective ligand in Lewis acid-base type complexation is influenced by the valence contributions from both substrate metals and sorbing species (Bargar et al., 1997) .

Further studies on a wider range of surfaces, substrates and under a wider range of conditions, are needed to determine if the proposed Fe(II) reaction pathways can be extended beyond the limited conditions studied to date. Nevertheless, the current work provides an improved understanding of the possible reaction pathways involved in the incipient reaction of Fe(II) with Fe(III)-(hydr)oxides, and provides structural models that can be used as a basis to understand structure-reactivity relationship for hematite in Fe(II) rich systems.

ACKNOWLEDGEMENTS

The authors acknowledge Christopher Iceman for helpful comments on the results and the manuscript, and Glenn Waychunas for access to the hematite sample. This research was supported by NSF grants CBET-0404400 and CHE-0431425, University of Alaska Fairbanks Graduate Fellowship (K.S.T.), and the Arctic Region Supercomputing Center (University of Alaska Fairbanks). This work was performed at GeoSoilEnviroCARS (Sector 13), Advanced Photon Source (APS), Argonne National Laboratory. GeoSoilEnviroCARS is supported by National Science Foundation - Earth Sciences (EAR-0622171) and Department of Energy - Geosciences (DE-FG02-94ER14466). Use of APS was supported by U.S. Department of Energy, Office of Science, Office of Basic Energy Sciences, under Contract No. DE-AC02-06CH11357.

REFERENCES

- Amonette J. E., Workman D. J., Kennedy D. W., Fruchter J. S., and Gorby Y. A. (2000) Dechlorination of carbon tetrachloride by Fe(II) associated with goethite. *Environ. Sci. Technol.* **34**, 4606-4613.
- Apted M. J., Waychunas G. A., and Brown G. E. (1985) Structure and specification of iron complexes in aqueous solutions determined by X-ray absorption spectroscopy. *Geochim. Cosmochim. Acta* **49**, 2081-2089.
- Barbier, A., Stierle, N., Kasper, N., Guittet, M.-J., and Jupille, J. (2007) Surface termination of hematite at environmental oxygen pressures: Experimental surface phase diagram. *Phys. Rev. B* **75**, 233406/1 - 233406/4.
- Bargar J. R., Brown G. E. Jr., and Parks G. A. (1997) Surface complexation of Pb(II) at oxide-water interfaces: II. XAFS and bond-valence determination of mononuclear Pb(II) sorption products and surface functional groups on iron oxides. *Geochim. Cosmochim. Acta* **61**, 2639-2652.
- Bergermayer, W., Schweiger, H., and Wimmer, E. (2004) Ab initio thermodynamics of oxide surfaces: O₂ on Fe₂O₃(0001). *Phys. Rev. B* **69**, 195409/1 - 195401/12.
- Brown I. D. and Altermatt D. (1985) Bond-valence parameters obtained from a systematic analysis of the inorganic crystal structure database. *Acta Cryst.* **B41**, 244-247.
- Buerge I. J. and Hug S. J. (1999) Influence of mineral surfaces on chromium(VI) reduction by iron(II). *Environ. Sci. Technol.* **33**, 4285-4291.
- Catalano J. G., Fenter P., and Park C. (2007) Interfacial water structure on the (012) surface of hematite: Ordering and reactivity in comparison with corundum. *Geochim. Cosmochim. Acta* **71**, 5313-5324.
- Chambers S. A. and Yi S. I. (1999) Fe termination for α -Fe₂O₃(0001) as grown by oxygen-plasma-assisted molecular beam epitaxy. *Surf. Sci.* **439**, L785-L791.
- Charlet L., Liger E., and Gerasimo P. (1998a) Decontamination of TCE- and U-rich waters by granular iron: role of sorbed Fe(II). *J. Environ. Eng.* **124**, 25-30.
- Charlet L., Silvester E., and Liger E. (1998b) N-compound reduction and actinide immobilization in surficial fluids by Fe(II): the surface $\equiv\text{Fe}^{\text{III}}\text{OFe}^{\text{II}}\text{OH}^0$ species, as major reductant. *Chem. Geol.* **151**, 85-93.

- Chun C. L., Penn R. L., and Arnold W. A. (2006) Kinetic and microscopic studies of reductive transformations of organic contaminants on goethite. *Environ. Sci. Technol.* **40**, 3299-3304.
- Cornell R. M. and Schwertmann U. (1996) *The Iron Oxides: Structure, Properties, Reactions, Occurrence and Uses*. Wiley-VCH.
- Coughlin B. R. and Stone A. T. (1995) Nonreversible adsorption of divalent metal ions (Mn^{II} , Co^{II} , Ni^{II} , Cu^{II} , and Pb^{II}) onto goethite: Effects of acidification, Fe^{II} addition, and picolinic acid addition. *Environ. Sci. Technol.* **29**, 2445-2455.
- Eary L. E. and Rai D. (1989) Kinetics of chromate reduction by ferrous ions derived from hematite and biotite at 25 DegC. *Am. J. Sci.* **289**, 180-213.
- Eggleston C. M., Stack A. G., Rosso K. M., Higgins S. R., Bice A. M., Boese S. W., Pribyl R. D., and Nichols J. J. (2003) The structure of hematite ($\alpha\text{-Fe}_2\text{O}_3$) (001) surfaces in aqueous media: scanning tunneling microscopy and resonant tunneling calculations of coexisting O and Fe terminations. *Geochim. Cosmochim. Acta* **67**, 985-1000.
- Elsner M., Haderlein S. B., Kellerhals T., Luzi S., Zwank L., Angst W., and Schwarzenbach R. P. (2004a) Mechanisms and products of surface-mediated reductive dehalogenation of carbon tetrachloride by $\text{Fe}(\text{II})$ on goethite. *Environ. Sci. Technol.* **38**, 2058-2066.
- Elsner M., Schwarzenbach R. P., and Haderlein S. B. (2004b) Reactivity of $\text{Fe}(\text{II})$ -bearing minerals toward reductive transformation of organic contaminants. *Environ. Sci. Technol.* **38**, 799-807.
- Farges F., Lefrere Y., Rossano S., Berthereau A., Calas G., and Brown G. E. (2004) The effect of redox state on the local structural environment of iron in silicate glasses: a combined XAFS spectroscopy, molecular dynamics, and bond valence study. *J. Non-Cryst. Solids* **344**(3), 176-188.
- Fenter P. and Park C. (2004) Termination interference along crystal truncation rods. *J. Appl. Crystallogr.* **37**, 977-987.
- Finger L. W. and Hazen R. M. (1980) Crystal structure and isothermal compression of iron(III) oxide, chromium(III) oxide, and vanadium(III) oxide to 50 kbars. *J. Appl. Phys.* **51**, 5362-5367.
- Fredrickson J. K., Zachara J. M., Kennedy D. W., Kukkadapu R. K., McKinley J. P., Heald S. M., Liu C., and Plymale A. E. (2004) Reduction of TcO_4^- by sediment-associated biogenic $\text{Fe}(\text{II})$. *Geochim. Cosmochim. Acta* **68**, 3171-3187.

- Hamilton W. C. (1965) Significance tests on the crystallographic R factor. *Acta Cryst.* **18**, 502-510.
- Hansel C. M., Benner S. G., and Fendorf S. (2005) Competing Fe(II)-induced mineralization pathways of ferrihydrite. *Environ. Sci. Technol.* **39**, 7147-7153.
- Hansel C. M., Benner S. G., Neiss J., Dohnalkova A., Kukkadapu R. K., and Fendorf S. (2003) Secondary mineralization pathways induced by dissimilatory iron reduction of ferrihydrite under advective flow. *Geochim. Cosmochim. Acta* **67**, 2977-2992.
- Hiemstra T. and van Riemsdijk W. H. (2007) Adsorption and surface oxidation of Fe(II) on metal (hydr)oxides. *Geochim. Cosmochim. Acta* **71**, 5913-5933.
- Jackson W. E., Farges F., Yeager M., Mabrouk P. A., Rossano S., Waychunas G. A., Solomon E. I., and Brown G. E. (2005) Multi-spectroscopic study of Fe(II) in silicate glasses: Implications for the coordination environment of Fe(II) in silicate melts. *Geochim. Cosmochim. Acta* **69**, 4315-4332.
- Jarvis E. A., and Chaka A. M. (2007) Oxidation mechanism and ferryl domain formation on the α -Fe₂O₃ (0001) surface. *Surf. Sci.* **601**, 1909 - 1914.
- Jeon B.-H., Dempsey B. A., and Burgos W. D. (2003) Kinetics and mechanisms for reactions of Fe(II) with iron(III) oxides. *Environ. Sci. Technol.* **37**, 3309-3315.
- Jeon B. H., Dempsey B. A., Burgos W. D., and Royer R. A. (2001) Reactions of ferrous iron with hematite. *Colloids Surf. A* **191**, 41-55.
- Kerisit S. and Rosso K. M. (2006) Computer simulation of electron transfer at hematite surfaces. *Geochim. Cosmochim. Acta* **70**, 1888-1903.
- Kerisit S. and Rosso K. M. (2007) Kinetic Monte Carlo model of charge transport in hematite (α -Fe₂O₃). *J. Chem. Phys.* **127**, 124706/1-124706/10.
- Ketteler G., Weiss W., and Ranke W. (2001) Surface structures of α -Fe₂O₃(0001) phases determined by LEED crystallography. *Surf. Rev. Lett.* **8**, 661-683.
- Larese-Casanova P. and Scherer M. M. (2007) Fe(II) sorption on hematite: new insights based on spectroscopic measurements. *Environ. Sci. Technol.* **41**, 471-477.
- Lemire C., Bertarione, S., Zecchina A., Scarano, D., Chaka, A., Shaikhutdinov, S., and Freund, H.-J. (2005) Ferryl (Fe=O) termination of the hematite α -Fe₂O₃(0001) surface *Phys. Rev. Lett.* **94**, 166101/1 - 166101/4

- Liger E., Charlet L., and Van Cappellen P. (1999) Surface catalysis of uranium (VI) reduction by iron(II). *Geochim. Cosmochim. Acta* **63**, 2939-2955.
- Liu C., Zachara J. M., Gorby Y. A., Szecsody J. E., and Brown C. F. (2001) Microbial reduction of Fe(III) and sorption/precipitation of Fe(II) on shewanella putrefaciens strain CN32. *Environ. Sci. Technol.* **35**, 1385-1393.
- Liu P., Kendelewicz T., Brown G. E., Jr., Nelson E. J., and Chambers S. A. (1998) Reaction of water vapor with α -Al₂O₃(0001) and α -Fe₂O₃(0001) surfaces: synchrotron X-ray photoemission studies and thermodynamic calculations. *Surf. Sci.* **417**, 53-65.
- Lo C. S., Tanwar K. S., Chaka A. M., and Trainor T. P. (2007) Density functional theory study of the clean and hydrated hematite (1 $\bar{1}$ 02) surfaces. *Phys. Rev. B: Condens. Matter* **75**, 075425/1-075425/15.
- Lovley D. R. (1991) Dissimilatory iron(III) and manganese(IV) reduction. *Microbiol. Rev.* **55**, 259-287.
- Lovley D. R. (1993) Dissimilatory metal reduction. *Annu. Rev. Microbiol.* **47**, 263-290.
- Pauling L. C. (1960) *The nature of the chemical bond and the structure of molecules and crystals. An introduction to modern structural chemistry. 3rd ed.*
- Pecher K., Haderlein S. B., and Schwarzenbach R. P. (2002) Reduction of polyhalogenated methanes by surface-bound Fe(II) in aqueous suspensions of iron oxides. *Environ. Sci. Technol.* **36**, 1734-1741.
- Pedersen H. D., Postma D., Jakobsen R., and Larsen O. (2005) Fast transformation of iron oxyhydroxides by the catalytic action of aqueous Fe(II). *Geochim. Cosmochim. Acta* **69**, 3967-3977.
- Robinson I. K. (1986) Crystal truncation rods and surface roughness. *Phys. Rev. B Condens. Matter* **33**, 3830-3836.
- Robinson I. K. (1991) Surface crystallography. In *Handbook on Synchrotron Radiation*, Vol. 3 (ed. G. S. Brown and D. E. Momcton). North-Holland, pp. 221-226.
- Roden E. E. (2006) Geochemical and microbiological controls on dissimilatory iron reduction. *C. R. Geoscience* **338**, 456-467.
- Roden E. E. and Urrutia M. M. (2002) Influence of biogenic Fe(II) on bacterial crystalline Fe(III) oxide reduction. *Geomicrobiol. J.* **19**, 209-251.

- Roden E. E. and Zachara J. M. (1996) Microbial reduction of crystalline iron(III) oxides: Influence of oxide surface area and potential for cell growth. *Environ. Sci. Technol.* **30**, 1618-28.
- Rosso K. M., Smith D. M. A., and Dupuis M. (2003a) An ab initio model of electron transport in hematite (α -Fe₂O₃) basal planes. *J. Chem. Phys.* **118**, 6455-6466
- Rosso K. M., Zachara J. M., Fredrickson J. K., Gorby Y. A., and Smith S. C. (2003b) Nonlocal bacterial electron transfer to hematite surfaces. *Geochim. Cosmochim. Acta* **67**, 1081-1087.
- Royer R. A., Dempsey B. A., Jeon B.-H., and Burgos W. D. (2004) Inhibition of biological reductive dissolution of hematite by ferrous iron. *Environ. Sci. Technol.* **38**, 187-193.
- Schleppütz C. M., Herger R., Wilmott P. R., Patterson B. D., Bunk O., Brönnimann Ch., Henrich B., Hülsen G., and Eickenberry E. F. (2005) Improved data acquisition in grazing incidence X-ray scattering experiments using a pixel detector. *Acta Cryst.* **A61**, 418-425.
- Shaikhutdinov S. K. and Weiss W. (1999) Oxygen pressure dependence of the α -Fe₂O₃(0001) surface structure. *Surf. Sci.* **432**, L627-L634.
- Silvester E., Charlet L., Tournassat C., Gehin A., Greneche J.-M., and Liger E. (2005) Redox potential measurements and moessbauer spectrometry of Fe^{II} adsorbed onto Fe^{III} (oxyhydr)oxides. *Geochim. Cosmochim. Acta* **69**, 4801-4815.
- Stumm W. and Sulzberger B. (1992) The cycling of iron in natural environments: Considerations based on laboratory studies of heterogeneous redox processes. *Geochim. Cosmochim. Acta* **56**, 3233-3257.
- Sulzberger B., Suter D., Siffert C., Banwart S., and Stumm W. (1989) Dissolution of iron(III) (hydr)oxides in natural waters; laboratory assessment on the kinetics controlled by surface coordination. *Mar. Chem.* **28**, 127-144.
- Tamaura Y., Ito K., and Katsura T. (1983) Transformation of γ -FeO(OH) to magnetite by adsorption of iron(II) ion on γ -FeO(OH). *J. Chem. Soc. Dalton Trans.* **1983**, 189-194.
- Tanwar K. S., Catalano J. G., Petitto S. C., Ghose S. K., Eng P. J., and Trainor T. P. (2007a) Hydrated α -Fe₂O₃ (1 $\bar{1}$ 02) surface structure: Role of surface preparation. *Surf. Sci.* **601**, L59-L64.

- Tanwar K. S., Lo C. S., Eng P. J., Catalano J. G., Walko D. A., Brown G. E., Waychunas G. A., Chaka A. M., and Trainor T. P. (2007b) Surface diffraction study of the hydrated hematite ($1\bar{1}02$) surface. *Surf. Sci.* **601**, 460-474.
- Tanwar K. S., Petitto S. C., Ghose S. K., Eng P., and Trainor T. (2008) Structural study of Fe(II) adsorption on hematite ($1\bar{1}02$). *Geochim. Cosmochim. Acta*, **In press**.
- Thevuthasan S., Kim Y. J., Yi S. I., Chambers S. A., Morais J., Denecke R., Fadley C. S., Liu P., Kendelewicz T., and Brown G. E., Jr. (1999) Surface structure of MBE-grown α -Fe₂O₃(0001) by intermediate-energy x-ray photoelectron diffraction. *Surf. Sci.* **425**, 276-286.
- Tobler N. B., Hofstetter T. B., and Schwarzenbach R. P. (2007a) Assessing iron-mediated oxidation of toluene and reduction of nitroaromatic contaminants in anoxic environments using compound-specific isotope analysis. *Environ. Sci. Technol.* **41**, 7773-7780.
- Tobler N. B., Hofstetter T. B., Straub K. L., Fontana D., and Schwarzenbach R. P. (2007b) Iron-mediated microbial oxidation and abiotic reduction of organic contaminants under anoxic conditions. *Environ. Sci. Technol.* **41**, 7765-7772.
- Tossell J. A. (1980) Calculation of bond distances and heats of formation for beryllium oxide, magnesium oxide, silicon dioxide, iron(II) oxide, and zinc oxide using the ionic model. *Am. Mineral.* **65**, 163-173.
- Trainor T. P., Chaka A. M., Eng P. J., Newville M., Waychunas G. A., Catalano J. G., and Brown G. E. (2004) Structure and reactivity of the hydrated hematite (0001) surface. *Surf. Sci.* **573**, 204-224.
- Trainor T. P., Eng P. J., and Robinson I. K. (2002) Calculation of crystal truncation rod structure factors for arbitrary rational surface terminations. *J. Appl. Crystallogr.* **35**, 696-701.
- Trainor T. P., Templeton A. S., and Eng P. J. (2006) Structure and reactivity of environmental interfaces: Application of grazing angle x-ray spectroscopy and long-period x-ray standing waves. *J. Electron Spectrosc. Relat. Phenom.* **150**, 66-85.
- Tronc E., Belleville P., Jolivet J. P., and Livage J. (1992) Transformation of ferric hydroxide into spinel by iron(II) adsorption. *Langmuir* **8**, 313-319.

- Vlieg E. (2000) ROD: a program for surface X-ray crystallography. *J. Appl. Crystallogr.* **33**, 401-405.
- Vlieg E., Van der Veen J. F., Gurman S. J., Norris C., and Macdonald J. E. (1989) X-ray diffraction from rough, relaxed and reconstructed surfaces. *Surf. Sci.* **210**, 301-321.
- Wang X. G., Weiss W., Shaikhutdinov S. K., Ritter M., Petersen M., Wagner F., Schlogl R., and Scheffler M. (1998) The hematite (α -Fe₂O₃) (0001) surface: Evidence for domains of distinct chemistry. *Phys. Rev. Lett.* **81**, 1038-1041.
- Waychunas G. A., Brown G. E., Jr., Ponader C. W., and Jackson W. E. (1988) Evidence from X-ray absorption for network-forming Fe²⁺ in molten alkali silicates. *Nature* **332**, 251-253.
- Whittaker E. J. W. and Muntus R. (1970) Ionic radii for use in geochemistry. *Geochim. Cosmochim. Acta* **34**, 945-956.
- Wilke M., Schmidt C., Farges F., Malavergne V., Gautron L., Simionovici A., Hahn M., and Petit P. E. (2006) Structural environment of iron in hydrous aluminosilicate glass and melt-evidence from X-ray absorption spectroscopy. *Chem. Geol.* **229**, 144-161.
- Williams A. G. B. and Scherer M. M. (2004) Spectroscopic evidence for Fe(II)-Fe(III) electron transfer at the iron oxide-water interface. *Environ. Sci. Technol.* **38**, 4782-4790.
- Yanina S. V. and Rosso K. M. (2008) Linked reactivity at mineral-water interfaces through bulk crystal conduction. *Science* **320**, 218-222.
- Yin S., Xiaoyan M., Ellis D. E. (2007) Initial stages of H₂O adsorption and hydroxylation of Fe-terminated α -Fe₂O₃(0001) surface. *Surf. Sci.* **601**, 2426-2437.
- Zachara J. M., Fredrickson J. K., Li S.-M., Kennedy D. W., Smith S. C., and Gassman P. L. (1998) Bacterial reduction of crystalline Fe³⁺ oxides in single phase suspensions and subsurface materials. *Am. Mineral.* **83**, 1426-1443.
- Zhang Y., Charlet L., and Schindler P. W. (1992) Adsorption of protons, iron(II) and aluminum on lepidocrocite (γ -FeOOH). *Colloids Surf.* **63**, 259-268.

Table 5.1 Unrelaxed surface unit cell coordinates and best fit model coordinates and parameters from CTR data analysis using a single structural domain for unreacted α -Fe₂O₃(0001).

Unrelaxed single Fe-layer termination (Fe-O ₃ -Fe-R)					Best fit model (O _{3y} -Fe _x -O ₃ -Fe-R)					$\chi^2 = 1.97$ $\beta = 0.21(3)$	
Layer		x	y	z	x	y	z	Δz (Å)	B _{iso} (Å ²)	Occ.	Σs
i	O	-	-	-	0.64(1)	0.67(2)	1.920(5)	-	0.40	0.52(8)	0.39(5)
	O	-	-	-	0.33(2)	0.97(2)	1.920(5)	-	0.40	0.52(8)	0.39(5)
	O	-	-	-	0.03(2)	0.36(1)	1.920(5)	-	0.40	0.52(8)	0.39(5)
1	Fe	0.333	0.667	1.811	0.333	0.667	1.815(2)	0.05(3)	0.32	0.44(2)	2.8(2)
2	O	0.694	0.000	1.750	0.694	0.000	1.747(2)	-0.04(3)	0.40	1.00(3)	1.61(2)
	O	0.000	0.694	1.750	0.000	0.694	1.747(2)	-0.04(3)	0.40	1.00(3)	1.61(2)
	O	0.306	0.306	1.750	0.306	0.306	1.747(2)	-0.04(3)	0.40	1.00(3)	1.61(2)
3	Fe	0.667	0.333	1.689	0.667	0.333	1.687(1)	-0.03(2)	0.32	1.0(1)	3.10(1)
4	Fe	0.000	0.000	1.645	0.000	0.000	1.648(1)	0.05(1)	0.32	1.00	3.10(1)
5	O	0.972	0.333	1.583	0.972	0.333	1.584(2)	0.01(3)	0.40	1.00	1.98(1)
	O	0.667	0.639	1.583	0.667	0.639	1.584(2)	0.01(3)	0.40	1.00	1.98(1)
	O	0.361	0.028	1.583	0.361	0.028	1.584(2)	0.01(3)	0.40	1.00	1.98(1)
6	Fe	0.333	0.667	1.522	0.333	0.667	1.523(1)	0.01(1)	0.32	1.00	2.94(6)
7	Fe	0.667	0.333	1.478	0.667	0.333	1.478	0.00	0.32	1.00	2.94(6)
8	O	0.028	0.667	1.417	0.028	0.667	1.417	0.00	0.40	1.00	1.97(1)
	O	0.333	0.361	1.417	0.333	0.361	1.417	0.00	0.40	1.00	1.97(1)
	O	0.639	0.972	1.417	0.639	0.972	1.417	0.00	0.40	1.00	1.97(1)
9	Fe	0.000	0.000	1.355	0.000	0.000	1.355	0.00	0.32	1.00	2.97
10	Fe	0.333	0.667	1.311	0.333	0.667	1.311	0.00	0.32	1.00	2.97
11	O	0.306	0.000	1.250	0.306	0.000	1.250	0.00	0.40	1.00	1.98
	O	0.000	0.306	1.250	0.000	0.306	1.250	0.00	0.40	1.00	1.98
	O	0.694	0.694	1.250	0.694	0.694	1.250	0.00	0.40	1.00	1.98
12	Fe	0.667	0.333	1.189	0.667	0.333	1.189	0.00	0.32	1.00	2.97
13	Fe	0.000	0.000	1.145	0.000	0.000	1.145	0.00	0.32	1.00	2.97
14	O	0.361	0.333	1.083	0.361	0.333	1.083	0.00	0.40	1.00	1.98
	O	0.667	0.028	1.083	0.667	0.028	1.083	0.00	0.40	1.00	1.98
	O	0.972	0.639	1.083	0.972	0.639	1.083	0.00	0.40	1.00	1.98
15	Fe	0.333	0.667	1.022	0.333	0.667	1.022	0.00	0.32	1.00	2.97

The estimated errors from least squares fit at the 96% confidence interval are given in parentheses. Values without errors were held fixed in the final fits. The Δz values are change in layer position with respect to unrelaxed termination. The B_{iso} are isotropic Debye-Waller factors, Occ are occupancy parameters and β is roughness factor. The bond-valence sums (Σs) were calculated assuming unit site occupancies. The atoms in the boldface represent atoms added to surface unit cell.

Table 5.2 Best-fit model coordinates and parameters for O-layer termination of unreacted α -Fe₂O₃(0001) obtained from two domain structural analysis.

Layer		Best fit model (O ₃ -Fe-Fe-R)							Surface fraction = 0.54(2) $\chi^2 = 1.66$ $\beta = 0.23(3)$	
		x	y	z	Δz (Å)	B _{iso} (Å ²)	Occ.	Σs		
i	O(H₂O)	0.65(2)	0.65(2)	1.862(1)	-	2.00	0.9(2)	-		
	O(H₂O)	0.35(2)	0.00(3)	1.862(1)	-	2.00	0.9(2)	-		
	O(H₂O)	1.00(3)	0.35(2)	1.862(1)	-	2.00	0.9(2)	-		
1	Fe	-	-	-	-	-	-	-		
2	O	0.694	0.000	1.747(2)	-0.04(3)	0.40	1.0(1)	1.05(1)		
	O	0.000	0.694	1.747(2)	-0.04(3)	0.40	1.0(1)	1.05(1)		
	O	0.306	0.306	1.747(2)	-0.04(3)	0.40	1.0(1)	1.05(1)		
3	Fe	0.667	0.333	1.685(1)	-0.06(2)	0.32	1.0(1)	3.12(2)		
4	Fe	0.000	0.000	1.649(1)	0.05(2)	0.32	1.00	3.13(2)		
5	O	0.972	0.333	1.585(3)	0.03(3)	0.40	1.00	1.99(1)		
	O	0.667	0.639	1.585(3)	0.03(3)	0.40	1.00	1.99(1)		
	O	0.361	0.028	1.585(3)	0.03(3)	0.40	1.00	1.99(1)		
6	Fe	0.333	0.667	1.523(1)	0.01(1)	0.32	1.00	2.90(1)		
7	Fe	0.667	0.333	1.479(1)	0.01(1)	0.32	1.00	2.90(1)		
8	O	0.028	0.667	1.416(2)	-0.01(3)	0.40	1.00	1.97(2)		
	O	0.333	0.361	1.416(2)	-0.01(3)	0.40	1.00	1.97(2)		
	O	0.639	0.972	1.416(2)	-0.01(3)	0.40	1.00	1.97(2)		
9	Fe	0.000	0.000	1.355	0.00	0.32	1.00	2.98(6)		
10	Fe	0.333	0.667	1.311	0.00	0.32	1.00	2.98(6)		
11	O	0.306	0.000	1.250	0.00	0.40	1.00	1.98		
	O	0.000	0.306	1.250	0.00	0.40	1.00	1.98		
	O	0.694	0.694	1.250	0.00	0.40	1.00	1.98		
12	Fe	0.667	0.333	1.189	0.00	0.32	1.00	2.97		
13	Fe	0.000	0.000	1.145	0.00	0.32	1.00	2.97		
14	O	0.361	0.333	1.083	0.00	0.40	1.00	1.98		
	O	0.667	0.028	1.083	0.00	0.40	1.00	1.98		
	O	0.972	0.639	1.083	0.00	0.40	1.00	1.98		
15	Fe	0.333	0.667	1.022	0.00	0.32	1.00	2.97		

The estimated errors from least squares fit at the 96% confidence interval are given in parentheses. Values without errors were held fixed in the final fits. The Δz values are change in layer position with respect to unrelaxed termination. The B_{iso} are isotropic Debye-Waller factors, Occ are occupancy parameters and β is roughness factor. The bond-valence sums (Σs) were calculated assuming unit site occupancies. The atoms in the boldface represent atoms added to surface unit cell. The physisorbed water layers are not included in presented model stoichiometry. The occupancy factors are for a given domain. The occupancy per surface unit cell can be given as Surface fraction*Occ.

Table 5.3 Best-fit model coordinates and parameters for hydroxylated Fe-layer termination of unreacted α -Fe₂O₃(0001) obtained via two domain structural analysis.

Layer		Best fit model (O ₃ -Fe-O ₃ -Fe-R)						Surface fraction = 0.46(2) $\chi^2 = 1.66$ $\beta = 0.23(3)$	
		x	y	z	Δz (Å)	B _{iso} (Å ²)	Occ.	Σ_s	
ii	O(H ₂ O)	0.2(4)	0.3(2)	2.13(3)	-	1.50	0.1(1)		
	O(H ₂ O)	0.7(2)	0.8(4)	2.13(3)	-	1.50	0.1(1)		
	O(H ₂ O)	0.2(4)	0.8(4)	2.13(3)	-	1.50	0.1(1)		
i	O	0.66(2)	0.69(2)	1.916	-	0.80	1.00	0.32(1)	
	O	0.31(2)	0.97(3)	1.916	-	0.80	1.00	0.32(1)	
	O	0.03(3)	0.34(2)	1.916	-	0.80	1.00	0.32(1)	
1	Fe	0.333	0.667	1.809(4)	-0.03(5)	0.32	1.00(6)	2.8(1)	
2	O	0.694	0.000	1.747(2)	-0.04(3)	0.40	1.0(1)	1.65(3)	
	O	0.000	0.694	1.747(2)	-0.04(3)	0.40	1.0(1)	1.65(3)	
	O	0.306	0.306	1.747(2)	-0.04(3)	0.40	1.0(1)	1.65(3)	
3	Fe	0.667	0.333	1.685(1)	-0.06(2)	0.32	1.0(1)	3.12(2)	
4	Fe	0.000	0.000	1.649(1)	0.05(2)	0.32	1.00	3.13(2)	
5	O	0.972	0.333	1.585(3)	0.03(3)	0.40	1.00	1.99(1)	
	O	0.667	0.639	1.585(3)	0.03(3)	0.40	1.00	1.99(1)	
	O	0.361	0.028	1.585(3)	0.03(3)	0.40	1.00	1.99(1)	
6	Fe	0.333	0.667	1.523(1)	0.01(1)	0.32	1.00	2.90(1)	
7	Fe	0.667	0.333	1.479(1)	0.01(1)	0.32	1.00	2.90(1)	
8	O	0.028	0.667	1.416(2)	-0.01(3)	0.40	1.00	1.97(2)	
	O	0.333	0.361	1.416(2)	-0.01(3)	0.40	1.00	1.97(2)	
	O	0.639	0.972	1.416(2)	-0.01(3)	0.40	1.00	1.97(2)	
9	Fe	0.000	0.000	1.355	0.00	0.32	1.00	2.98(6)	
10	Fe	0.333	0.667	1.311	0.00	0.32	1.00	2.98(6)	
11	O	0.306	0.000	1.250	0.00	0.40	1.00	1.98	
	O	0.000	0.306	1.250	0.00	0.40	1.00	1.98	
	O	0.694	0.694	1.250	0.00	0.40	1.00	1.98	
12	Fe	0.667	0.333	1.189	0.00	0.32	1.00	2.97	
13	Fe	0.000	0.000	1.145	0.00	0.32	1.00	2.97	
14	O	0.361	0.333	1.083	0.00	0.40	1.00	1.98	
	O	0.667	0.028	1.083	0.00	0.40	1.00	1.98	
	O	0.972	0.639	1.083	0.00	0.40	1.00	1.98	
15	Fe	0.333	0.667	1.022	0.00	0.32	1.00	2.97	

The estimated errors from least squares fit at the 96% confidence interval are given in parentheses. Values without errors were held fixed in the final fits. The Δz values are change in layer position with respect to unrelaxed termination. The B_{iso} are isotropic Debye-Waller factors, Occ are occupancy parameters and β is roughness factor. The bond-valence sums (Σ_s) were calculated assuming unit site occupancies. The atoms in the boldface represent atoms added to surface unit cell. The physisorbed water layers are not included in presented model stoichiometry. The occupancy factors are for a given domain. The occupancy per surface unit cell can be given as Surface fraction*Occ.

Table 5.4 Best-fit model coordinates and parameters for the single domain structural model of Fe(II) reacted α -Fe₂O₃(0001).

Layer		Best fit model (O _{3e} -Fe _d -O _{3c} -Fe _b -Fe _a -O ₃ -Fe-R)					$\chi^2 = 1.02$ $\beta = 0.18(2)$	
		x	y	z	Δz (Å)	B _{iso} (Å ²)	Occ.	Σs
iv	O	0.68(1)	0.66(2)	2.084(5)	-	0.50	0.25(6)	0.32(6)
	O	0.34(2)	0.02(2)	2.084(5)	-	0.50	0.25(6)	0.32(6)
	O	0.98(2)	0.32(1)	2.084(5)	-	0.50	0.25(6)	0.32(6)
iii	Fe	0.667	0.333	1.976(3)	-	0.32	0.29(2)	2.8(2)
ii	O	0.641	0.669	1.917	-	0.40	0.90(6)	1.60(1)
	O	0.331	0.972	1.917	-	0.40	0.90(6)	1.60(1)
	O	0.028	0.359	1.917	-	0.40	0.90(6)	1.60(1)
i	Fe	0.000	0.000	1.851(1)	-	0.32	0.47(2)	3.02(5)
1	Fe	0.333	0.667	1.813(1)	0.03(2)	0.32	0.75(2)	2.96(5)
2	O	0.694	0.000	1.750(2)	0.00(2)	0.40	1.00	2.03(1)
	O	0.000	0.694	1.750(2)	0.00(2)	0.40	1.00	2.03(1)
	O	0.306	0.306	1.750(2)	0.00(2)	0.40	1.00	2.03(1)
3	Fe	0.667	0.333	1.691(1)	0.03(1)	0.32	1.00	2.99(1)
4	Fe	0.000	0.000	1.646(1)	0.01(1)	0.32	1.00	2.99(1)
	O	0.972	0.333	1.584(2)	0.01(2)	0.40	1.00	1.96(1)
	O	0.667	0.639	1.584(2)	0.01(2)	0.40	1.00	1.96(1)
6	O	0.361	0.028	1.584(2)	0.01(2)	0.40	1.00	1.96(1)
	Fe	0.333	0.667	1.524(1)	0.03(1)	0.32	1.00	2.92(1)
	Fe	0.667	0.333	1.477(1)	-0.01(1)	0.32	1.00	2.92(1)
8	O	0.028	0.667	1.416(1)	-0.01(2)	0.40	1.00	1.98(1)
	O	0.333	0.361	1.416(1)	-0.01(2)	0.40	1.00	1.98(1)
	O	0.639	0.972	1.416(1)	-0.01(2)	0.40	1.00	1.98(1)
9	Fe	0.000	0.000	1.356(1)	0.01(1)	0.32	1.00	2.97(1)
10	Fe	0.333	0.667	1.312(1)	0.01(1)	0.32	1.00	2.97(1)
11	O	0.306	0.000	1.249(1)	-0.01(2)	0.40	1.00	1.97(1)
	O	0.000	0.306	1.249(1)	-0.01(2)	0.40	1.00	1.97(1)
	O	0.694	0.694	1.249(1)	-0.01(2)	0.40	1.00	1.97(1)
12	Fe	0.667	0.333	1.189	0.00	0.32	1.00	3.00(4)
13	Fe	0.000	0.000	1.145	0.00	0.32	1.00	3.00(4)
14	O	0.361	0.333	1.083	0.00	0.40	1.00	1.98
	O	0.667	0.028	1.083	0.00	0.40	1.00	1.98
	O	0.972	0.639	1.083	0.00	0.40	1.00	1.98
15	Fe	0.333	0.667	1.022	0.00	0.32	1.00	2.97

The estimated errors from least squares fit at the 96% confidence interval are given in parentheses. Values without errors were held fixed in the final fits. The Δz values are change in layer position with respect to unrelaxed termination. The B_{iso} are isotropic Debye-Waller factors, Occ are occupancy parameters and β is roughness factor. The bond-valence sums (Σs) were calculated assuming unit site occupancies. The atoms in the boldface represent atoms added to surface unit cell. In presented model stoichiometry, the a, b, c, d and e represent occupancy of a given layer.

Table 5.5 Best-fit model coordinates and parameters for Fe(II) reacted O-layer termination of α -Fe₂O₃(0001) obtained via two domain structural analysis.

Layer		Best fit model (O _{3n} -Fe _m -O ₃ -Fe-Fe-R)							Surface fraction = 0.54 $\chi^2 = 1.07$ $\beta = 0.20(2)$	
		x	y	z	Δz (Å)	B _{iso} (Å ²)	Occ.	Σs		
ii	O	0.639	0.667	1.921(4)	-	0.40	0.60(9)	0.32(1)		
	O	0.333	0.972	1.921(4)	-	0.40	0.60(9)	0.32(1)		
	O	0.028	0.361	1.921(4)	-	0.40	0.60(9)	0.32(1)		
i	Fe	0.333	0.667	1.809(2)	-	0.32	0.51(3)	2.86(7)		
2	O	0.69(1)	0.997(6)	1.747(3)	-0.04(4)	0.40	1.00	1.71(1)		
	O	0.003(6)	0.692(9)	1.747(3)	-0.04(4)	0.40	1.00	1.71(1)		
	O	0.308(9)	0.31(1)	1.747(3)	-0.04(4)	0.40	1.00	1.71(1)		
3	Fe	0.667	0.333	1.686(1)	-0.03(2)	0.32	1.00	3.0(2)		
4	Fe	0.000	0.000	1.651(1)	0.08(2)	0.32	1.00	3.0(1)		
5	O	0.972	0.333	1.582(3)	-0.01(4)	0.40	1.00	1.94(1)		
	O	0.667	0.639	1.582(3)	-0.01(4)	0.40	1.00	1.94(1)		
	O	0.361	0.028	1.582(3)	-0.01(4)	0.40	1.00	1.94(1)		
6	Fe	0.333	0.667	1.525(1)	0.05(2)	0.32	1.00	3.03(1)		
7	Fe	0.667	0.333	1.474(1)	-0.05(2)	0.32	1.00	3.03(2)		
8	O	0.028	0.667	1.418(3)	0.01(5)	0.40	1.00	1.99(1)		
	O	0.333	0.361	1.418(3)	0.01(5)	0.40	1.00	1.99(1)		
	O	0.639	0.972	1.418(3)	0.01(5)	0.40	1.00	1.99(1)		
9	Fe	0.000	0.000	1.356(1)	0.01(1)	0.32	1.00	2.92(1)		
10	Fe	0.333	0.667	1.311(1)	0.00(2)	0.32	1.00	2.91(1)		
11	O	0.306	0.000	1.249(3)	-0.01(4)	0.40	1.00	1.96(1)		
	O	0.000	0.306	1.249(3)	-0.01(4)	0.40	1.00	1.96(1)		
	O	0.694	0.694	1.249(3)	-0.01(4)	0.40	1.00	1.96(1)		
12	Fe	0.667	0.333	1.188(1)	-0.01(2)	0.32	1.00	3.00(9)		
13	Fe	0.000	0.000	1.145	0.00	0.32	1.00	3.00(9)		
14	O	0.361	0.333	1.083	0.00	0.40	1.00	1.99(1)		
	O	0.667	0.028	1.083	0.00	0.40	1.00	1.99(1)		
	O	0.972	0.639	1.083	0.00	0.40	1.00	1.99(1)		
15	Fe	0.333	0.667	1.022	0.00	0.32	1.00	2.97		

The estimated errors from least squares fit at the 96% confidence interval are given in parentheses. Values without errors were held fixed in the final fits. The Δz values are change in layer position with respect to unrelaxed termination. The B_{iso} are isotropic Debye-Waller factors, Occ are occupancy parameters and β is roughness factor. The bond-valence sums (Σs) were calculated assuming unit site occupancies. The atoms in the boldface represent atoms added to surface unit cell. In presented model stoichiometry, the m and n represent occupancy of a given layer. The occupancy factors are for a given domain. The occupancy per surface unit cell can be given as Surface fraction*Occ.

Table 5.6 Best-fit model coordinates and parameters for Fe(II) reacted hydroxylated Fe-layer termination of α -Fe₂O₃(0001) obtained via two domain structural analysis.

Layer		Best fit model (O _{3n} -Fe _m -O ₃ -Fe-Fe-O ₃ -Fe-R) Surface fraction = 0.46 $\chi^2 = 1.07$ $\beta = 0.20(2)$						
		x	y	z	Δz (Å)	B _{iso} (Å ²)	Occ.	Σs
iv	O	0.361	0.333	2.087(4)	-	0.40	0.60(9)	0.32(1)
	O	0.667	0.028	2.087(4)	-	0.40	0.60(9)	0.32(1)
	O	0.972	0.639	2.087(4)	-	0.40	0.60(9)	0.32(1)
iii	Fe	0.667	0.333	1.976(2)	-	0.32	0.51(3)	2.86(7)
ii	O	0.641(9)	0.664(6)	1.914(3)	-	0.40	1.00	1.71(1)
	O	0.336(6)	0.98(1)	1.914(3)	-	0.40	1.00	1.71(1)
	O	0.03(1)	0.359(9)	1.914(3)	-	0.40	1.00	1.71(1)
i	Fe	0.000	0.000	1.853(1)	-	0.32	1.00	3.0(2)
1	Fe	0.333	0.667	1.817(1)	0.08(2)	0.32	1.00	3.0(1)
2	O	0.694	0.000	1.749(3)	-0.01(4)	0.40	1.00	1.94(1)
	O	0.000	0.694	1.749(3)	-0.01(4)	0.40	1.00	1.94(1)
	O	0.306	0.306	1.749(3)	-0.01(4)	0.40	1.00	1.94(1)
3	Fe	0.667	0.333	1.692(1)	0.05(2)	0.32	1.00	3.03(1)
4	Fe	0.000	0.000	1.641(1)	-0.05(2)	0.32	1.00	3.03(2)
5	O	0.972	0.333	1.584(3)	0.01(5)	0.40	1.00	1.99(1)
	O	0.667	0.639	1.584(3)	0.01(5)	0.40	1.00	1.99(1)
	O	0.361	0.028	1.584(3)	0.01(5)	0.40	1.00	1.99(1)
6	Fe	0.333	0.667	1.523(1)	0.01(1)	0.32	1.00	2.92(1)
7	Fe	0.667	0.333	1.478(1)	0.00(2)	0.32	1.00	2.91(1)
8	O	0.028	0.667	1.416(3)	-0.01(4)	0.40	1.00	1.96(1)
	O	0.333	0.361	1.416(3)	-0.01(4)	0.40	1.00	1.96(1)
	O	0.639	0.972	1.416(3)	-0.01(4)	0.40	1.00	1.96(1)
9	Fe	0.000	0.000	1.354(1)	-0.01(2)	0.32	1.00	3.00(9)
10	Fe	0.333	0.667	1.311	0.00	0.32	1.00	3.00(9)
11	O	0.306	0.000	1.250	0.00	0.40	1.00	1.99(1)
	O	0.000	0.306	1.250	0.00	0.40	1.00	1.99(1)
	O	0.694	0.694	1.250	0.00	0.40	1.00	1.99(1)
12	Fe	0.667	0.333	1.189	0.00	0.32	1.00	2.97
13	Fe	0.000	0.000	1.145	0.00	0.32	1.00	2.97
14	O	0.361	0.333	1.083	0.00	0.40	1.00	1.98
	O	0.667	0.028	1.083	0.00	0.40	1.00	1.98
	O	0.972	0.639	1.083	0.00	0.40	1.00	1.98
15	Fe	0.333	0.667	1.022	0.00	0.32	1.00	2.97

The estimated errors from least squares fit at the 96% confidence interval are given in parentheses. Values without errors were held fixed in the final fits. The Δz values are change in layer position with respect to unrelaxed termination. The B_{iso} are isotropic Debye-Waller factors, Occ are occupancy parameters and β is roughness factor. The bond-valence sums (Σs) were calculated assuming unit site occupancies. The atoms in the boldface represent atoms added to surface unit cell. In presented model stoichiometry, the m and n represent occupancy of a given layer. The occupancy factors are for a given domain. The occupancy per surface unit cell can be given as Surface fraction*Occ.

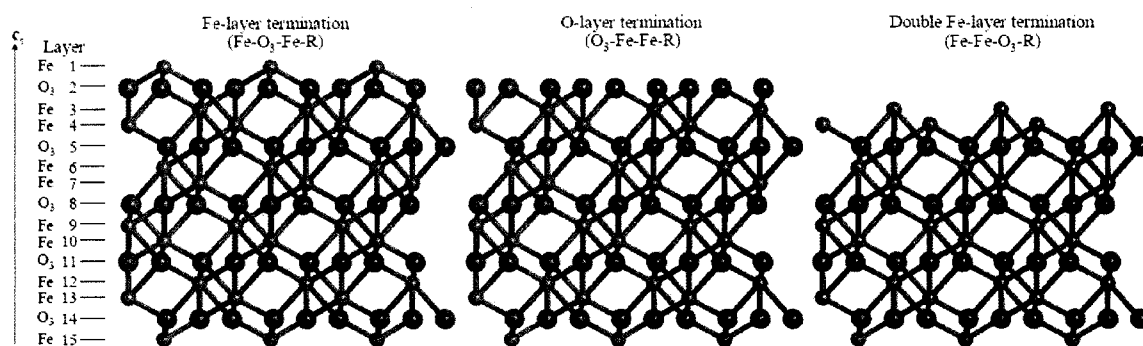


Figure 5.1 Structural models and the Fe/O stoichiometry of three chemically distinct surface terminations of $\alpha\text{-Fe}_2\text{O}_3(0001)$. The notation used for representing stoichiometry identifies top three atomic layers which uniquely identify a given termination and R represents the stoichiometric stacking sequence. The layer stacking sequence is shown along the c_s axis. The large spheres are O and small spheres are Fe atoms.

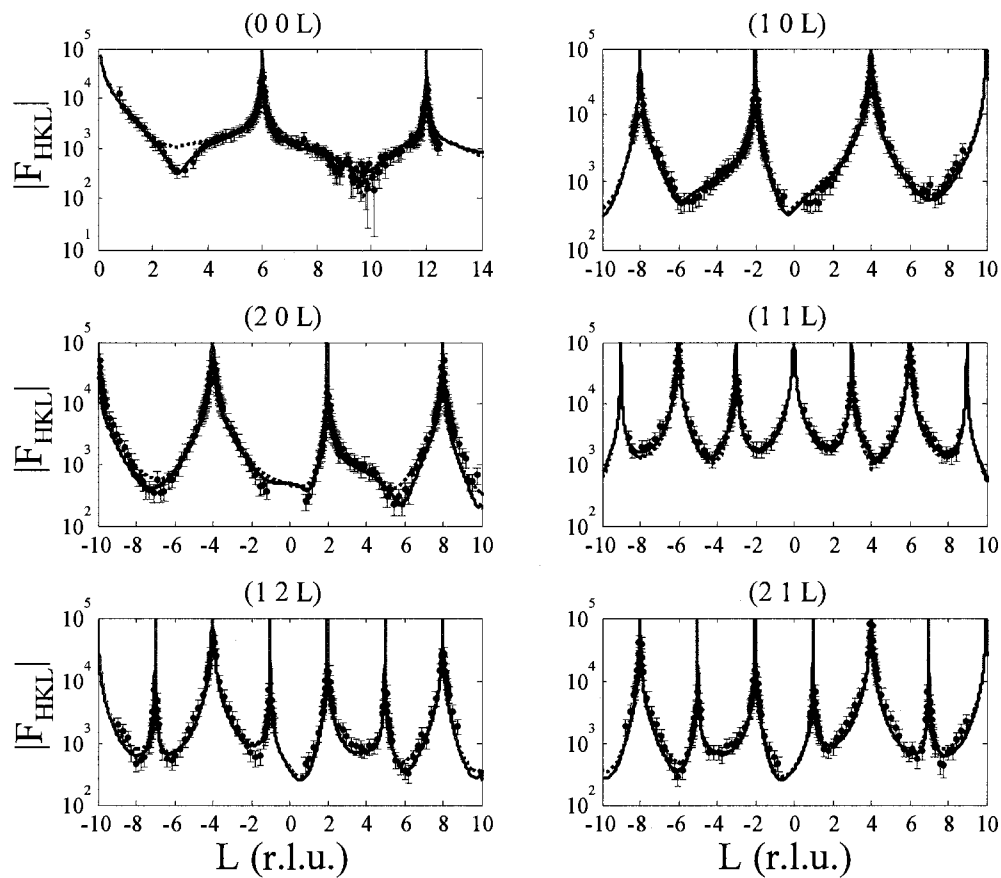


Figure 5.2 The magnitudes of experimental structure factors ($|F_{HKL}|$) (dots) and calculated structure factor magnitudes from single domain (dashed lines) and two domain (solid lines) model as a function of perpendicular momentum transfer (L , in reciprocal lattice units) for unreacted $\alpha\text{-Fe}_2\text{O}_3(0001)$.

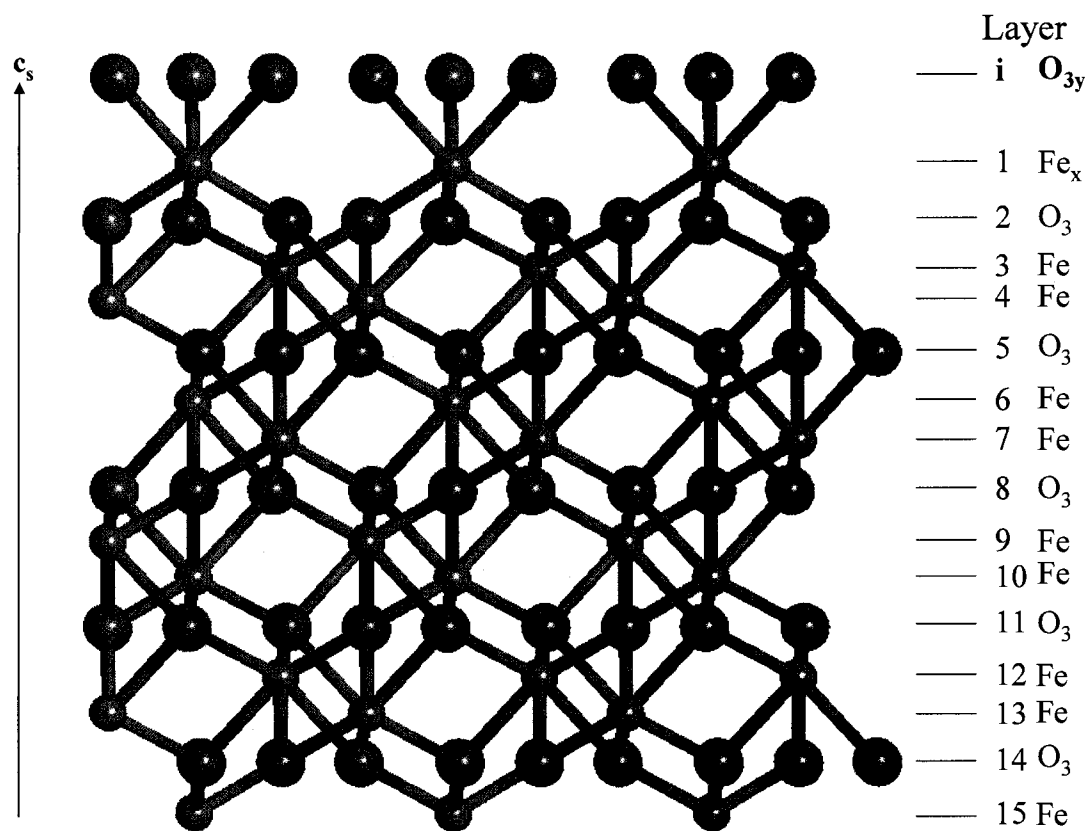


Figure 5.3 The layer stacking sequence along c_s axis for best fit single domain model for unreacted α -Fe₂O₃(0001) with Fe/O stoichiometry of O_{3y} -Fe_x-O₃-Fe-R, where x and y represent site occupancy of given atomic layers (Table 5.1). The atoms shown in bold face represent atoms that were added to the surface unit cell. The large spheres are O and small spheres are Fe atoms.

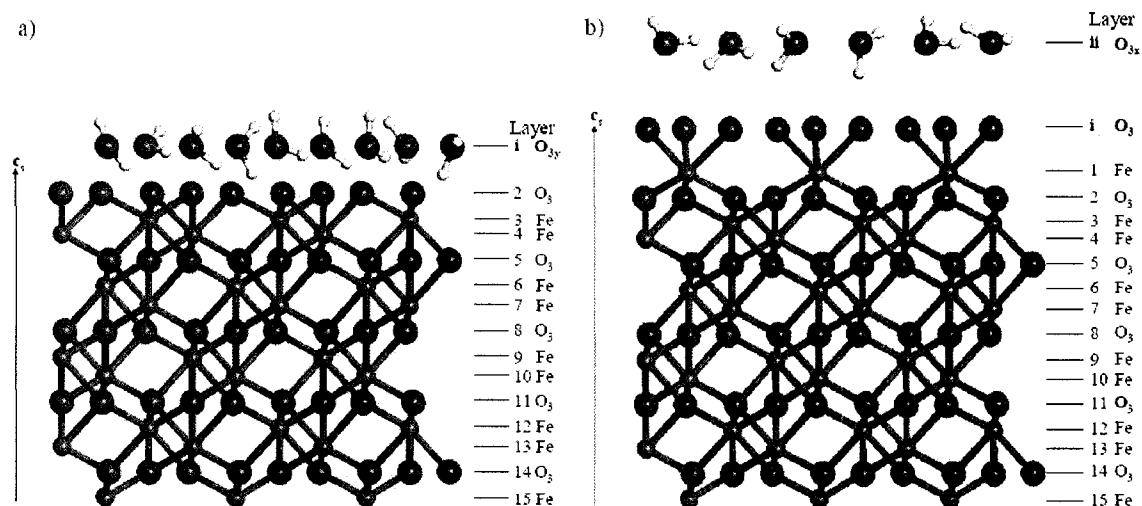


Figure 5.4 The structure for the best fit two-domain model of unreacted $\alpha\text{-Fe}_2\text{O}_3(0001)$ which includes relaxed (a) O-layer termination and, (b) hydroxylated Fe-layer termination with Fe/O stoichiometry of $O_3\text{-Fe-Fe-R}$ and $O_3\text{-Fe-}O_3\text{-Fe-R}$, respectively. The atoms shown in bold face were added to the surface unit cell. The layer stacking sequence is shown along c_s axis. The large spheres are O, medium spheres are Fe atoms and smallest sphere are H atoms. The water molecules are shown with random orientations. The best fit model parameters are given in Table 5.2 and 5.3.

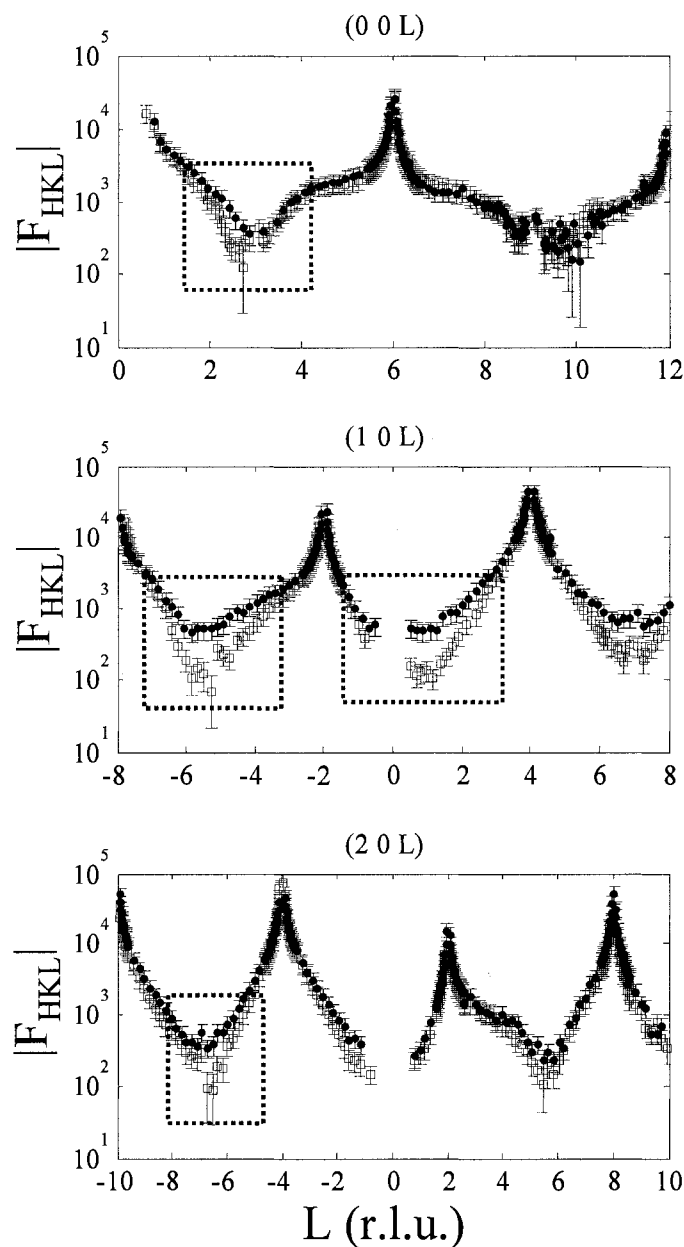


Figure 5.5 A comparison of experimental structure factor magnitudes as a function of perpendicular momentum transfer (L , in reciprocal lattice units) for unreacted (dots) and Fe(II) reacted (empty squares) $\alpha\text{-Fe}_2\text{O}_3(0001)$. The dotted boxes are used to highlight differences in CTR profile.

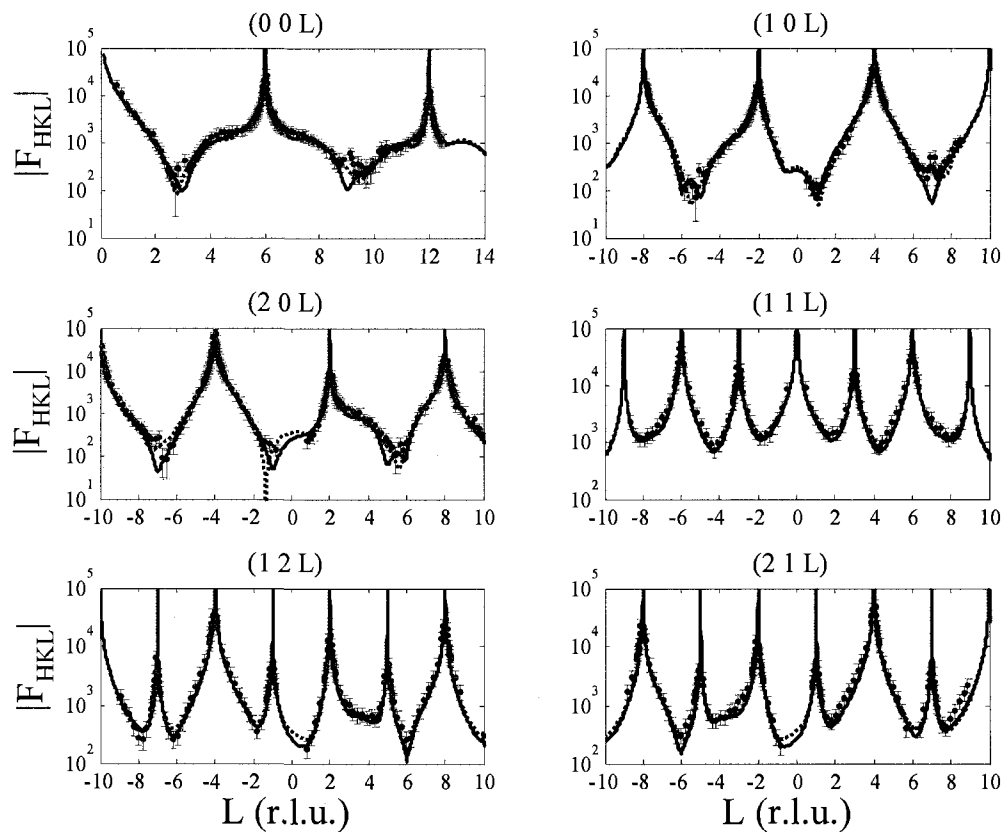


Figure 5.6 The magnitudes of experimental structure factors ($|F_{HKL}|$) (dots) and calculated structure factor magnitudes from single domain (dashed lines) and two domain (solid lines) model as a function of perpendicular momentum transfer (L , in reciprocal lattice units) for Fe(II) reacted α - $\text{Fe}_2\text{O}_3(0001)$.

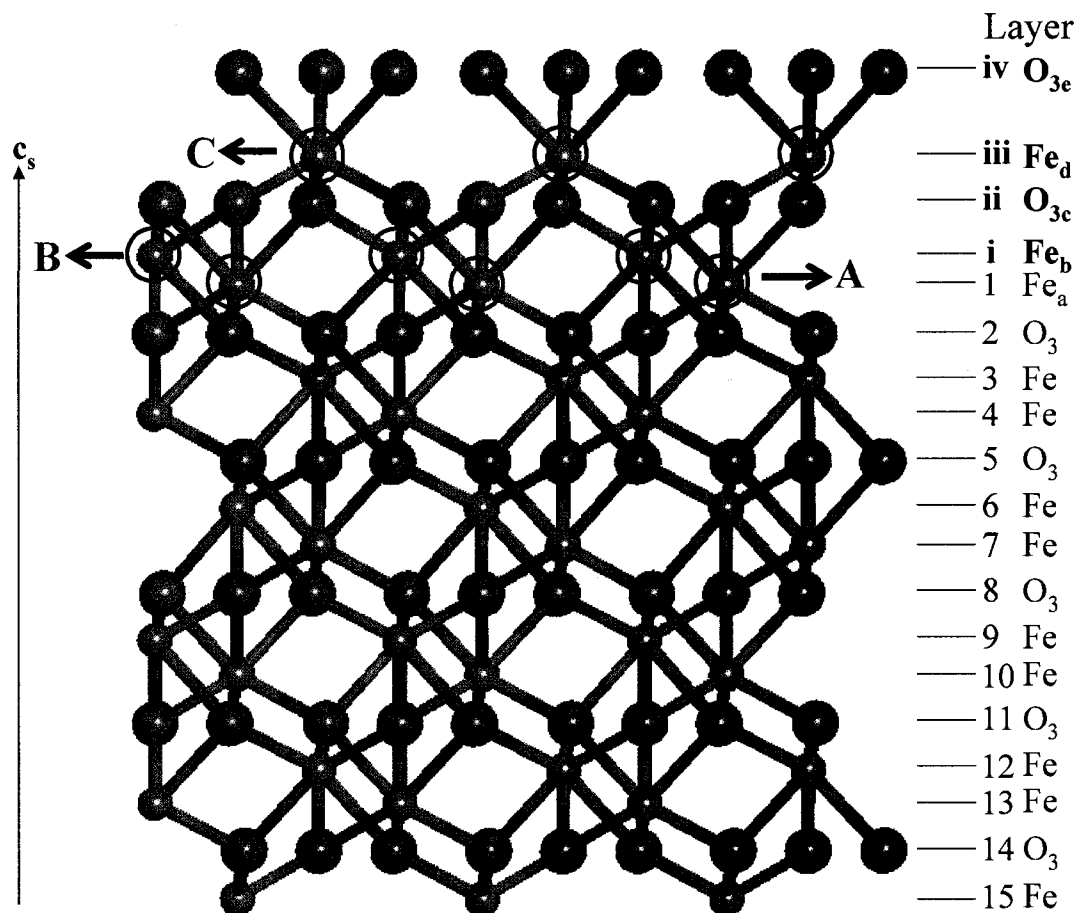


Figure 5.7 The layer stacking sequence along c_s axis for best fit single domain model for Fe(II) reacted α - $Fe_2O_3(0001)$ with Fe/O stoichiometry of $O_{3c}\text{-}Fe_d\text{-}O_{3c}\text{-}Fe_b\text{-}Fe_a\text{-}O_3\text{-}Fe\text{-}R$, where a, b, c, d, and e represent site occupancy of given atomic layers (Table 5.4). The atoms shown in bold face represent atoms that were added to the surface unit cell. The large spheres are O and small spheres are Fe atoms. The atoms shown in circles denote adsorbed Fe. The layers labeled as A, B, and C represent Fe adsorption sites.

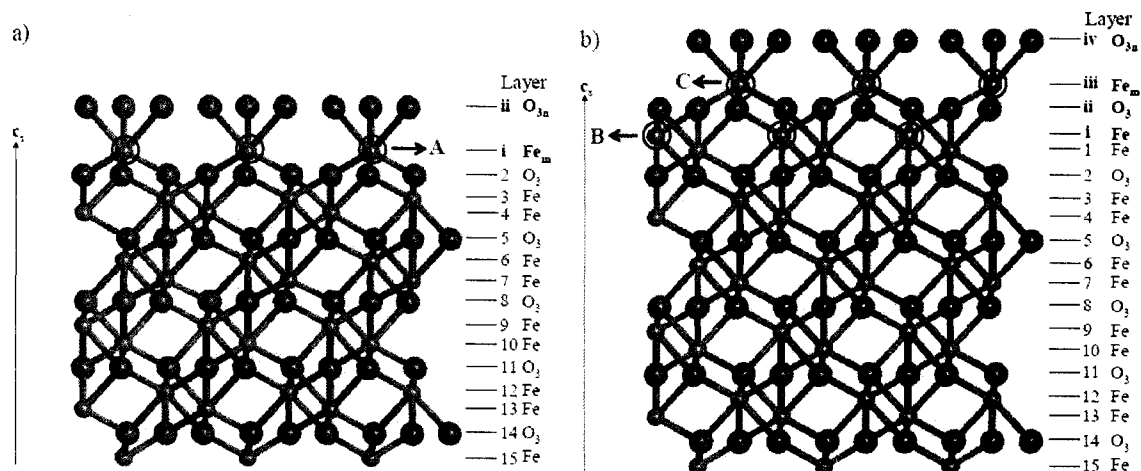


Figure 5.8 The structure for the best fit two-domain model for Fe(II) reacted α - $Fe_2O_3(0001)$ which includes relaxed (a) O-layer termination and, (b) hydroxylated Fe-layer termination with Fe/O stoichiometry of $O_{3n}\text{-}Fe_m\text{-}O_3\text{-}Fe\text{-}Fe\text{-}R$ and $O_{3n}\text{-}Fe_m\text{-}O_3\text{-}Fe\text{-}Fe\text{-}O_3\text{-}Fe\text{-}R$, respectively. The m and n in above stoichiometry represent occupancy of given layers (Table 5.5 and 5.6). The atoms shown in bold face were added to the surface unit cell. The large spheres are O and small spheres are Fe atoms. The atoms shown in circles denote adsorbed Fe. The layer stacking sequence is shown along c_s axis. The layers labeled as A, B, and C represent Fe adsorption sites.

Chapter 6 CONCLUSIONS

The detailed experimental studies to determine the molecular scale structure of hydrated hematite surfaces and their modification due to interactions with Fe(II) are presented in previous chapters. This chapter integrates the specific results discussed in previous chapters to discuss broader implications of the research presented in this thesis.

6.1 HYDRATED HEMATITE SURFACE STRUCTURE

Reactions at ubiquitous hematite surfaces affect the global transport and bioavailability of important nutrients and contaminants. The reactivity of hematite surfaces can be attributed to (hydr)oxo surface functional groups, which form complexes with aqueous ions and sequester them from solution to surface. Understandably, the surface complexation models that predict and explain the macroscopic uptake of aqueous species on the hematite surfaces are based on assumptions about the nature and coordination of surface (hydr)oxo reactive sites. Therefore, to improve predictive capabilities of surface complexation models a detailed molecular scale depiction of surface functional groups is required. However, there are limited studies that provide structural information about the coordination and arrangement of surface functional groups at the hematite surfaces under aqueous conditions. The current study utilized single crystals of hematite($1\bar{1}02$) and (0001) as model systems to develop structural understanding of hydrated hematite surfaces.

Based on the predominant growth faces of natural hematite (i.e. $(1\bar{1}02)$ and (0001)), a simplified model for a hematite particle can be envisioned as shown in Figure 6.1a. The experimental studies focused on determining the surface structure of hydrated $\alpha\text{-Fe}_2\text{O}_3(1\bar{1}02)$ are discussed in chapters 2 and 3. The results show that there are two possible surface structures for $\alpha\text{-Fe}_2\text{O}_3(1\bar{1}02)$. First, a structure in which the top Fe layer is vacant as compared to the bulk stoichiometric termination, and second, a structure that is consistent with hydroxylation of the stoichiometric termination. The surface consistent with vacant Fe layer termination has predominantly three types of surface oxo groups, which are singly ($^{\text{I}}\text{O}$), doubly ($^{\text{II}}\text{O}$), and triply ($^{\text{III}}\text{O}$) coordinated to Fe (Figure 6.1). In comparison, the hydroxylated stoichiometric termination is characterized by $^{\text{I}}\text{O}$ and $^{\text{III}}\text{O}$ groups (Figure 6.1).

For hydrated $\alpha\text{-Fe}_2\text{O}_3(0001)$, the results presented in chapter 5 show that two structural domains co-exist at the surface. The first domain is consistent with hydroxylation of the Fe-layer termination and the second domain is similar to the O-layer termination. The hydroxylated Fe-layer termination has two types of surface functional groups ($^{\text{I}}\text{O}$ and $^{\text{III}}\text{O}$), and the O-layer termination consists of $^{\text{II}}\text{O}$ groups (Figure 6.1). The above discussed results on the hydrated surface structures can be integrated to present a simplified structural model of hematite where both $(1\bar{1}02)$ and (0001) co-exist (Figure 6.1b). It is important to note that the integrated structural results shown in Figure 6.1 are obtained under simplified controlled conditions and do not account for the presence of organic matter or aqueous species common in natural geochemical environments.

However, these results are valuable as they provide a basis for understanding how the surface structure of hydrated hematite might evolve in aqueous systems.

6.2 HEMATITE SURFACE MODIFICATION VIA Fe(II)

In anoxic environments, the microbially promoted reductive dissolution of iron (hydr)oxides results in release of high concentrations of aqueous Fe(II). The presence of aqueous Fe(II) with solid phase ferric hydroxides gives rise to Fe(II)-Fe(III) oxides redox couple. The redox interactions of aqueous Fe(II) with Fe(III)-oxides significantly affects the biogeochemical cycling of Fe and is also linked to enhanced reductive transformations of a number of inorganic and organic contaminants. Therefore, it is critical to understand how Fe(II) interacts with iron (hydr)oxides in order to develop robust models for predicting global cycling and bioavailability of Fe and a number of environmentally relevant contaminants. The conceptual understanding of Fe(II) adsorption has been developed via surface complexation models, a majority of which assume that the adsorbed Fe(II) forms a mono-dentate surface complex, i.e. $\equiv\text{Fe(III)-O-Fe(II)}^+$ and/or $\equiv\text{Fe(III)-O-Fe(II)-OH}$, where $\equiv\text{Fe(III)-O}$ denotes a surface site on various iron (hydr)oxides such as hematite ($\alpha\text{-Fe}_2\text{O}_3$), goethite ($\alpha\text{-FeOOH}$), magnetite (Fe_3O_4), lepidocrocite ($\gamma\text{-FeOOH}$), and ferrihydrite (Fe(OH)_3)[1-5]. More recently, surface comeplexation modeling of Fe(II) adsorption is significantly advanced by including multi-dentate adsorption complexes, accounting for Fe(II) oxidation at the surface, and considering reaction sites based on the substrate structure [6].

The detailed studies on understanding the Fe(II) adsorption on hematite are presented in chapters 4 and 5. The results show that the adsorbed Fe modifies the crystalline termination of $\alpha\text{-Fe}_2\text{O}_3(1\bar{1}02)$ and (0001) by binding at crystallographic lattice sites on the substrate, and that the Fe(II) is oxidized to Fe(III) following adsorption. There was only one adsorbed Fe layer on $\alpha\text{-Fe}_2\text{O}_3(1\bar{1}02)$. In comparison, there were two adsorbed Fe layers on the single Fe-layer termination of $\alpha\text{-Fe}_2\text{O}_3(0001)$ and one adsorbed Fe layer on O-layer termination of $\alpha\text{-Fe}_2\text{O}_3(0001)$. The results on Fe(II) induced surface modification of $\alpha\text{-Fe}_2\text{O}_3(1\bar{1}02)$ and (0001) can be combined to depict how the simplified model of hematite (Figure 6.1) can be structurally altered in Fe(II) rich environments (Figure 6.2).

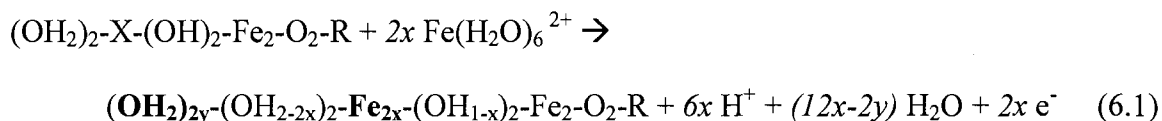
The structural understanding of how Fe(II) binds to the hematite surfaces can provide new directions for improving the existing surface complexation models for predicting the Fe(II) uptake affinity and pH dependence on iron (hydr)oxides. The structural results presented in this thesis indicate that the assumption of only one type of surface reaction site (e.g. $\equiv\text{Fe(III)-O}$ in most of the above cited models) is not sufficient. For instance, the hydrated $\alpha\text{-Fe}_2\text{O}_3(1\bar{1}02)$ and (0001) surfaces consist of three different types of surface oxo groups: singly ($^{\text{I}}\text{O}$), doubly ($^{\text{II}}\text{O}$) and triply ($^{\text{III}}\text{O}$) coordinated to Fe associated with the substrate (Figure 6.1b). Furthermore, the structural studies of Fe(II) adsorption on $\alpha\text{-Fe}_2\text{O}_3(1\bar{1}02)$ and (0001) surfaces show that all three types of surface oxo groups (i.e. $^{\text{I}}\text{O}$, $^{\text{II}}\text{O}$, and $^{\text{III}}\text{O}$) are involved in binding with adsorbed Fe (Figure 6.2), which indicates that

assuming one type of surface reaction site for Fe(II) adsorption is not viable. In addition, the adsorbed Fe binds at crystallographic lattice sites on both $\alpha\text{-Fe}_2\text{O}_3(1\bar{1}02)$ and (0001) resulting in a multi-dentate binding geometry and octahedral coordination for the adsorbed Fe (Figure 6.2), which highlights that modeling Fe(II) adsorption by assuming mono-dentate adsorption complexes may not be appropriate.

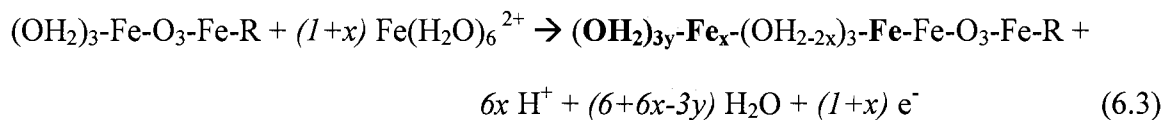
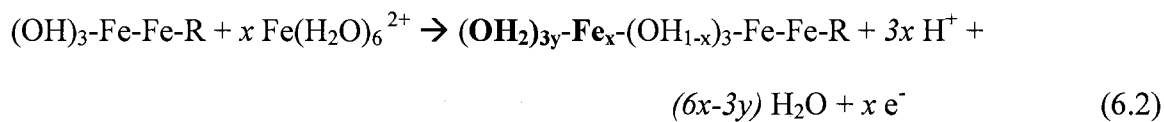
The accurate modeling of Fe(II) adsorption using explicit description of surface binding sites is tedious because it requires knowledge of predominant surface functional groups and structural identification of adsorbed Fe. The structural results presented in the current study suggest a different approach can be taken for modeling of Fe(II) adsorption on iron (hydr)oxides by utilizing a key result of Fe(II) adsorption studies on model system substrates (i.e. $\alpha\text{-Fe}_2\text{O}_3(1\bar{1}02)$ and (0001)), i.e. adsorbed Fe binds at the crystallographic lattice sites resulting in octahedrally coordinated surface Fe and modification of the surface stoichiometry (chapters 4 and 5).

For example, the Fe/O stoichiometry of unreacted $\alpha\text{-Fe}_2\text{O}_3(1\bar{1}02)$ surface can be given as $\text{O}_2\text{-X-O}_2\text{-Fe}_2\text{-O}_2\text{-R}$, where X denotes a vacant Fe-layer and R denotes the stoichiometric stacking sequence (chapter 2). Exposing hydrated $\alpha\text{-Fe}_2\text{O}_3(1\bar{1}02)$ surface to aqueous Fe(II) modified the Fe/O surface stoichiometry to $\text{O}_{2y}\text{-O}_2\text{-}\mathbf{Fe}_{2x}\text{-O}_2\text{-Fe}_2\text{-O}_2\text{-R}$, where x and y denote occupancy of given layers, and atoms in the boldface represent the atoms added to the surface stoichiometry to account for Fe(II) adsorption (chapter 4).

Based on changes in surface stoichiometry, we can derive a reaction stoichiometry for adsorption of Fe(II) on $\alpha\text{-Fe}_2\text{O}_3(1\bar{1}02)$ as:



In equation 6.1, protons are added to the surface oxo groups based on the assumptions that the valences of $^{\text{I}}\text{O}$ and $^{\text{II}}\text{O}$ groups are completed by adding two and one protons, respectively. Additionally, the $^{\text{III}}\text{O}$ groups are not assumed to hydroxylate because addition of a proton to these groups results in over-saturation. We note that these assumptions are consistent with the previous structural studies of hydrated $\alpha\text{-Fe}_2\text{O}_3(1\bar{1}02)$ (chapter 2 and ref. [7]). Similarly, using above assumptions and the structural results presented in Chapter 5, we can derive the reaction stoichiometry of Fe(II) adsorption on the O-layer and the hydroxylated Fe-layer termination of $\alpha\text{-Fe}_2\text{O}_3(0001)$ as given in equations 6.2 and 6.3, respectively.



In equations 6.2 and 6.3, the atoms shown in the bold face represent atoms added to the surface stoichiometry to account for Fe(II) adsorption and R represents continuation of the bulk stacking sequence.

The use of surface stoichiometries to describe the surface complexation of adsorbed Fe will result in models that will properly account for octahedral coordination of adsorbed Fe. In addition, the above reactions (6.1-6.3) show that the Fe(II) is oxidized indicating that the reaction must be coupled with a redox reaction to proceed as written, which is consistent with the previous studies which show that the electrons injected in the hematite substrate are mobile, and can possibly reduce Fe(III) at defects or relatively unstable surface sites resulting in release of Fe(II) in solution [8,9]. Furthermore, the reactions also show that the Fe(II) adsorption/oxidation will result in a surface of modified stoichiometry, which will provide additional reactive sites for continued reaction consistent with the recent observation of continued growth of the (0001) surface [8]. The modified (or product) surface (stoichiometry) may have a substantially different reactivity than the initial surface (stoichiometry). If the conceptual model shown in equations (1-3) is correct, it suggests that the distinction between Fe(II) sorptive behavior and substrate growth is limited by overcoming the (presumably thermodynamic) barrier of uptake on the product surfaces of reactions (6.1-6.3). These results may also have significant implications for understanding the heterogeneous transformations of aqueous species at the hematite-water interface. As shown reactions (6.1-6.3), the substrate in contact with Fe(II) effectively may act as an electrode to promote reduction distal to the

Fe(II) binding site. For instance, the reduction of structural Fe(III) will result in solid phase associated Fe(II), which can potentially donate an electron to promote reductive transformations of aqueous contaminants. Furthermore, the reaction of solution phase Fe(II) with the ferric-oxide will regenerate the solid phase Fe(II) sites to facilitate contaminant reduction, which also explains the observation that the enhanced contaminant reduction requires the presence of aqueous Fe(II) in contact with ferric-oxides [10]. We note that above reaction stoichiometries are based on experimental results that show inclusion of adsorbed Fe in crystal lattice sites on $\alpha\text{-Fe}_2\text{O}_3(1\bar{1}02)$ and (0001). Further studies on a wider range of surfaces, substrates and under a wider range of conditions, are needed to determine if the proposed Fe(II) reaction pathways can be extended beyond the limited conditions studied to date. Moreover, additional surface complexation modeling studies are also required to examine the efficacy of using surface stoichiometries to describe Fe(II) adsorption on iron (hydr)oxides.

6.3 IMPACT OF SURFACE MODIFICATION ON SURFACE REACTIVITY:

PRELIMINARY INDICATIONS

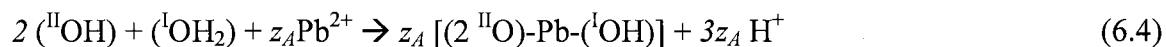
The core of the research work presented in this thesis was focused on determining the surface structure of hematite under hydrated conditions in absence and presence of aqueous Fe(II). The next step in continuing the research is to understand the interactions of common environmental contaminants (e.g. Pb(II), As(V), Sb(V), and Hg(II)) with the hematite surfaces and how these reactions are affected by Fe(II) induced surface modification.

Preliminary experiments have been conducted to study the interactions of Pb(II) (200 μm at pH 5) with unreacted and Fe(II) reacted $\alpha\text{-Fe}_2\text{O}_3(1\bar{1}02)$. A comparison of a subset of CTR data for unreacted and Pb(II) reacted $\alpha\text{-Fe}_2\text{O}_3(1\bar{1}02)$ surface (Figure 6.3) shows that there are significant changes in the CTR profile after reaction with Pb(II). These changes clearly suggest that the surface structure of $\alpha\text{-Fe}_2\text{O}_3(1\bar{1}02)$ is modified due to adsorption of Pb(II) at ordered sites on the surface. To quantitatively determine the structural details of adsorbed Pb(II), a detailed analysis of CTR data is required. In addition to the CTR data, we also collected resonant anomalous X-ray scattering (RAXS) data which will aid in providing better constraints on the coordinates and occupancy of the surface bound Pb(II). More details on CTR and RAXS data collection are provided in the Appendix.

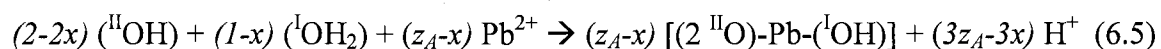
We further performed Pb(II) adsorption experiments on Fe(II) reacted $\alpha\text{-Fe}_2\text{O}_3(1\bar{1}02)$. A subset of CTR data for the Pb(II) reacted $\alpha\text{-Fe}_2\text{O}_3(1\bar{1}02)$ is compared with CTR data for the surface which was reacted with Fe(II) prior to Pb(II) adsorption in Figure 6.4. The significant differences in CTR profiles (Figure 6.4) suggest that Pb(II) adsorption geometry (and/or occupancy) is appreciably affected by Fe(II) induced surface modification of $\alpha\text{-Fe}_2\text{O}_3(1\bar{1}02)$ indicating that the unreacted and Fe(II) reacted surfaces exhibit different reactivity towards Pb(II).

A comparison of unreacted and Fe(II) reacted $\alpha\text{-Fe}_2\text{O}_3$ surfaces show the coordination of surface (hydr)oxo groups is altered due to adsorption of Fe(II) on the surface. For example, the unreacted $\alpha\text{-Fe}_2\text{O}_3(1\bar{1}02)$ surface has three types surface oxo groups, i.e. singly ($^{\text{I}}\text{O}$), doubly ($^{\text{II}}\text{O}$) and triply ($^{\text{III}}\text{O}$) coordinated to Fe, respectively (Figure 6.5). After Fe(II) adsorption, the surface is dominated by $^{\text{I}}\text{O}$ and $^{\text{III}}\text{O}$ surface (hydr)oxo groups. The modification in number and type of predominant surface functional groups is likely to influence the surface reactivity of $\alpha\text{-Fe}_2\text{O}_3(1\bar{1}02)$ with respect to Pb(II).

A qualitative insight into the structure of Pb(II) adsorbed on $\alpha\text{-Fe}_2\text{O}_3(1\bar{1}02)$ can be gained by using the knowledge of unreacted surface structure and including Pb(II) in the surface unit cell at positions which result in reasonable Pb-O bond lengths and coordination. However, there are a large number of possible models that have plausible Pb-O bond lengths and coordination (e.g. mono-, bi-, tri-dentate), all of which must be examined using the data presented in the Appendix. However, the number of plausible models will reduce if we account for the preferred local geometry of Pb(II). Previous experimental studies focused on identifying the local structure of adsorbed Pb(II) show that it binds to hematite as a tri-dentate complex [11, 12]. There are two chemically plausible tri-dentate adsorption geometries of Pb(II) on $\alpha\text{-Fe}_2\text{O}_3(1\bar{1}02)$ as shown in Figure 6.6. Based on these predicted binding geometries, the reaction stoichiometry for Pb(II) adsorption can also be postulated. For example, the reaction stoichiometry (based on binding sites) for the model shown Figure 6.6a can be given as:



where z_A is the uptake of Pb(II) per surface unit cell. The protons are added to the surface oxo groups using assumptions discussed in section 6.2. In addition, we can qualitatively understand how the modification of the $\alpha\text{-Fe}_2\text{O}_3(1\bar{1}02)$ surface due to adsorption of Fe at crystal lattice sites will affect the surface reactivity. For example, the inclusion of adsorbed Fe at crystal lattice sites will result in a decrease in total number of $^{\text{II}}\text{OH}$ and $^{\text{I}}\text{OH}_2$ sites. Assuming that the adsorbed Pb(II) binds in a mode similar to that shown Figure 6.6a, the reaction stoichiometry of Pb(II) adsorption on a Fe(II) reacted surface can be given as:



where x denotes number of unavailable sites due to surface modification by adsorbed Fe. A comparison of reaction stoichiometries presented in equations 6.4 and 6.5 suggests that decrease in the number total binding sites can result in relatively lower uptake of Pb(II) on the Fe(II) reacted surface (equation 6.5) as compared to the unreacted $\alpha\text{-Fe}_2\text{O}_3(1\bar{1}02)$ surface (equation 6.4). It is also possible that Pb(II) binding geometry on Fe(II)-modified surface differs from the one shown in Figure 6.6a which would result in a reaction stoichiometry inconsistent with equation 6.5. In any case, it is clear that the overall reaction stoichiometry for Pb(II) adsorption will change due to changes in surface structure, which will result in an altered Pb(II) adsorption affinity for Fe(II)-modified

surfaces. However, to completely decipher how the extent and adsorption geometry of Pb(II) adsorbed on α -Fe₂O₃ is affected by Fe(II) induced surface modification a more detailed analysis of the experimental data (shown in the Appendix) is required.

REFERENCES

- [1] L. Charlet, E. Silvester and E. Liger, *Chem. Geol.* 151 (1998) 85.
- [2] B. R. Coughlin and A. T. Stone, *Environ. Sci. Technol.* 29 (1995) 2445.
- [3] E. Liger, L. Charlet and P. Van Cappellen, *Geochim. Cosmochim. Acta* 63 (1999) 2939.
- [4] E. Silvester, L. Charlet, C. Tournassat, A. Gehin, J.-M. Greneche and E. Liger, *Geochim. Cosmochim. Acta* 69 (2005) 4801.
- [5] Y. Zhang, L. Charlet and P. W. Schindler, *Colloids Surf.* 63 (1992) 259.
- [6] T. Hiemstra and W. H. van Riemsdijk, *Geochim. Cosmochim. Acta* 71 (2007) 5913.
- [7] C. S. Lo, K. S. Tanwar, A. M. Chaka and T. P. Trainor, *Phys. Rev. B: Condens. Matter* 75 (2007) 075425/1.
- [8] S. V. Yanina and K. M. Rosso, *Science* 320 (2008) 218.
- [9] S. Kerisit and K. M., *Geochim. Cosmochim. Acta* 70 (2006) 1888.
- [10] A. G. B. Williams and M. M. Scherer, *Environ. Sci. Technol.* 38 (2004) 4782.
- [11] J. R. Bargar, G. E. Brown, Jr. and G. A. Parks, *Geochim. Cosmochim. Acta* 61 (1997) 2639.
- [12] J. R. Bargar, T. P. Trainor, J. P. Fitts, S. A. Chambers and G. E. Brown, Jr., *Langmuir* 20 (2004) 1667.

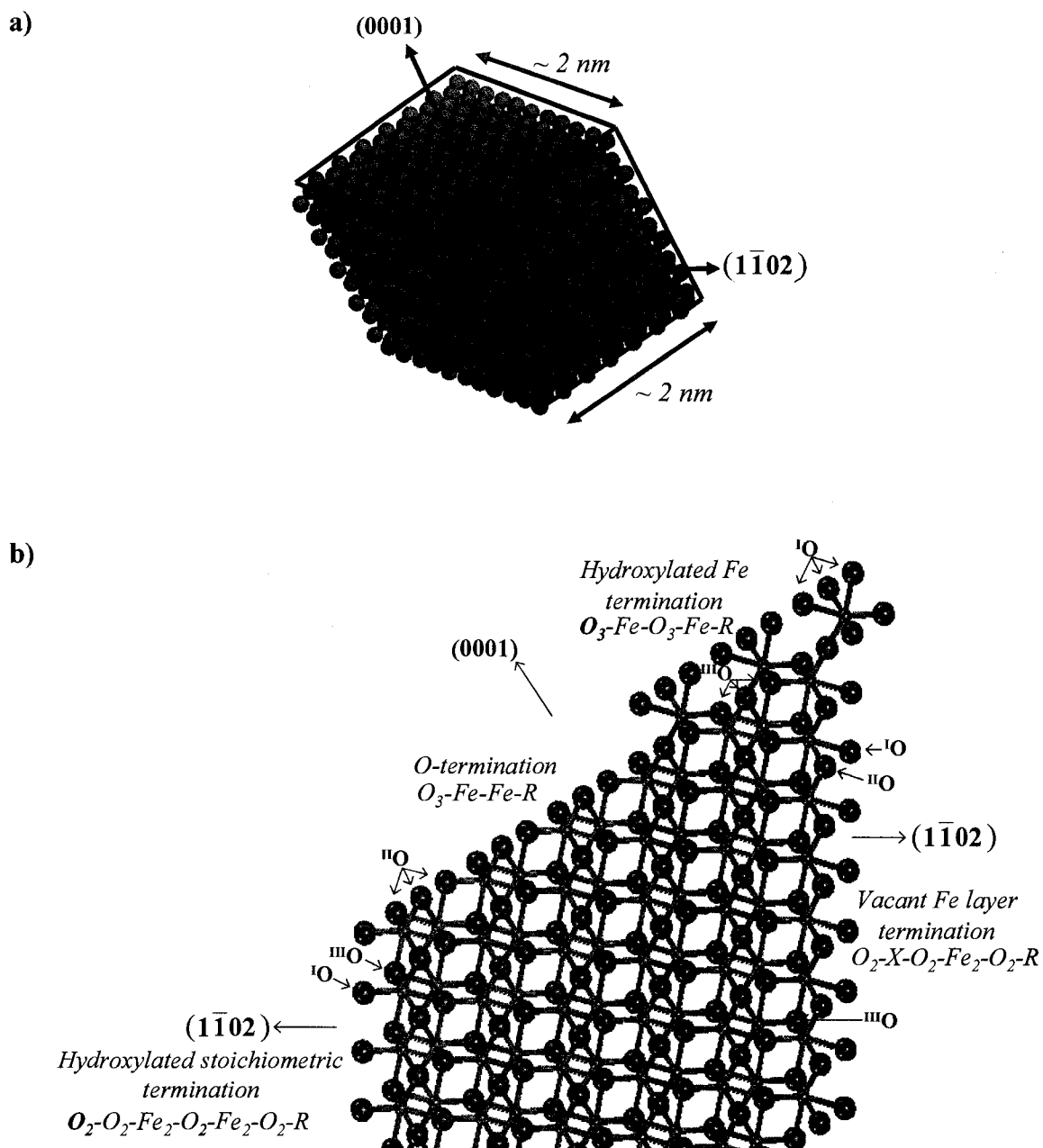


Figure 6.1 a) A simplified model of a hematite particle which has two predominant surface orientations (i.e. (1 $\bar{1}$ 02) and (0001)) of hematite, and b) structural model of the simplified hematite particle based on results from CTR studies on hydrated $\alpha\text{-Fe}_2\text{O}_3$ (1 $\bar{1}$ 02) and (0001). The smaller spheres represent Fe atoms and the larger spheres represent O atoms. The I°O , II°O , and III°O represent oxygen atoms singly, doubly and triply coordinated to Fe, respectively.

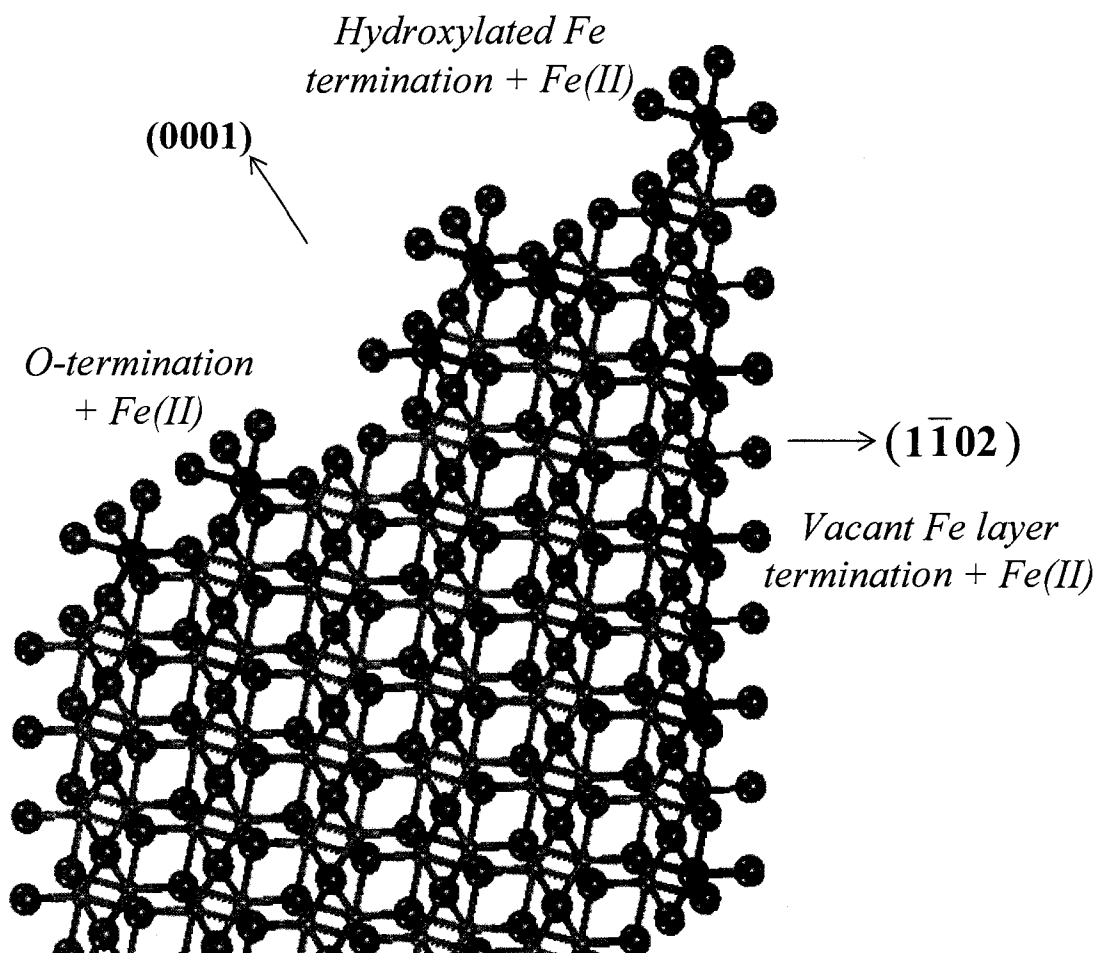


Figure 6.2 A structural model of the simplified hematite particle after reacted with Fe(II) based on results from CTR studies on Fe(II) reacted $\alpha\text{-Fe}_2\text{O}_3(1\bar{1}02)$ and (0001). The smaller spheres are Fe and the larger spheres are O atoms. The atoms shown in circles represent adsorbed Fe atoms.

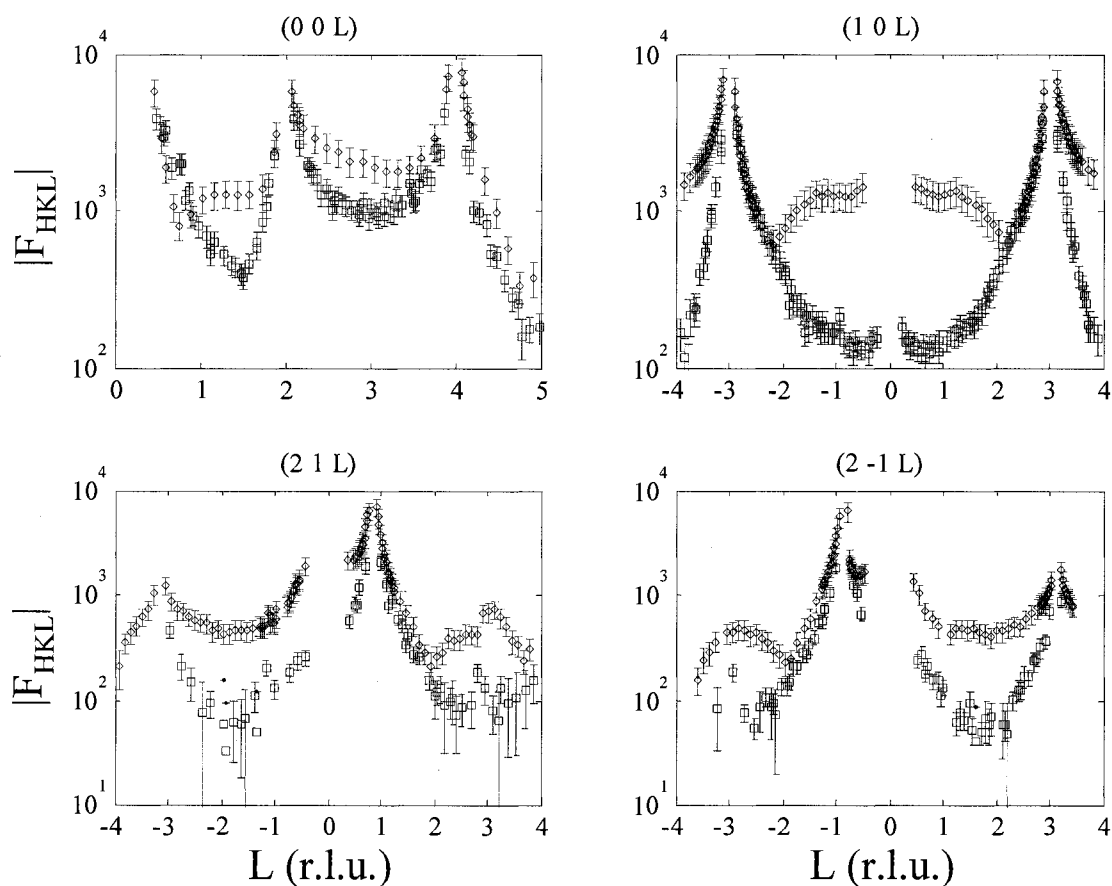


Figure 6.3 A comparison of experimental structure factors ($|F_{HKL}|$) as a function of perpendicular momentum transfer (L , in reciprocal lattice units) for unreacted (squares) and Pb(II) reacted (diamonds) $\alpha\text{-Fe}_2\text{O}_3(1\bar{1}02)$. The data for Pb(II) reacted surface is scaled higher than unreacted surface for clarity.

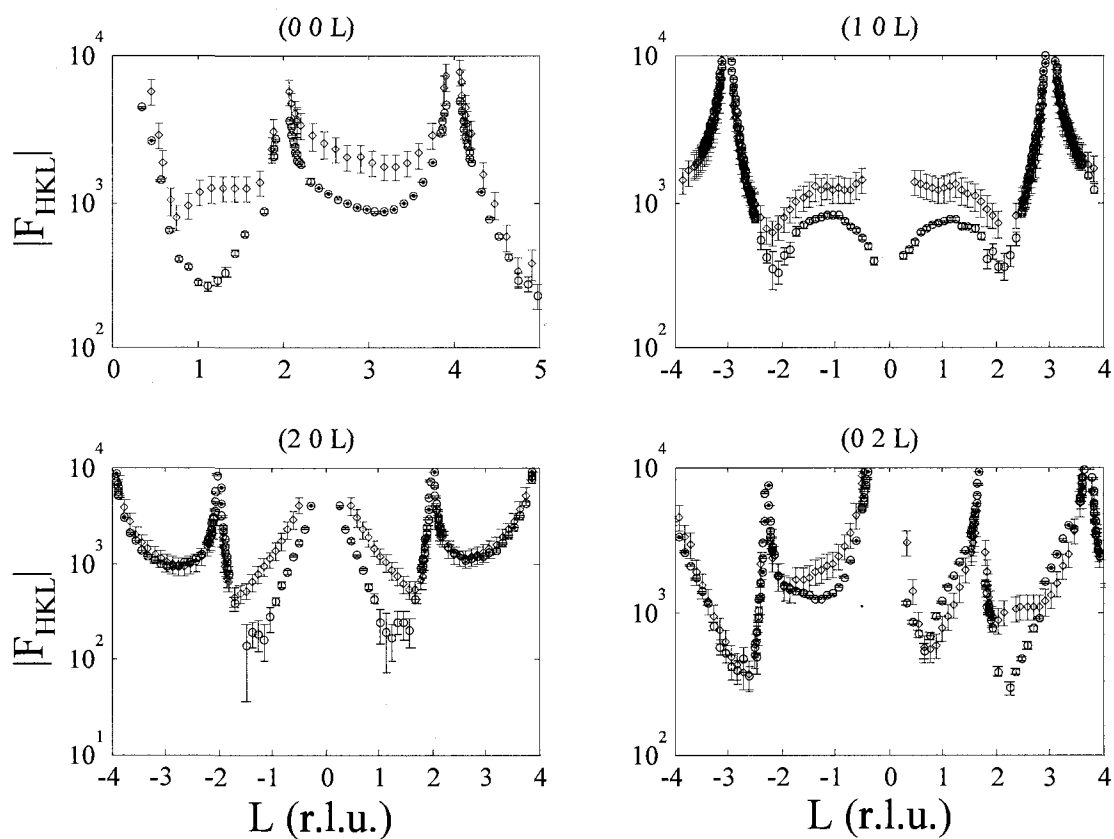


Figure 6.4 A comparison of experimental structure factors ($|F_{HKL}|$) as a function of perpendicular momentum transfer (L , in reciprocal lattice units) for Pb(II) adsorption on $\alpha\text{-Fe}_2\text{O}_3(1\bar{1}02)$ (diamonds) and Pb(II) adsorption on Fe(II) reacted $\alpha\text{-Fe}_2\text{O}_3(1\bar{1}02)$ (circles).

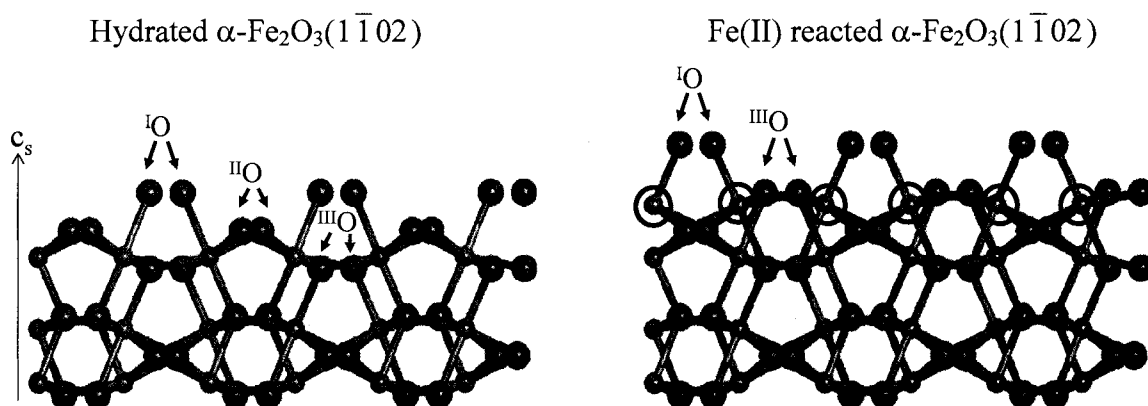


Figure 6.5 A comparison of surface structure of unreacted and Fe(II) reacted $\alpha\text{-Fe}_2\text{O}_3(1\bar{1}02)$. The I^O , II^O , and III^O represent oxygen atoms singly, doubly and triply coordinated to Fe, respectively. The smaller spheres are Fe and the larger spheres are O atoms. The atoms shown in circles represent adsorbed Fe atoms.

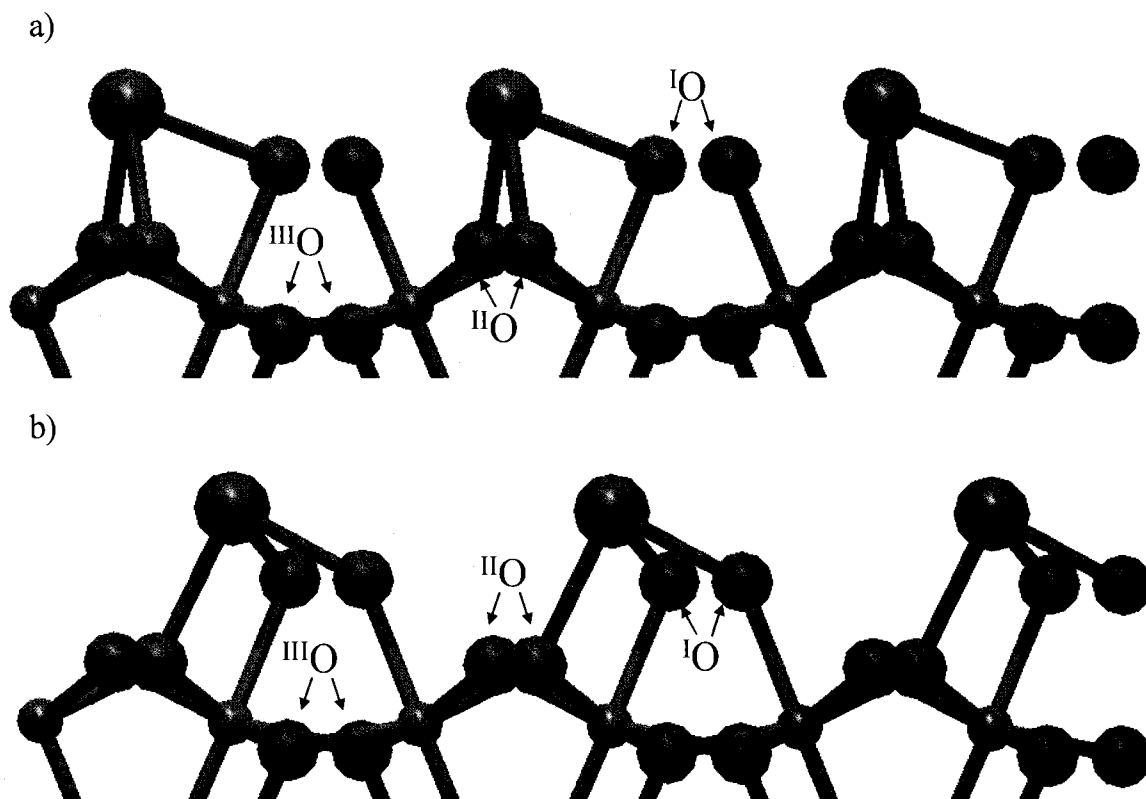


Figure 6.6 Structural models of two possible tri-dentate Pb(II) binding geometries on α - $\text{Fe}_2\text{O}_3(1\bar{1}02)$. The small, medium and large spheres represent Fe, O and Pb atoms, respectively. The $^{\text{I}}\text{O}$, $^{\text{II}}\text{O}$ and $^{\text{III}}\text{O}$ represent oxygen atoms which singly, doubly and triply coordinated to Fe associated with the substrate, respectively. Only top four layers of the substrate are shown for clarity.

APPENDIX

Pb(II) ADSORPTION ON UNREACTED AND Fe(II) REACTED $\alpha\text{-Fe}_2\text{O}_3(1\bar{1}02)$

A.1 INTRODUCTION

The differences in coordination of predominant surface functional groups on unreacted and Fe(II) reacted $\alpha\text{-Fe}_2\text{O}_3(1\bar{1}02)$ surface suggest the corresponding surface reactivity may also be dissimilar. To quantitatively explain the differences in surface reactivity, we conducted Pb(II) adsorption experiments on unreacted and Fe(II) pre-reacted $\alpha\text{-Fe}_2\text{O}_3(1\bar{1}02)$. The choice of Pb(II) as a reactive probe for the above-mentioned experiments is based on two important reasons: (1) Pb is an environmental contaminant of concern, therefore, it is important to understand its interactions with abundant iron (hydr)oxide substrates, (2) Pb possesses high X-ray scattering cross-section, which makes it an ideal probe for surface X-ray scattering measurements. We collected in situ crystal truncation rod (CTR) diffraction and resonant anomalous X-ray scattering (RAXS) data for Pb(II) adsorption on unreacted and Fe(II) pre-reacted $\alpha\text{-Fe}_2\text{O}_3(1\bar{1}02)$ surface. The details of experiments and a few pointers to aid in data analysis are given below.

A.2 EXPERIMENTAL DETAILS

A.2.1 Sample Preparation

A.2.1.1 Unreacted $\alpha\text{-Fe}_2\text{O}_3(1\bar{1}02)$

All experiments were conducted using natural single crystals of hematite which were obtained from Bahia, Brazil. The samples were polished along $(1\bar{1}02)$ face. The α -

$\text{Fe}_2\text{O}_3(1\bar{1}02)$ samples were prepared using a wet chemical and mechanical polishing (CMP) procedure [1]. After CMP, the samples were etched in 0.01 N HNO_3 for 2 h followed by thorough rinsing with ultra-pure ($> 18 \text{ M}\Omega$) water. The sample preparation and cleaning procedure discussed above results in high quality surfaces for CTR data collection [1,2]

A.2.1.2 Pb(II) adsorption on $\alpha\text{-Fe}_2\text{O}_3(1\bar{1}02)$

One of the CMP prepared $\alpha\text{-Fe}_2\text{O}_3(1\bar{1}02)$ samples was mounted on the $2 + 2 + \text{kappa}$ geometry Newport diffractometer at APS Sector 13 followed by sample orientation. The $\alpha\text{-Fe}_2\text{O}_3(1\bar{1}02)$ samples were then reacted in situ with 200 μm Pb(II) solutions (at pH 5) using a reaction cell which was also mounted on the diffractometer. The reaction cell was equipped with X-ray transparent windows [3], which allowed us to collect in situ CTR data for Pb(II) reaction with $\alpha\text{-Fe}_2\text{O}_3(1\bar{1}02)$.

A.2.1.3 Pb(II) adsorption on Fe(II) reacted $\alpha\text{-Fe}_2\text{O}_3(1\bar{1}02)$

The CMP prepared $\alpha\text{-Fe}_2\text{O}_3(1\bar{1}02)$ sample was first reacted ex-situ with 4 mM Fe(II) (at pH 5) for 4 h under strict anoxic conditions using a N_2 glove box. After reaction with Fe(II), the sample was rinsed with ultra-pure DI water. The sample was then mounted on diffractometer and was reacted with 200 μm Pb(II) solutions (at pH 5) followed by in situ CTR data collection for Pb(II) adsorption on Fe(II) reacted $\alpha\text{-Fe}_2\text{O}_3(1\bar{1}02)$.

A.2.2 CTR Data Collection

All in situ CTR measurements were conducted at Advanced Photon Source (APS) on an undulator beamline 13-IDC using a $2 + 2 + \text{kappa}$ -geometry Newport diffractometer for sample orientation and scanning. The incident beam energy was tuned to 12.025 keV for Pb(II) reacted sample and to 12 keV for Pb(II) adsorption on Fe(II) reacted $\alpha\text{-Fe}_2\text{O}_3(1\bar{1}02)$ using a liquid N_2 cooled double crystal Si(111) monochromator. The X-ray beam was focused on the center of the diffractometer to a beam size of 0.20×1.50 mm (horizontal \times vertical) using two Rhodium (Rh) coated Si mirrors. X-ray scattering intensity was measured using a Bede detector which was set to reject Fe fluorescence counts. The non-specular rods were collected at an incident angle of 2° by performing rocking scans through the truncation rods using a continuous (trajectory) scan of the diffractometer ϕ -axis at a particular reciprocal lattice setting. Specular rods were collected by scanning the ω -axis of the diffractometer.

The magnitudes of individual structure factors ($|F_{\text{HKL}}|$) were determined by taking square root of background subtracted intensity of the rocking curves and correcting for active area, polarization, step size and Lorentz factors [4]. In the notation used above, the reciprocal vector indices H and K correspond to in-plane momentum transfer and L corresponds to perpendicular momentum transfer. The data was averaged in the p1 plane group. The full data set consisted of nine crystal truncation rods for both samples (Figure A.1 and A.2). A subset of the data set repeated to check for beam induced surface damage showed the surfaces were stable during the full course of measurements.

A.2.3 Pb(II) Resonant Anomalous X-ray Scattering (RAXS) Data Collection

Following CTR data collection, the in situ Pb(II) resonant anomalous X-ray scattering data was collected for both samples i.e. $\alpha\text{-Fe}_2\text{O}_3(1\bar{1}02)$ reacted with Pb(II) (Figure A.3), and Pb(II) adsorbed on $\alpha\text{-Fe}_2\text{O}_3(1\bar{1}02)$ which was pre-reacted with Fe(II) (Figure A.4). The RAXS data was collected at various fixed (HKL) values by measuring $|F_{\text{HKL}}|$ as a function of incident beam energy. The range for incident beam energy was 12.543-13.293 keV for Pb(II) reacted sample and 12.193-13.543 keV for the sample which was reacted with Fe(II) before exposing it to Pb(II) solutions.

A.3 POINTERS FOR INITIATING DATA ANALYSIS

First, the analysis of CTR and RAXS data for Pb(II) adsorption on CMP prepared $\alpha\text{-Fe}_2\text{O}_3(1\bar{1}02)$ should be conducted in order to understand Pb(II) binding. Next, the Pb(II) binding on Fe(II) reacted $\alpha\text{-Fe}_2\text{O}_3(1\bar{1}02)$ should be elucidated to quantitatively depict differences in surface reactivity of unreacted and Fe(II) reacted $\alpha\text{-Fe}_2\text{O}_3(1\bar{1}02)$ with respect to Pb(II).

The surface structure of CMP prepared $\alpha\text{-Fe}_2\text{O}_3(1\bar{1}02)$ surface allows for a number of possible Pb(II) adsorption geometries. Three of the possible Pb(II) binding models are shown in Figure A.5, which include one bi-dentate and two different tri-dentate Pb(II) adsorption geometries. The atomic coordinates of the three models are given in Tables

A.1-A.3. We have conducted a very limited preliminary CTR data analysis (not shown) where we could not exclude the possibility of Pb(II) binding similar to any of the three models shown in Figure A.5. Furthermore, the possibility of Pb(II) binding simultaneously in multiple geometries also needs to be explored.

In addition to CTR data, we also collected in situ Pb(II) RAXS data to correctly identify the predominant Pb(II) binding geometry and to achieve better constraints on coordinates of Pb(II) adsorbed at the surface. Details about theory, formalism and application of RAXS to study structure of adsorbates on mineral surfaces can be found elsewhere [5-8]. A brief introduction to RAXS is given here. The experimentally derived total structure factor magnitude at a given (HKL) can be given by equation A1,

$$|F_T| = SR(|F_{bc}F_{CTR} + F_{sc}|) \quad (A.1)$$

where, F_T is total structure factor, S is an overall scale factor, R is roughness factor, F_{bc} is the structure factor of the bulk unit cell and F_{sc} is structure factor of the surface unit cell. We note Debye-Waller parameters are ignored in the given equations for simplicity of discussion. The F_{CTR} is given as,

$$F_{CTR} = 1/[1 - \exp(-i2\pi L)] \quad (A.2)$$

The structure factor of the surface unit cell can be given as,

$$F_{sc} = \sum_{j=1}^n \theta_j f_j \exp(iQ \cdot r_j) \quad (A.3)$$

where Q is the scattering vectors and the sum is taken over n atoms of the surface unit cell having fractional coordinates r_j and atomic scattering factors f_j .

The atomic scattering factor f_j has three components and can be given as,

$$f_j = f_j^0 + f_j' + if_j'' \quad (\text{A.4})$$

where f_j^0 is the atomic scattering factor, and f_j' and f_j'' are anomalous scattering factors which arise mainly due to absorption of X-rays by the scattering atom and gains significance when the data is collected near X-ray absorption edge of the scattering atom.

The $|F_T|$ collected via CTR measurements at energy far from absorption edges of constituent atoms of a system has contributions from f_j^0 only. In case of RAXS measurements, the F_T is collected as function of energy, where the energy range includes the X-ray absorption edge of a particular scattering atom. Due to X-ray absorption by a given atom, the contributions of f_j' and f_j'' also become significant. Importantly, the choice of energy range for data collection means the f_j' and f_j'' are only relevant for a particular atom highlighting the resonant scattering signal is element specific in this case. Thus, analysis of RAXS data along with CTR data can serve as excellent tool to determine positions and occupancy of adsorbates bound on mineral surfaces.

For data presented here, the analysis of experimental Pb(II) RAXS data has not been conducted so far. However, we performed theoretical RAXS simulations to gain initial insight into how RAXS profile of Pb(II) adsorbed on $\alpha\text{-Fe}_2\text{O}_3(1\bar{1}02)$ might differ for different Pb(II) adsorption models, and the effect of parameters such as occupancy on overall RAXS profile (Figure A.6 and A.7). The simulations were performed by

including the resonant contribution of Pb(II) only, which is reasonable considering the energy range (i.e. 12.8 - 13.3 keV) for these calculations includes Pb L_{III} X-ray absorption edge (~ 13.035 keV) but is far from X-ray absorption edge of Fe (K-edge ~7.112 keV)

A comparison of simulated RAXS profile for the three possible Pb adsorption models (Figure A.5) are shown in Figure A.6, where solid, dashed and dotted lines represent models A, B and C, respectively. The occupancy factor for Pb(II) was fixed (= 1.0) for the calculations shown in Figure A.6. The simulation show the RAXS profiles at various (HKL) are different for the three models highlighting the sensitivity of RAXS to various modes of Pb(II) binding. Furthermore, the simulations for model C show there is no Pb resonant signal at (HKL) values of (1 0 1.25) and (1 0 1.89). The absence of resonant signal can be explained by analyzing Pb coordinates in model C (Table A.3). There are two Pb atoms in the unit cell placed at chemically equivalent sites which are half a unit cell apart in x-direction (Table A.3). The two Pb atoms likely cancel out each other's resonant signal for (HKL) values sensitive to only x-positions of the two Pb atoms (at same z-coordinate). The calculation (not shown) involving only one of the two chemically equivalent Pb atoms results in a clear resonant signal. In comparison to these simulations, the experimental data shows a strong resonant scattering profile at (HKL) values of (1 0 1.25) and (1 0 1.89) (Figure A.3). Thus, based on the preliminary RAXS simulations, the model C where no resonant signal at the above discussed (HKL) was

observed can be excluded. However, a more detailed analysis is necessary to understand full structural details of surface bound Pb(II).

To understand the effect of occupancy parameter on RAXS, simulations were performed using model A where the occupancy of Pb was varied (Figure A.7). As occupancy of Pb is increased, the resonant signal becomes stronger. Therefore, the magnitude of resonant signal can be used as a guide to constrain the occupancy of Pb. In summary, RAXS simulations shown in Figures A.6 and A.7 clearly show the sensitivity of RAXS to different binding models and parameters such as occupancy.

A more detailed and general discussion about theory of RAXS and approach to data analysis can be found in recent literature [5-8]. There can be at least two approaches to analyze complementary CTR and RAXS data for a given system. The first approach is to perform a simultaneous analysis of CTR and RAXS data, which is conceptually simple but will require development of an analysis software which can simultaneously handle CTR data (collected at a fixed energy) and RAXS data (collected as a function of energy). The second approach is to perform sequential analysis of CTR and RAXS data iteratively. In other words, the CTR data can be analyzed first to obtain coordinates of Pb, which can be used to further refine Pb positions using RAXS data. The sequential CTR and RAXS analysis should be repeated every time with new refined Pb positions till models obtained via CTR and RAXS analysis agree with each other. The advantage of second approach is that the existing programs for CTR data analysis can be utilized. However, a RAXS

analysis program still needs to be developed and the iterative nature of second approach is not likely to be time efficient for complicated systems (e.g., Pb(II) adsorption of Fe(II) pre-reacted α -Fe₂O₃(1 $\bar{1}$ 02)). Overall, a combination CTR and RAXS analysis can serve as an excellent tool to elucidate the surface structure of substrates such as iron (hydr)oxides in absence and presence of adsorbed species such as Pb(II).

REFERENCES

- [1] K.S. Tanwar, C.S. Lo, P.J. Eng, J.G. Catalano, D.K. Walko, G.E. Brown Jr., G.A. Waychunas, A.C. Chaka, T.P. Trainor, *Surf. Sci.* 601 (2007) 460.
- [2] T.P. Trainor, A.M. Chaka, P.J. Eng, M. Newville, G.A. Waychunas, J.G. Catalano, G.E. Brown Jr., *Surf. Sci.* 573 (2004) 204.
- [3] T.P. Trainor, A.S. Templeton, P.J. Eng, *J. Electron. Spectrosc. Relat. Phenom.* 150 (2006) 66.
- [4] I.K. Robinson, in: G. Brown, D.E. Moncton (Eds.), *Handbook on Synchrotron Radiation*, Elsevier, Amsterdam, 1991, p. 221.
- [5] G. Materlik, C. Sparks, K. Fischer, *Resonant Anomalous X-ray Scattering: Theory and Applications*, Elsevier, Amsterdam, 1994.
- [6] P. Fenter, C. Park, K. Nagy, N. Sturchio, *Thin Solid Films*, 515 (2007) 5654.
- [7] C. Park, P. Fenter, *J. Appl. Cryst.*, 40 (2007) 290.
- [8] C. Park, P. Fenter, N. Sturchio, J. Regalbuto, *Phys. Rev. Lett.*, 94 (2005) 076104.

Table A.1 Surface unit cell coordinates for $\alpha\text{-Fe}_2\text{O}_3(1\bar{1}02)$ including Pb adsorbed at the surface in a geometry similar to model A (Figure A.5).

Layer		x	y	z
i	Pb	0.250	0.360	2.010
	Pb	0.250	0.860	2.010
1	O	0.653	0.974	1.903
	O	0.847	0.474	1.903
2	O	0.194	0.105	1.750
	O	0.306	0.605	1.750
3	Fe	0.000	0.380	1.645
	Fe	0.500	0.880	1.645
4	O	0.653	0.237	1.597
	O	0.847	0.737	1.597
5	O	0.153	0.404	1.403
	O	0.347	0.904	1.403
6	Fe	0.500	0.261	1.355
	Fe	0.000	0.761	1.355
7	O	0.694	0.535	1.250
	O	0.806	0.035	1.250
8	Fe	0.500	0.810	1.145
	Fe	0.000	0.310	1.145
9	O	0.153	0.667	1.097
	O	0.347	0.166	1.097

Table A.2 Surface unit cell coordinates for $\alpha\text{-Fe}_2\text{O}_3(1\bar{1}02)$ including Pb adsorbed at the surface in a geometry similar to model B (Figure A.5).

Layer		x	y	z
i	Pb	0.750	0.224	2.14
	Pb	0.750	0.724	2.14
1	O	0.653	0.974	1.903
	O	0.847	0.474	1.903
2	O	0.194	0.105	1.750
	O	0.306	0.605	1.750
3	Fe	0.000	0.380	1.645
	Fe	0.500	0.880	1.645
4	O	0.653	0.237	1.597
	O	0.847	0.737	1.597
5	O	0.153	0.404	1.403
	O	0.347	0.904	1.403
6	Fe	0.500	0.261	1.355
	Fe	0.000	0.761	1.355
7	O	0.694	0.535	1.250
	O	0.806	0.035	1.250
8	Fe	0.500	0.810	1.145
	Fe	0.000	0.310	1.145
9	O	0.153	0.667	1.097
	O	0.347	0.166	1.097

Table A.3 Surface unit cell coordinates for $\alpha\text{-Fe}_2\text{O}_3(1\bar{1}02)$ including Pb adsorbed at the surface in a geometry similar to model C (Figure A.5).

Layer		x	y	z
i	Pb	0.000	0.140	2.030
	Pb	0.500	0.640	2.030
1	O	0.653	0.974	1.903
	O	0.847	0.474	1.903
2	O	0.194	0.105	1.750
	O	0.306	0.605	1.750
3	Fe	0.000	0.380	1.645
	Fe	0.500	0.880	1.645
4	O	0.653	0.237	1.597
	O	0.847	0.737	1.597
5	O	0.153	0.404	1.403
	O	0.347	0.904	1.403
6	Fe	0.500	0.261	1.355
	Fe	0.000	0.761	1.355
7	O	0.694	0.535	1.250
	O	0.806	0.035	1.250
8	Fe	0.500	0.810	1.145
	Fe	0.000	0.310	1.145
9	O	0.153	0.667	1.097
	O	0.347	0.166	1.097

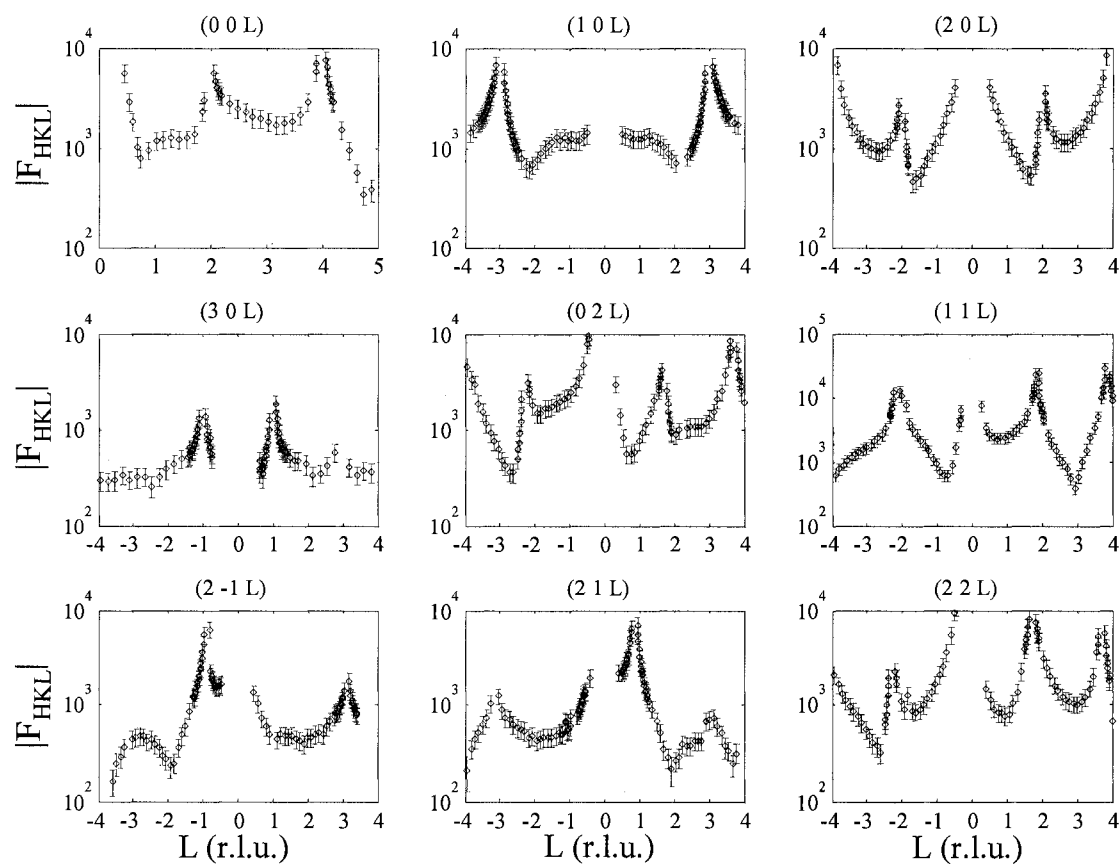


Figure A.1 Experimental structure factor magnitudes ($|F_{HKL}|$) as a function of perpendicular momentum transfer (L , in reciprocal lattice units) for Pb(II) reacted α - $\text{Fe}_2\text{O}_3(1\bar{1}02)$.

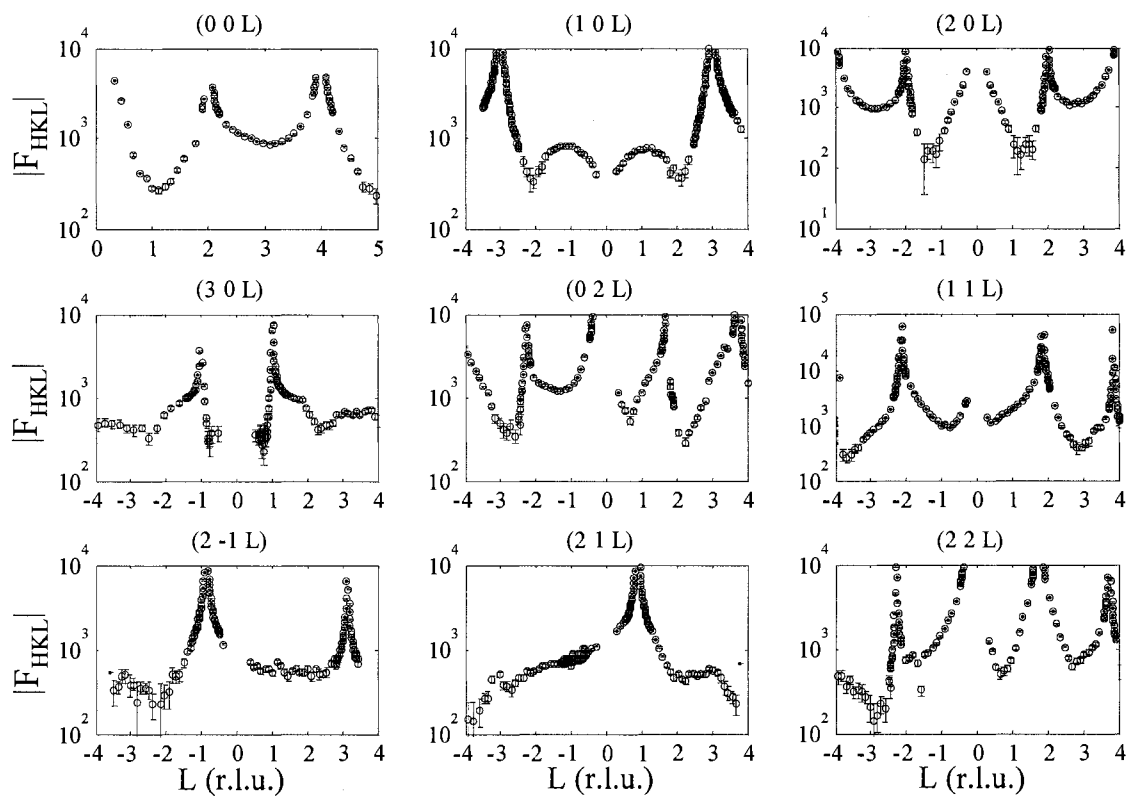


Figure A.2 Experimental structure factor magnitudes ($|F_{HKL}|$) as a function of perpendicular momentum transfer (L , in reciprocal lattice units) for Pb(II) adsorption on Fe(II) pre-reacted α -Fe₂O₃(1 $\bar{1}$ 02).

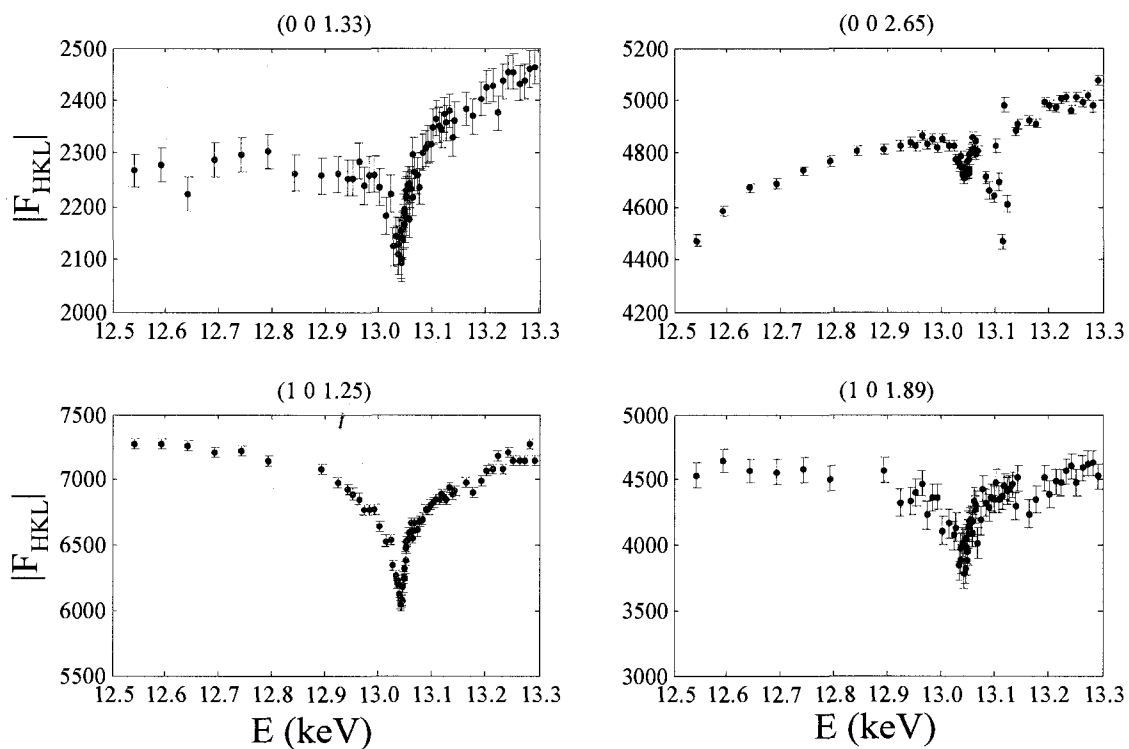


Figure A.3 Resonant anomalous X-ray scattering (RAXS) data, i.e. experimental structure factor magnitudes ($|F|$) as a function of incident beam energy at a fixed (HKL) value which is identified at the top of each subplot, for Pb(II) reacted α -Fe₂O₃(1 $\bar{1}$ 02).

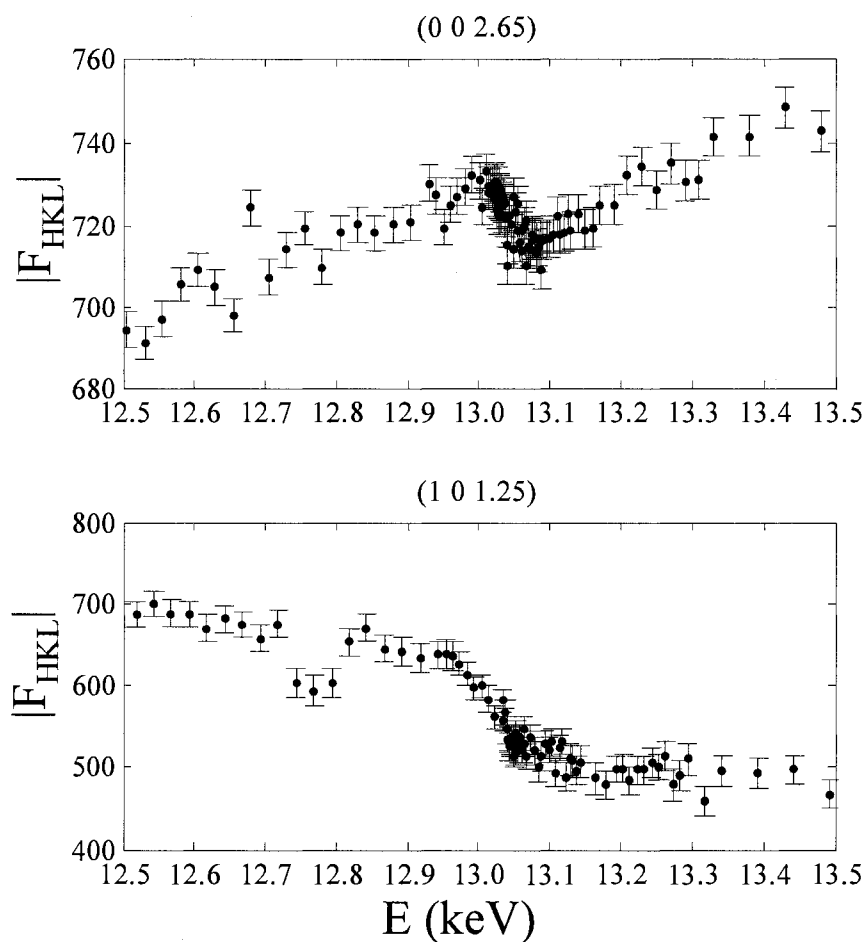


Figure A.4 Resonant anomalous X-ray scattering (RAXS) data, i.e. experimental structure factor magnitudes ($|F|$) as a function of incident beam energy at a fixed (HKL) value which is identified at the top of each subplot, for Pb(II) adsorbed on Fe(II) pre-reacted α -Fe₂O₃(1 $\bar{1}$ 02).

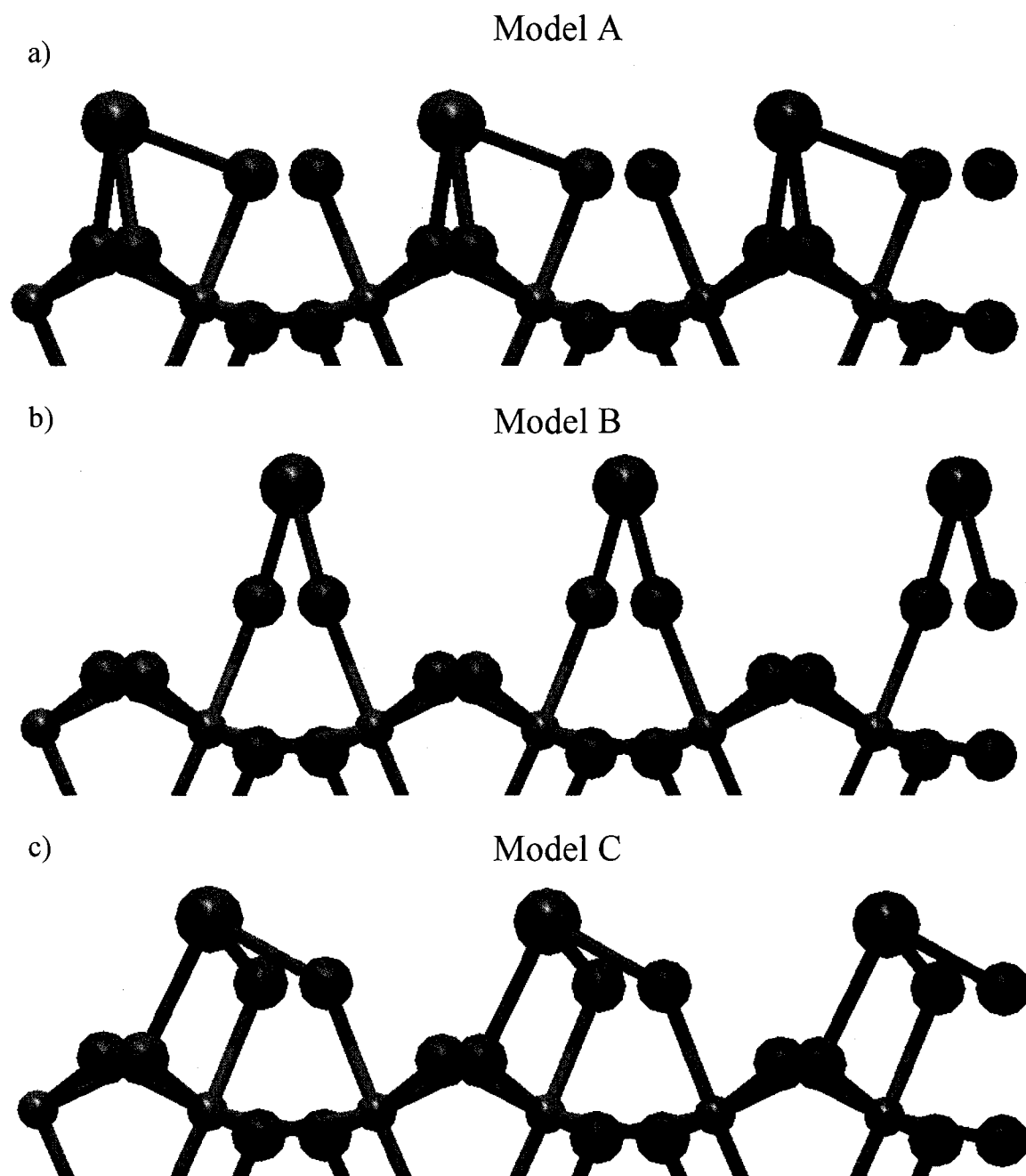


Figure A.5 Structural models of three possible Pb binding geometries on $\alpha\text{-Fe}_2\text{O}_3(1\bar{1}02)$. The small, medium and large spheres represent Fe, O and Pb atoms, respectively. Only top four layers of the substrate are shown and only one of the two chemically equivalent Pb atoms is shown for clarity.

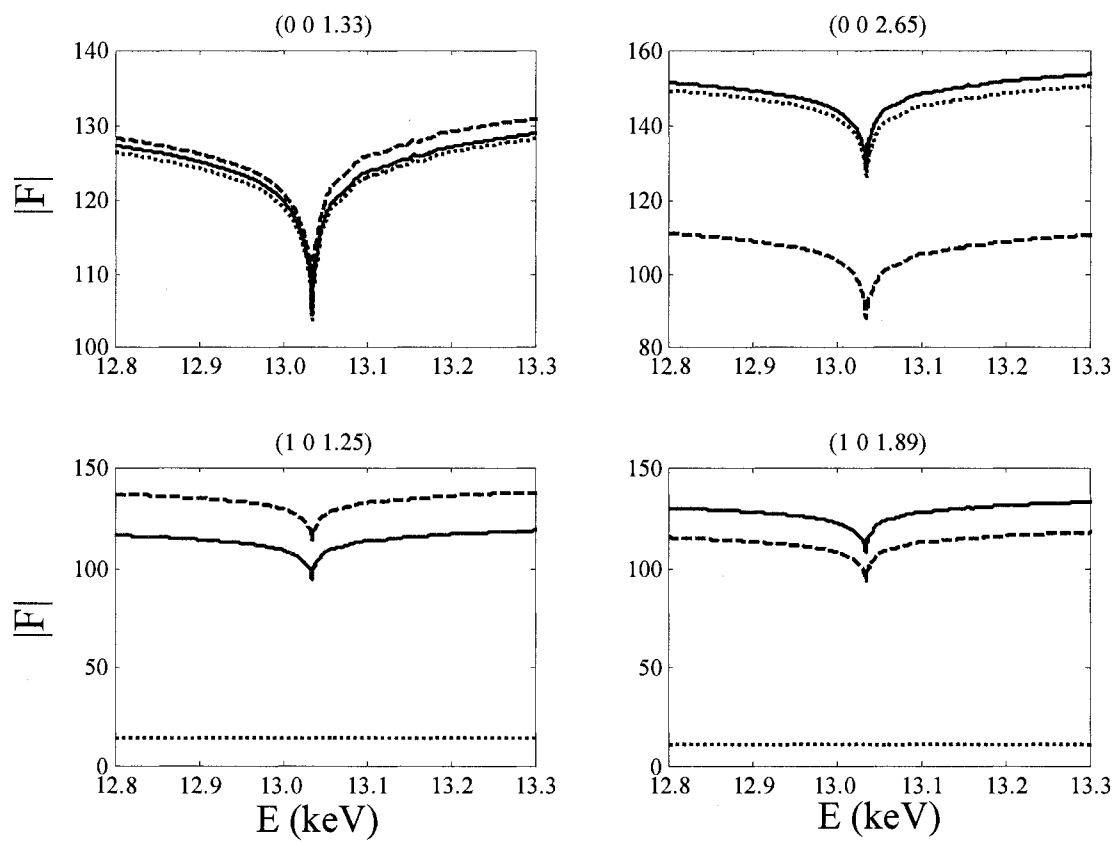


Figure A.6 Simulations of RAXS profiles for three different models shown in Figure A.5. The solid, dashed and dotted lines represent models A, B, and C, respectively.

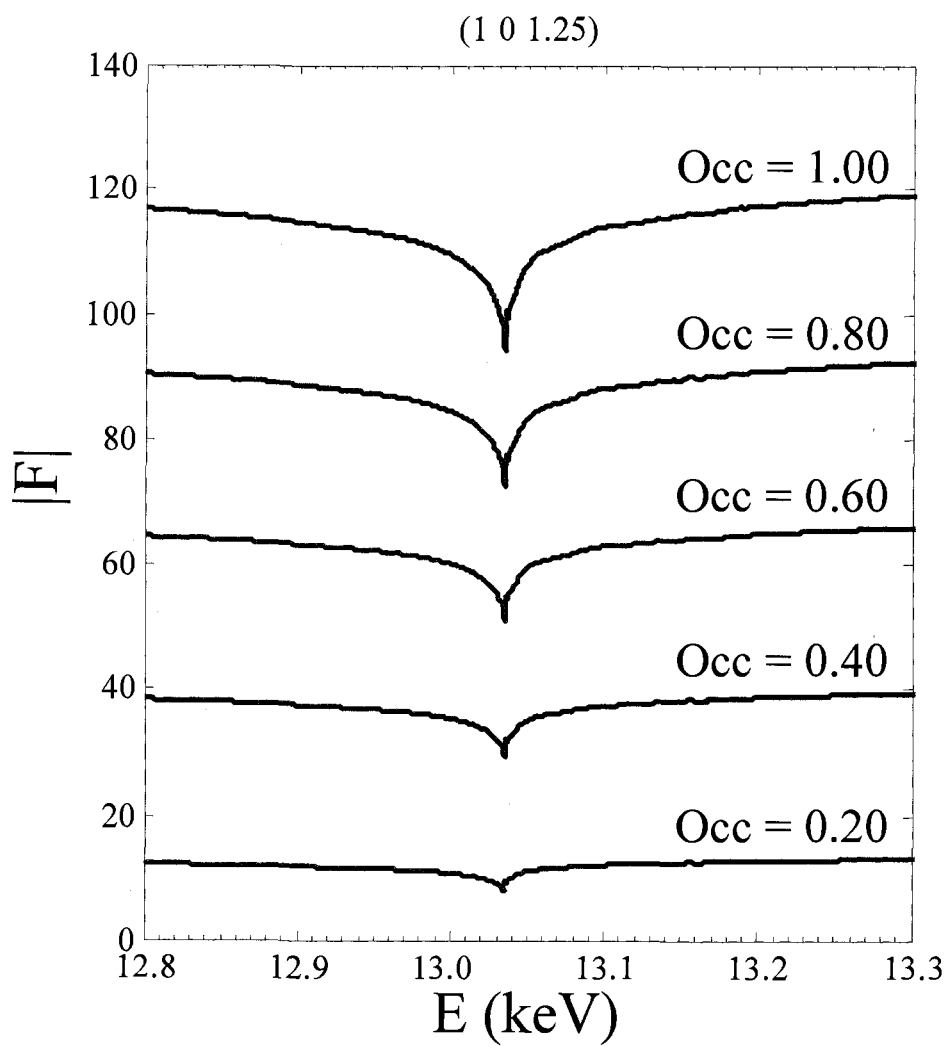


Figure A.7 Simulations of RAXS profiles for model A (Figure A.5) as a function of Pb(II) occupancy.